Coupling of Surface Plasmons and Semiconductor Nanocrystals for Nanophotonics Applications

A DISSERTATION
SUBMITTED TO THE FACULTY OF
UNIVERSITY OF MINNESOTA
BY

Sriharsha V. Jayanti

IN PARTIAL FULFILLMENT OF THE REQUIREMENTS
FOR THE DEGREE OF
DOCTOR OF PHILOSOPHY

David J. Norris, Co-Advisor
Eray Aydil, Co-Advisor

August 2015

Acknowledgements

I am extremely grateful to all the people that have been a part of my journey over the last 5 years. First and foremost, I would like to thank my advisors, David Norris and Eray Aydil, for their intellectual insight and guidance. They gave me the freedom to design and conduct experiments, allowing me to pursue topics of my liking.

I thank all my colleagues in Zurich for creating a friendly and highly educational environment. In particular, I would like to acknowledge the support of Kevin McPeak and David Kim, who spent countless hours with me in the lab and discussing ideas. I also thank Stephan Kress for valuable discussions and cherish all of our collaborations. I am grateful to all of my collaborators and friends while at the Optical Materials Engineering Laboratory: Daniele Braga, Vincent Holmberg, Ayaskanta Sahu, Jong Hyuk Park, Eva de Leo, Lisa Poulikakos, Jian Cui, Ferry Prins, Yasmina Reis, Michael Heinrich, Felipe Antolinez, Andreas Riedinger, Florian Ott, Paul Erickson, Ava Faridi, Aurelio Rossinelli, Stefan Meyer, Martin Baldinger, Alexandr Dejneka, Dagmar Chvostova, Maximillian Fischer, Jonas Greiner, and Marianne Aellen.

My friends and colleagues in Minneapolis played an important role in making my PhD experience fun and productive. I thank Palak Ambwani, Neema Rastgar, Xiaoshu Chen, Jikku Thomas, Boris Chernomordik, Ankur Khare, Hyungsoon Im, Nathan Lindquist, Prashant Nagpal, Balasubramanian Gopalakrishnan, Aruna Ramakrishnan, Suma Karnam, and Selin Tosun. I also thank William Tisdale for guiding me in the lab through my first year in Ph.D.

I am deeply indebted to Prof. Sang-Hyun Oh and all of his lab members for graciously sharing their lab space with me. I am also very thankful to members of Eray Aydil's lab, who shared equipment freely and allowed me to conduct experiments.

Finally, I would like to thank Akshya Saxena and my family for their unwavering love and support through the highs and lows.

Dedicated to Akshya and my loving family

Abstract

The goal of this thesis is to engineer the interaction between surface plasmons and semiconductor nanocrystals for nanophotonic applications. Plasmonic metals support surface plasmon polaritons, hybrid photon and electron waves that propagate along a metal-dielectric interface. Unlike photons, surface plasmons can be confined in sub-diffraction geometries. This has two important consequences: 1) optical devices can be designed at the nanoscale, and 2) the high density of electromagnetic fields allows study of enhanced light-matter interactions. Surface plasmons have been exploited to demonstrate components of optoelectronic circuits, optical antennas, surface enhanced spectroscopy, enhanced fluorescence from fluorophores, and nanolasers. Despite the advances, surface plasmon losses limit their propagation lengths to tens of micrometers in the visible wavelengths, hindering many applications. Recently, the template-stripping approach was shown to fabricate metal films that exhibit larger grains and smoother surface, reducing the grain boundary and roughness scattering. To further improve the plasmonic properties, we investigate the importance of deposition conditions in the template-stripping approach. We provide insight and recipes to enhance the plasmonic performance of the most commonly used metals in the ultraviolet, visible, and near-infrared. We also explore the potential of low temperatures to improve the performance of metal films, where the electron-electron and electron-phonon scattering should be reduced. This sets a limit on the minimum loss metals can exhibit. Using this knowledge, we study the optical properties of quantum-confined semiconductor nanocrystals near metal structures. Semiconductor nanocrystals have many attractive characteristics that make them suitable for solid-state lighting and solar cells among others. Specifically, CdSe nanocrystals have been heavily studied for their large absorption and emission cross-sections, size dependent emission wavelengths, photostability, and high quantum yields. Here, we focus on studying the emission from CdSe nanocrystals near plasmonic structures in the weak and strong coupling regimes. In the weak coupling regime, plasmonic structures can be used to selectively modify the radiative rates at the desired wavelengths. We tailor plasmonic structures to enhance and tune the emission from the surface states of CdSe nanocrystals throughout the visible. Due

to their size, a significant fraction of atoms are on the surface; however, electron-hole recombination via surface states is typically dark. We further use electrochemistry to probe the energy levels of the surface states. In the strong coupling regime, the energy levels of the surface plasmons and nanocrystals hybridize to form polariton states. In this regime, we demonstrate polariton emission from CdSe/CdSZnS core/shell/shell nanocrystals on silver hole arrays. Emission from these polariton states should be coherent and has implications for thresholdless lasing. While the above studies focus on the change in nanocrystal behavior near metals, these nanocrystals can also be used to improve plasmonic performance. We study the potential of thin layers of CdSe nanocrystals to amplify surface plasmons and enhance their propagation lengths. When the nanocrystals are excited using an external pump, propagating surface plasmons can stimulate emission from these nanocrystals and amplify. If more surface plasmons are generated than lost, then surface-plasmon signals can propagate over extremely long distances and even amplified. We calculate the gain provided and discuss the importance of key parameters such as the absorption and emission cross section, spacer layer thickness, nanocrystal lifetime, and temperature. Finally, we systematically study the emission properties and exciton decay in Ag-doped CdSe nanocrystals, which were recently shown to exhibit enhanced photoluminescence. Overall, this thesis aims to improve plasmonic performance with and without the presence of a gain medium, and advances the understanding of optical behavior of CdSe nanocrystals near metal structures in the weak and strong coupling regimes.

Table of Contents

Chapter 1. Introduction 1

1.1 Introduction 1

1.2 Thesis Overview 3

1.3 Basics of Surface Plasmons and Quantum Dots 6

1.4 References 9

Chapter 2. Plasmonic Films Can Easily Be Better: Rules and Recipes 14

2.1 Introduction 15

2.2 Rules 16

2.3 Optical Performance 22

2.4 Recipes 29

2.5 Materials and Methods 32

2.6 References 34

Chapter 3. Low-Temperature Enhancement of Plasmonic Performance in Silver Films 38

3.1 Introduction 39

3.2 Experiment 40

3.3 Results and Discussion 42

3.4 References 49

Chapter 4. Surface Plasmon Amplification Using Quantum Dots and Experimental Limitations 52

4.1 Introduction 53

4.2 Results and Discussion 55

4.3 Materials and Methods 71

4.4 References 74

Chapter 5. Plasmonic Control of Surface-State Recombination in CdSe Nanocrystals for Tunable Emission 81
5.1 Introduction 82
5.2 Results and Discussion 85
5.3 Materials and Methods 98
5.4 References 107
Chapter 6. Polariton Emission from Strongly Coupled Quantum Dots on Plasmonic Films 114
6.1 Introduction 115
6.2 Results and Discussion 117
6.3 Materials and Methods 128
6.4 References 133
Chapter 7. Exciton Decay in Ag-Doped CdSe Nanocrystals 138
7.1 Introduction 139
7.2 Results and Discussion 141
7.3 Materials and Methods 152
7.4 References 155
Bibliography 158

List of Figures

Figure 2.1 Homologous temperature (T_{sub}/T_{mp} in Kelvin) versus standard electrode potential in volts for Al (black), Cu (red), Au (green), and Ag (blue). 17

Figure 2.2 Scanning electron micrographs of structured films of (a) Al, (b) Cu, (c) Ag, and (d) Au, which were template-stripped from Si templates pre-patterned by focused-ion-beam lithography. 18

Figure 2.3 Atomic force micrographs for template-stripped silver films deposited at a base pressure of $3x10^{-8}$ Torr but at different deposition rates: (a) 1, (b) 5, and (c) 25 Å/sec. 19

Figure 2.4 Optical properties and figures-of-merit for the silver template-stripped films shown in Figure 2.3. 20

Figure 2.5. Optical properties and figures-of-merit for our metallic films of Al (black), Cu (red), Au (green), and Ag (blue). 25

Figure 2.6. Atomic force micrographs of silver films deposited at 0.2 Å/sec at a base pressure of (a) $3x10^{-6}$ Torr and (b) $3x10^{-8}$ Torr. 26

Figure 2.7 Atomic force micrographs of films deposited at $3x10^{-8}$ Torr using the rates detailed in Figure 2.2 in the main text. 28

Figure 2.8 Optical properties and figures-of-merit for Al films deposited at room temperature at a base pressure of $3x10^{-8}$ Torr. 30

Figure 3.1 Atomic force microscope (AFM) images of the three types of Ag films investigated: (a) single-crystalline film (Sample SC), (b) template-stripped polycrystalline film (Sample TS), and (c) rough polycrystalline film (Sample Ro). 41

Figure 3.2 The measured real (a) and imaginary (b) parts of the dielectric function for a single-crystalline Ag film (Sample SC) at various temperatures. The measured real (c) and imaginary (d) parts of the dielectric functions for: (i) Sample SC, (ii) a template-stripped smooth polycrystalline film (Sample TS), and (iii) a rough film (Sample Ro) at 298 (RT) and 5 K. 42

Figure 3.3 Propagation lengths versus temperature expected for a rough film (blue), template-stripped polycrystalline film (red), and single-crystalline film (black). 47

Figure 3.4 (a) Expected enhancements at various temperatures (relative to 298 K) in the surface-plasmon-polariton (SPP) propagation length, L_{SPP}, for sample SC calculated from the measured dielectric functions. (b) The expected enhancements in L_{SPP} at 5 K (relative to 298 K) for samples SC, TS, and Ro. (c) Direct measurements of L_{SPP} from

single-crystalline Ag films at 298 (RT) and 25 K. 200-nm-wide slits and grooves were milled into four identical films using a focused ion beam. 48

Figure 4.1 Emitter dissipation, SPP decay, and lifetime near a metal.....60

Figure 4.2 SPP propagation length calculations. 63

Figure 4.3 The different plasmonic and photonic modes supported in our geometry for different QD thicknesses.....63

Figure 4.4 Gain calculations as a function of pump intensity, spacer thickness, temperature, number of QD layers, and cross-section enhancement. 66

Figure 4.5 Photostability of QD monolayers. 67

Figure 4.6 Experimental setup for measuring gain experiment.....68

Figure 4.7 Characterization of sample for SPP amplification. 69

Figure 4.8 SPP amplification preliminary experiments. 70

Figure 5.1 Deep-trap-emission enhancement from CdSe nanocrystals on rough silver islands. 86

Figure 5.2 Scanning electron microscope images of silver films of different thicknesses when thermally evaporated onto a (100) Si wafer at 0.2 Å/s and pressures below 4 x 10^{-6} Torr. 87

Figure 5.3 Strong deep-trap emission and color gradients are observed at localized surface plasmon hotspots.....88

Figure 5.4 Scanning electron micrographs of quantum dots at rough silver pyramid tips.89

Figure 5.5. Enhanced deep-trap emission and photostability in nitrogen. 91

Figure 5.6 Color tunable emission from CdSe nanocrystals on tailored plasmonic structures.....92

Figure 5.7 The Purcell factor calculated by normalizing the emission in the hole array to the emission on a flat unstructured silver of the same area. 94

Figure 5.8 Scanning electron micrographs of quantum dots on plasmonic structures. 95

Figure 5.9 Electrochemical control of emission in CdSe nanocrystals.....97

Figure 5.10 Lifetimes of CdSe nanocrystals with absorption maximum at 578 nm spin coated on a nominally 10 nm thick rough silver film without an alumina layer.....102

Figure 5.11 Characterization of single-crystalline silver films. 102

Figure 5.12 Scanning electron microscope image of CdSe self-assembled monolayer on a silver hole array. 105

Figure 6.1 Photostability of 320 nm thick film of CdSe-CdS-ZnS nanocrystals on glass pumped with a 400 nm laser of 80 fs pulse width and fluence of 785 μJ/cm^2.....117

Figure 6.2 Strong coupling in transmission measurements. 118

Figure 6.3 Transmission and photoluminescence dispersion curves and lifetimes. 121

Figure 6.4 Modeling of surface plasmon resonances in hole arrays.....122

Figure 6.5 Quality factors in hole arrays obtained using JCMWave simulations.....123

Figure 6.6 Experimental set up for polariton emission nmeasurements. 123

Figure 6.7 Polariton emission from strong couple quantum dots on hexagonal hole arrays. 124

Figure 6.8 Polariton emission dynamics. 127

Figure 7.1 Possible mechanisms for fluorescence enhancement in lightly doped CdSe nanocrystals.....140

Figure 7.2 Photoluminescence spectra and relative quantum yields of NCs for various sizes and doping concentrations. 142

Figure 7.3 Quantum yield for doped 3 nm CdSe NCs after different washes. 143

Figure 7.4 Characterization of Ag doped 2 nm nanocrystals in a toluene dispersion.....145

Figure 7.5 The radiative and the non-radiative rates of 2 nm NCs in toluene at room temperature as a function of doping assuming a 10% quantum yield. 145

Figure 7.6 Temperature dependent PL measurements in poly-lauryl methacrylate matrix. 147

Figure 7.7 Lifetimes as a function of temperature for various doping concentrations in a) 2 nm NCs, b) 2.5 nm NCs, and c) 3 nm NCs. 148

Figure 7.8 Fine structure in doped NCs. 150

List of Tables

Table 2.1 Percentage increase in the figures-of-merit for Al, Cu, Au, and Ag at ultraviolet (280 nm), visible (650 nm), near-infrared (1000 nm), and telecommunication (1550 nm) wavelengths. 26

Table 3.1 Drude parameters extracted from fits of the measured dielectric functions.....45

Table 3.2 Drude-Lorentz parameters extracted from fits of the measured dielectric Functions.....45

Table 4.1 Parameters used for SPP gain calculations.. 61

Chapter 1.

1.1 Introduction

Optical devices, devices that use light, are ubiquitous in our lives, from the display in our televisions to optical fibers that transmit information over thousands of miles in a split-second. Light travels at very high speeds, orders of magnitude larger than those of electrons. Devices or circuits utilizing photons have been shown to be much faster than electrical devices. Despite this, most of the technology is driven by electrical current. The primary reason for this is that conventional optical devices are limited by the diffraction limit, meaning devices that use light cannot be made smaller than half the wavelength of photons (typical wavelengths that humans can perceive range between 400 and 700 nm).[1] Meanwhile, electron based transistors are now of 10 nm dimensions, almost two orders of magnitude smaller.[2]

Recently, the field of plasmonics has emerged due to advances in nanofabrication; it allows optical devices smaller than the diffraction limit.[3] Plasmonic metals support surface plasmons, hybrid electronic and electromagnetic oscillations at the surface of the metal. Surface plasmons retain many of the features of photons, such as the frequencies (therefore, similar bandwidths), energy, and speeds.[4] They also undergo interference.[5] However, surface plasmons are different from photons in key ways. They can be much more spatially confined than photons, approaching nanoscale dimensions. One branch of plasmonics aims to develop nanoscale plasmonic circuitry to replace electronic components on a chip. Such a fundamental re-design of circuitry combines the best of conventional optics and semiconductors electronics: bandwidth and ultrasmall sizes.[1]

A major limitation in plasmonics is surface-plasmon loss.[6-8] Surface plasmons, due to their electronic component, scatter and lose energy to the metal. As a result, their propagation lengths are limited to tens to hundreds of microns. Photonic cavities can routinely be made with quality factors that are orders of magnitude larger than those in plasmonic cavities. One approach to reducing surface-plasmon loss is to fabricate higher quality metal structures. Recently, template stripping was utilized to obtain high-quality

metals with sub-nanometer roughness.[32] Regardless of the fabrication approach, the inherent losses due to electron-electron scattering electron-phonon scattering cannot be overcome.

Another route to overcoming losses of surface plasmons is to compensate by generating additional surface plasmons.[6, 9-14] If the generation of surface plasmons equals the losses, then the net losses are zero and surface plasmons appear to propagate forever. Recently, efforts have tried to use emitters to compensate for losses and increase propagation lengths. However, these efforts were only partially successful. If surface-plasmon generation is larger than losses, then surface plasmons can be amplified.

Surface-plasmon amplification is a prerequisite to the development of a spaser, a nanoscale analog of laser.[9, 15, 16] The spaser was first proposed by Bergman and Stockman as a surface-plasmon analog of laser, producing coherent build up of surface plasmons in a single mode. A spaser could also operate as an ultrafast, bistable transistor to replace conventional semiconductor transistor.[16] Over the last few years, the term spaser has come to include surface-plasmon-based nanolasers, or for that matter, any laser based on surface plasmons.[17-19]

Despite the drawbacks, the spatial confinement of surface plasmons enables study of enhanced interactions with fluorescent materials. These interactions fall into the weak-coupling regime and the strong-coupling regime. In the weak-coupling regime, metal structures can be designed to control an emitter's brightness, directionality, and decay mechanism. This has been used to show enhanced photoluminescence,[20] beaming,[21] and enhanced energy transfer between emitters.[22]

In the strong-coupling regime, the surface plasmon and emitter energy levels hybridize to form new states. These states have completely different properties than the bare states of either the surface plasmons or the emitter. Furthermore, emission from these polaritons is expected to be spatially coherent. This could potentially lead to thresholdless lasers.

A suitable emitter system for all of the above applications is quantum dots. Quantum dots are zero-dimensional semiconductor nanocrystals that have important technological applications in solid-state lighting,[23] solar cells,[24, 25] bioimaging,[26] and

lasers.[27] Compared to other fluorescent materials, quantum dots are promising because they have color-tunable,[28] spectrally narrow, high-quantum-yield,[29] and highly photostable emission.[30]

The interaction of quantum dots with plasmonic structures is a complicated one. Fermi's golden rule states that the emission rate in a fluorophore depends on the optical density of states of the surrounding medium. Consequently, the interaction of the quantum dots with their electromagnetic surrounding determines their emission properties, such as their emission rate,[20, 31] directionality,[21] and even photostability.[32] The presence of metal and metal structures adds additional modes into which the quantum dots can give their energy. Near a metal, the quantum dot can donate its energy to generate an electron-hole pair in the metal, generate surface plasmons, or generate photons. This additionally depends on the structure of the metal, and the distance of the quantum dot to the metal. The design of the optical surrounding (in our case, plasmonic structures) offers exciting opportunities to engineer the emission for targeted applications.

1.2 Thesis Overview

The goal of this dissertation is to study the interaction between quantum dots and plasmonic materials, and engineer this interaction towards three specific applications: overcome surface plasmon loss, enhance and tune the emission from surface states in the weak coupling regime, and demonstrate polariton emission in the strong coupling regime. The rest of this thesis is divided into six chapters. In chapters 2 and 3, I discuss the importance of and methods for reducing surface-plasmon losses. Chapter 4 discusses the amplification of surface plasmons using quantum dots as the gain medium. Chapters 5 and 6 experimentally demonstrate different interaction regimes of surface plasmons and quantum dots. Finally, in chapter 7, Ag-doped CdSe nanocrystals are studied in detail.

In chapter 2, I discuss the deposition of high-quality metal films. The limiting issue in plasmonics is surface-plasmon losses. Surface plasmons can scatter due to multiple mechanisms as they propagate: electron-electron scattering, electron-phonon scattering, grain-boundary scattering, and roughness scattering. Fabricating high-quality metal films is a prerequisite to developing nanoscale plasmonic devices. High quality means two

things: 1) the surface of the metal or structure is very smooth such that roughness scattering is reduced, and 2) the grains are large, so the probability of grain-boundary scattering is reduced. While template stripping has been shown to be an effective approach to producing high-quality films,[33] the deposition conditions can be controlled to further improve the optical quality. In addition, the optimal deposition conditions depend on the metal. Specifically, evaporation conditions for important plasmonic metals, Au, Ag, Al, and Cu, are discussed, and the room-temperature optical constants for the optimized films are reported.

Chapter 3 addresses further this issue of losses. Once the grain-boundary scattering and roughness scattering are reduced to the extent possible, two important scattering mechanisms severely limit device performance: the electron-electron scattering and the electron-phonon scattering. The losses are large in the visible part of the spectrum. These scattering components can be further reduced by lowering the temperature. Such attempts to reduce losses by lowering temperature have previously been only partially successful.[34-36] We tabulate the optical constants, measured by ellipsometry, at various temperatures down to liquid helium temperatures. We further show that the improvements in plasmonic performance depends on the original film quality. The percentage improvement in performance is increased in higher-quality films.

Chapter 4 is a more fundamental undertaking that explores the potential of quantum dots as a gain material for surface-plasmon amplification.[6, 10] Despite the optimization of metal fabrication and lowering temperature, surface-plasmon losses are limiting the propagation lengths and quality factors in plasmonic structures. If propagating surface plasmons can be amplified by stimulated emission from nearby quantum dots and balance the losses, then the surface plasmons can propagate infinitely. First, the emission of quantum dot near a metallic structure is discussed quantitatively, and the expected surface-plasmon amplification is calculated using measured and literature values for important quantum dot parameters. The calculated gain is evaluated in the context of experimental limitations and challenges. We focus on one, the photostability. We improve the stability of core/shell nanocrystals by isolating them in an oxygen- and moisture-free environment. We discuss our preliminary results and provide future direction.

In chapter 5, plasmonic structures are used to tune the emission from CdSe nanocrystals. Due to their small sizes, CdSe nanocrystals have a significant fraction of their atoms on the surface, leading to dangling bonds and a large number of mid-band gap recombination centers. The recombination through these "deep trap" states is typically weak or dark, and very few studies have sought to exploit this emission.[37-39] We tailored plasmonic structures to selectively enhance or suppress the deep-trap emission following Fermi's golden rule. We demonstrate that the color of the emission can be tuned throughout the visible at the spatial coordinates of choice. Furthermore, we use electrochemistry to shift the Fermi level up and down to demonstrate that hole traps are responsible for the optically active deep-trap emission.

While chapter 5 took advantage of weak interactions between surface plasmons and quantum dots, chapter 6 demonstrates strong coupling of surface plasmons and quantum dots. In the strong-coupling regime, the strong interaction of the surface plasmons with the quantum dots leads to hybridization of the energy levels of the surface plasmons and quantum dots and new states are formed that are neither surface plasmon nor quantum dot in nature.[40] Emission from these polariton states is widely expected to be spatially coherent.[41, 42] Additionally, because this coupled system is by default in a coherent state, no population inversion or stimulated emission is necessary. Our results could therefore lead to thresholdless lasers. While strong coupling has previously been shown with organic semiconducting fluorophores, quantum dots provide a color-tunable and photostable emitter system.

Chapter 7 discusses doped quantum dots. Introducing electronic impurities into nanocrystals can improve their conductivity and optical properties. Recently, CdSe nanocrystals doped with a few Ag atoms were shown to exhibit brighter emission and improved electrical properties.[43] We investigate this carefully to explain the origin of the observations. We synthesize nanocrystals with various amounts of dopants, and characterize them thoroughly using temperature-dependent photoluminescence spectra, photoluminescence excitation spectra, fluorescence-line-narrowing spectra and temperature-dependent lifetimes. We show that the longitudinal optical phonon coupling strength is increased in lightly doped nanocrystals and decreased in heavily doped

nanocrystals. Our lifetime and photoluminescence trends are consistent with the previously suggested mechanism of Ag acting as an interstitial cation in the lightly doped nanocrystals, and forming a substitutional dopant in heavily doped nanocrystals.

1.3 Basics of Surface Plasmons and Quantum Dots

Surface Plasmons

Surface-plasmon resonances are hybrid electromagnetic and electronic oscillations that are confined to the interface between a metal and a dielectric.[44, 45] Depending on the localization of surface plasmons, they are termed localized surface plasmons or surface plasmon polaritons. Localized surface plasmons are confined in all three dimensions, and occur as standing wave resonances of the electron cloud in sub-wavelength metal structures. An incident electric-field accelerates the electrons, while a restoring force (resulting from the induced polarization) acts in the opposite direction, causing the resonance. On the other hand, surface plasmon polaritons can propagate along the interface, and typically occur on smooth or periodic metal surfaces. The surface-plasmon-polariton field and intensity peak at the metal-dielectric interface and decay exponentially away from the surface. By proper design of metal and dielectric structures, surface plasmons can be spatially confined in mode volumes that are orders of magnitude smaller than photonic mode volumes. Consequently, electromagnetic energy can be manipulated at the nanoscale.

Unless otherwise stated, the term surface plasmon is used interchangeably with surface plasmon polariton, since these are the focus of this dissertation. The existence of a surface plasmon is dictated by Maxwell's equations. Specifically, the real parts of the dielectric constants of the two media at an interface should have opposite signs.[45] Dielectric materials have a positive and real dielectric constant, whereas metals have a complex dielectric constant, with a negative real part. The negative real part implies that electromagnetic waves cannot propagate through the metal, and the imaginary part determines the absorption or loss of electromagnetic energy to the metal.

The hybrid nature of surface plasmons means that their momentum is larger than that of photons at the same frequency.[45] To conserve momentum, momentum needs to be provided (subtracted) to photons (surface plasmons) to convert them into surface plasmons (photons). This can be achieved by introducing a grating on the metal with a periodicity matching the photon's wavelength.[46] Metals can be structured to control the directionality of surface plasmon to photon coupling, and in general, to control the band structure of surface plasmons on an energy-momentum dispersion diagram.

Quantum Dots

Quantum dots (QDs) are semiconductor nanocrystals with dimensions less than the exciton Bohr radius.[47] At such dimensions, the electron and hole of the quantum dot are spatially confined by the particle border, and can be treated as individual particles in a spherical box. As a result, the nanocrystals' energy levels become discretized and their band gap becomes a strong function of the size. Hence, the band-gap energy can be tuned by controlling the size. For example, the band gap of CdSe QDs, the primary system of this work, can be varied over the entire visible range by controlling the diameter between 1 nm and 6 nm.

When electrons in the QDs are excited from the valence band edge to the conduction band edge, the electrons can relax to the ground state either radiatively or non-radiatively. In radiative recombination, the excited electron relaxes by emitting a photon. In non-radiative recombination, the electron relaxes through surface trap states or an Auger process (when the electron gives its energy to other electrons). In the presence of a metal, the electrons can also non-radiatively transfer their energy to ohmic loss in the metal or to surface plasmons.[31, 48]

Since QDs contain only a few hundred to a few thousand atoms, a large fraction of atoms are on the surface and have dangling bonds, resulting in surface-trap states.[49] This increases non-radiative recombination and decreases the quantum yield. Ligands, such as trioctylphosphine oxide, are used to reduce dangling bonds by binding to the Cd or Se sites on CdSe QDs.[50] To further increase the quantum yield or the photostability, a shell of semiconducting material is often added over the QD core.[51, 52] The shell, typically

exhibiting a lattice mismatch of less than 10%, reduces the dangling bonds on the surface and further confines the carriers to the core.[52] In all of our work, the focus will be on CdSe, a direct-gap semiconductor. CdSe QDs have been widely studied because of their tunable optical properties in the visible range of wavelengths.[28] Furthermore, they can be easily prepared in lab with high quantum yields and photostability.[53]

1.4 References

[1] A. Boltasseva, H. A. Atwater, "Low-loss plasmonic metamaterials." *Science* **331**, 290-291 (2011).

[2] D. James, *Custom Integrated Circuits Conference*. (IEEE, 2012).

[3] T. W. Ebbesen, H. Lezec, H. Ghaemi, T. Thio, P. Wolff, "Extraordinary optical transmission through sub-wavelength hole arrays." *Nature* **391**, 667-669 (1998).

[4] W. L. Barnes, A. Dereux, T. W. Ebbesen, "Surface plasmon subwavelength optics." *Nature* **424**, 824-830 (2003).

[5] M. Steel, "Quantum plasmonics: Two-plasmon interference." *Nature Photonics* **8**, 273-275 (2014).

[6] P. Berini, I. De Leon, "Surface plasmon-polariton amplifiers and lasers." *Nature Photonics* **6**, 16-24 (2012).

[7] M. Nezhad, K. Tetz, Y. Fainman, "Gain assisted propagation of surface plasmon polaritons on planar metallic waveguides." *Optics Express* **12**, 4072-4079 (2004).

[8] D. K. Gramotnev, S. I. Bozhevolnyi, "Plasmonics beyond the diffraction limit." *Nature Photonics* **4**, 83-91 (2010).

[9] M. I. Stockman, "Spaser action, loss compensation, and stability in plasmonic systems with gain." *Physical Review Letters* **106**, 156802 (2011).

[10] P. Bolger, W. Dickson, A. Krasavin, L. Liebscher, S. Hickey, D. Skryabin, A. Zayats, "Amplified spontaneous emission of surface plasmon polaritons and limitations on the increase of their propagation length." *Optics Letters* **35**, 1197-1199 (2010).

[11] I. De Leon, P. Berini, "Amplification of long-range surface plasmons by a dipolar gain medium." *Nature Photonics* **4**, 382-387 (2010).

[12] S. M. García-Blanco, M. Pollnau, S. I. Bozhevolnyi, "Loss compensation in long-range dielectric-loaded surface plasmon-polariton waveguides." *Optics Express* **19**, 25298-25311 (2011).

[13] S. p. Kéna-Cohen, P. N. Stavrinou, D. D. Bradley, S. A. Maier, "Confined surface plasmon–polariton amplifiers." *Nano Letters* **13**, 1323-1329 (2013).

[14] M. Noginov, V. A. Podolskiy, G. Zhu, M. Mayy, M. Bahoura, J. Adegoke, B. Ritzo, K. Reynolds, "Compensation of loss in propagating surface plasmon polariton by gain in adjacent dielectric medium." *Optics Express* **16**, 1385-1392 (2008).

[15] D. J. Bergman, M. I. Stockman, "Surface plasmon amplification by stimulated emission of radiation: Quantum generation of coherent surface plasmons in nanosystems." *Physical Review Letters* **90**, 027402 (2003).

[16] M. I. Stockman, "The spaser as a nanoscale quantum generator and ultrafast amplifier." *Journal of Optics* **12**, 024004 (2010).

[17] R. Flynn, C. Kim, I. Vurgaftman, M. Kim, J. Meyer, A. Mäkinen, K. Bussmann, L. Cheng, F.-S. Choa, J. Long, "A room-temperature semiconductor spaser operating near 1.5 μm." *Optics Express* **19**, 8954-8961 (2011).

[18] M. Noginov, G. Zhu, A. Belgrave, R. Bakker, V. Shalaev, E. Narimanov, S. Stout, E. Herz, T. Suteewong, U. Wiesner, "Demonstration of a spaser-based nanolaser." *Nature* **460**, 1110-1112 (2009).

[19] N. I. Zheludev, S. Prosvirnin, N. Papasimakis, V. Fedotov, "Lasing spaser." *Nature Photonics* **2**, 351-354 (2008).

[20] K. Shimizu, W. Woo, B. Fisher, H. Eisler, M. Bawendi, "Surface-enhanced emission from single semiconductor nanocrystals." *Physical Review Letters* **89**, 117401 (2002).

[21] Y. C. Jun, K. C. Huang, M. L. Brongersma, "Plasmonic beaming and active control over fluorescent emission." *Nature Communications* **2**, 283 (2011).

[22] P. Andrew, W. Barnes, "Energy transfer across a metal film mediated by surface plasmon polaritons." *Science* **306**, 1002-1005 (2004).

[23] S. Coe, W.-K. Woo, M. Bawendi, V. Bulović, "Electroluminescence from single monolayers of nanocrystals in molecular organic devices." *Nature* **420**, 800-803 (2002).

[24] I. Gur, N. A. Fromer, M. L. Geier, A. P. Alivisatos, "Air-stable all-inorganic nanocrystal solar cells processed from solution." *Science* **310**, 462-465 (2005).

[25] P. V. Kamat, "Quantum dot solar cells. Semiconductor nanocrystals as light harvesters†." *The Journal of Physical Chemistry C* **112**, 18737-18753 (2008).

[26] X. Michalet, F. F. Pinaud, L. A. Bentolila, J. M. Tsay, S. Doose, J. J. Li, G. Sundaresan, A. M. Wu, S. S. Gambhir, S. Weiss, "Quantum dots for live cells, in vivo imaging, and diagnostics." *Science* **307**, 538-544 (2005).

[27] V. Klimov, A. Mikhailovsky, S. Xu, A. Malko, J. Hollingsworth, C. Leatherdale, H.-J. Eisler, M. Bawendi, "Optical gain and stimulated emission in nanocrystal quantum dots." *Science* **290**, 314-317 (2000).

[28] C. Murray, D. J. Norris, M. G. Bawendi, "Synthesis and characterization of nearly monodisperse cde (e= sulfur, selenium, tellurium) semiconductor nanocrystallites." *Journal of the American Chemical Society* **115**, 8706-8715 (1993).

[29] O. Chen, J. Zhao, V. P. Chauhan, J. Cui, C. Wong, D. K. Harris, H. Wei, H.-S. Han, D. Fukumura, R. K. Jain, "Compact high-quality cdse–cds core–shell nanocrystals with narrow emission linewidths and suppressed blinking." *Nature Materials* **12**, 445-451 (2013).

[30] Y. Chen, J. Vela, H. Htoon, J. L. Casson, D. J. Werder, D. A. Bussian, V. I. Klimov, J. A. Hollingsworth, "“Giant” multishell CdSe nanocrystal quantum dots with suppressed blinking." *Journal of the American Chemical Society* **130**, 5026-5027 (2008).

[31] W. Barnes, "Fluorescence near interfaces: The role of photonic mode density." *journal of Modern Optics* **45**, 661-699 (1998).

[32] J. Jasieniak, P. Mulvaney, "From Cd-rich to Se-rich-the manipulation of CdSe nanocrystal surface stoichiometry." *Journal of the American Chemical Society* **129**, 2841-2848 (2007).

[33] P. Nagpal, N. C. Lindquist, S.-H. Oh, D. J. Norris, "Ultrasmooth patterned metals for plasmonics and metamaterials." *Science* **325**, 594-597 (2009).

[34] J.-S. G. Bouillard, W. Dickson, D. P. O’Connor, G. A. Wurtz, A. V. Zayats, "Low-temperature plasmonics of metallic nanostructures." *Nano Letters* **12**, 1561-1565 (2012).

[35] M. Liu, M. Pelton, P. Guyot-Sionnest, "Reduced damping of surface plasmons at low temperatures." *Physical Review B* **79**, 035418 (2009).

[36] M. Mayy, G. Zhu, E. Mayy, A. Webb, M. Noginov, "Low temperature studies of surface plasmon polaritons in silver films." *Journal of Applied Physics* **111**, 094103 (2012).

[37] D. R. Baker, P. V. Kamat, "Tuning the emission of CdSe quantum dots by controlled trap enhancement." *Langmuir* **26**, 11272-11276 (2010).

[38] M. J. Bowers, J. R. McBride, S. J. Rosenthal, "White-light emission from magic-sized cadmium selenide nanocrystals." *Journal of the American Chemical Society* **127**, 15378-15379 (2005).

[39] M. A. Schreuder, K. Xiao, I. N. Ivanov, S. M. Weiss, S. J. Rosenthal, "White light-emitting diodes based on ultrasmall CdSe nanocrystal electroluminescence." *Nano Letters* **10**, 573-576 (2010).

[40] P. Törmä, W. Barnes, "Strong coupling between surface plasmon polaritons and emitters." *Reports on Progress in Physics* **78**, 013901 (2015).

[41] S. A. Guebrou, C. Symonds, E. Homeyer, J. Plenet, Y. N. Gartstein, V. M. Agranovich, J. Bellessa, "Coherent emission from a disordered organic semiconductor induced by strong coupling with surface plasmons." *Physical Review Letters* **108**, 066401 (2012).

[42] L. Shi, T. Hakala, H. Rekola, J.-P. Martikainen, R. Moerland, P. Törmä, "Spatial coherence properties of organic molecules coupled to plasmonic surface lattice resonances in the weak and strong coupling regimes." *Physical Review Letters* **112**, 153002 (2014).

[43] A. Sahu, M. S. Kang, A. Kompch, C. Notthoff, A. W. Wills, D. Deng, M. Winterer, C. D. Frisbie, D. J. Norris, "Electronic impurity doping in CdSe nanocrystals." *Nano Letters* **12**, 2587-2594 (2012).

[44] H. Raether, *Surface Plasmons on Smooth Surfaces*. (Springer, 1988).

[45] S. A. Maier, *Plasmonics: Fundamentals and Applications*. (Springer Science & Business Media, 2007).

[46] M. Moskovits, "Surface-enhanced spectroscopy." *Reviews of Modern Physics* **57**, 783 (1985).

[47] V. I. Klimov, *Semiconductor and metal nanocrystals: Synthesis and electronic and optical properties*. (CRC Press, 2003).

[48] R. Chance, A. Prock, R. Silbey, "Molecular fluorescence and energy transfer near interfaces." *Advances in Chemical Physics* **37**, 65 (1978).

[49] C. B. Murray, C. Kagan, M. Bawendi, "Synthesis and characterization of monodisperse nanocrystals and close-packed nanocrystal assemblies." *Annual Review of Materials Science* **30**, 545-610 (2000).

[50] X. Huang, E. Lindgren, J. R. Chelikowsky, "Surface passivation method for semiconductor nanostructures." *Physical Review B* **71**, 165328 (2005).

[51] W. Li, S. Xie, L. Qian, B. Chang, B. Zou, W. Zhou, R. Zhao, G. Wang, "Large-scale synthesis of aligned carbon nanotubes." *Science* **274**, 1701-1703 (1996).

[52] S. Kim, B. Fisher, H.-J. Eisler, M. Bawendi, "Type-ii quantum dots: CdTe/CdSe (core/shell) and CdSe/ZnTe (core/shell) heterostructures." *Journal of the American Chemical Society* **125**, 11466-11467 (2003).

[53] P. Reiss, J. Bleuse, A. Pron, "Highly luminescent CdSe/ZnSe core/shell nanocrystals of low size dispersion." *Nano Letters* **2**, 781-784 (2002).

Chapter 2.

Plasmonic Films Can Easily Be Better: Rules and Recipes[1]

High-quality materials are critical for advances in plasmonics, especially as researchers now investigate quantum effects at the limit of single surface plasmons or exploit ultraviolet- or CMOS-compatible metals such as aluminum or copper. Unfortunately, due to inexperience with deposition methods, many plasmonics researchers deposit metals under the wrong conditions, severely limiting performance unnecessarily. This is then compounded as others follow their published procedures. Here, we describe simple rules collected from the surface-science literature that allow high-quality plasmonic films of aluminum, copper, gold, and silver to be easily deposited with commonly available equipment (a thermal evaporator). Recipes are also provided so that films with optimal optical properties can be routinely obtained.

[1] Reproduced with permission from Kevin M. McPeak, Sriharsha V. Jayanti, Stephan J. P. Kress, Stefan Meyer, Stelio Iotti, Aurelio Rossinelli, and David J. Norris, "Plasmonic films can easily be better: rules and recipes," *ACS Photonics* **2015**. Copyright ©2015 American Chemical Society.

2.1 Introduction

Plasmonics requires simple methods to deposit metallic films with optimized optical performance and precise microstructure. Such films allow low-loss plasmonic devices with well-placed nanoscale features to be created. However, for a given metal, the dielectric function (or relative permittivity) and film morphology depend greatly on the deposition conditions. Many plasmonics researchers struggle with this problem, particularly if film growth is not within their area of expertise. Fortunately, surface scientists have reported extensively over the past 60 years on the relationships between how a metallic film is deposited and its properties.[1-4] Here, we aim to condense this knowledge into a useful form for the plasmonics community. We discuss the key issues and then provide recipes that can be used to improve the properties of plasmonic films without any additional effort.

Experimentally, the goal is to deposit dense metallic films with high purity, low surface roughness, and large grain sizes (*i.e.* grain diameters of approximately the film thickness). In such films, losses are reduced and precise structures can be formed with focused-ion-beam (FIB) lithography or other techniques. To grow these films, here we assume the reader has access to a commonly available deposition apparatus, a thermal evaporator. Further, we assume that the evaporator is limited to high-vacuum conditions (with pressures in the 10^{-6} to 10^{-8} Torr range) instead of ultra-high vacuum. For simplicity, we consider standard silicon wafers (including their native oxide) as the substrates with the deposition performed at room temperature. This temperature allows simple evaporators without substrate heaters to be utilized. It also avoids undesirable dewetting of the metal from the substrate, which can occur at elevated temperatures, as discussed below. Under these conditions, we then exploit prior literature knowledge and show how to deposit four common plasmonic metals (Al, Cu, Au, and Ag). Silver and gold are well-known plasmonic metals. Aluminum and copper are becoming increasingly important for ultraviolet (UV) and CMOS-compatible applications.[5-8]

2.2 Rules

In general, many experimental factors affect the optical performance and microstructure of pure polycrystalline metallic films. This includes the deposition rate, the base pressure in the deposition chamber, the substrate temperature, and the overall film thickness. How sensitive the final behavior of the film is to these experimental parameters also depends on the intrinsic properties both of the metal (*e.g.*, its reactivity, bulk- and surface-diffusion coefficients, and surface energy) and of the substrate (*e.g.*, its roughness and surface energy). The question we wish to address is which of these factors is the most important for optimizing the deposition of plasmonic metallic films. In other words, what rules should we follow?

Previous work by surface scientists has shown[1-4] that the homologous temperature of the deposition (T_h), which is defined as the ratio of the substrate temperature, T_{sub}, to the melting temperature of the metal, T_{mp}, is useful for describing the growth mechanism and resulting microstructure in a variety of thin films. Specifically, T_h provides an effective scale for describing fundamental thermally activated phenomena in film formation (*e.g.* nucleation, crystal growth, and grain growth). However, one can imagine that additional factors, such as the reactivity of the metal (*e.g.* how easily it reacts with residual gases in the chamber)[9, 10] as well as the metal-substrate contact angle[11, 12] (*e.g.* wetting) will also strongly affect the purity, density, and hence quality of the deposited film.

We reduce the complexity of all of these factors by representing each metal in terms of just two key parameters. This oversimplifies many of the details of the deposition, but is sufficient for our purposes. Specifically, Figure 2.1 plots the homologous temperature of the deposition versus the standard electrode potential for Al, Cu, Au, and Ag. Metals with higher standard electrode potentials are more reactive, as indicated qualitatively by the arrow at the top of the graph.

What can we learn from such a plot? First, all of the metals studied here are deposited with $T_h \sim 0.3$ (assuming T_{sub} is at room temperature). Surface science teaches that films deposited with $0.15 < T_h < 0.3$ contain metastable phases with surface-diffusion-driven grain growth proceeding for the mobile grain boundaries.[2] Growth models refer to this

range of T_h as a transition zone since more than one but not all grain boundaries are mobile.[2, 3] This results in a bimodal distribution in grain size. Indeed, this effect can be observed in the scanning electron micrographs of our deposited films (see Figure 2.2). Considering that all of our metals have similar T_h values, it is not surprising that their grain sizes are similar, in the 500 nm to 1 μm range. Perhaps more importantly for our present goals, their similar T_h values indicate that it is reasonable to pick a fixed deposition temperature for all four metals (*e.g.* room temperature) and not consider this parameter further for their optimization. This is the first rule learned from Figure 2.1.

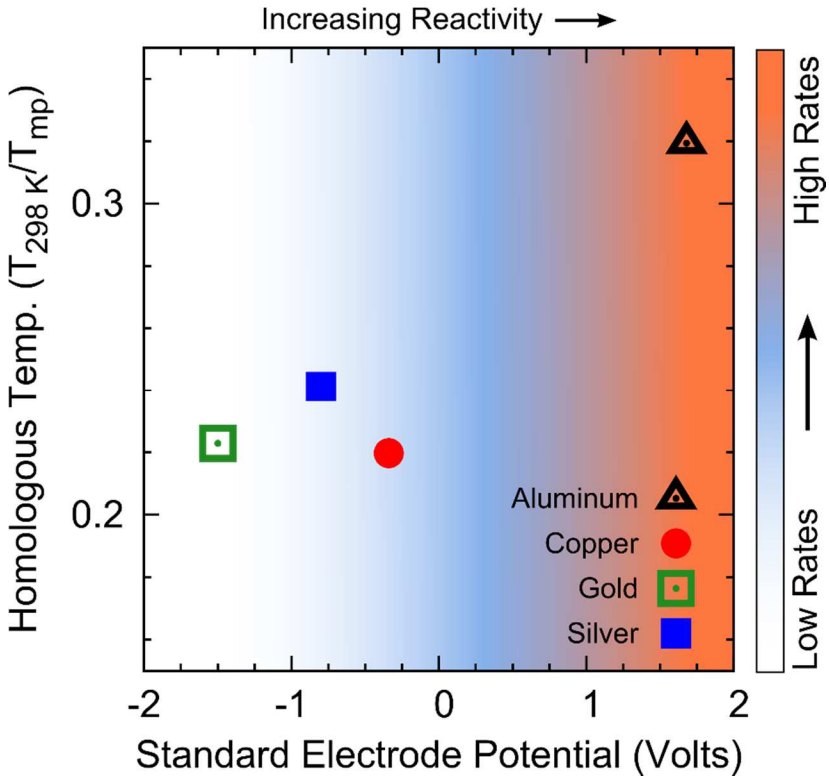

Figure 2.1 Homologous temperature (T_{sub}/T_{mp} in Kelvin) versus standard electrode potential in volts for Al (black), Cu (red), Au (green), and Ag (blue). The reactivity of the metal increases to the right. The background color represents the qualitative trend in deposition rates necessary to achieve high-quality metallic films in the high-vacuum regime, as discussed in the text.

Second, Figure 2.1 shows that our metals have a range of reactivities. This parameter is important to consider because it describes how readily the metal atoms will interact with residual gas molecules in the chamber (*i.e.* gas molecules that have not been removed by the vacuum pump). The dominant residual gas in the high-vacuum regime is water

vapor.[13] Oxygen typically has a partial pressure an order of magnitude lower, but is more reactive.[14] Even for metals with low reactivity, these residual gases can be problematic. They adsorb on the freshly deposited film and pin grain boundaries, which reduces the average grain size in the film, thus creating more electron-scattering centers.[10, 15] This can be particularly harmful to the optical properties of metallic films in the UV and visible regimes due to their large number of free electrons.[10, 16] Thus, the second rule from Figure 2.1 is that we should always deposit under the best vacuum conditions possible to reduce the effects of residual gases. (Acceptable pressure ranges for each metal are listed in the Recipes section below.)

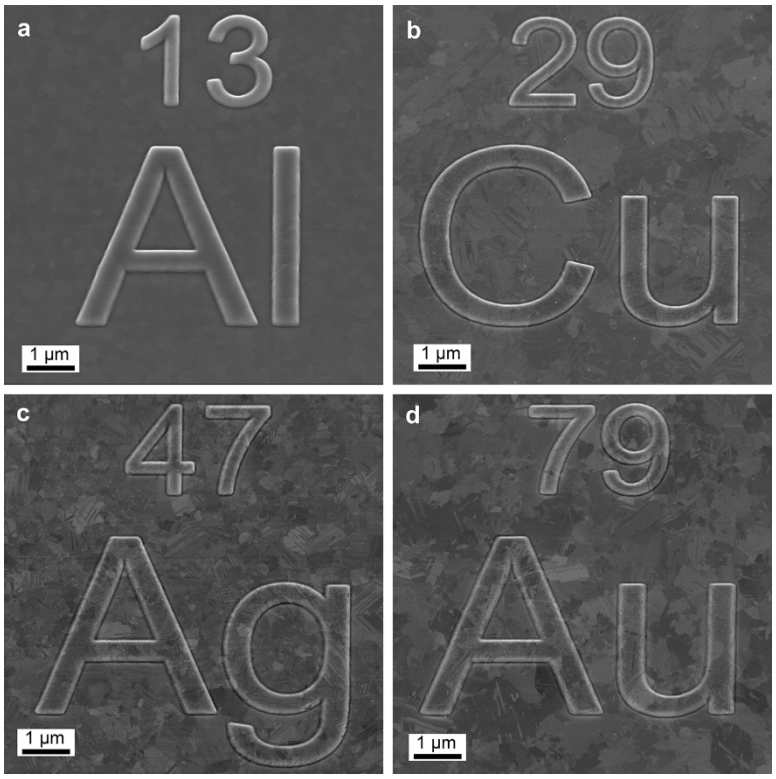

Figure 2.2 Scanning electron micrographs of structured films of (a) Al, (b) Cu, (c) Ag, and (d) Au, which were template-stripped from Si templates pre-patterned by focused-ion-beam lithography. The depositions were performed at room temperature at a base pressure of 3×10^{-8} Torr and rates of 150, 35, 50, and 10 Å/sec, respectively.

However, for reactive metals, our best vacuum may not be sufficient. In this case, the metal atoms can still react with trace water or oxygen molecules in the chamber before depositing on the substrate. The film will then be contaminated with metal oxide. To avoid this, we should deposit reactive metals at fast rates to reduce the interaction time. Furthermore, ultrafast deposition of reactive metals offers the added benefit that the concentration of residual gases can actually be reduced (or gettered) by reactions in the chamber before deposition begins (*i.e.* before the substrate shutter is opened). Thus, the third rule from Figure 2.1 is that we should increase the deposition rate for reactive metals.

Even for Ag, which is not particularly reactive but is susceptible to grain-boundary pinning by residual gases (mentioned above), fast deposition rates can improve film quality. For example, Figure 2.3 shows atomic force micrographs for three Ag films deposited under our best vacuum conditions ($3x10^{-8}$ Torr), but at different rates. Even at this low pressure, the deposition rate of 25 Å/sec results in a significant increase in grain size compared to the more commonly used 1 Å/sec. Figure 2.4 confirms a gradual reduction in optical losses as the rate is increased, consistent with reduced electron scattering in films with larger grain size.

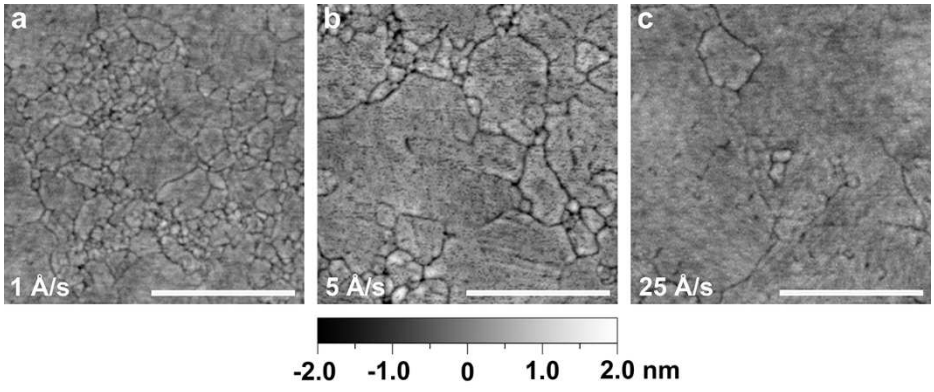

Figure 2.3 Atomic force micrographs for template-stripped silver films deposited at a base pressure of $3x10^{-8}$ Torr but at different deposition rates: (a) 1, (b) 5, and (c) 25 Å/sec. The roughness values for the films over a 2.5 μm x 2.5 μm area are: (a) 0.32, (b) 0.45, and (c) 0.32 nm RMS. While all the films have similar roughness, their grain size increases with faster deposition rates. This results in a reduction in the optical losses, as shown in Figure 2.4. The scale bar corresponds to 500 nm.

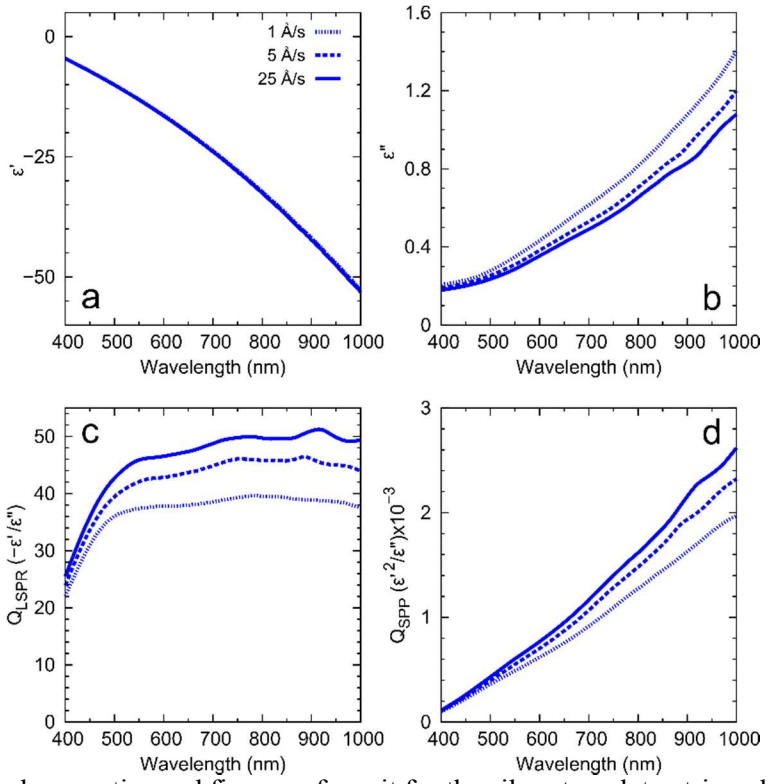

Figure 2.4 Optical properties and figures-of-merit for the silver template-stripped films shown in Figure 2.3. Films were evaporated at a base pressure of 3×10^{-8} Torr and at rates of 1, 5, and 25 Å/sec. (a) and (b) show the real and imaginary part of the dielectric function, respectively. (c) and (d) plot calculated quality factors[17] for the localized surface plasmon resonance in spherical structures (Q_{LSPR}) and surface plasmon polaritons (Q_{SPP}), respectively. The data for the films were smoothed with a five-point moving average.

Should one conclude from the above discussion that fast deposition rates are always better? Fast rates can also potentially have negative consequences. In addition to wasting material during ramp-up of the evaporator (which for expensive metals is a relevant issue), fast rates also reduce the time that freshly added metal atoms (adatoms) can diffuse on the substrate before being bombarded by additional atoms. This has the tendency to produce smaller grains, especially at low substrate temperatures where surface diffusion is minimal.[2, 18] However, in the high-vacuum regime, where the amount of residual gases can still be considerable, the ability of these contaminants to pin grain boundaries and form metal-oxide inclusions can be a larger concern, depending on the metal.

Based on all of these considerations, we have added a graded background color in Figure 2.1 to provide a qualitative guide for the relative deposition rates necessary to obtain a particular metal with good optical properties and low roughness under the assumed experimental conditions. Highly reactive metals, such as Al, should be deposited at 100 Å/sec or faster.[16] Unreactive metals such as Au are far less susceptible to residual gases and therefore can be deposited at lower rates (*e.g.* 1 Å/sec) without deleterious effects to their optical properties. We note, however, that for a given metal, the required deposition rate can change depending on the vacuum conditions (*i.e.* the amount of residual gases). We give examples of this below.

Following this discussion, it is interesting to now return and ask whether substrate heating would improve the films further. In other words, above we followed our first rule and fixed the substrate temperature for all of our metals at room temperature for experimental simplicity. Would we gain in performance by increasing the substrate temperature (and hence T_h)? Higher T_h can certainly increase grain size by providing more energy for surface diffusion. Larger grain sizes could potentially be a benefit for plasmonic applications. Unfortunately, elevated temperatures can also result in dewetting of the metastable film.[12] Dewetting is a process driven by minimization of surface energy and can occur at temperatures well below the melting point of the material.[12] Noble metals deposited on oxide-coated Si are particularly susceptible to this effect since weak adhesion at the metal-substrate interface lowers the barrier for dewetting.[19] Ag films in particular have shown dewetting phenomena such as pinhole formation and aggregation at temperatures as low as 100 °C in our laboratory and by others.[20] This can lead to significant increases in porosity and roughness in the film. Thus, room-temperature deposition can actually provide a better outcome in such cases.

If room temperature is beneficial, one might also worry that under fast growth rates the substrate temperature will be increased through heat-transfer processes during the deposition. This could lead to the detrimental dewetting phenomena just discussed. In fact, fast deposition rates actually do the opposite; they help minimize substrate heating. While seemingly counterintuitive, radiant heating from long deposition times at slow rates in a thermal evaporator typically results in a larger increase in the substrate temperature than

from short deposition times at fast rates.[21] Furthermore, the heat of condensation, which is released when a solid metal film is deposited on the substrate, does not begin to contribute significantly to substrate heating until the evaporation rate is in excess of 500 Å/sec, even for highly reactive metals such as Al.[21] Such rates are more than three times faster than the fastest rates used in the recipes given below. Therefore, fast deposition rates not only help mitigate contamination but also help avoid undesirable substrate heating, which can increase film roughness through dewetting.

We now summarize the key rules for depositing metallic films for plasmonics via a simple thermal evaporator. Residual gases should be avoided with the lowest pressure one can attain. One should not expect good optical films from a poor vacuum (pressures above 10^{-5} Torr). In the high-vacuum regime, one can deposit metals with optimized optical properties. However, the more reactive the metal, the faster the deposition rate should be to combat the detrimental effects of residual gases. For less reactive metals, one must select a deposition rate that balances grain growth and grain-boundary pinning caused by the residual gases. Finally, although heated substrates could potentially increase grain size during growth, this benefit is frequently outweighed by undesirable dewetting effects in the film, especially for Ag. Thus, the example films described below are obtained from room-temperature deposition, which is also amenable to a simple apparatus.

2.3 Optical Performance

Above we presented rules to give the reader intuition about the deposition process. If these rules are followed in practice, how do they impact optical performance? In the next section we list recipes that are based on these rules (*i.e.* they follow the prior surface-science literature). We used them to deposit 300-nm thick films of Al, Cu, Au, and Ag on native-oxide-coated Si wafers. To have the smoothest surfaces possible for accurately extracting optical properties, all films were then template-stripped from their substrates.[22, 23] After deposition, an adhesive and counter-substrate were added to the top "as-deposited" surfaces of the films and they were peeled off the wafer, exposing the metal interface that initially formed at the native oxide. The measured root-mean-squared (RMS) surface roughness of the as-deposited surfaces was typically a few nanometers. The values reported

below for the template-stripped surfaces are significantly lower. (Figure 2.2 demonstrates Al, Cu, Au, and Ag films that were deposited according to the recipes and then template stripped from wafers that were first structured via FIB lithography.) Template-stripping is also beneficial for providing pristine films (*i.e.* avoiding contamination) as the metal interface can be protected until the last moment. We template stripped our films immediately prior to optical measurements. Atomic force microscopy (AFM) images were collected within the hour.

Optical properties were obtained with a variable-angle spectroscopic ellipsometer (V-VASE or VUV-VASE, J. A. Woollam Co.). Because of the smooth template-stripped surfaces, we could exploit a simple two-layer vacuum-metal model to extract the dielectric function of each metal (except for Al, where an oxide layer was also included). If we instead measured the as-deposited surfaces, which are rougher, the fit of the ellipsometry data would be less reliable. Further, our goal is not to address the impact of residual roughness on the effective dielectric functions obtained by ellipsometry, but to summarize how deposition conditions affect the dielectric function of each metal. Finally, we note that we explored a range of pressures and deposition rates, and observed significant changes in the optical performance, even on the smooth template-stripped surfaces (see details below). Our results are in agreement with the prior surface-science literature and the rules summarized above.

From the best-recipe films, we show experimental data for the real and imaginary components of the dielectric functions (solid lines) in Figure 2.5a,b, respectively. Figure 2.5a,b also shows literature values (dashed lines) from Palik[24] (Cu, Au, and Ag) and Rakić[25] (Al) for comparison. Palik and Rakić were chosen as standards due to their widespread use in the plasmonic community. The real components (ε') of the dielectric functions for the recipe films of Cu, Au, and Ag agree well with Palik, while their imaginary components (ε"), which are related to losses, are significantly better. For Al, our values are very similar to those from Rakić. These results show that by following the rules discussed above, films with optimal optical performance can be obtained even with a simple apparatus. Such films exhibit properties significantly better than those obtained

under deposition conditions commonly used in the plasmonics community (*i.e.* at slow rates). Indeed, they have properties better than the standard literature values.

Is it surprising that the recipe films have better dielectric functions than in the standard references? Within this context, it is important to point out that the standard values[24-26] were obtained from films deposited according to the rules summarized above, which is another indication of their validity. However, these films were typically a factor of ten thinner than the films presented here. Under similar deposition conditions, thinner films will have smaller grains. Thus, our thicker films can exhibit smaller losses due to reduced grain-boundary scattering. The standard references may have also exploited thinner films because they can provide smoother as-deposited surfaces. Unfortunately, the surface roughness values were not reported. If their films were rougher than our template-stripped surfaces, this could also affect the reported dielectric functions. In either case (due to smaller grain size or increased roughness), the data in Figure 2.5a,b indicate that the standard reference values should not be used to simulate perfect, ideal plasmonic structures. Better values can easily be obtained in practice.

The impact of these improvements is demonstrated in Figure 2.5c,d, where two figures-of-merit are plotted. Quality factors (Qs)[17] for our films (solid lines) are compared with literature values (dashed lines) for both localized surface plasmon resonances (LSPR) and surface plasmon polaritons (SPPs). Table 1 shows the percentage improvement in the Qs at selected wavelengths for the different metals. Clearly, significant boosts in performance are possible. The message of this work is that such an improvement can easily be achieved, in fact without any additional experimental effort. The deposition simply needs to be performed under the appropriate conditions.

We now discuss the optical performance of each of the metals separately.

Silver Ag is perhaps the most widely used plasmonic material due to its low losses in the visible regime. Because it is a noble metal, it is often considered to be a material that is easy to deposit via thermal evaporation. However, we caution that the optical properties of Ag films can be significantly reduced by water vapor and oxygen in the vacuum chamber.[10] In fact, in many respects, Ag is the most unforgiving of the four metals to deposit. As already mentioned, Ag is susceptible to dewetting and grain-boundary pinning.

For example, compared to Cu, which is at a similar position in Figure 2.1, the adhesion energy of Ag on silica is nearly 50% lower,[27] leading to a tendency of the metal to dewet or "ball up," even at room temperature. Another complication is the crystalline orientation of the grains in the film, a factor that we ignored for simplicity in our rules above. For Ag, template-stripped films with the desired (111)-oriented grains are obtained only for pressures around $1x10^{-7}$ Torr or better.[28] Above these pressures, random grains with irregular grain boundaries are formed. [For comparison, the (111) orientation dominates in Au all the way up to $1x10^{-5}$ Torr.] Therefore, due to all of these effects, Ag films with pinholes and increased grain structure can easily form under poor vacuum conditions or at rates that are too slow. Figure 2.6 highlights these effects showing two AFM images of template-stripped Ag deposited at a slow rate of 0.2 Å/sec with a base pressure of $2x10^{-6}$ Torr (Figure 2.6a) and $3x10^{-8}$ Torr (Figure 2.6b). The film deposited at $2x10^{-6}$ Torr has a roughness of 1.23 nm RMS whereas the film deposited at $3x10^{-8}$ Torr has a roughness of 0.32 nm RMS.

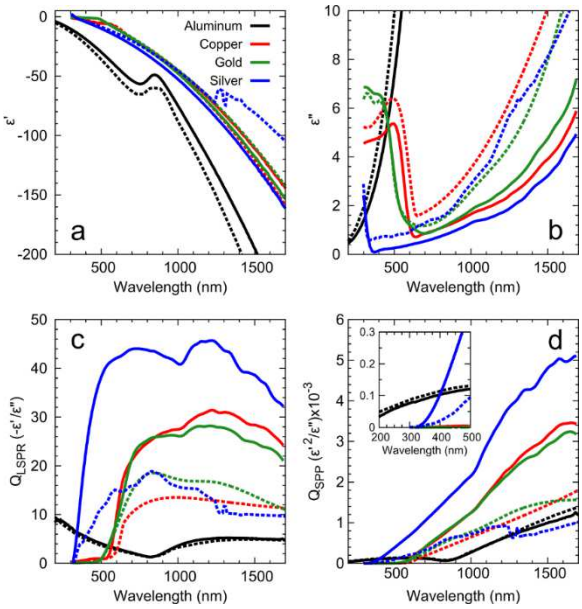

Figure 2.5. Optical properties and figures-of-merit for our metallic films of Al (black), Cu (red), Au (green), and Ag (blue). The films were deposited as described in Figure 2.2. Solid lines are for measured values for the template-stripped recipe films and dashed lines are from Palik[24] (Cu, Au, and Ag) and Rakić[25] (Al). (a) and (b) show the real and imaginary part of the dielectric function, respectively. (c) and (d) plot calculated quality factors[17] for the localized surface plasmon resonance in spherical structures (Q_{LSPR}) and surface plasmon polaritons (Q_{SPP}), respectively. The data for the films were smoothed with a five-point moving average.

Table 2.1 Percentage increase in the figures-of-merit for Al, Cu, Au, and Ag at ultraviolet (280 nm), visible (650 nm), near-infrared (1000 nm), and telecommunication (1550 nm) wavelengths. The increase is based on comparison to Palik[24] (Cu, Au, and Ag) and Rakić[25] (Al). The quality factors[17] for localized surface plasmon resonances (Q_{LSPR}) and surface plasmon polaritons (Q_{SPP}) are shown along with the calculated surface plasmon propagation lengths (L_{SPP}) based on the measured dielectric functions of the recipe films. Specifically, the films were deposited under the conditions detailed in Figure 2.2. Very similar films could be obtained over a range of conditions, as described in the text.

		Increase over Standard References[24, 25]		
Wavelength Regime	**Metal**	**Q_{LSPR} (%)**	**Q_{SPP} (%)**	**L_{SPP} (μm)**
Ultraviolet (280 nm)	Al	11	-12	2.5
Visible (650 nm)	Ag	200	250	84
	Cu	120	130	24
	Au	32	38	20
Near-Infrared (1000 nm)	Ag	160	200	340
	Cu	100	93	190
	Au	51	61	190
Telecom (1550 nm)	Ag	270	480	1200
	Cu	140	120	820
	Au	81	95	730

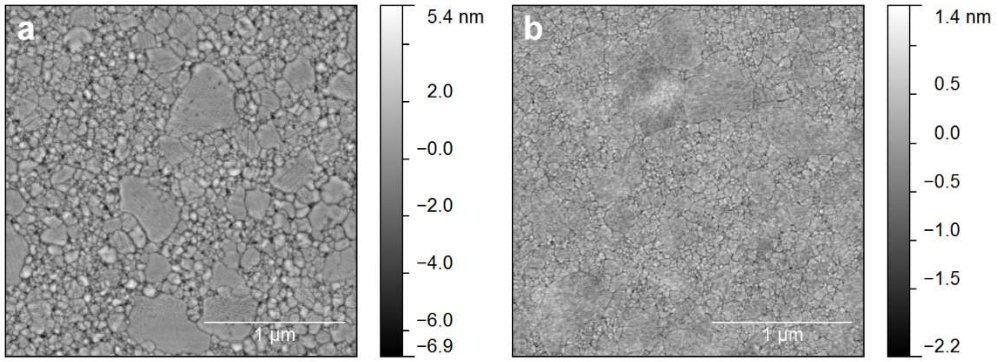

Figure 2.6. Atomic force micrographs of silver films deposited at 0.2 Å/sec at a base pressure of (a) $3x10^{-6}$ Torr and (b) $3x10^{-8}$ Torr. The template-stripped side of the film is shown. The roughness values, calculated over the 2.5 μm by 2.5 μm area, are (a) 1.23 and (b) 0.32 nm RMS.

Under our best vacuum conditions ($3x10^{-8}$ Torr) we deposited Ag at rate of 50 Å/sec to obtain films that are significantly better than Palik,[24] showing at least a 160% improvement in the LSPR figure-of-merit and at least a 200% improvement in the SPP

figure-of-merit, over a large spectral range (see Table 1). The surface roughness was 0.37 nm RMS (see Figure 2.7a). When our vacuum was an order of magnitude worse ($3x10^{-7}$ Torr), we could still obtain films of similar or better surface roughness (0.30 nm RMS) and optical quality, but only by increasing our deposition rate to 150 Å/sec, consistent with the rules above. At even higher pressures, the quality of the Ag films deteriorates significantly. Thus, for Ag, a good vacuum is required.

Copper Cu is a low-cost CMOS compatible metal that is slightly more reactive than Ag (Figure 2.1) and thus, according to the rules, slightly more susceptible to residual-gas contaminants during deposition. Ideally, we should increase the deposition rate compared to Ag. However, the fastest attainable deposition in our evaporator was 35 Å/sec (due to Cu creep, see Recipes section). We used this rate at a base pressure of $3x10^{-8}$ Torr. The resulting materials exhibit a 30-100% improvement over Palik for both the LSPR and SPP figures-of-merit (see Table 1). Perhaps more remarkable is that such Cu films outperform our best Au films for most of the near-infrared (near-IR) and specifically at 1550 nm. The predicted SPP propagation length at 1550 nm on our Cu film is 820 μm. This is significant given recent interest in Cu for CMOS-compatible plasmonic interconnects.[5] The surface roughness of the Cu films was 0.25 nm RMS (see Figure 2.7b).

We note that, while Figure 2.1 indicates that Cu is slightly more reactive than Ag, in practice Cu requires much less stringent deposition conditions in comparison. This can be due to a combination of the effects already discussed above for Ag. Cu has a weaker tendency to dewet[27] leading to a less-complicated grain structure. It has also been reported that (111)-oriented grains do not dominate in deposited Cu until pressures below $1x10^{-8}$ Torr.[28] Thus, under our conditions, the grains are randomly oriented. For Cu, the good adhesion and random grains lead to smooth films with good optical performance. Indeed, when we deposited Cu at a base pressure of $3x10^{-7}$ Torr at 25 Å/sec we obtained essentially the same optical properties and roughness as at $3x10^{-8}$ Torr.

Gold Au is another widely used plasmonic metal, particularly in bio-related devices at red wavelengths.[29-31] The inertness of Au means that residual gases have far less impact on its optical properties. That said, the Au-recipe films outperform Palik by 30 to 95% in the red and near-IR regime for both LSPR and SPP figures-of-merit (see Table 1). These

films were deposited at a base pressure of $3x10^{-8}$ Torr and 10 Å/sec. The surface roughness was 0.3 nm RMS (see Figure 2.7c). Films that were deposited at $2x10^{-6}$ Torr and 0.5 Å/sec had optical properties marginally worse and marginally better in the visible and IR, respectively. The surface roughness increased to 0.4 nm RMS.

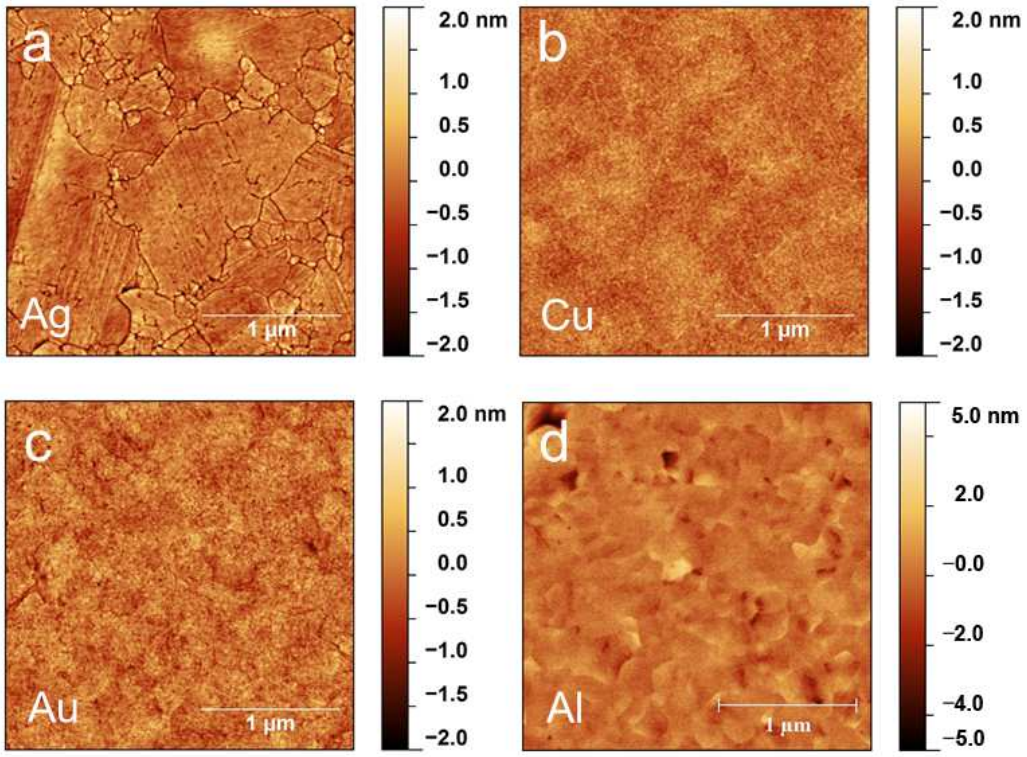

Figure 2.7 Atomic force micrographs of films deposited at $3x10^{-8}$ Torr using the rates detailed in Figure 2.2. The template-stripped side of the film is shown. (a) Silver film with 0.37 nm RMS roughness. (b) Copper film with 0.25 nm RMS roughness. (c) Gold film with 0.30 nm RMS roughness. (d) Aluminum film with 0.58 nm RMS roughness. The scan area in each image is 2.5 µm by 2.5 µm.

Aluminum Al is considered the best plasmonic metal for the UV[7, 8] and has recently been of interest for metal-enhanced fluorescence,[32] deep-UV Raman scattering,[33, 34] non-linear plasmonics,[35] high-energy plasmonics,[36] and CMOS-compatible color filters.[6] Unfortunately, Al is also extremely reactive (Figure 2.1) and therefore highly sensitive to residual gases in the deposition chamber. Following the work of Hass,[16] we found that extremely fast evaporation rates (~150 Å/sec) were necessary to closely match the LSPR and SPP figures-of-merit from Rakić in the UV. Ultra-fast deposition rates result in more

compact films that are also less susceptible to oxidation over time.[16] We stress that the optical properties suffered significantly in both the UV and visible regimes at more commonly used deposition rates of 1 to 5 Å/sec, even if the chamber pressure was as low as $3x10^{-8}$ Torr (see Figure 2.8). Indeed, under such commonly used deposition rates, our data show that the SPP propagation lengths in the UV were 80% less than predicted by the data from Rakić. Films deposited at slower rates were also not template strippable presumably due to strong adhesion between oxidized aluminum and the native oxide on the silicon wafer. Therefore, in the high-vacuum regime extremely fast deposition rates are critical to achieve high-quality Al films. Under these conditions, we also achieved a surface roughness of 0.58 nm RMS (see Figure 2.7d).

2.4 Recipes

All films were deposited in a Kurt J. Lesker Nano36 thermal evaporator equipped with the standard 3.3 V, 375 A power supply and dual source/substrate shutters. The source-to-substrate-distance for all deposition runs was 30 cm. The chamber was pumped with a 685 L/sec turbo pump. A custom-built Meissner trap was also installed in the chamber to aid water-vapor removal and decrease pump-down times of the deposition chamber. It consisted of two copper plates (roughly 30 by 30 cm) cooled by a coiled copper tube that was filled with liquid N_2. The trap was required for our chamber to achieve our lowest base pressure of $3x10^{-8}$ Torr.

All films were deposited on native-oxide-covered Si(100) wafers. These substrates were cleaned with 10 min of sonication in both acetone (Univar AG) and isopropyl alcohol (Thommen Furler AG), followed by 10 min of sonication at 45 °C in RCA cleaning solution, which contained 20 mL of 30% hydrogen peroxide (VWR Chemicals, AnalaR NORMAPUR), 4 mL of 30-32% aqueous ammonium hydroxide (Sigma Aldrich, ACS reagent), and 100 mL of H_2O (deionized by a MilliQ Advantage A10 System, 18.2 MΩcm at 25 °C).

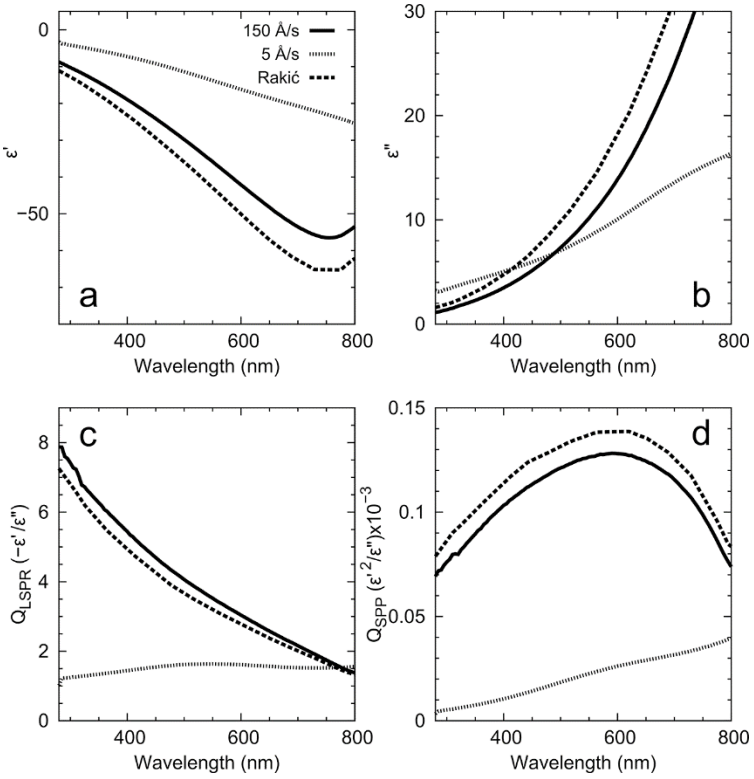

Figure 2.8 Optical properties and figures-of-merit for Al films deposited at room temperature at a base pressure of $3x10^{-8}$ Torr. Solid and dotted lines compare properties for a template-stripped film deposited at a fast rate (150 Å/sec) and the as-deposited surface from a film grown at a rate more typically found in the plasmonics literature (5 Å/sec), respectively. Despite the additional roughness in the latter case, the measured dielectric functions are dominated by the presence of aluminum oxide in the film. Note how the fast rates are consistent with Rakić[25] (dashed lines). (a) and (b) show the real and imaginary part of the dielectric function, respectively. (c) and (d) plot calculated quality factors[17] for the localized surface plasmon resonance in spherical structures (Q_{LSPR}) and surface plasmon polaritons (Q_{SPP}), respectively.

Silver A 49-mm-long by 12-mm-wide by 0.4-mm-thick tungsten dimple boat (Umicore) was used with 1/8-inch by 1/8-inch 99.99% Ag pellets (Kurt J. Lesker) as the source material. The base pressure in the chamber was $3x10^{-8}$ Torr. The deposition rate was 50 Å/sec. We also tested deposition at a base pressure of $3x10^{-7}$ Torr. In this case, to maintain the quality of the film, a faster deposition rate of 150 Å/sec was required.

Copper A 4-inch-long by 0.5-inch-wide by 0.015-inch-thick tungsten dimple boat (R. D. Mathis) was used with 1/8" x 1/8" 99.99% Cu pellets (Kurt J. Lesker) as the source

material. The base pressure in the chamber was $3x10^{-8}$ Torr. The deposition rate was 35 Å/sec. Similar results were obtained at $3x10^{-7}$ Torr and 25 Å/sec. Note that Cu will creep considerably on the tungsten boat during deposition. If too much power is applied, the Cu can reach the electrodes and result in shorting. This limited our fastest deposition rate to 35 Å/sec.

Gold A 49-mm-long by 12-mm-wide by 0.4-mm-thick tungsten dimple boat (Umicore) was used with 1/8-inch by 1/8-inch 99.999% Au pellets (ACI Alloys) as the source material. The base pressure in the chamber was $3x10^{-8}$ Torr. The deposition rate was 10 Å/sec. Films were also deposited at $2x10^{-6}$ Torr and 0.5 Å/sec with minor changes in the properties.

Aluminum A 4-inch-long by 0.5-inch-wide by 0.01-inch-thick tungsten dimple boat (R. D. Mathis) was used with 1/8-inch by 1/8-inch 99.999% Al pellets (Kurt J. Lesker) as the source material. Thinner boats are not advised due to alloying between aluminum and tungsten at elevated temperatures. Base pressures in the chamber of $1x10^{-6}$ Torr and below were used successfully for Al deposition. Once the base pressure was reached, the boat was heated slowly (~5 to 10 min ramp) until the Al pellets melted. The power was gradually increased until a slow rate (~0.1 Å/sec) of metal deposition was detected on the quartz crystal microbalance. The power was then increased quickly by at least 50% (without exceeding the current limit of the power supply). The Al spread quickly across the tungsten boat. The rate on the quartz crystal microbalance was monitored and the substrate shutter was opened when a rate of ~150 Å/sec or greater was reached. Rates even higher than 150 Å/sec did not show improved optical properties but did result in increased roughness (*e.g.* 0.58 nm RMS for 150 Å/sec and 0.8 nm RMS for 400 Å/sec).

Conclusion

We have presented a series of rules and recipes to aid researchers in depositing plasmonic metallic films with optimized structural and optical properties. We have restricted our discussion to room-temperature deposition with a standard thermal evaporator. In this case, the primary experimental parameters to consider are the base pressure in the vacuum chamber and the deposition rate. One should always use the lowest

pressure possible; good optical films cannot be expected from poor vacuum conditions (pressures above 10^{-5} Torr). Even under good vacuum conditions (10^{-8} Torr), reactive metals such as aluminum require fast deposition rates to avoid metal-oxide contamination. Less reactive metals require a deposition rate that balances grain growth and grain-boundary pinning. Of course, due to our focus on thermal evaporation, we have not addressed more sophisticated deposition strategies that have recently been explored in plasmonics to improve material quality. These have included the growth of single-crystalline flakes and films.[37-42] By avoiding grain structure, such films can allow more precise patterning of plasmonic structures, which is clearly beneficial. However, these techniques, while not overly difficult to implement in the laboratory, do require additional experimental capabilities beyond most optics labs, such as high-temperature sputtering or low-temperature molecular beam epitaxy. In our experience, the improvement in optical properties over what one can obtain with a well-deposited polycrystalline film is also marginal. Thus, for many experiments in plasmonics, the very simple approach presented here is sufficient.

2.5 Materials and Methods

Characterization

Ellipsometry

A J. A. Woollam V-VASE variable-angle spectroscopic ellipsometer with rotating analyzer was used to determine the optical constants for Cu, Au, and Ag in Figure 2.5 and the 5 Å/sec deposited Al film in Figure 2.8 of the main text. Psi and delta values were collected every 10 nm from 400 to 1750 nm at incident angles of 65, 70, and 75 degrees.
A J. A. Woollam VUV-VASE variable-angle spectroscopic ellipsometer with rotating analyzer was used to determine the optical constants for Al in Figure 2.5 and the 150 Å/sec deposited Al film in Figure 2.8 of the main text. Psi and delta values were collected every 5 nm from 150 to 1700 nm at incident angles of 65, 70, and 75 degrees.

The complex dielectric functions for Cu, Ag, and Au were determined using the two-phase (substrate-ambient) model:[22]

$$\frac{\varepsilon}{\varepsilon_a} = \sin^2\varphi\left[1 + \tan^2\varphi\left(\frac{1-\rho}{1+\rho}\right)^2\right]$$

Where ε and ε_a are the complex dielectric functions for the metal and ambient environment, respectively, φ is the angle of incidence, and $\rho = \frac{r_p}{r_s} = \tan(\psi)e^{i\Delta}$. $\frac{r_p}{r_s}$ is the complex reflectance ratio, $\tan(\psi)$ is the amplitude ratio upon reflection, and Δ is the phase difference.

For Al, an aluminum oxide top layer was added to the two-phase model and the oxide thickness was fit via a point-by-point method.

Atomic Force Microscopy

A Bruker FastScan atomic force microscope (AFM) was used with a ScanAsyst-Air tip to image grain structure and measure surface roughness for each of our films. The scan area was 2.5 μm x 2.5 μm. Root-mean-squared (RMS) roughness values were extracted using the Gwyddion software package.

Fabrication

Focused Ion Beam

Metal films were template stripped from silicon templates that had been milled with a FEI Helios focused-ion-beam instrument using 30 kV as the acceleration voltage and 80 pA as the ion-beam current.

Template Stripping

Metal films were template stripped using soda lime glass counter-substrates and Norland NOA61 UV epoxy.

2.6 References

[1] B. A. Movchan, A. V. Demchishin, "Investigation of the structure and properties of thick vacuum-deposited films of nickel, titanium, tungsten, alumina and zirconium dioxide." *Fizika Metallov i Metallovedenie* **28**, 653-660 (1969).

[2] C. R. M. Grovenor, H. T. G. Hentzell, D. A. Smith, "The development of grain structure during growth of metallic films." *Acta Metallurgica* **32**, 773-781 (1984).

[3] J. A. Thornton, "The microstructure of sputter-deposited coatings." *Journal of Vacuum Science & Technology A* **4**, 3059-3065 (1986).

[4] I. Petrov, P. B. Barna, L. Hultman, J. E. Greene, "Microstructural evolution during film growth." *Journal of Vacuum Science & Technology A* **21**, S117-S128 (2003).

[5] C. Delacour, S. Blaize, P. Grosse, J. M. Fedeli, A. l. Bruyant, R. Salas-Montiel, G. Lerondel, A. Chelnokov, "Efficient directional coupling between silicon and copper plasmonic nanoslot waveguides: Toward metal−oxide−silicon nanophotonics." *Nano Letters* **10**, 2922-2926 (2010).

[6] S. Yokogawa, S. P. Burgos, H. A. Atwater, "Plasmonic color filters for CMOS image sensor applications." *Nano Letters* **12**, 4349-4354 (2012).

[7] M. W. Knight, N. S. King, L. F. Liu, H. O. Everitt, P. Nordlander, N. J. Halas, "Aluminum for plasmonics." *ACS Nano* **8**, 834-840 (2014).

[8] Y. Ekinci, H. H. Solak, J. F. Loffler, "Plasmon resonances of aluminum nanoparticles and nanorods." *Journal of Applied Physics* **104**, 083107 (2008).

[9] P. B. Barna, M. Adamik, "Fundamental structure forming phenomena of polycrystalline films and the structure zone models." *Thin Solid Films* **317**, 27-33 (1998).

[10] R. C. O'Handley, D. K. Burge, S. N. Jasperson, E. J. Ashley, "Residual gas and the optical properties of silver films." *Surface Science* **50**, 407-433 (1975).

[11] D. Flötotto, Z. M. Wang, L. P. H. Jeurgens, E. Bischoff, E. J. Mittemeijer, "Effect of adatom surface diffusivity on microstructure and intrinsic stress evolutions during Ag film growth." *Journal of Applied Physics* **112**, 043503 (2012).

[12] C. V. Thompson, "Solid-state dewetting of thin films." *Annual Review of Materials Research* **42**, 399-434 (2012).

[13] R. A. Outlaw, in *Handbook of Vacuum Science and Technology,* D. M. Hoffman, B. Singh, J. H. Thomas, Eds. (Academic Press, San Diego, 1998), 335-375.

[14] J. W. Geus, in *Chemisorption and Reactions on Metallic Films,* J. R. Anderson, Ed. (Academic Press, 1971), Volume 1, 129-224.

[15] K. Yoshihara, K. Nii, "The effect of oxygen potential on the surface self-diffusion coefficient of silver." *Transactions of the Japanese Institute of Metals* **20**, 533-542 (1979).

[16] G. Hass, "Filmed surfaces for reflecting optics." *Journal of the Optical Society of America* **45**, 945-952 (1955).

[17] M. G. Blaber, M. D. Arnold, M. J. Ford, "A review of the optical properties of alloys and intermetallics for plasmonics." *Journal of Physics-Condensed Matter* **22**, 143201 (2010).

[18] H. Savaloni, M. A. Player, "Influence of deposition conditions and of substrate on the structure of UHV deposited erbium films." *Vacuum* **46**, 167-179 (1995).

[19] P. R. Gadkari, A. P. Warren, R. M. Todi, R. V. Petrova, K. R. Coffey, "Comparison of the agglomeration behavior of thin metallic films on sio_2." *Journal of Vacuum Science & Technology A* **23**, 1152-1161 (2005).

[20] H. C. Kim, T. L. Alford, D. R. Allee, "Thickness dependence on the thermal stability of silver thin films." *Applied Physics Letters* **81**, 4287-4289 (2002).

[21] A. N. Pargellis, "Evaporating and sputtering: Substrate heating dependence on deposition rate." *Journal of Vacuum Science & Technology A* **7**, 27-30 (1989).

[22] M. Hegner, P. Wagner, G. Semenza, "Ultralarge atomically flat template-stripped Au surfaces for scanning probe microscopy." *Surface Science* **291**, 39-46 (1993).

[23] P. Nagpal, N. C. Lindquist, S.-H. Oh, D. J. Norris, "Ultrasmooth patterned metals for plasmonics and metamaterials." *Science* **325**, 594-597 (2009).

[24] E. D. Palik, *Handbook of optical constants of solids*. E. D. Palik, Ed., (Academic Press, Burlington, 1997).

[25] A. D. Rakić, "Algorithm for the determination of intrinsic optical constants of metal films: Application to aluminum." *Applied Optics* **34**, 4755-4767 (1995).

[26] P. B. Johnson, R. W. Christy, "Optical constants of the noble metals." *Physical Review B* **6**, 4370-4379 (1972).

[27] K. S. Gadre, T. L. Alford, "Contact angle measurements for adhesion energy evaluation of silver and copper films on parylene-n and SiO_2 substrates." *Journal of Applied Physics* **93**, 919-923 (2003).

[28] K. K. Kakati, H. Wilman, "The development of oriented crystal growth during condensation of gold, silver and copper films in vacuum, and its systematic dependence on the residual gas pressure and adsorption, and the film thickness, atomic mobility and chemical reactivity." *Journal of Physics D: Applied Physics* **6**, 1307-1317 (1973).

[29] M. E. Stewart, C. R. Anderton, L. B. Thompson, J. Maria, S. K. Gray, J. A. Rogers, R. G. Nuzzo, "Nanostructured plasmonic sensors." *Chemical Reviews* **108**, 494-521 (2008).

[30] P. K. Jain, X. H. Huang, I. H. El-Sayed, M. A. El-Sayed, "Noble metals on the nanoscale: Optical and photothermal properties and some applications in imaging, sensing, biology, and medicine." *Accounts of Chemica Research* **41**, 1578-1586 (2008).

[31] M. Hu, J. Y. Chen, Z. Y. Li, L. Au, G. V. Hartland, X. D. Li, M. Marquez, Y. N. Xia, "Gold nanostructures: Engineering their plasmonic properties for biomedical applications." *Chemical Society Reviews* **35**, 1084-1094 (2006).

[32] K. Ray, M. H. Chowdhury, J. R. Lakowicz, "Aluminum nanostructured films as substrates for enhanced fluorescence in the ultraviolet-blue spectral region." *Analytical Chemistry* **79**, 6480-6487 (2007).

[33] S. K. Jha, Z. Ahmed, M. Agio, Y. Ekinci, J. F. Loffler, "Deep-UV surface-enhanced resonance raman scattering of adenine on aluminum nanoparticle arrays." *Journal of the American Chemical Society* **134**, 1966-1969 (2012).

[34] T. Dorfer, M. Schmitt, J. Popp, "Deep-UV surface-enhanced raman scattering." *Journal of Raman Spectroscopy* **38**, 1379-1382 (2007).

[35] M. Castro-Lopez, D. Brinks, R. Sapienza, N. F. van Hulst, "Aluminum for nonlinear plasmonics: Resonance-driven polarized luminescence of Al, Ag, and Au nanoantennas." *Nano Letters* **11**, 4674-4678 (2011).

[36] F. Bisio, R. Proietti Zaccaria, R. Moroni, G. Maidecchi, A. Alabastri, G. Gonella, A. Giglia, L. Andolfi, S. Nannarone, L. Mattera, M. Canepa, "Pushing the high-energy limit of plasmonics." *ACS Nano* **8**, 9239-9247 (2014).

[37] M. Kuttge, E. J. R. Vesseur, J. Verhoeven, H. J. Lezec, H. A. Atwater, A. Polman, "Loss mechanisms of surface plasmon polaritons on gold probed by cathodoluminescence imaging spectroscopy." *Applied Physics Letters* **93**, 113110 (2008).

[38] B. J. Wiley, D. J. Lipomi, J. Bao, F. Capasso, G. M. Whitesides, "Fabrication of surface plasmon resonators by nanoskiving single-crystalline gold microplates." *Nano Letters* **8**, 3023-3028 (2008).

[39] J. S. Huang, V. Callegari, P. Geisler, C. Bruning, J. Kern, J. C. Prangsma, X. F. Wu, T. Feichtner, J. Ziegler, P. Weinmann, M. Kamp, A. Forchel, P. Biagioni, U. Sennhauser, B. Hecht, "Atomically flat single-crystalline gold nanostructures for plasmonic nanocircuitry." *Nature Communications* **1**, 150 (2010).

[40] J. H. Park, P. Ambwani, M. Manno, N. C. Lindquist, P. Nagpal, S. H. Oh, C. Leighton, D. J. Norris, "Single-crystalline silver films for plasmonics." *Advanced Materials* **24**, 3988-3992 (2012).

[41] Y. J. Lu, J. Kim, H. Y. Chen, C. H. Wu, N. Dabidian, C. E. Sanders, C. Y. Wang, M. Y. Lu, B. H. Li, X. G. Qiu, W. H. Chang, L. J. Chen, G. Shvets, C. K. Shih, S. Gwo, "Plasmonic nanolaser using epitaxially grown silver film." *Science* **337**, 450-453 (2012).

[42] Y. W. Wu, C. D. Zhang, N. M. Estakhri, Y. Zhao, J. Kim, M. Zhang, X. X. Liu, G. K. Pribil, A. Alu, C. K. Shih, X. Q. Li, "Intrinsic optical properties and enhanced plasmonic response of epitaxial silver." *Advanced Materials* **26**, 6106-6110 (2014).

Chapter 3.

Low-Temperature Enhancement of Plasmonic Performance in Silver Films[2]

While plasmonic metals can manipulate optical energy at the nanoscale, they suffer from significant losses at visible wavelengths. We investigate the potential of low temperature to decrease such losses in optically thick Ag films. We extract the complex dielectric function (or relative permittivity) from spectroscopic ellipsometry measurements for smooth single-crystalline, smooth polycrystalline, and rough polycrystalline films down to liquid-helium temperatures and fit these data to a temperature-dependent Drude model. Smooth single-crystalline films exhibited the largest improvements relative to room temperature. Below 50 K, the surface plasmon polariton propagation lengths increased by ~50% at 650 nm. In rough polycrystalline films, improvements of 10% are expected.

[2] Reproduced with permission from Sriharsha V. Jayanti, Jong Hyuk Park, Alexandr Dejneka, Dagmar Chvostova, Kevin M. McPeak, Xiaoshu Chen, Sang-Hyun Oh, and David J. Norris, "Low-temperature enhancement of plasmonic performance in silver films," *Optical Materials Express* **2015**.

3.1 Introduction

Surface plasmon polaritons are electromagnetic oscillations that exist at metal surfaces. [1, 2] They allow sub-diffraction confinement and nanoscale manipulation of electromagnetic energy, [3] enabling applications in sensing, [4, 5] spectroscopy, [6] and optoelectronic circuits.[7, 8] However, the most commonly used plasmonic metals, Ag and Au, which exhibit the best properties at visible frequencies, still suffer significant energy losses that limit performance. [3, 9, 10] On the high-frequency end of the visible spectrum, large losses occur due to interband transitions.[11] These can be avoided by operating at lower frequencies, but dissipation caused by electron-electron, electron-phonon, grain-boundary, and surface-defect scattering in the metal remains.[12-22] Despite attempts to reduce these scattering processes by decreasing surface roughness and increasing grain size,[23-29] additional improvements are sought.

A possible route to limit further the effect of these scattering losses is to decrease temperature. Thus, several efforts have recently studied plasmonic behavior in metallic nanoparticles or thin films at low temperatures.[10, 30, 31] Linewidth narrowing was observed in the extinction spectra of cooled Au nanorod arrays.[10] Based on these results, a doubling of the surface-plasmon-polariton (SPP) propagation length was predicted at 860 nm for planar gold surfaces cooled to 80 K. However, experiments aiming to observe such an increase on thin Ag films reported only modest improvements of the SPP propagation length.[31] The measured propagation was limited by surface and defect scattering (*i.e.* film quality). To date, similar experiments have yet to be performed on high-quality Ag films.

More generally, reliable low-temperature values for the experimental dielectric function of Ag are not available. Instead, tabulated room-temperature data (*e.g.* those of Johnson and Christy[11]) are often combined with the Drude model to predict the low-temperature plasmonic response. This approach can be inaccurate for two reasons. First, experimental films often exhibit dielectric functions (ε) that are different than those reported by Johnson and Christy.[11] They often have less negative real components (ε_R) and more positive imaginary components (ε_{Im}). Second, the assumption of the Drude model with room-temperature parameters may not be applicable.

To provide more reliable data while also exploring the potential of low temperature to improve plasmonic performance, here we investigate the optical properties of high-quality Ag films at cryogenic temperatures. To avoid the interband transitions, where optical losses are high, we limit our experiments to wavelengths longer than 450 nm. We report the experimental dielectric function (relative permittivity) and tabulate the relevant Drude and Drude-Lorentz parameters for optically thick Ag films over a broad range of temperatures, *T*. We also examine how the quality of the film affects the optical response. Finally, we measure experimental SPP propagation lengths on ultrasmooth, single-crystalline Ag films at 298 and 25 K.

3.2 Experiment

Film Preparation

We prepared three types of 200-nm-thick Ag films of different crystallinity and surface quality. First, single-crystalline films [28] (Sample SC) were grown epitaxially by sputtering Ag onto freshly cleaved mica substrates (Highest Grade V1 AFM Mica Discs, Ted Pella). Specifically, the mica substrates were pumped down in the sputtering chamber (Kurt J. Lesker PVD 75) to a pressure below 10^{-6} Torr. They were then heated to 360 °C at a rate of 3 °C/min and pre-annealed for 1 h. Ag (99.99%, Kurt J. Lesker) was sputtered at an optimized rate of 110 nm/min at 470 W and a target distance of 17 cm under an Ar pressure of 6 x 10^{-3} Torr. After a 30 min post-anneal, the films were allowed to cool to room temperature. Atomic force microscopy (AFM) measurements over a 2.5 x 2.5 μm^2 area revealed a root-mean-squared (RMS) roughness of 0.47 nm (Figure 3.1a).

Second, smooth polycrystalline films (Sample TS) were obtained by thermal evaporation of Ag followed by template stripping.[24, 32] Ag (99.99%, Kurt J. Lesker) was deposited at 0.2 Å/s and 2 x 10^{-6} Torr via a Kurt J. Lesker Nano 36 onto clean Si wafers (sonicated in acetone, isopropanol, methanol, and water, each for 10 min). A glass counter substrate was then attached to the as-deposited Ag surface via thermal epoxy (EpoTek 377), which was cured at 130 ˚C for 1 h. The glass and metal film were then peeled off the silicon to reveal a Ag surface with 0.7-nm RMS roughness (Figure 3.1b). (We note that ε

can be further improved in polycrystalline films if lower pressures and faster rates are used [33].)

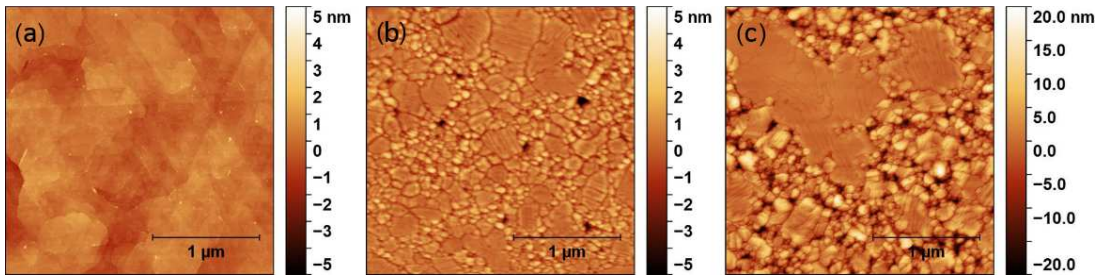

Figure 3.1 Atomic force microscope (AFM) images of the three types of Ag films investigated: (a) single-crystalline film (Sample SC), (b) template-stripped polycrystalline film (Sample TS), and (c) rough polycrystalline film (Sample Ro).

Lastly, rough polycrystalline films (Sample Ro) were prepared by sputtering Ag at room temperature at 160 nm/min onto clean Si wafers using 470 W, 10 mTorr Ar pressure, and a target distance of 13 cm. A glass counter substrate was then attached to the as-deposited surface with optical epoxy (Norland NOA63) followed by template stripping.[24, 32] The measured roughness of the exposed Ag surface varied from sample to sample between 2 and 5 nm RMS depending on the region [see Figure 3.1c for one example]. The particular sample used for dielectric-function measurements had an RMS roughness of 4.5 nm, determined from AFM images from two regions.

Ellipsometry Measurements

To quantify the optical quality of the films we determined their complex dielectric functions. The magnitude of ε_R indicates how much energy the metal can store, and ε_{Im} is related to loss. A good plasmonic material exhibits a large negative ε_R and a small positive ε_{Im}.

The ellipsometry experiments utilized freshly prepared, pristine films (2 days old). Each sample was first lowered into a liquid-N_2 bath to confirm the absence of delamination upon cooling. Identical films were then placed into a spectroscopic ellipsometer (J. A. Woollam, VUV-VASE) equipped with a cryostat. Data were collected under high vacuum (4×10^{-9} Torr) at temperatures of 298, 200, 100, 50, and 5 K at an incidence angle of 70°. By fitting to a two-layer vacuum-metal model (WVASE32 software) we extracted values

for ε_R and ε_{Im}. We note that these represent effective dielectric functions that include both bulk and surface effects.

3.3 Results and Discussion

Dielectric Functions

Figures 3.2a and 3.2b plot ε_R and ε_{Im} versus wavelength, respectively, for Sample SC as a function of temperature. With decreasing T, ε_R becomes slightly less negative while ε_{Im}

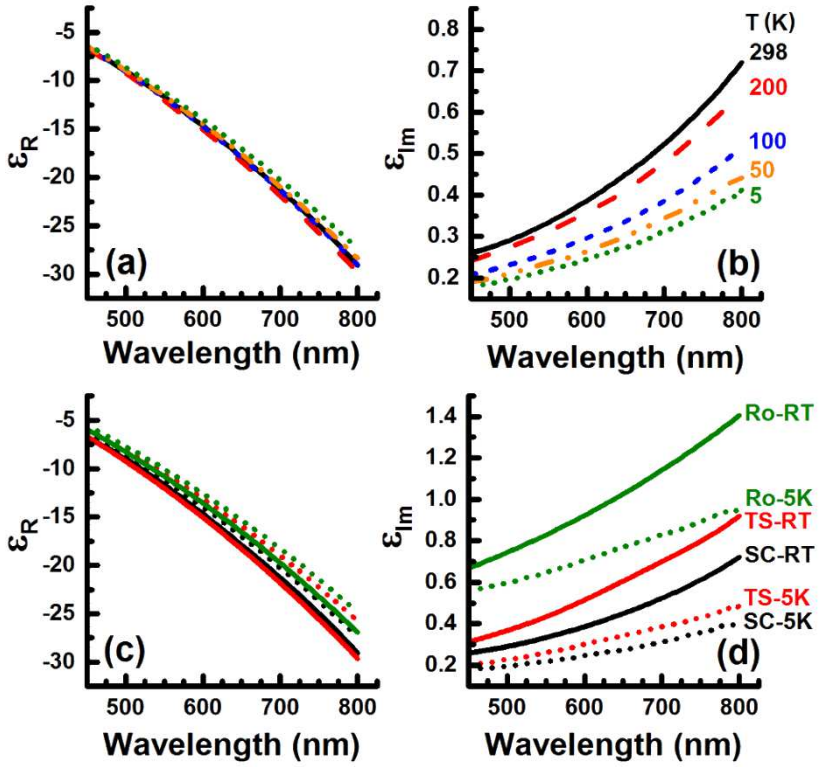

Figure 3.2 The measured real (a) and imaginary (b) parts of the dielectric function for a single-crystalline Ag film (Sample SC) at various temperatures. The measured real (c) and imaginary (d) parts of the dielectric functions for: (i) Sample SC, (ii) a template-stripped smooth polycrystalline film (Sample TS), and (iii) a rough film (Sample Ro) at 298 (RT) and 5 K.

decreases more significantly. The latter indicates that losses decrease at lower T, consistent with a reduction in scattering (confirmed by our analysis below). Figures 3.2c and 3.2d plot ε_R and ε_{Im} at 298 and 5 K for all three types of samples. The same trends seen in the single-

crystalline film appear for the polycrystalline samples. For $\varepsilon_{\mathrm{lm}}$, Sample Ro exhibits higher values overall. In such films, temperature-independent surface scattering remains significant even at low T. Samples SC and TS, which are smoother, reach lower values, with Sample SC being the best, as expected due to the lack of grains.

Drude Parameters

The Drude model permits a simple analysis of the temperature dependence. Because it assumes a free-electron gas moving against a fixed background of positive ions, it cannot account for interband electronic transitions, which become important for Ag in the blue region of the visible spectrum. For longer wavelengths, the complex dielectric function can be written as

$$\varepsilon(\omega, T) = \varepsilon_{\infty} - \frac{\omega_{\mathrm{p}}^2(T)}{\omega\,[\omega + i\omega_{\mathrm{c}}(\omega, T)]}, \tag{1}$$

where ε_{∞} is the dielectric constant at infinite frequency, ω is the angular frequency, ω_{p} is the plasma frequency, and ω_{c} is the damping rate (or collision frequency). ω_{c} includes contributions from electron-electron scattering, ω_{ee},[22] and electron-phonon scattering, ω_{ep},[21] defined as

$$\omega_{\mathrm{ee}}(\omega, T) = \frac{\pi^3 \Gamma \Delta}{12 \hbar E_{\mathrm{F}}}\left[(k_{\mathrm{B}}T)^2 + \left(\frac{\hbar\omega}{2\pi}\right)^2\right], \text{ and} \tag{2}$$

$$\omega_{\mathrm{ep}}(T) = \omega_0\left[\frac{2}{5} + \frac{4T^5}{\theta_{\mathrm{D}}^5}\int_0^{\theta_{\mathrm{D}}/T}\frac{z^4}{e^z - 1}\,dz\right]. \tag{3}$$

ω_{ee} is a frequency and temperature-dependent term with Γ as the Fermi-surface average for the scattering probability, Δ the fractional Umklapp scattering coefficient, E_{F} the Fermi energy (5.5 eV for Ag), $\hbar$ Planck's constant divided by 2π, and k_{B} the Boltzmann constant. ω_{ep} is a frequency-independent term that depends on a constant, ω_0, and the Debye temperature, θ_{D} (215 K for Ag). Because $k_{\mathrm{B}}T$ is much smaller than ω, electron-electron scattering is very weakly temperature dependent [Eq. (2)]. Meanwhile, electron-phonon scattering is strongly temperature dependent [Eq. (3)]. Therefore, reduced electron-phonon scattering should be the origin of the decreased $\varepsilon_{\mathrm{lm}}$ at low T. (We note that, because Eqs.

(1) to (3) neglect interband transitions as well as surface roughness and grain boundaries, they can only strictly be applied to smooth single-crystalline films at long wavelengths.)

By fitting our data to this model, we could extract the Drude parameters for our three samples at each temperature. Table 1 summarizes the results. We also list the percent error (or normalized standard deviation) for each data set. The normalized deviations between the calculated and measured ε_R and ε_{Im} are determined at each wavelength. The RMS deviation for a set of all such values is then reported. This method was used to weight the real and imaginary deviations equally.

Table 2 summarizes a second set of fits, exploiting a one-oscillator Drude-Lorentz model,

$$\varepsilon(\omega,T) = \varepsilon_\infty - \frac{\omega_p^2(T)}{\omega\left(\omega + i\omega_c(\omega,T)\right)} + \frac{s_1\omega_1^2}{\omega_1^2 - \omega^2 - i\omega\gamma_1}. \qquad (4)$$

While even better agreement (<0.5% error) could be obtained with this model, which contains three additional parameters (s_1, ω_1, and γ_1), it provides less insight into the physics of the temperature dependence. Thus, below we focus on the Drude model.

As seen in Table 1, the electron-phonon scattering rate decreases monotonically with T for all films, as expected. Furthermore, the product $\Gamma\Delta$, which is a measure of surface scattering in the film, increases as the surface roughness and grain density increases. Also, while $\Gamma\Delta$ was fit without constraints at each temperature, it varies only ~10% from the average for each film. This agrees with Eq. (2), which assumes these values are temperature independent. Lastly, note that the measured $\Gamma\Delta$ for Sample Ro is ~0.3, consistent with a previous estimate of ~0.4.[19]

Table 3.1 Drude parameters extracted from fits of the measured dielectric functions

Sample	T (K)	$\hbar\omega_p$ (eV)	$\hbar\omega_{ep}$ (eV)	ε_∞	$\Gamma\Delta$	Error (%)
SC	298	8.85	0.0177	3.67	0.084	1.6
	200	9.02	0.0142	3.99	0.080	1.5
	100	8.90	0.0097	3.84	0.075	1.5
	50	8.80	0.0078	3.70	0.072	1.4
	5	8.65	0.0066	3.57	0.072	1.6
TS	298	8.99	0.0251	3.92	0.097	0.5
	200	8.84	0.0193	3.66	0.095	0.6
	100	8.65	0.0126	3.30	0.095	0.7
	50	8.47	0.0107	3.23	0.091	0.8
	5	8.37	0.0104	3.32	0.086	0.7
Ro	298	8.59	0.0162	3.70	0.299	0.6
	200	8.56	0.0087	3.63	0.301	0.7
	100	8.52	0.0026	3.56	0.299	0.7
	50	8.41	0.0003	3.46	0.297	0.8
	5	8.25	0.0000	3.35	0.290	0.9

Table 3.2 Drude-Lorentz parameters extracted from fits of the measured dielectric functions

Sample	T (K)	$\hbar\omega_p$ (eV)	$\hbar\omega_c$ (eV)	ε_∞	s_1	$\hbar\omega_1$ (eV)	γ_1 (eV)	Error (%)
SC	298	8.86	0.0291	3.54	0.250	6.72	13.03	0.4
	200	9.04	0.0244	3.90	0.245	6.49	14.30	0.3
	100	8.92	0.0190	3.76	0.224	6.30	14.30	0.3
	50	8.81	0.0164	3.64	0.214	5.98	14.40	0.6
	5	8.66	0.0154	3.50	0.204	6.20	14.30	0.5
TS	298	9.00	0.0244	3.97	2.433	1.65	11.0	0.5
	200	8.85	0.0195	3.67	2.437	3.36	50.0	0.6
	100	8.66	0.0126	3.34	1.855	2.09	15.3	0.7
	50	8.47	0.0107	3.24	4.960	1.95	39.1	0.8
	5	8.39	0.0141	3.34	0.460	3.72	15.0	0.7
Ro	298	8.66	0.0410	3.71	1.04	4.60	13.6	0.2
	200	8.63	0.0322	3.55	1.19	9.85	63.7	0.3
	100	8.59	0.0254	3.49	1.20	10.09	68.8	0.4
	50	8.48	0.0245	3.46	1.02	4.72	14.6	0.5
	5	8.32	0.0220	3.27	1.09	11.21	82.6	0.5

So far we have not considered thermal expansion in the Drude model. The plasma frequency should be temperature dependent through the linear thermal expansion coefficient, γ, as

$$\omega_p(T) = \frac{\omega_p(T_0)}{\sqrt{1+3\gamma(T-T_0)}}. \quad (5)$$

with T_0 as the reference temperature. According to this expression, the plasma frequency should then increase with decreasing T. However, assuming 1.5 x 10^{-5} K^{-1} for γ,[34] we expect only a +0.7% change in ω_p in going from 298 to 5 K. Experimentally, we find the opposite trend. The extracted plasma frequencies (Table 1) decrease by several percent upon cooling. In practice, the fits use ω_p and ε_∞ to correct for deviations from the Drude model, including the influence of interband transitions. When we instead constrain ω_p according to Eq. (5), much worse fits are obtained.

Plasmon Propagation Lengths

As shown above, cooling reduces ε_{lm} and thus plasmonic losses. Because losses limit the propagation distance of the SPPs, this distance should increase at low T. Using our measured dielectric functions, we calculated the expected SPP propagation lengths, L_{SPP}, at the vacuum-Ag interface[1, 2] (see Figure 3.3). Figure 3.4a shows the expected enhancement in L_{SPP} at various temperatures (compared to 298 K) for Sample SC. Figure 3.4b compares the expected enhancement at 5 K for our three sample types. We see a clear dependence on the crystallinity and roughness of the Ag. Compared to SPP propagation lengths at room temperature, Sample SC at 5 K should show enhancements from 35 to 55% between 500 and 800 nm. Sample TS should show enhancements from 23 to 40% in this range. While the roughness of the single-crystalline and template-stripped films is similar, grain boundaries in the latter contribute to additional temperature-independent losses. Sample Ro had a much higher roughness and smaller grains. Consequently, it should exhibit smaller enhancements from 10 to 22% between 500 and 800 nm.

To test these predictions, we also measured L_{SPP} directly using the slit-groove technique.[24, 28] Pairs of parallel slits and grooves were etched into single-crystalline films with a dual-beam focused-ion beam (FIB) operating at 30 kV and 33 pA (FEI, Helios). All slits and grooves were 200 nm wide and 20 μm long; the slits were etched through the entire film and the grooves were 50 to 60 nm deep. Each slit-groove pair was separated by a distance d, which we varied from 10 to 40 μm. When the films were illuminated from the

backside with a 250-W tungsten-halogen lamp, SPPs were generated at the slits. They then propagated towards the groove. Spectra were obtained by collecting the scattered light at 298 and 25 K. Propagation lengths at each wavelength were determined by fitting an exponentially decaying function to the spectra for a range of *d*.

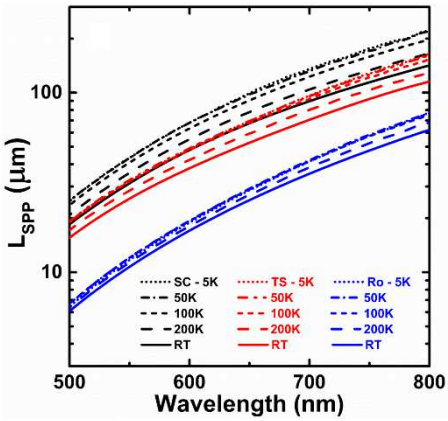

Figure 3.3 Propagation lengths versus temperature expected for a rough film (blue), template-stripped polycrystalline film (red), and single-crystalline film (black). These values are calculated from the measured dielectric functions using a two-layer vacuum-Ag model.

Figure 3.4(c) shows the measured L_{SPP} values averaged from four different single-crystalline Ag films. As in previous slit-groove experiments on such samples,[28, 29] our measured values are less than those predicted from our ε data (*e.g.* 12.5 versus 60 μm for 630 nm at RT, see Figure 3.3). However, we note that unlike in reference 28, we assumed that the SPPs are launched from the slits only in the normal direction. If we included an angular distribution of the launched SPPs, our measured L_{SPP} would increase by up to 150%. Lower L_{SPP} values could also be caused by film contamination (during the FIB process or general oxidation/sulfidation). Our sample preparation required more than a week for AFM, sample shipment, and FIB etching before optical measurements could be performed. However, despite these issues, the measured enhancements in L_{SPP} (Figure 3.4d) are in reasonable agreement with the expected values (Figure 3.4b), especially at wavelengths longer than 580 nm where enhancements between 40 and 60% are observed.

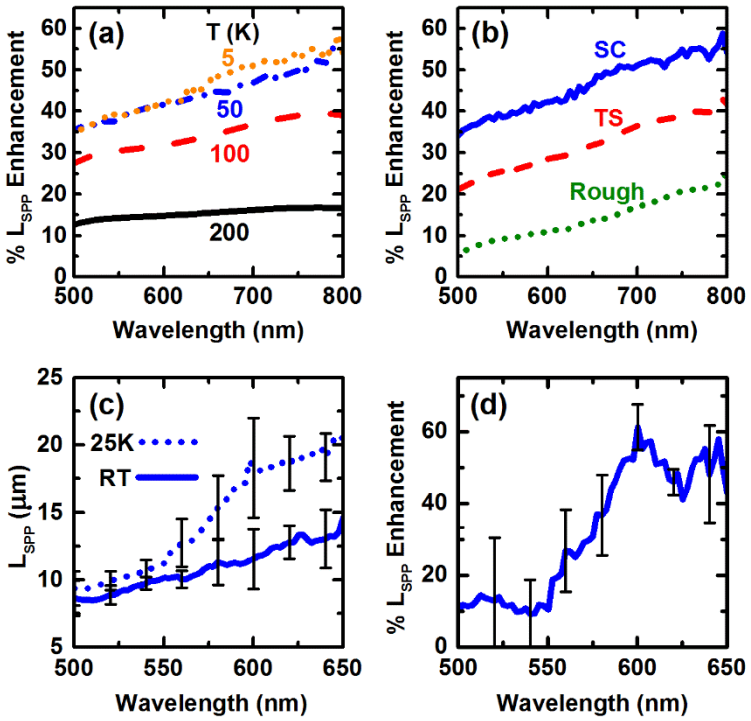

Figure 3.4 (a) Expected enhancements at various temperatures (relative to 298 K) in the surface-plasmon-polariton (SPP) propagation length, L_{SPP}, for Sample SC calculated from the measured dielectric functions. (b) The expected enhancements in L_{SPP} at 5 K (relative to 298 K) for Samples SC, TS, and Ro. (c) Direct measurements of L_{SPP} from single-crystalline Ag films at 298 (RT) and 25 K. 200-nm-wide slits and grooves were milled into four identical films using a focused ion beam. Illumination on the bottom of the film launches SPPs along the vacuum-Ag interface from the slit towards the groove. Scattered light from the slit is collected using a spectrometer. L_{SPP} is extracted by fitting data from various slit-groove separations, d, to an exponential decay. Error bars represent standard deviations for the four samples. (d) Measured enhancements in L_{SPP} determined from the data in (c).

Conclusion

In summary, we report experimental values for the dielectric functions of Ag films at cryogenic temperatures. The measurements were fit to Drude and Drude-Lorentz models and the parameters tabulated. The results are consistent with reduced electron-phonon scattering upon cooling. We show that this can lead to a 40 to 60% increase in the surface plasmon polariton propagation length for red wavelengths at low temperature. While our focus here has been on plasmonic applications, the dielectric functions and model parameters reported are useful for many low-temperature experiments and calculations on planar or structured Ag.

3.4 References

[1] H. Raether, *Surface plasmons on smooth surfaces*. (Springer, 1988).

[2] S. A. Maier, *Plasmonics: Fundamentals and applications*. (Springer, New York, 2007).

[3] W. L. Barnes, A. Dereux, T. W. Ebbesen, "Surface plasmon subwavelength optics." *Nature* **424**, 824-830 (2003).

[4] R. Gordon, D. Sinton, K. L. Kavanagh, A. G. Brolo, "A new generation of sensors based on extraordinary optical transmission." *Acc. Chem. Res.* **41**, 1049-1057 (2008).

[5] J. Homola, "Surface plasmon resonance sensors for detection of chemical and biological species." *Chemical Reviews* **108**, 462-493 (2008).

[6] M. Moskovits, "Surface-enhanced raman spectroscopy: A brief retrospective." *Journal of Raman Spectroscopy* **36**, 485-496 (2005).

[7] T. W. Ebbesen, C. Genet, S. I. Bozhevolnyi, "Surface-plasmon circuitry." *Physics Today* **61**, 44-50 (2008).

[8] P. Bai, H. Son Chu, M. Gu, O. Kurniawan, E. Li, "Integration of plasmonics into nanoelectronic circuits." *Physica B: Condensed Matter* **405**, 2978-2981 (2010).

[9] A. Boltasseva, H. A. Atwater, "Low-loss plasmonic metamaterials." *Science* **331**, 290-291 (2011).

[10] J.-S. G. Bouillard, W. Dickson, D. P. O'Connor, G. A. Wurtz, A. V. Zayats, "Low-temperature plasmonics of metallic nanostructures." *Nano Letters* **12**, 1561-1565 (2012).

[11] P. B. Johnson, R. W. Christy, "Optical constants of the noble metals." *Physical Review B* **6**, 4370-4379 (1972).

[12] T. Holstein, "Optical and infrared volume absorptivity of metals." *Physical Review* **96**, 535 (1954).

[13] R. Gurzhi, "On the theory of the infrared absorptivity of metals." *Soviet Journal of Experimental and Theoretical Physics* **6**, 506 (1958).

[14] R. Gurzhi, "Mutual electron correlations in metal optics." *Soviet Journal of Experimental and Theoretical Physics* **8**, 673-675 (1959).

[15] H. Ehrenreich, H. R. Philipp, "Optical properties of Ag and Cu." *Physical Review* **128**, 1622-1629 (1962).

[16] T. Holstein, "Theory of transport phenomena in an electron-phonon gas." *Annals of Physics* **29**, 410-535 (1964).

[17] W. E. Lawrence, J. W. Wilkins, "Umklapp electron-phonon scattering in the low-temperature resistivity of polyvalent metals." *Physical Review B* **6**, 4466-4482 (1972).

[18] W. E. Lawrence, J. W. Wilkins, "Electron-electron scattering in the transport coefficients of simple metals." *Physical Review B* **7**, 2317-2332 (1973).

[19] W. E. Lawrence, "Electron-electron scattering in the low-temperature resistivity of the noble metals." *Physical Review B* **13**, 5316-5319 (1976).

[20] J. A. McKay, J. A. Rayne, "Temperature dependence of the infrared absorptivity of the noble metals." *Physical Review B* **13**, 673-685 (1976).

[21] R. T. Beach, R. W. Christy, "Electron-electron scattering in the intraband optical conductivity of Cu, Ag, and Au." *Physical Review B* **16**, 5277-5284 (1977).

[22] G. R. Parkins, W. E. Lawrence, R. W. Christy, "Intraband optical conductivity σ(ω,t) of cu, ag, and au: Contribution from electron-electron scattering." *Physical Review B* **23**, 6408-6416 (1981).

[23] E. J. R. Vesseur, R. de Waele, H. J. Lezec, H. A. Atwater, F. J. G. de Abajo, A. Polman, "Surface plasmon polariton modes in a single-crystal au nanoresonator fabricated using focused-ion-beam milling." *Applied Physics Letters* **92**, 083110 (2008).

[24] P. Nagpal, N. C. Lindquist, S. H. Oh, D. J. Norris, "Ultrasmooth patterned metals for plasmonics and metamaterials." *Science* **325**, 594-597 (2009).

[25] N. C. Lindquist, T. W. Johnson, D. J. Norris, S.-H. Oh, "Monolithic integration of continuously tunable plasmonic nanostructures." *Nano Letters* **11**, 3526-3530 (2011).

[26] J. Hyuk Park, P. Nagpal, S.-H. Oh, D. J. Norris, "Improved dielectric functions in metallic films obtained via template stripping." *Applied Physics Letters* **100**, 081105 (2012).

[27] Y. J. Lu, J. Kim, H. Y. Chen, C. H. Wu, N. Dabidian, C. E. Sanders, C. Y. Wang, M. Y. Lu, B. H. Li, X. G. Qiu, W. H. Chang, L. J. Chen, G. Shvets, C. K. Shih, S. Gwo, "Plasmonic nanolaser using epitaxially grown silver film." *Science* **337**, 450-453 (2012).

[28] J. H. Park, P. Ambwani, M. Manno, N. C. Lindquist, P. Nagpal, S.-H. Oh, C. Leighton, D. J. Norris, "Single-crystalline silver films for plasmonics." *Advanced Materials* **24**, 3988-3992 (2012).

[29] Y. Wu, C. Zhang, N. M. Estakhri, Y. Zhao, J. Kim, M. Zhang, X.-X. Liu, G. K. Pribil, A. Alù, C.-K. Shih, X. Li, "Intrinsic optical properties and enhanced plasmonic response of epitaxial silver." *Advanced Materials* **26**, 6106-6110 (2014).

[30] M. Liu, M. Pelton, P. Guyot-Sionnest, "Reduced damping of surface plasmons at low temperatures." *Physical Review B* **79**, (2009).

[31] M. Mayy, G. Zhu, E. Mayy, A. Webb, M. A. Noginov, "Low temperature studies of surface plasmon polaritons in silver films." *Journal of Applied Physics* **111**, 094103 (2012).

[32] M. Hegner, P. Wagner, G. Semenza, "Ultralarge atomically flat template-stripped Au surfaces for scanning probe microscopy." *Surface Science* **291**, 39-46 (1993).

[33] K. M. McPeak, S. V. Jayanti, S. J. P. Kress, S. Meyer, S. Iotti, A. Rossinelli, D. J. Norris, "Plasmonic films can easily be better: Rules and recipes." *ACS Photonics* **2**, 326-333 (2015).

[34] F. C. Nix, D. MacNair, "The thermal expansion of pure metals. Ii: molybdenum, palladium, silver, tantalum, tungsten, platinum, and lead." *Physical Review* **61**, 74-78 (1942).

Chapter 4.

Surface-Plasmon Amplification Using Quantum Dots and Experimental Limitations

Surface plasmon polaritons (SPPs) are hybrid electromagnetic and electronic oscillations that propagate at a metal-dielectric interface. Their sub-diffraction confinement allows nanoscale manipulation of electromagnetic energy, leading to exciting applications such as surface- plasmon waveguides, optoelectronic circuits, and spasers. However, surface plasmon losses severely limit many plasmonic applications. An active medium can be used to stimulate emission of SPPs and rejuvenate them as they propagate. Here, we specifically study the ability of thin layers of quantum dots to amplify SPPs. We apply previously reported models and include near-field effects to calculate the expected propagation length enhancements. We explore the importance of key parameters such as the dipole strength, lifetimes in the near field, distance from the metal, and thickness of quantum-dot layers, Furthermore, we consider the experimental limitations on the calculations. Specifically, we study the emission dynamics and photostability of the quantum dots to obtain realistic gain parameters and expected SPP amplification.

4.1 Introduction

Surface plasmon polaritons (SPPs) are coupled electromagnetic and electronic oscillations that propagate on a metal surface. Compared to photons, they offer several advantages that are important to realizing nanoscale optical devices. Foremost among them are the nanoscale confinement of optical energy and enhanced field density at the interface. Surface plasmons have been studied in great detail for applications in optoelectronic circuits,[1, 2] nanoimaging,[3-6] solar cells,[7-11] and surface-plasmon amplification by stimulated emission of radiation.[12-16] The high field densities have been exploited to show proof-of-concept ideas such as surface-enhanced photoluminescence,[17-19] passive and active components for optoelectronics,[20-23] non-linear interaction with dipole emitters,[24] and versions of a spaser.[14, 16]

The limiting problem in plasmonics is the surface-plasmon loss.[12, 15, 25-33] While light in photonic waveguides can carry information over thousands of kilometers, the propagation distance of SPPs is limited to tens of micrometers for visible wavelengths. This has led to a strong interest in understanding the fundamental limitations of SPPs and exploring the physics of SPP amplification. Surface plasmons scatter due to electron-electron scattering, electron-phonon scattering, interband transitions, grain boundary scattering, roughness scattering, and radiative damping. On a flat, unstructured metal, the radiative damping is negligible. The grain boundary and roughness can be controlled to a large degree by optimizing the deposition of metal films.[34-36] For example, the template-stripping approach can be used to deposit metals onto a Si wafer with native oxide under appropriate conditions, and then peel it off using an adhesive to reveal an ultrasmooth, polycrystalline surface with large grain sizes.[36] While the electron-electron scattering and electron-phonon scattering can be partially reduced by lowering the temperature, they still limit the long-distance propagation of SPPs.[26, 37]

One way to increase the SPP propagation length is by using a gain medium [such as dyes, organic semiconductors, rare-earth ions, and semiconductor quantum dots (QDs)] to amplify the SPPs.[12, 38-43] When the gain medium is excited by a pump source, incoming SPPs can interact and stimulate the emission of more identical SPPs. If the number of

stimulated SPPs balances the number of lost (or scattered) SPPs, then the SPPs appear to propagate indefinitely. Previously, many groups have tried to experimentally address this issue. PbS QDs were used to amplify SPPs by 27% at telecom wavelength in a dielectric-loaded SPP waveguide.[41] In a more successful demonstration, dye molecules were pumped in solution above a symmetric stripe waveguide supporting long-range SPPs to obtain a gain of 8.55 dB/mm.[44] Complete loss compensation was observed at 633 nm using an organic gain medium in an SPP waveguide; the best waveguide showed a net gain of 93 dB/mm.[43] However, few works have studied the fundamental limitations and tried to optimize key parameters for maximizing gain. Surface-plasmon gain was modeled in planar metallic geometries by incorporating distance dependent lifetimes and pump intensities and gain coefficients were calculated for R6G dye in CYTOP next to a silver film.[38]

In this work, we develop a theoretical model based on previous reports to understand whether we can fully compensate for SPP loss using colloidal semiconductor QDs. Semiconductor QDs are color-tunable[45] dipole emitters that have large absorption cross-sections,[46, 47] high photoluminescence quantum yields,[48, 49] and high photostabilities.[50, 51] We specifically focus on thin layers of QDs (between 1 and 4 monolayers), and calculate the SPP amplification using realistic parameters based on our measurements and calculations. We discuss and optimize key design parameters, such as the spacer layer thickness, the QD lifetime, the thickness of the QD layer, the absorption and emission cross-sections, and the temperature. A thin spacer layer of 10 nm and long lifetime maximizes the interaction of the SPP and the QD. To this end, we synthesize and characterize high quality CdSe/CdS core/shell QDs with single-exponential lifetimes of 52 ns at room temperature. Our calculations suggest that SPP amplification could be achieved using only a few monolayers of QDs. While previous reports use free-space cross-sections for calculations, cross-sections accounting for interactions with SPPs are a better indicator of gain (since free-space cross sections are based on vacuum fluctuations and interactions with photons). We show that small increases in the cross-section can lower the pump intensity requirements drastically. Finally, lowering the temperature helps for two

important reasons: SPP loss is reduced due to lower electron-electron and electron-phonon scattering, and the QD lifetimes are longer by more than 2-fold.[52-55]

One issue when using QDs is their photostability. More than three decades of research on CdSe based QDs has led to their consideration for solar cells,[56] imaging,[57] LEDs,[58, 59] and lasers.[60, 61] Despite this, their photostability still presents challenges for their implementation in devices. We demonstrate increased photostability of our QDs by isolating them in an inert atmosphere and reducing exposure to oxygen and moisture. Based on our observations, we predict that without any cross-section enhancement, a monolayer of QDs cannot fully compensate for SPP losses at room temperature. At high intensities, the QDs enter the bi-exciton or multi-exciton regime, where the lifetimes are very short. This lowers the time of interaction with a SPP, and increases spontaneous emission at the expense of gain.

Finally, we briefly study gain experimentally and show promising preliminary results. Note that gain is the prerequisite for any surface-plasmon-based laser or spaser. The results herein are directly useful to understand the physics of a SPP based spaser.

4.2 Results and Discussion

We study the SPP gain in a 4-layer geometry at 630 nm. By solving the Maxwell's equations with appropriate boundary conditions, the SPP propagation length can be calculated.[62] Here, by including the intensity-dependent gain coefficient in the dielectric constant of the QD layer, we can obtain propagation length enhancements as a function of the pump intensity, and other important parameters. We simply need to know the dielectric constants of each of the 4 layers.

The first layer is a semi-infinite silver slab. We choose to work with silver because it exhibits the lowest loss of all plasmonic metals in the visible. The dielectric constants of silver are calculated using the results in reference [37]. The second layer is alumina, which acts as a spacer layer between the silver and the QDs. The alumina refractive index is fixed at 1.7, consistent with our ellipsometry measurements. The third layer is the QD layer, for which we calculate a homogeneous dielectric constant based on the assumption and calculation below. The fourth layer is semi-infinite air, with a refractive index of 1.

When pumped by an external source at 436 nm (λ_P), the QDs are excited and their interaction with an incoming SPP is included in its dielectric constant. The complex permittivity for the QD is given by[38]

$$\varepsilon_{QD} = \varepsilon'_{QD} + i\frac{\lambda_e}{2\pi}g(z, I_P)\left(\varepsilon'_{QD}\right)^{1/2} \quad (1)$$

where ε'_{QD} is the real part of the dielectric constant in the absence of absorption or stimulated emission, λ_e is the emission wavelength (630 nm), and g is the small-signal gain coefficient that is dependent on the pump intensity, I_P, and the distance from the silver-alumina interface, z. The dielectric constant of the QD layer therefore incorporates the gain.

To find ε'_{QD}, we assume that the QDs are spin-coated to result in a uniformly thick, hexagonal close-packed layer. Therefore, the volume fraction of the QDs is 0.74 and that of air is 0.26. The dielectric constant is estimated to be 3.2 based on previous works[63],[64] using a weighted refractive index of 2.4 for $CdSe_xS_{1-x}$ quantum dots[65] at the band gap wavelength of 630 nm.

The small-signal gain coefficient is given by[66]

$$g = N_1\sigma_e - N_1\sigma_a^h - N_0\sigma_a \quad (2)$$

where N_1 is the density of nanocrystals in the excited state, N_0 is the density of nanocrystals in the ground state, σ_e is the emission cross section at the lowest excited state energy, σ_a is the absorption cross section for the transition from the ground state to the excited state, and σ_a^h is the cross section for any higher energy absorption events. The gain provided is a competition between the number of SPPs generated by nanocrystals in the excited state and the number of SPPs absorbed by nanocrystals in the ground state. If many more nanocrystals are in the ground state than in the excited state, SPP are likely to be absorbed. If more are in the excited state, then SPPs will be generated. The cross-sections are proportional to the probability of the transition and include the dipole strength, the strength of the interaction with the electromagnetic surrounding. Dipole emitters with the largest cross-section will interact strongly with the SPPs, and are more likely to undergo stimulated emission. Note that the cross-section can be significantly modified near plasmonic metals.[19]

We assume a continuous wave pump source exciting the QDs under steady state conditions.

$$\frac{dN_1}{dt} = -\frac{N_1}{\tau_1} + \frac{I_P}{\hbar\omega_P}\sigma_P N_0 \tag{3}$$

Using conservation of nanocrystals $N = N_0 + N_1$, we can get the final expression for the excited state population.

$$N_1 = \frac{NI_P\tau_1(z)\sigma_P(z)}{I_P\tau_1(z)\sigma_P(z)+\hbar\omega_P} \tag{4}$$

Note that we assume that the pump intensity is independent of the distance from the silver surface. We include the distance dependence of both the lifetime and the cross-section. Substituting this result into equation 2, we get

$$g = \frac{NI_P\tau_1(z)\sigma_P(z)}{I_P\tau_1(z)\sigma_P(z)+\hbar\omega_P}\sigma_e - \frac{NI_P\tau_1(z)\sigma_P(z)}{I_P\tau_1(z)\sigma_P(z)+\hbar\omega_P}\sigma_a^h - \left(\frac{N\hbar\omega_P}{I_P\tau_1(z)\sigma_P(z)+\hbar\omega_P}\right)\sigma_a \tag{5}$$

Lumping the contribution from the σ_a^h into σ_e, we define an effective cross section $\sigma_{e,eff}$,

$$g = \frac{NI_P\tau_1(z)\sigma_P(z)}{I_P\tau_1(z)\sigma_P(z)+\hbar\omega_P}\sigma_{e,eff} - \left(\frac{N\hbar\omega_P}{I_P\tau_1(z)\sigma_P(z)+\hbar\omega_P}\right)\sigma_a \tag{6}$$

The important parameters that need to be optimized for maximum gain are the lifetime, the density of QDs, and the absorption and emission cross sections. Increasing the lifetime increases the likelihood of interaction of a SPP with an excited QD, and reduces the probability of interaction with an absorbing QD in the ground state. Similarly, a larger emission cross-section means stronger interaction with an incoming SPP and increases the probability of stimulated emission. At the same time, a larger absorption cross-section at the pump wavelength increases the probability of exciting a QD, leading to larger gain per number of pump photons. Note that while the absorption cross section at the emission wavelength should be minimized, most often the emission and absorption cross-section are coupled. It is still in our best interest to enhance the emission cross-section.

To evaluate the distance-dependent lifetime and cross-section, we calculate the power dissipated by dipole emitters near a metal surface.[67-71] This was theoretically studied in detail in the 1970s.[68]

The lifetime and the cross-section depend on the photonic density of states in the surrounding medium. An emitter in the excited state in vacuum can decay by generating a photon or undergo non-radiative transitions. Near a metal, the dipole emitter can generate

a photon, surface plasmon, electron-hole pairs in the metal (Ohmic losses), or undergo intrinsic non-radiative decay mechanisms. The additional modes near a metal tend to increase the rate of exciton decay in a quantum dot, and therefore, decrease the lifetime.

Before approaching this quantitatively, a qualitative understanding of the physics provides intuition on the key parameters. Very close to the metal, the emitter donates most of its energy into the metal, generating electron-hole pairs. This is a very localized effect and dominates within a few nanometers of the metal surface.[70] In this region, the lifetime of the emitter is very short due to the large number of electron-hole pair acceptors. Very far from the metal, the emitter does not feel the presence of the metal and donates most of its energy into generating photons. The lifetime here is similar to that in vacuum. At intermediate distances, the emitter generates a combination of photons and SPPs. Therefore, we add a spacer layer of alumina to space the QDs from the silver. Note that the SPP field decays exponentially away from the silver with a decay length of approximately 200 nm. This sets an upper limit on the spacer thickness. At these distance, the lifetime is a fraction of its vacuum value, and depends on the distance.

To quantify the lifetime, we have to integrate the power dissipated by the emitter into all modes.[38, 70, 72]

$$\gamma_1 = \gamma_{nr}(1-\phi) + \gamma\phi \int_0^\infty P(u,z)du \qquad (7)$$

Here γ_1 is the decay rate and is equal to the inverse of the lifetime, γ_{nr} is the intrinsic non-radiative decay rate, γ is the decay rate in the absence of the metal (inverse of lifetime measured in the absence of metal), ϕ is the quantum yield, P is the power dissipation density normalized to that in the absence of the metal, and u is the component of the dipole's wave vector parallel to the metal normalized to that in vacuum. The QDs used for this study typically had quantum yields in liquid dispersions above 80%; here we assume that they have a quantum yield of 100%. To obtain the isotropic power dissipation, we average over all the possible dipole orientations.

$$P = \frac{2}{3}P_{\parallel} + \frac{1}{3}P_{\perp} \qquad (8)$$

Here $P_{\parallel}$ is the power dissipated by a dipole oriented parallel to the metal surface, and $P_{\perp}$ is the power dissipated by a dipole oriented perpendicular to the metal. These were treated extensively[68],[72] and are given by[38]

$$P_{\parallel} = Re\left\{\frac{3}{4}\frac{u}{\sqrt{1-u^2}}\left[1 + r_s e^{i2l_1 kz} + (1-u^2)\left(1 - r_p e^{i2l_1 kz}\right)\right]\right\} \quad (9)$$

$$P_{\perp} = Re\left\{\frac{3}{2}\frac{u^3}{\sqrt{1-u^2}}\left[1 + r_p e^{i2l_1 kz}\right]\right\} \quad (10)$$

Here, k is the magnitude of the far-field wavevector. The r_s and r_p are the Fresnel reflection coefficients for the s-polarized and p-polarized waves. These are given by

$$r_s = \frac{l_1 - l_2}{l_1 + l_2} \quad (11)$$

$$r_p = \frac{\varepsilon_1 l_2 - \varepsilon_2 l_1}{\varepsilon_1 l_2 + \varepsilon_2 l_1} \quad (12)$$

The parameters l_j are related to the components of wavevector perpendicular and parallel to the interface. These are given by $l_j = -i\left(\frac{\varepsilon_j}{\varepsilon_1} - u^2\right)^{1/2}$, where the ε_j are the dielectric constants of the layers.

The power dissipated by the dipole emitter as a function of the wavevector is shown in Figure 4.1a. Table 1 lists the parameters used for the calculations. The peak appearing at a wavevector just above 1 is the SPP contribution. The photon component remains roughly constant at different dipole distances from the metal. However, at small distances, a dominant broad shoulder appears at large u, indicating that most of the QD energy is lost into the metal. The SPP contribution is shown in Figure 4.1b. Because the SPP field is strongest at the interface (therefore the highest SPP density of states), the SPP generation rate peaks at the interface (z=0). However, note that directly on the metal, the quenching from Ohmic losses dominates; therefore, the fraction of SPPs generated is small. The lifetime goes to 0 directly at the metal (Figure 4.1c). At a distance of about 5-20 nm from the Ag, the fraction of SPP generated (and therefore, interaction of SPPs-QDs relative to photon-QD and electron hole pairs-QD) is maximized. Figure 4.1c and 4.1d confirm that lifetimes calculated in this manner are close to the measured values.

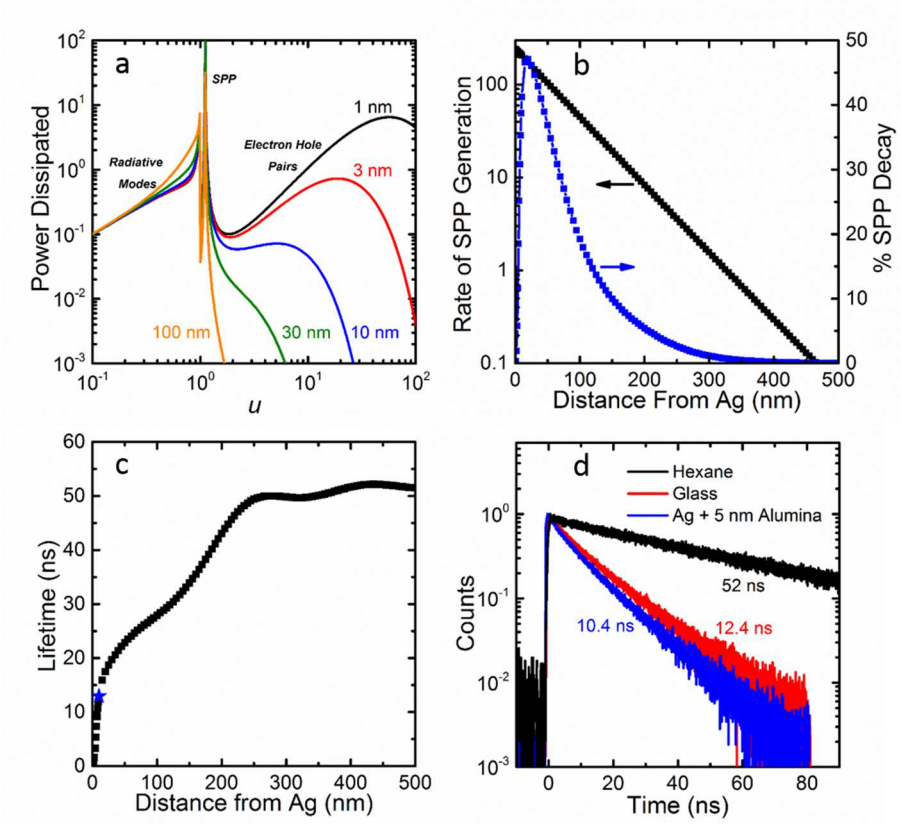

Figure 4.1 Emitter dissipation, SPP decay, and lifetime near a metal. a) Power dissipated as a function of the parallel component of the dipole's field wave vector for various distance from the silver interface. Note there are three contributions in the plots. For wave vectors smaller than 1, the dipole generates photons, as labeled in the left of the plot. At a specific wave vector slightly larger than 1, a peak corresponding to the SPP generation appears. To the right of the SPP, a broad peak/shoulder indicates the generation of electron hole pairs. Note that this contribution increases as the dipole gets closer to the interface, and becomes dominant at distances below 5 nm. b) The black curve shows the rate of generation of the SPPs (obtained from part a) as a function of the distance. Note that as expected this is close to an exponential decrease consistent with the exponential decay of SPP field and intensity from the silver-dielectric interface. Normalizing the SPP contribution to the total power dissipated, the fraction of SPP generated at each distance is calculated. The SPP contribution peaks around 10 to 20 nm from the silver surface. c) The lifetime is obtained following equation 7. Near the metal, the lifetime decreases significantly due to Ohmic losses. At around 10 nm, where the SPP interaction with the dipole is maximum, the lifetime is expected to be about 12 ns (blue star) based on a 52 ns lifetime in the absence of metal. d) The QD lifetime away from the metal was obtained by measuring it in hexane at low concentrations. The lifetime was also measured on Ag with 5 nm alumina. Due to the size of the particle (10 nm diameter), this dipole is 10 nm from the silver surface. The lifetime of 10.4 ns is close to that calculated by our model.

The last parameter in the gain coefficient is the cross-section enhancement. The cross-section is a measure of the probability of an absorption or emission event occurring.

This depends on the strength of the transition dipole, the electromagnetic surrounding, and the particle in question. For example, consider a dipole in vacuum, with an emission cross section of ρ_0 and a lifetime τ_0. If the dipole strength increases by 10 fold, the new particle would have an emission cross section of ρ_1 (equal to 10 ρ_0). However, the lifetime also decreases by about 10-fold. Therefore, we can't simply consider the decrease in lifetime without accounting for any increase in cross-sections. All previous calculations use the far-field absorption and emission cross-sections of the dipole. However, this is not always a good assumption. Previously, absorption and emission cross-section enhancements of ~70 were observed for single QDs on rough gold surfaces.[19] We specifically have to calculate the cross-section enhancement for the QD and SPP interaction, and distinguish this from the QD and photon interaction.

Table 4.1 Parameters used for SPP gain calculations. The dielectric constants for silver were obtained from reference [37].

Parameter	Value at 298K	Value at 10K (when different from 298K)
ε_{Ag}	$\varepsilon_\infty - \frac{\omega_p^2}{\omega\left(\omega + i\left(\omega_{ee} + \omega_{ep}\right)\right)}$	
$\hbar\omega_p$	8.85 eV	8.65
ε_∞	3.67	3.57
$\hbar\omega_{ep}$	0.0177 eV	0.0066 eV
$\varepsilon_{Al_2O_3}$	3	
ε'_{QD}	3.2	
λ_e (emission wavelength)	630 nm	
λ_p (pump wavelength)	436 nm	
τ (Lifetime away from metal)	52 ns	150 ns
σ_e	2.65 x 10^{-14} cm^2	
σ_a	7.5 x 10^{-16} cm^2	
σ_p	4.1 x 10^{-15} cm^2	

In our calculations, we account for the absorption and emission cross-section for SPP interactions by using an enhancement factor equal to the relative contribution of SPP

decay compared to the radiative decay. We assume that the cross-section (normalized to that in free space) for photon interaction is always 1. As a result, close to the metal surface, the cross-section for SPPs is larger and decays to 0 far from the metal. While this is not perfectly accurate, at the least it accounts for the distance dependence of the SPP density of states. Note that these factors range from about 1.4 near the surface to about 0.7 about 40 – 50 nm from the silver surface. Therefore, this contribution is small.

In reality, the cross-section can be enhanced or suppressed by larger factors. For example, a dipole perpendicular to the metal surface will induce an image dipole in the metal that increases the net dipole.[70] Meanwhile, a parallel dipole will induce an equal and opposite image dipole, strongly decreasing the net dipole. To complicate matters in a densely packed film of QDs, the nearby QD dipole and its image dipole also affect the final cross-section enhancement. As shown later, we also calculate the SPP amplification for different cross-section enhancements.

Once the dielectric constants of all layers are known, we can find the propagation lengths by solving Maxwell's equations.[62] The propagation lengths in the absence of gain are shown in Figure 4.2a for various geometries. As different layers are added above the silver, the SPP becomes more confined in the dielectric. Consequently, it spends more time near the metal, and exhibit more loss and shorter propagation lengths. Figure 4b shows the propagation length as a function of the QD thickness. The important point here is that care should be taken when simply calculating the gain in a geometry like ours. While thicker layers of QDs can provide larger gain, more losses have to be overcome. Simply calculating the gain is not fully meaningful. This is an important reason we plot the propagation length in our calculations of SPP amplification.

Another reason we cannot arbitrarily increase the QD-layer thickness is that additional pathways contribute to exciton decay and make experiments more prone to artifacts. For example, QD layers above a cutoff thickness (about 90 nm) can support waveguided photonic modes. This is illustrated in Figure 4.3. As the QD thickness is increased, additional TM and TE modes propagate in the QD waveguide. If the photons in the waveguide interact strongly with the dipole, the lifetime would be reduced, decreasing

the SPP gain. Furthermore, distinguishing SPPs and other waveguided modes can become difficult experimentally.

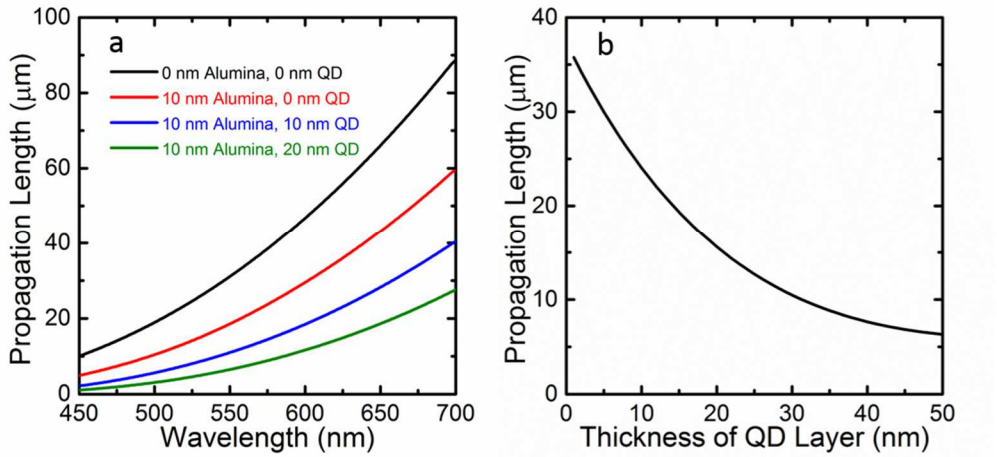

Figure 4.2 SPP propagation-length calculations. a) Propagation length as a function of wavelength in the visible for a silver film (black), a silver film with 10 nm of alumina (red), and an additional 10 nm of QDs (blue) or 20 nm of QDs (green). b) The propagation length at 630 nm decreases as a function of the thickness of the QD layer on top of silver with 10 nm of alumina.

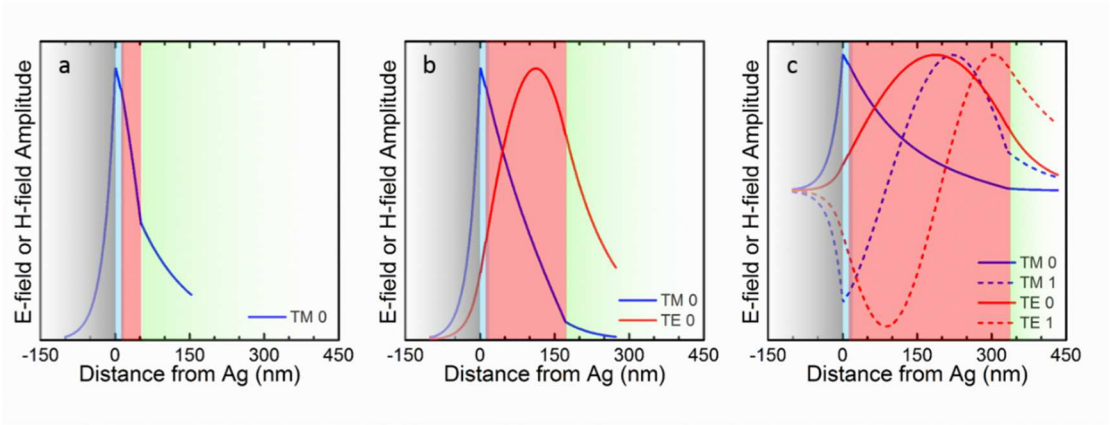

Figure 4.3 The different plasmonic and photonic modes supported in our geometry for different QD thicknesses. The silver layer is shown in the gray gradient to the left at distance below 0 nm. A small alumina spacer layer of 10 nm is included (light blue). The QD layer is treated as a homogeneous layer with thicknesses of 40 nm in (a), 160 nm in (b), and 320 nm in (c). When the thickness is small, only the SPP mode is supported. As expected, all SPP modes are transverse magnetic modes, denoted TM 0, and have a maximum field amplitude at the silver-alumina interface. As the thickness is increased to 160 nm, a TE mode appears that is photonic in nature and is more strongly confined the QD layer than at the metal interface. At even larger thicknesses, even more photonic modes are supported. In a multi-mode geometry as in (c), the gain provided to the SPPs decreases and their experimental observation becomes difficult.

Since the dielectric constant of the QD layer includes the gain coefficient, it indirectly accounts for the gain provided as a function of the pumping intensity. The SPP amplification is shown in Figure 4.4 for various scenarios. The propagation length as a function of pump intensity is plotted for different alumina thicknesses in Figure 4.4a. Only a single monolayer is used. The optimal alumina thickness is about 10 nm, and the SPP losses are fully compensated near 15 W/mm^2. At this point, the SPP propagation can continue indefinitely. In our experiments, the typical saturation intensities for a monolayer of QDs on silver are on the order of 10 W/mm^2. Therefore, a single layer of QDs may not fully compensate for SPP losses at room temperature.

Gain from QDs is typically limited to the single exciton regime. When bi- or multi-excitons are generated, the lifetime becomes very short, lowering the interaction time for stimulated emission.

Figure 4.4b shows that significantly larger gains can be provided by going to low temperature. At low temperature, the lifetime of the QDs increases, and the SPP losses decrease. Therefore, less power is required to compensate fully for the losses. In our calculations, the compensation power is lower by about 70 – 80% at 10K compared to that at room temperature. The compensation powers are plotted for different alumina thicknesses in Figure 4.4c.

The gain can be further increased by increasing the thickness of the QD layers. Despite the additional losses, lower pump intensities are needed to compensate for the losses (Figures 4.4d and 4.4e). These pump powers are now below the QD saturation intensities.

As mentioned earlier, the cross-section is an important parameter that needs more attention. In all of our calculations, we used cross-sections calculated based on the CdSe core of roughly 3.5 nm diameter. However, the nanocrystals are much larger, closer to 10 nm. Therefore, we use a severely underestimated cross-section in our calculations. Furthermore, the cross-sections can be enhanced or suppressed near the metal. It is difficult to calculate exactly the cross-sections since they are strongly dependent on the electromagnetic surrounding. SPP amplification at room temperature for a monolayer of QDs and 10 nm alumina is plotted for different cross-section enhancements in Figure 4.4f.

Even a 2-fold enhancement of cross-section reduced the compensation power below 10W/mm^2. Further increases in cross-section increase the gain by an order of magnitude.

Experimental realization of loss-compensation using QDs has not been shown. An important issue is the photostability of the QDs. We synthesized CdSe/CdS core/shell QDs with over 80% quantum yields using a recent recipe.[49] Despite varying the shell thickness over many batches[73, 74] of synthesis, all of the QDs (deposited on glass) bleached by 60% to 80% over the course of 10 minutes at pump intensities of 12.8 W/mm^2 when pumped with a continuous wave 405 nm laser (LDH-D-C 405, Picoquant) (Figure 4.5a). It has been previously shown that exposure to air (in particular, oxygen, water, and other reactive species) decreases the photostability of the QDs.[75-77] When deposited on Ag with 5 nm of alumina, the QDs bleached even more. We find that adding a layer of alumina on top of the QDs dramatically increases the photostability (Figure 4.5c). Sealing the samples in an inert nitrogen atmosphere similarly increases the photostability (Figure 4.5d).

A schematic of our experimental set up for SPP gain is shown in Figure 4.6. Briefly, a single crystalline silver film is deposited onto mica by sputtering (PVD 75, Kurt J. Lesker) at 360°C.[78] The film is milled using a focused ion beam (Helios, FEI) with parallel slit and groove pairs. The ion beam acceleration voltage is 30 kV and the current is set to 40 pA. An alumina layer and the QDs are deposited using atomic layer deposition (Picosun) at 100°C. SPPs are launched at the slit by a 633 nm HeNe laser source, and get amplified by the stimulated emission from QDs as they propagate towards the groove and scatter. The scattered signal is detected by a photodiode. The initial set of experiments were performed by chopping the HeNe laser, and pumping the QDs with a CW 405 nm laser.

The sample preparation is captured in Figure 4.7. CdSe/CdS core/shell QDs emitting at 630 nm were synthesized to obtain maximum overlap with the probe laser wavelength of 633 nm. The QDs have a typical full-width-at-half-maximum (FWHM) of about 27 nm. At the laser wavelength, the QDs are very weakly absorbing. Therefore, SPP reabsorption should be small. A slit and groove pair etched into silver are shown in Figure 4.7b. And a scanning electron micrograph of an optimized monolayer deposition on silver is shown in Figure 4.7c and 4.7d. The QDs form a uniform layer and appear to be well packed.

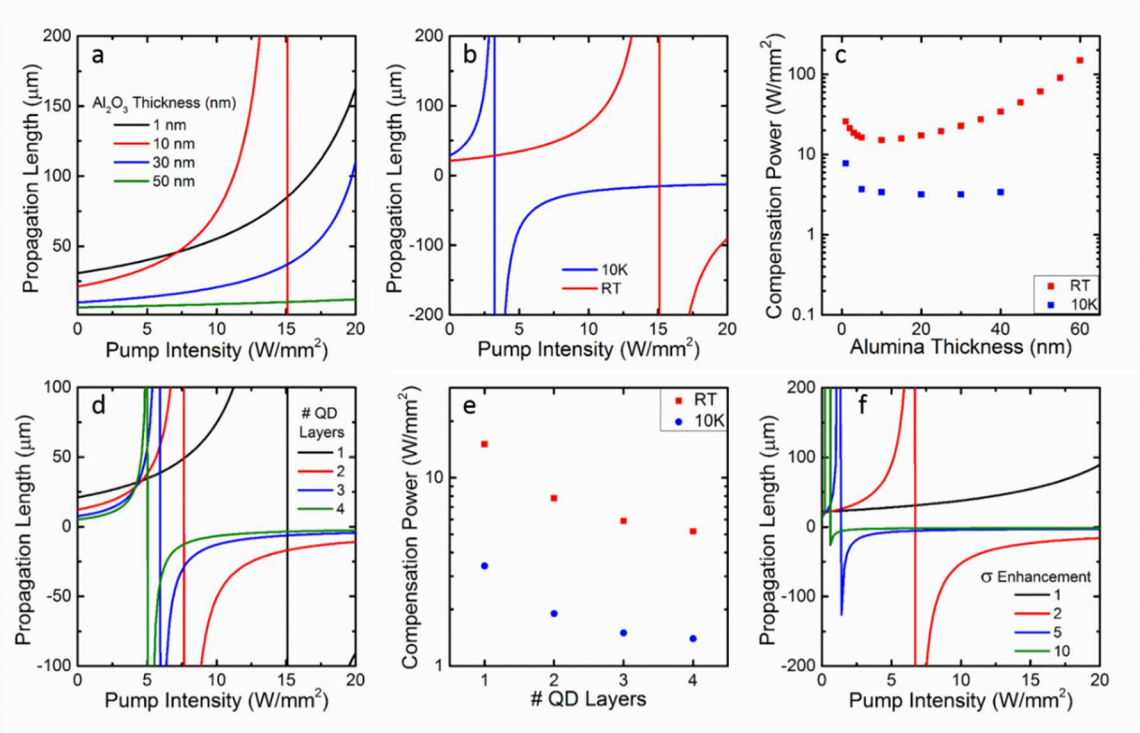

Figure 4.4 Gain calculations as a function of pump intensity, spacer thickness, temperature, number of QD layers, and cross-section enhancement. (a) Propagation length as a function of the CW pump intensity for various thicknesses of alumina layers and a single QD layer of 10 nm. Note that the propagation length increases with pump intensity. As expected, the starting propagation length decreases as the alumina thickness increases. When the alumina layer is 50 nm thick, the QDs are far and provide little gain. At the optimal distance of 10 nm, SPP propagation length goes to infinity at 15 W/mm^2. At this point, the losses are completely compensated, as the asymptote shows. Note that the dipole position is assume to be 5 nm above the alumina thickness, since the QDs are 10 nm in diameter. (b) The SPP amplification at room temperature and 10K are compared. At low temperature, the SPP losses are lower and due to the increased lifetime of the QD, less power is required to amplify the SPPs. Once the intensity is increased beyond the full compensation power, the propagation length becomes negative. Since the propagation length is defined as the distance over which the SPP intensity decays to 1/*e*, a negative propagation length is the distance over which SPP intensity increases by a factor of *e*, implying amplification of SPPs. (c) We find the pump intensity required to compensate for the losses for various alumina thickness at room temperature and 10K. As expected, the optimal spacer thickness is about 10 nm; pump intensities of 3 and 15 W/mm^2 fully compensate for losses at 10K and room temperature, respectively. (d) Thicker layers of QDs can provide more gain, and while the initial losses are higher, lower pump intensities are required to fully compensate for losses as QD layer gets thicker. (e) The power required to compensate for losses as a function of the number of QD layers is shown. (f) SPP gain increases strongly as the cross-section for the absorption and emission are enhanced. We assume equal enhancement factor for the absorption and emission cross-sections. The actual cross-section enhancement calculations are beyond the scope of this work.

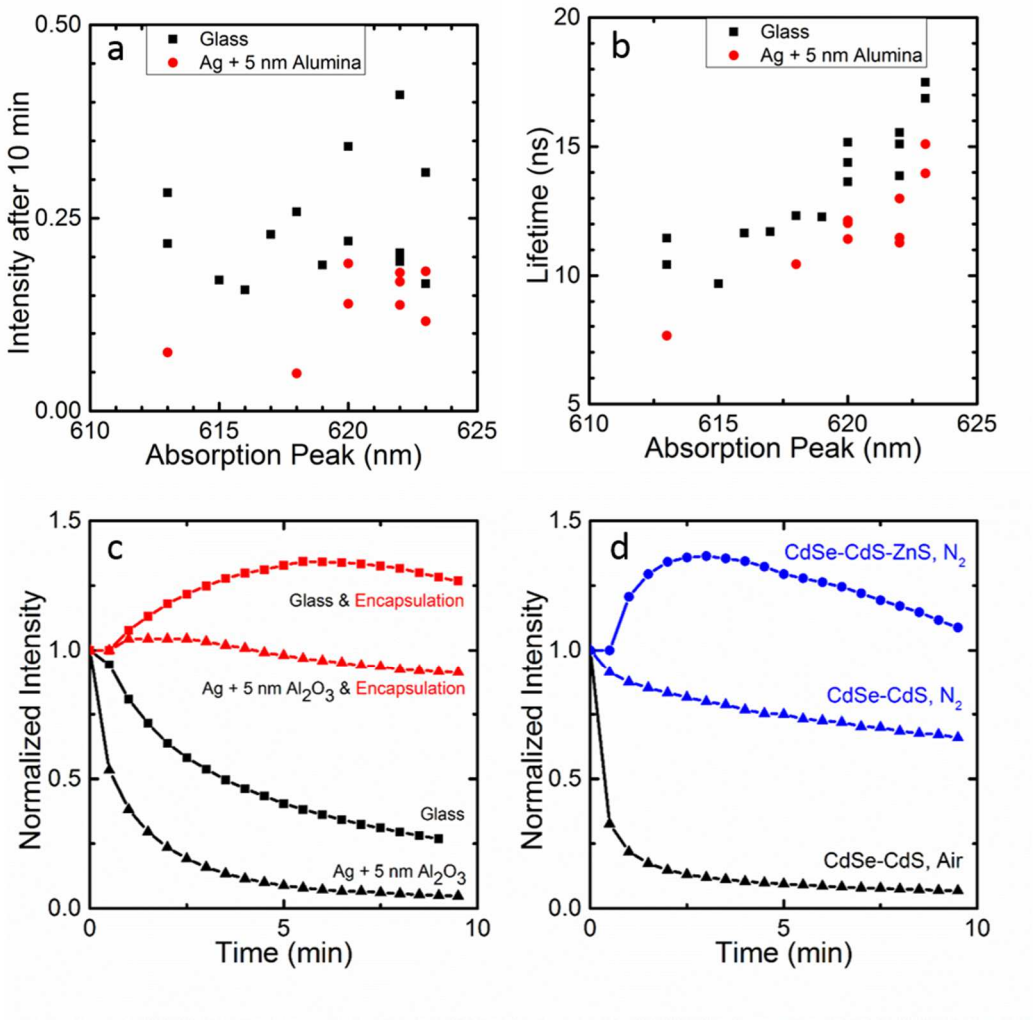

Figure 4.5 Photostability of QD monolayers. (a) The photoluminescence intensity after 10 minutes of illumination using a CW 405 nm laser at 1200 W/cm^2 for various batches of CdSe/CdS core/shell QDs synthesized and spun-cast as a monolayer onto a glass slide. The intensity is plotted as a function of the lowest energy absorption peak of the QDs. Since the core size (band-edge absorption wavelength) was kept constant at 3.8 nm (578 nm), the absorption peak here is indicative of the CdS shell thickness. The thicker the shell, the redder the absorption wavelength. The intensity in most cases decreases by 60% to 80%. The photoluminescence decreases even more on a silver film with alumina deposited by atomic layer deposition. (b) The lifetime of a monolayer of CdSe/CdS core/shell QDs on glass and on Ag with 5 nm of alumina increases as the shell thickness is increased. (c) Upon adding a thick layer of alumina on top of the nanocrystals to encapsulate them and isolate them from exposure to air, the photoluminescence becomes remarkably stable on glass and on silver. (d) The photostability is also increased by sealing the samples in a nitrogen environment, consistent with previous observations.

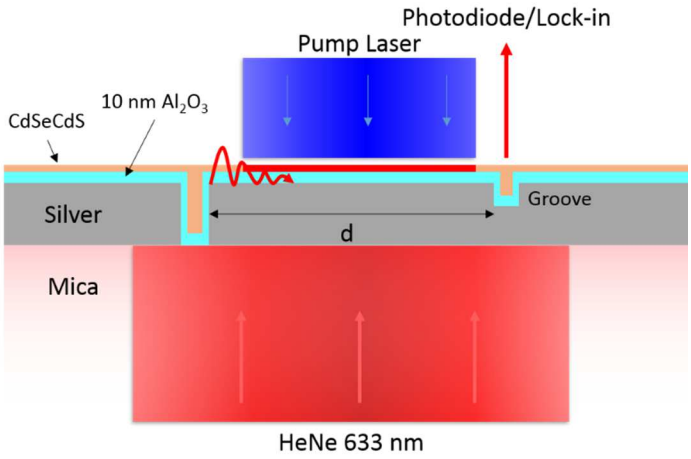

Figure 4.6 Experimental setup for our experiments to measure gain. A single-crystalline 300 nm film was deposited onto a transparent mica substrate. A slit (etched through the silver) and a groove of 60 nm depth and 200 nm width were milled into the silver using the focused ion beam at an acceleration voltage of 30 kV and an ion beam current of 40 pA. Slit-groove pairs at various distances, d, were milled. Subsequently, a 10 nm alumina layer was deposited by atomic layer deposition. QDs were spin-coated as a monolayer, and partially filled the slit and the groove. A 633 nm HeNe laser chopped around 1.5 kHz was used as an SPP source at the slit. The SPPs propagate from the slit towards the groove, where they scatter and are detected by a NewFocus photodiode connected to an SR850 lock-in amplifier. The signal at the photodiode was detected before and after pumping with a CW 405 nm source. The pump illuminated a 20 micrometer diameter spot between the slit and the groove.

Preliminary experiments were conducted to observe SPP amplification. A silver sample was first milled with 50 micrometer long and 200 nm wide slits and grooves at different distances. After depositing a 10 nm alumina layer at 80°C by atomic layer deposition (ALD), a monolayer of QDs was spin-coated. Note that this experiment was conducted in air. By measuring the SPP scattering signal at the grooves for various distance, a propagation length of 13.1 μm was obtained (Figure 4.8a).

An increase in the signal with pumping was observed (Figure 4.8b). However, these modest enhancements are not proof of SPP amplification. The signal can increase if the QDs are all in the excited state, due to reduced absorption of SPPs from the ground state. Note also that very high pumping intensities tend to affect the photostability of the sample. The SPP signal at the photodiode at 0 pump power changes after the sample is exposed to high pump intensities. This could be due to a couple of reasons. The laser is irreversibly damaging the QDs (either charging or photochemical degradation) such that the ground

state absorption or SPP loses are higher. The laser power could also be damaging the silver, although this is unlikely.

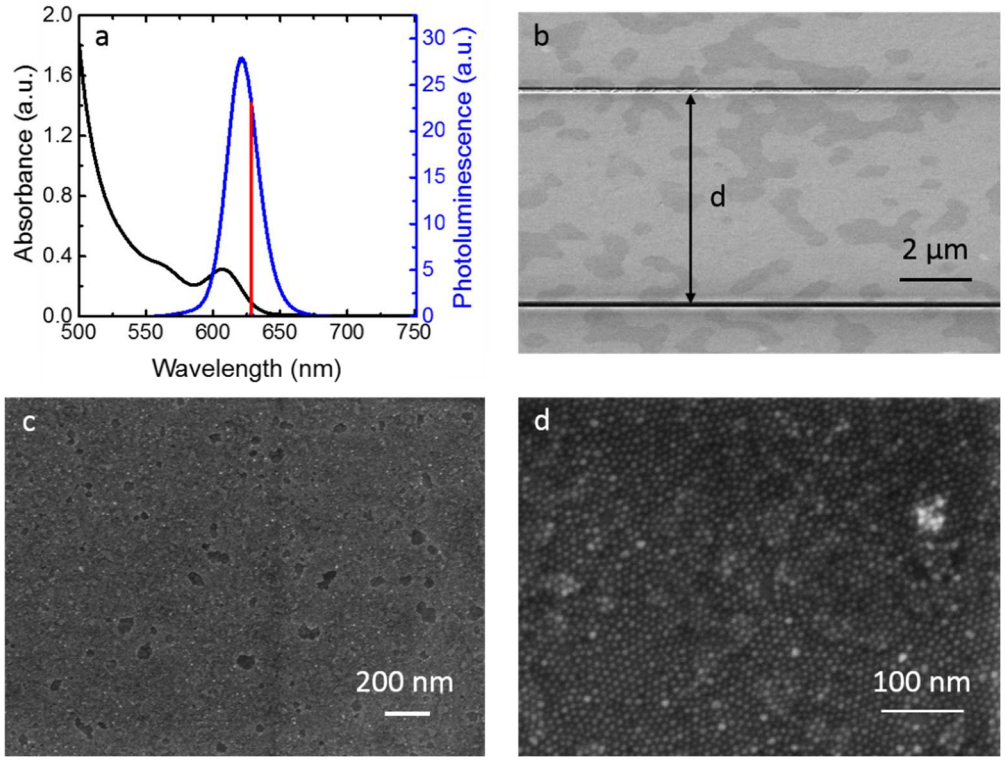

Figure 4.7 Characterization of the sample for SPP amplification. a) Absorption and emission spectra of the CdSe/CdS core/shell QDs used for this study. The red line indicates the SPP input signal from the HeNe laser. b) Scanning electron micrograph (SEM image) of a single-crystalline film milled with a slit and a groove using focused ion beam. c) SEM image showing optimized monolayer deposition of QDs on the silver film. The monolayer is uniform over tens of microns with few defect areas. d) A zoomed image of the QDs showing the densely packed layer (the silver grains below the QDs confirm that this is a monolayer).

The percentage signal enhancement was measured at various slit-groove distances between 20 µm and 26 µm. Because the illumination spot was approximately constant and 20 µm in diameter, the same enhancement is expected at all the distances, as seen in our experiments. The maximum signal enhancement is still small, casting doubts over whether this is actual SPP amplification or simply ground state bleaching.

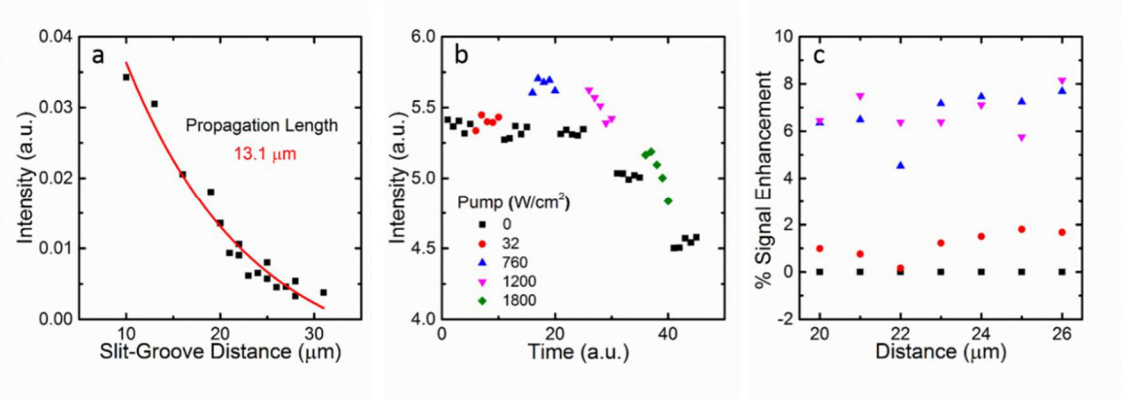

Figure 4.8 SPP amplification preliminary experiments. a) Propagation length measured by detecting the scattered signal at various slit-groove distances in the presence of QDs but without pumping. This is roughly half of the expected propagation length, consistent with previous measurements using this technique. b) The intensity measured by the photodiode for various pump intensities. Note that up to a power of 760 W/cm^2, the sample appears stable and returns to the original intensity at 0 pump power. At higher power, the off-state intensity decreases. Despite this, an increase in the signal is clearly observed when the QDs are pumped. c) The percentage increase in the signal at various slit-groove distances. Note that because the pump is always illuminating a fixed length of 20 micrometers, the percentage signal change is constant, but increases for increasing pump powers.

A better experimental design involves setting up a pump-probe experiment. QDs are more stable under pulsed excitation and a majority of stimulated-emission experiments have been conducted under pulsed excitation. In the simplest scenario, the same sample can be used with an ultrafast white light probe replacing the HeNe and an ultrafast pump replacing the CW 405 source. The white light probe will generate SPPs at all wavelengths at the slit, some of which will be amplified by the excited QDs. By adjusting the delay time between the pump and the probe, gain can be quantitatively studied. An additional variable that can be controlled is the excitation area. By controlling the length of amplification, the gain value can be extracted.

In summary, we have calculated SPP propagation length enhancement for various scenarios in a 4-layer geometry consisting of silver, alumina, thin QD layer, and air. A monolayer pumped under CW source is not likely to fully compensate for the SPP losses, but this depends strongly on the emission and absorption cross-section enhancements. Even a 2-fold enhancement can allow for amplification of SPPs. Multi-layers of QDs and low temperature significantly increase the gain and the possibility of SPP amplification.

Experimentally, the photostability of QDs presents a major road-block, but can be overcome to a large extent by encapsulation with alumina or sealing them in an inert atmosphere like nitrogen. A preliminary design for gain measurement is described, and pump-probe experiments are currently underway using a newly purchased ultrafast laser.

4.3 Materials and Methods

CdSe/CdS Core/Shell Nanocrystal Synthesis

Materials

Cadmium oxide (CdO, 99.99%) was purchased from Strem Chemicals. n-dodecylphosphonic acid (DDPA, 98%) was purchased from Epsilon Chimie. Trioctylphosphine oxide (TOPO, 90%), hexadecylamine (HDA, 90%), trioctylphosphine (TOP, 90%) selenium shot (99.999%), sulfur (>99.5%), 1-octadecene (ODE, 90%), oleylamine (OAm, 70%), oleic acid (OLA, 90%), 1-octanethiol (> 98.5%), and zinc acetate [Zn(acet)2, 99.99 %] were purchased from Sigma.

Synthesis of Core CdSe Nanocrystals

CdSe cores (3.8 nm, 578 nm band-edge) were synthesized following a modified version of a previous reported procedure.[79] Briefly, 6.4 mmol CdO, 12.8 mmol DDPA, 41.9 mmol TOPO and 153 mmol HDA were heated to 90°C with a heating mantle and then degassed three times. The reaction mixture was then heated to 320°C under nitrogen. Once the solution turned clear, the temperature was lowered to 280°C and 40 mL of 0.2M trioctylphosphine selenide (TOP:Se) was rapidly injected. After injection, the nanocrystals were grown for about 30 minutes at 260°C. The reaction mixture was cooled by removing the heating mantle, adding a water bath at 200°C and injecting 40 mL of 1-butanol at 130°C to prevent solidification. Nanocrystals were precipitated by adding 1:1 methanol and centrifugation at 4000 rpm. The precipitate was redispersed in n-hexane, allowed to sit overnight and centrifuged at 4000 rpm to precipitate unreacted material. The supernatant was washed twice more by repeated precipitation/dispersion in ethanol/hexane. After washing, the nanocrystals were redispersed in a hexane and stored until further use.

Cadmium Oleate Preparation for Core/Shell Synthesis

The cadmium oleate stock solution was prepared by combining 2.0 mmol of CdO, 8.0 mmol of OLA and 20 mL of ODE. It was then degassed and heated to 270°C under nitrogen until a clear, colorless solution was formed. The clear solution was degassed at 100°C for thirty minutes and then transferred into a glovebox for future use. Over time, cadmium oleate would solidify to a white solid. Prior to precursor injection, the Cd-oleate solution was heated at 70°C for twenty minutes to reform a clear, colorless solution. Then a desired amount of stock solution was diluted with ODE to give a total volume of 6 mL.

Synthesis of Epitaxially Grown CdS Shell on CdSe Nanocrystals

The CdS shell was epitaxially grown by following Chen *et al.*[49] Briefly, 100 nmol of CdSe nanocrystals in hexane, 3 mL of ODE and 3 mL of OAam were added to a 3-neck 100 mL flask, and degassed for an hour. The temperature was raised to 120°C, and it was allowed to stir at 1000 rpm for 20 minutes under vacuum. The reaction mixture was then heated to 305°C at a rate of 16°C/min under nitrogen. When the temperature reached 220°C, two separate syringes of Cd-oleate (between 0.2 and 0.33 mmol) and octanethiol (between 28 to 56 uL) were diluted in ODE to give a total volume of 6 mL and injected with a syringe pump at a rate of 3 mL/hour. After precursor injection, 1 mL of OLA was quickly injected and the solution was annealed for an additional hour at 305°C and then cooled to room temperature. The nanocrystals were cleaned by three rounds of precipitation/dispersion in ethanol/hexane.

Template-Stripped Silver Films

All the lifetime and the photostability studies were conducted on template-stripped Ag.[36] Briefly, silver was evaporated (Nano 36, Kurt J. Lesker) using 99.99% pure Ag pellets (Kurt J. Lesker) at a rate of 0.2 Å/s at a base pressure below 2 x 10^{-6} Torr. A soda lime glass was attached to the back using Norland 63 optical adhesive, and the film was

peeled off. A 5 nm alumina layer was deposited using atomic layer deposition (Picosun) at a temperature between 80˚C and 100˚C.

Single-Crystalline Silver Films

Freshly cleaved mica substrates (10 mm discs, highest grade, Ted Pella) were loaded into the sputterer (PVD 75, Kurt J. Lesker) and pumped to a pressure of 2 x 10^{-6} Torr.[78] The temperature was ramped to 360˚C at a rate of 3˚C/min. Following a 60 minute pre-anneal, silver was sputtered at a rate of 110 nm/min under a 6 mTorr Ar pressure and a substrate-source distance of 17 cm. After a 30 minute post-anneal, the samples were allowed to cool to room temperature.

Optical Experiments

All spectra and photostability measurements were conducted on a Nikon TE 200 inverted microscope. The photostability measurements were conducted using a 100x/0.9 NA objective. The laser beam was focused onto a 20 micrometer diameter spot. The resulting emission was directed to an imaging spectrometer (Triax 320, Jobin Yvon) with a grating blazed at 500 nm (150 lines/mm, Jobin Yvon). The spectra were recorded using a liquid-nitrogen-cooled CCD (Spec-10, Princeton Instruments).

For the gain experiments, the emission was directed to a photodiode connected to a lock-in (SR850, Stanford Research Systems). A rectangular slit was placed in the image plane and used to isolate the signal from just the groove on the single-crystalline silver film.

4.4 References

[1] W. L. Barnes, A. Dereux, T. W. Ebbesen, "Surface plasmon subwavelength optics." *Nature* **424**, 824-830 (2003).

[2] T. W. Ebbesen, C. Genet, S. I. Bozhevolnyi, "Surface-plasmon circuitry." *Physics Today* **61**, 44 (2008).

[3] T. W. Johnson, Z. J. Lapin, R. Beams, N. C. Lindquist, S. G. Rodrigo, L. Novotny, S.-H. Oh, "Highly reproducible near-field optical imaging with sub-20-nm resolution based on template-stripped gold pyramids." *ACS Nano* **6**, 9168-9174 (2012).

[4] S. Kawata, Y. Inouye, P. Verma, "Plasmonics for near-field nano-imaging and superlensing." *Nature Photonics* **3**, 388-394 (2009).

[5] E. J. Sánchez, L. Novotny, X. S. Xie, "Near-field fluorescence microscopy based on two-photon excitation with metal tips." *Physical Review Letters* **82**, 4014 (1999).

[6] A. V. Zayats, I. I. Smolyaninov, A. A. Maradudin, "Nano-optics of surface plasmon polaritons." *Physics Reports* **408**, 131-314 (2005).

[7] K. Catchpole, A. Polman, "Plasmonic solar cells." *Optics Express* **16**, 21793-21800 (2008).

[8] V. E. Ferry, M. A. Verschuuren, H. B. Li, E. Verhagen, R. J. Walters, R. E. Schropp, H. A. Atwater, A. Polman, "Light trapping in ultrathin plasmonic solar cells." *Optics Express* **18**, A237-A245 (2010).

[9] M. A. Green, S. Pillai, "Harnessing plasmonics for solar cells." *Nature Photonics* **6**, 130-132 (2012).

[10] X. Li, W. C. Choy, L. Huo, F. Xie, W. E. Sha, B. Ding, X. Guo, Y. Li, J. Hou, J. You, "Dual plasmonic nanostructures for high performance inverted organic solar cells." *Advanced Materials* **24**, 3046-3052 (2012).

[11] S. Pillai, K. Catchpole, T. Trupke, M. Green, "Surface plasmon enhanced silicon solar cells." *Journal of Applied Physics* **101**, 093105 (2007).

[12] P. Berini, I. De Leon, "Surface plasmon-polariton amplifiers and lasers." *Nature Photonics* **6**, 16-24 (2012).

[13] D. J. Bergman, M. I. Stockman, "Surface plasmon amplification by stimulated emission of radiation: Quantum generation of coherent surface plasmons in nanosystems." *Physical Review Letters* **90**, 027402 (2003).

[14] M. Noginov, G. Zhu, A. Belgrave, R. Bakker, V. Shalaev, E. Narimanov, S. Stout, E. Herz, T. Suteewong, U. Wiesner, "Demonstration of a spaser-based nanolaser." *Nature* **460**, 1110-1112 (2009).

[15] M. I. Stockman, "Spaser action, loss compensation, and stability in plasmonic systems with gain." *Physical Review Letters* **106**, 156802 (2011).

[16] N. I. Zheludev, S. Prosvirnin, N. Papasimakis, V. Fedotov, "Lasing spaser." *Nature Photonics* **2**, 351-354 (2008).

[17] T. Liebermann, W. Knoll, "Surface-plasmon field-enhanced fluorescence spectroscopy." *Colloids and Surfaces A: Physicochemical and Engineering Aspects* **171**, 115-130 (2000).

[18] P. Pompa, L. Martiradonna, A. Della Torre, F. Della Sala, L. Manna, M. De Vittorio, F. Calabi, R. Cingolani, R. Rinaldi, "Metal-enhanced fluorescence of colloidal nanocrystals with nanoscale control." *Nature Nanotechnology* **1**, 126-130 (2006).

[19] K. Shimizu, W. Woo, B. Fisher, H. Eisler, M. Bawendi, "Surface-enhanced emission from single semiconductor nanocrystals." *Physical Review Letters* **89**, 117401 (2002).

[20] E. Ozbay, "Plasmonics: Merging photonics and electronics at nanoscale dimensions." S*cience* **311**, 189-193 (2006).

[21] F. López-Tejeira, S. G. Rodrigo, L. Martín-Moreno, F. J. García-Vidal, E. Devaux, T. W. Ebbesen, J. R. Krenn, I. Radko, S. I. Bozhevolnyi, M. U. González, "Efficient unidirectional nanoslit couplers for surface plasmons." *Nature Physics* **3**, 324-328 (2007).

[22] H. Ditlbacher, A. Hohenau, D. Wagner, U. Kreibig, M. Rogers, F. Hofer, F. R. Aussenegg, J. R. Krenn, "Silver nanowires as surface plasmon resonators." *Physical Review Letters* **95**, 257403 (2005).

[23] A. Hohenau, J. R. Krenn, A. L. Stepanov, A. Drezet, H. Ditlbacher, B. Steinberger, A. Leitner, F. R. Aussenegg, "Dielectric optical elements for surface plasmons." *Optics Letters* **30**, 893-895 (2005).

[24] P. Törmä, W. Barnes, "Strong coupling between surface plasmon polaritons and emitters." *Reports on Progress in Physics* **78**, 013901 (2015).

[25] A. Boltasseva, H. A. Atwater, "Low-loss plasmonic metamaterials." *Science* **331**, 290-291 (2011).

[26] J.-S. G. Bouillard, W. Dickson, D. P. O'Connor, G. A. Wurtz, A. V. Zayats, "Low-temperature plasmonics of metallic nanostructures." *Nano Letters* **12**, 1561-1565 (2012).

[27] T. Holstein, "Theory of transport phenomena in an electron-phonon gas." *Annals of Physics* **29**, 410-535 (1964).

[28] W. Lawrence, "Electron-electron scattering in the low-temperature resistivity of the noble metals." *Physical Review B* **13**, 5316 (1976).

[29] W. Lawrence, J. Wilkins, "Umklapp electron-phonon scattering in the low-temperature resistivity of polyvalent metals." *Physical Review B* **6**, 4466 (1972).

[30] W. E. Lawrence, J. W. Wilkins, "Electron-electron scattering in the transport coefficients of simple metals." *Physical Review B* **7**, 2317-2332 (1973).

[31] H. Ehrenreich, H. Philipp, "Optical properties of Ag and Cu." *Physical Review* **128**, 1622 (1962).

[32] P. B. Johnson, R.-W. Christy, "Optical constants of the noble metals." *Physical Review B* **6**, 4370 (1972).

[33] R. Beach, R. Christy, "Electron-electron scattering in the intraband optical conductivity of Cu, Ag, and Au." *Physical Review B* **16**, 5277 (1977).

[34] V. Logeeswaran, N. P. Kobayashi, M. S. Islam, W. Wu, P. Chaturvedi, N. X. Fang, S. Y. Wang, R. S. Williams, "Ultrasmooth silver thin films deposited with a germanium nucleation layer." *Nano Letters* **9**, 178-182 (2008).

[35] K. M. McPeak, S. V. Jayanti, S. J. Kress, S. Meyer, S. Iotti, A. Rossinelli, D. J. Norris, "Plasmonic films can easily be better: Rules and recipes." *ACS Photonics*, (2015).

[36] P. Nagpal, N. C. Lindquist, S.-H. Oh, D. J. Norris, "Ultrasmooth patterned metals for plasmonics and metamaterials." *Science* **325**, 594-597 (2009).

[37] S. V. Jayanti, J.-H. Park, A. Dejneka, D. Chvostova, K. M. McPeak, X. Chen, S.-H. Oh, D. J. Norris, "Low-temperature enhancement of plasmonic performance in silver films." *Optical Materials Express* **5**, 5 (2015).

[38] I. De Leon, P. Berini, "Modeling surface plasmon-polariton gain in planar metallic structures." *Optics Express* **17**, 20191-20202 (2009).

[39] M. C. Gather, K. Meerholz, N. Danz, K. Leosson, "Net optical gain in a plasmonic waveguide embedded in a fluorescent polymer." *Nature Photonics* **4**, 457-461 (2010).

[40] D. Y. Fedyanin, A. V. Krasavin, A. V. Arsenin, A. V. Zayats, "Surface plasmon polariton amplification upon electrical injection in highly integrated plasmonic circuits." *Nano Letters* **12**, 2459-2463 (2012).

[41] J. Grandidier, G. C. Des Francs, S. Massenot, A. Bouhelier, L. Markey, J.-C. Weeber, C. Finot, A. Dereux, "Gain-assisted propagation in a plasmonic waveguide at telecom wavelength." *Nano Letters* **9**, 2935-2939 (2009).

[42] M. Nezhad, K. Tetz, Y. Fainman, "Gain assisted propagation of surface plasmon polaritons on planar metallic waveguides." *Optics Express* **12**, 4072-4079 (2004).

[43] S. p. Kéna-Cohen, P. N. Stavrinou, D. D. Bradley, S. A. Maier, "Confined surface plasmon–polariton amplifiers." *Nano Letters* **13**, 1323-1329 (2013).

[44] I. De Leon, P. Berini, "Amplification of long-range surface plasmons by a dipolar gain medium." *Nature Photonics* **4**, 382-387 (2010).

[45] C. Murray, D. J. Norris, M. G. Bawendi, "Synthesis and characterization of nearly monodisperse CdE (E= sulfur, selenium, tellurium) semiconductor nanocrystallites." *Journal of the American Chemical Society* **115**, 8706-8715 (1993).

[46] C. Leatherdale, W.-K. Woo, F. Mikulec, M. Bawendi, "On the absorption cross section of CdSe nanocrystal quantum dots." *The Journal of Physical Chemistry B* **106**, 7619-7622 (2002).

[47] W. W. Yu, L. Qu, W. Guo, X. Peng, "Experimental determination of the extinction coefficient of CdTe, CdSe, and CdS nanocrystals." *Chemistry of Materials* **15**, 2854-2860 (2003).

[48] B. Dabbousi, J. Rodriguez-Viejo, F. V. Mikulec, J. Heine, H. Mattoussi, R. Ober, K. Jensen, M. Bawendi, "(CdSe) ZnS core-shell quantum dots: Synthesis and characterization of a size series of highly luminescent nanocrystallites." *The Journal of Physical Chemistry B* **101**, 9463-9475 (1997).

[49] O. Chen, J. Zhao, V. P. Chauhan, J. Cui, C. Wong, D. K. Harris, H. Wei, H.-S. Han, D. Fukumura, R. K. Jain, "Compact high-quality CdSe–CdS core–shell nanocrystals with narrow emission linewidths and suppressed blinking." *Nature Materials* **12**, 445-451 (2013).

[50] X. Wang, X. Ren, K. Kahen, M. A. Hahn, M. Rajeswaran, S. Maccagnano-Zacher, J. Silcox, G. E. Cragg, A. L. Efros, T. D. Krauss, "Non-blinking semiconductor nanocrystals." *Nature* **459**, 686-689 (2009).

[51] Y. Chen, J. Vela, H. Htoon, J. L. Casson, D. J. Werder, D. A. Bussian, V. I. Klimov, J. A. Hollingsworth, "“Giant” multishell CdSe nanocrystal quantum dots with suppressed blinking." *Journal of the American Chemical Society* **130**, 5026-5027 (2008).

[52] O. Labeau, P. Tamarat, B. Lounis, "Temperature dependence of the luminescence lifetime of single CdSe/ZnS quantum dots." *Physical Review Letters* **90**, 257404 (2003).

[53] C. de Mello Donegá, M. Bode, A. Meijerink, "Size-and temperature-dependence of exciton lifetimes in CdSe quantum dots." *Physical Review B* **74**, 085320 (2006).

[54] S. Crooker, T. Barrick, J. Hollingsworth, V. Klimov, "Multiple temperature regimes of radiative decay in cdse nanocrystal quantum dots: Intrinsic limits to the dark-exciton lifetime." *Applied Physics Letters* **82**, 2793-2795 (2003).

[55] S. Brovelli, R. Schaller, S. Crooker, F. García-Santamaría, Y. Chen, R. Viswanatha, J. Hollingsworth, H. Htoon, V. Klimov, "Nano-engineered electron–hole exchange interaction controls exciton dynamics in core–shell semiconductor nanocrystals." *Nature Communications* **2**, 280 (2011).

[56] A. Nozik, "Quantum dot solar cells." *Physica E: Low-dimensional Systems and Nanostructures* **14**, 115-120 (2002).

[57] I. L. Medintz, H. T. Uyeda, E. R. Goldman, H. Mattoussi, "Quantum dot bioconjugates for imaging, labelling and sensing." *Nature Materials* **4**, 435-446 (2005).

[58] J. Caruge, J. Halpert, V. Wood, V. Bulović, M. Bawendi, "Colloidal quantum-dot light-emitting diodes with metal-oxide charge transport layers." *Nature Photonics* **2**, 247-250 (2008).

[59] Q. Sun, Y. A. Wang, L. S. Li, D. Wang, T. Zhu, J. Xu, C. Yang, Y. Li, "Bright, multicoloured light-emitting diodes based on quantum dots." *Nature Photonics* **1**, 717-722 (2007).

[60] V. Klimov, A. Mikhailovsky, S. Xu, A. Malko, J. Hollingsworth, C. Leatherdale, H.-J. Eisler, M. Bawendi, "Optical gain and stimulated emission in nanocrystal quantum dots." *Science* **290**, 314-317 (2000).

[61] E. Rafailov, M. Cataluna, W. Sibbett, "Mode-locked quantum-dot lasers." *Nature Photonics* **1**, 395-401 (2007).

[62] S. A. Maier, *Plasmonics: Fundamentals and applications*. (Springer Science & Business Media, 2007).

[63] E. Rabani, B. Hetenyi, B. J. Berne, L. E. Brus, "Electronic properties of CdSe nanocrystals in the absence and presence of a dielectric medium." *The Journal of Chemical Physics* **110**, 5355-5369 (1999).

[64] J. Reynolds, J. Hough, "Formulae for dielectric constant of mixtures." *Proceedings of the Physical Society. Section B* **70**, 769 (1957).

[65] B. Jensen, A. Torabi, "Refractive index of hexagonal ii–vi compounds CdSe, CdS, and $CdSe_xS_{1-x}$." *Journal of the Optical Society of America B* **3**, 857-863 (1986).

[66] L. Nair, "Dye lasers." *Progress in Quantum Electronics* **7**, 153-268 (1982).

[67] R. Chance, A. Prock, R. Silbey, "Lifetime of an emitting molecule near a partially reflecting surface." *The Journal of Chemical Physics* **60**, 2744-2748 (1974).

[68] R. Chance, A. Prock, R. Silbey, "Molecular fluorescence and energy transfer near interfaces." *Advanced Chemical Physics* **37**, 65 (1978).

[69] E. H. Hellen, D. Axelrod, "Fluorescence emission at dielectric and metal-film interfaces." *Journal of the Optical Society of America B* **4**, 337-350 (1987).

[70] W. Barnes, "Fluorescence near interfaces: The role of photonic mode density." *Journal of Modern Optics* **45**, 661-699 (1998).

[71] E. Fort, S. Grésillon, "Surface enhanced fluorescence." *Journal of Physics D: Applied Physics* **41**, 013001 (2008).

[72] G. W. Ford, W. H. Weber, "Electromagnetic interactions of molecules with metal surfaces." *Physics Reports* **113**, 195-287 (1984).

[73] S. F. Lee, M. A. Osborne, "Brightening, blinking, bluing and bleaching in the life of a quantum dot: Friend or foe?" *ChemPhysChem* **10**, 2174-2191 (2009).

[74] M. Oda, A. Hasegawa, N. Iwami, K. Nishiura, N. Ando, A. Nishiyama, H. Horiuchi, T. Tani, "Reversible photobluing of CdSe/ZnS/TOPO nanocrystals." *Colloids and Surfaces B: Biointerfaces* **56**, 241-245 (2007).

[75] H. Asami, Y. Abe, T. Ohtsu, I. Kamiya, M. Hara, "Surface state analysis of photobrightening in CdSe nanocrystal thin films." *The Journal of Physical Chemistry B* **107**, 12566-12568 (2003).

[76] H. Asami, I. Kamiya, M. Hara, "Photobrightening and photodarkening in CdSe nanocrystal/polymer thin films." *International Journal of Nanoscience* **1**, 641-644 (2002).

[77] J. Jasieniak, P. Mulvaney, "From Cd-rich to Se-rich-the manipulation of CdSe nanocrystal surface stoichiometry." *Journal of the American Chemical Society* **129**, 2841-2848 (2007).

[78] J. H. Park, P. Ambwani, M. Manno, N. C. Lindquist, P. Nagpal, S. H. Oh, C. Leighton, D. J. Norris, "Single-crystalline silver films for plasmonics." *Advanced Materials* **24**, 3988-3992 (2012).

[79] P. Reiss, J. Bleuse, A. Pron, "Highly luminescent CdSe/ZnSe core/shell nanocrystals of low size dispersion." *Nano Letters* **2**, 781-784 (2002).

Chapter 5.

Plasmonic Control of Surface-State Recombination in CdSe Nanocrystals for Tunable Emission[3]

The surface of CdSe colloidal nanocrystals plays a significant role in determining their optical properties. Only a few studies have sought to exploit this surface-related emission, the so-called "deep-trap" emission, for optical applications. These studies have been primarily limited to extremely small nanocrystals, for which the deep-trap emission is significant at room temperature. Moreover, these works lacked control over the spectra and the intensities of the surface-state emission. In this work, we strongly enhance the deep-trap emission to get broad (band-edge and deep-trap) emission in nanocrystals of all sizes on rough silver films that exhibit broad plasmonic resonances. In particular, nanocrystals with a blue-green band-edge state showed white-light emission. Additionally, we tailored plasmonic structures to strongly enhance and tune the surface-state emission of standard CdSe nanocrystals. Because these effects depend on where the nanocrystals are placed on the metal film, the same nanocrystals could be used to generate various colors on the same substrate. This leads to new possibilities for semiconductor nanocrystals in light-emitting devices and plasmonic circuits.

[3] This chapter is under preparation for submission as Sriharsha V. Jayanti, Martin Baldinger, Daniele Braga, Vincent Holmberg, David K. Kim, Kevin M. McPeak, Stephan J. P. Kress, Shimpei Ono, & David J. Norris, "Plasmonic control of surface-state recombination in CdSe nanocrystals for tunable emission".

5.1 Introduction

Quantum-confined semiconductor nanocrystals have been an active area of investigation for applications in light-emitting devices[1], fluorescence labeling, solar cells[2], and lasers.[3] Over the last three decades, our understanding and control of emission has advanced at a rapid rate. Due to the size of the nanocrystals, a significant fraction of the atoms are on the surface. For a 2 nm CdSe nanocrystal, roughly 70% of the atoms are on the surface; for a 4 nm nanocrystal, 20% of the atoms are on the surface. Therefore, control of the surface in large part determines the optical quality.[4],[5] It was observed that the quantum yield of as-synthesized nanocrystals with a Cd-rich surface is more than an order of magnitude higher than nanocrystals with a Se rich surface; furthermore, the Cd-rich samples were shown to be more photostable than Se-rich samples in a nitrogen environment.

Previous calculations suggest that the presence of unpassivated sites on the surface manifests as energy states within the band gap of the nanocrystals.[6] However, only a few studies have investigated and utilized the surface of the nanocrystals for radiative emission.[5, 7-9] Most of the efforts have focused on synthesizing nanocrystals with narrow linewidth[10], large transition dipoles, and high photostabilities. Due to a larger surface-based contribution to exciton decay in small nanocrystals, the few works that have sought to obtain surface state emission were limited to extremely small nanocrystals.[7-9, 11-15] In particular, the synthesis of ultrasmall nanocrystals was optimized to obtain white-light emission. Magic-sized ultrasmall CdSe nanocrystals were optimized to emit white light and their emission has been characterized.[9, 14, 15] Furthermore, the deep-trap emission of nanocrystals in dispersion was tuned by controlling the concentration of 3-mercaptopropionic acid.[7] In general, however, these works had limited control of the emission spectrum. Furthermore, many of the studies above were conducted with the colloidal quantum dots in a dispersion. It is difficult to predict how the deep-trap emission would change in a useful form, such as in a film or a matrix.

In this work, we explore the potential of plasmonic structures to enhance and control the deep-trap recombination to obtain tunable emission from the same quantum

dots. Plasmonic metals support hybrid electron-electromagnetic waves called surface plasmons.[16] Because surface plasmons are confined in sub-diffraction volumes, they exhibit very large electric-field densities and local density of states (the number of modes that can accept energy). Based on Fermi's golden rule, which states that the decay rate of a fluorophore is directly proportional to the local density of states in the surrounding media, this should lead to large enhancements in spontaneous emission rates (quantified by the Purcell factor).

Previous work has shown theoretically and experimentally that the photoluminescence from quantum dots can be strongly enhanced or quenched on plasmonic substrates.[17-20] The decay dynamics in single core-shell nanocrystals near rough metal surfaces revealed that the radiative rates were significantly enhanced despite a decrease in the overall quantum efficiency.[17] By extrapolation, one should be able to enhance emission from the deep-trap states in quantum dots.

Furthermore, structuring the metals should allow spectral control of deep trap emission. Plasmonic structures can be designed to enhance or suppress the density of states at the desired wavelengths.[16, 21, 22] For example, by changing the periodicity of holes in a hole array or rings in a bull's eye (series of concentric rings) on a silver film, the surface plasmon resonance can be tuned throughout the visible spectrum. Design of plasmonic structures in this manner further allows control over emission directionality.[23]

In this work, we show that significant deep trap emission can be obtained from CdSe nanocrystals of all sizes on rough silver films. We further show that precise structuring of hole arrays and bull's eye patterns on Ag films allows spectral control of emission from the same nanocrystals. By depositing blue-green CdSe quantum dots on tailored structures, we continuously tune the color of the emission from blue-green to red.

This type of plasmonic control of emission has many benefits. First, due to the large Purcell factors, plasmonic structures can be used to increase emission rates from the band-edge and the deep-trap states in core nanocrystals to match intensities observed from core/shell quantum dots on non-plasmonic substrates. Second, plasmonic structures can be made to resonate with either the band-edge or the deep trap states. We can enhance the band-edge preferentially over the deep trap, thereby "suppressing" the deep trap emission.

This is especially applicable to small CdSe nanocrystals because synthesizing narrow linewidth blue quantum dots has remained a challenge.[7, 15] By placing small dots in plasmonic structures, it is possible to get narrow linewidth blue light. On the other hand, we can modify our structures to have multiple surface-plasmon resonances to obtain the desired combination of deep-trap and band-edge wavelengths; this would allow us to uniquely tune the color and emission intensity.

The results we obtain also have implications for near-field broadband emitters in plasmonic circuits. Due to the large momentum mismatch between surface plasmons and photons, momentum has to be added to photons to generate surface plasmons. Various types of structures can be designed to convert the incoming photons into surface plasmons. Unfortunately, to generate broadband SPPs in a plasmonic circuit, far-field techniques involve a broadband source and some scattering sites to convert the photons into SPPs.[24] Near-field emitters provide an effective alternative for generating surface plasmons. However, these have been limited to narrow-linewidth emitters such as dyes or quantum dots.[25] Using our quantum dot-metal hybrid with tunable broadband emission allows one to generate the desired broadband spectrum of light in the visible and near infrared simply by exciting with far-field UV source.

Finally, we use electrolyte-gating of quantum dots on plasmonic structures to understand the origins of the deep-trap emission. Although much about CdSe nanocrystals has been uncovered, key questions remain after decades of research. What energy states are responsible for the deep trap emission? And how does this affect the radiative and non-radiative exciton decay? Calculations and experiments have implied the presence of hole traps in CdSe nanocrystals.[6, 26-28] However, it is not clear if these trap states are responsible for the deep-trap emission. Furthermore, the long-standing model of deep-trap emission resulting from a manifold of states in the mid-band gap was recently contested; it was claimed that the temperature-dependent behavior of the deep-trap spectrum is consistent with a single surface state.[29-31] For ZnO nanocrystals, a single defect state was shown to be responsible for the deep-trap emission by looking at the energy transfer between the exciton and an organic dye bound to the surface.[32]

Electrochemical experiments on quantum dots have allowed a deeper understanding of the emission dynamics. Previously, electrochemistry has been used to inject charges into the quantum dot and understand the kinetics of exciton decay.[26, 33-45] Injection of electrons into the conduction band of CdSe nanocrystals was shown to reduce the quantum dots and switch their emission off.[37, 38, 46] The effect was also reversible. In contrast, it was found that CdSe nanocrystals are unstable under hole-injection conditions, because the dissolution of CdSe became favorable at such potentials.[45] Furthermore, the energy levels of Cu dopants in quantum dots were probed by observing the emission from the band-edge and dopant states under electrochemical control.[39] It was found that applying a negative potential activates the hole traps by reducing Cu^{2+} to Cu^{+}, leading to increased Cu-related emission relative to the band-edge emission.

Here, we gate the semiconducting quantum dots on plasmonic surfaces by using a gel-electrolyte and electrochemically move the Fermi level to understand if surface recombination can be controlled or manipulated. Fundamentally, such a study on our quantum dot-plasmonic system will enable us to determine where the surface states lie with respect to the Fermi level and the band-edge.[13] On a more practical side, if the deep-trap and band-edge emissions can be controlled with electrochemistry, we can tune the emission in real time. Such a demonstration for dot-in-bulk nanocrystals was reported recently where the ratio of core and bulk emissions were electrochemically modulated to tune photoluminescence color.[47]

5.2 Results and Discussion

The absorption and photoluminescence curves of five different core-only CdSe nanocrystals in dispersion are shown in Figure 5.1. The absorption curves show well-defined features for all of the nanocrystals, confirming high quality and near monodispersity. The photoluminescence in dispersion shows a sharp band-edge dominated emission characteristic of these nanocrystals. Only the blue nanocrystals show a noticeable deep-trap emission. Typical quantum yields of these quantum dots in a hexane or toluene dispersion ranged from 3% to 10%.

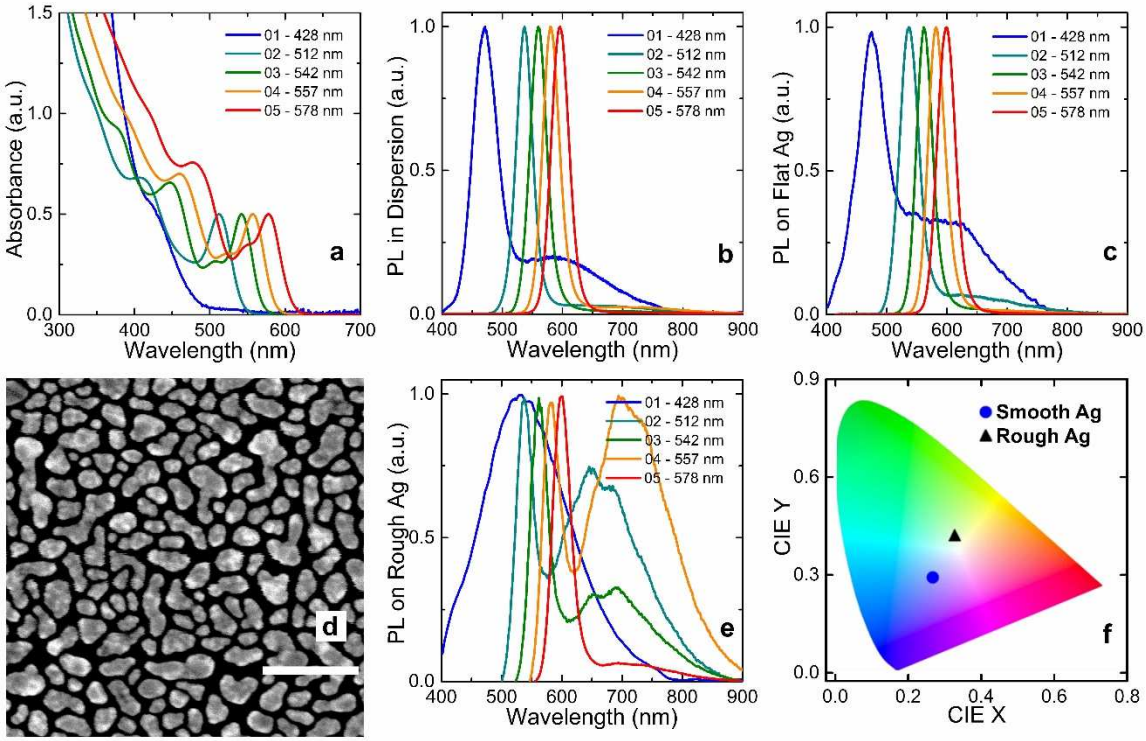

Figure 5.1 Deep-trap-emission enhancement from CdSe nanocrystals on rough silver islands. (a) Absorption spectra of CdSe nanocrystals of five different sizes dispersed in either hexane or toluene. The wavelengths in the legend correspond to the lowest energy absorption peaks of the different nanocrystals. (b) Photoluminescence spectra of the CdSe nanocrystals in the dispersion. (c) Photoluminescence spectra of the nanocrystals deposited onto a flat 200 nm silver film, with typical roughness of 1 nm or lower. (d) Scanning electron micrograph of a silver film evaporated onto a flat (100) Si wafer with a nominal thickness of 10 nm. The silver forms discontinuous islands. The scale bar is 200 nm. (e) Fluorescence spectra on rough silver films shows strong emission from the deep trap in nanocrystals of all sizes. (f) The 1931 CIE color coordinates of the blue nanocrystals with a 428 nm band edge on a smooth silver and a rough silver film. On the rough silver film, the nanocrystals emit white light.

The emission from a single layer from these nanocrystals spin-coated from an octane dispersion at an optical density of 2.0 at the band-edge on plasmonic films is shown in Figure 5.1c and 5.1e. On a smooth silver film with a roughness below 1 nm, a sub-monolayer was deposited and very little or no deep trap emission is observed, similar to that observed in a dispersion. When deposited on a rough, discontinuous silver film (with typical island sizes of the order 100 nm, see Figure 5.2), the emission spectrum in all nanocrystals showed significant deep-trap emission in addition to the band-edge. Rough silver films support strongly localized surface plasmons over a broad spectral range. As a

result, a large fraction of the electron-hole pair decay includes the generation of surface plasmons, which eventually scatter into far-field photons.[25]

Depending on the nanocrystal, this deep trap emission is as intense as the band-edge; in the case of blue cores, it's even higher. In fact, in blue nanocrystals, the emission from these nanocrystals on the rough silver falls in the white light coordinates in a 1931 CIE color plot. It is unusual to see such strong deep-trap emission from quantum dots of all sizes. In the past, such emission was observed primarily in small quantum dots due to the high fraction of surface atoms and the difficulty of passivating all of them.

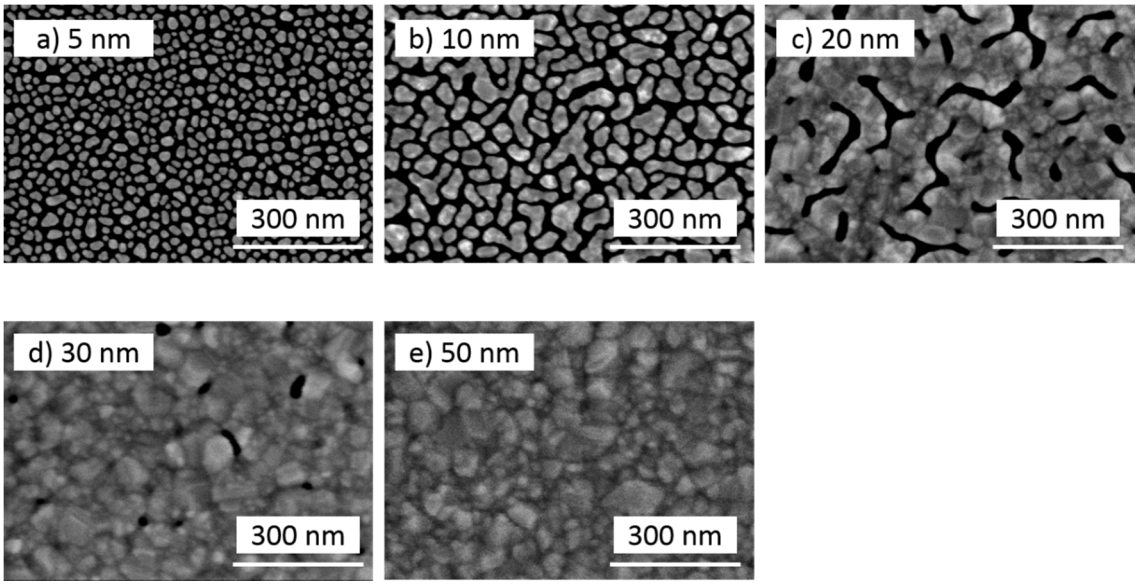

Figure 5.2 Scanning electron microscope images of silver films of different thicknesses when thermally evaporated onto a (100) Si wafer at 0.2 Å/s and pressures below 4 x 10^{-6} Torr. The nominal thickness of evaporation is indicated, and at very small thicknesses, silver prefers to "ball up" and form islands instead of a continuous film. This leads to localized surface-plasmon resonances in the thin films.

The deep-trap emission from the quantum dots is strongly concentration dependent. The electric fields of a surface plasmon are strongest near the metal surface, and for a SPP at a silver-air interface typically extend about 200 nm above the silver for visible wavelengths. For a localized surface plasmon near silver spheres or islands, the field is even more strongly confined and extends only up to a few tens of nanometers. As a result, the deep-trap contribution should progressively decrease with increasing thickness of the

quantum dot layer. To test this, we used a concentration gradient of quantum dots on rough, inverted pyramids arrays to tune the emission from the quantum dots (Figure 5.3).

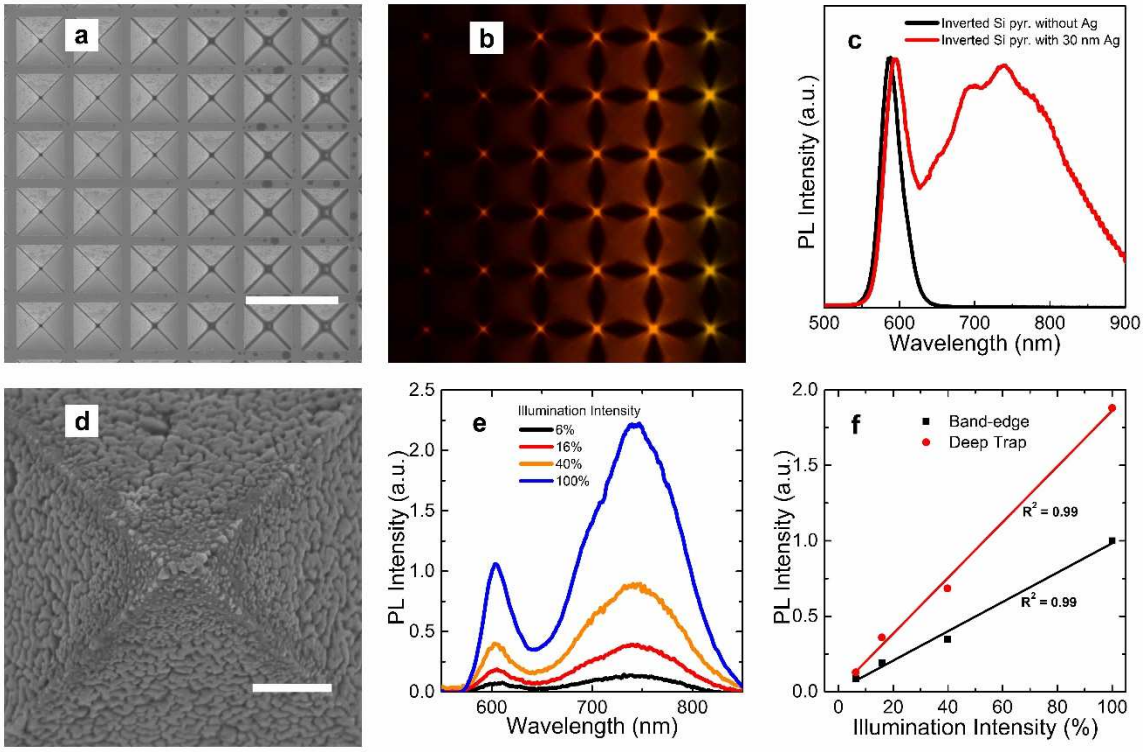

Figure 5.3 Strong deep-trap emission and color gradients are observed at localized-surface-plasmon hotspots. (a) Scanning electron micrograph of a concentration gradient of 2.5 CdSe nanocrystals obtained by drop-casting a microliter droplet into an array of large and rough Ag inverted pyramids. (b) Due to the concentration gradient in 2.5 nm nanocrystals and limited spatial extent of the localized-surface-plasmon fields, the relative intensity of the deep-trap to the band-edge emission and therefore, the color changes. (c) As a control, 4 nm nanocrystals deposited into Si inverted pyramids show no deep-trap emission, and those deposited into Si inverted pyramids with a thin layer of rough Ag show pronounced deep trap emission. (d) Scanning electron micrograph of 4 nm nanocrystals deposited at rough Ag pyramid tips. (e) At the rough tips, the 4 nm nanocrystals show even stronger and narrower deep-trap emission. The sample is illuminated using the 436 nm line of a 100W high pressure mercury arc lamp from Nikon. The maximum intensity is 2.5 W/cm^2. (f) Furthermore, the band-edge and deep-trap emissions scale linearly with power over at least two orders of magnitude.

Large arrays of silicon pyramid trench pits with bases larger than 10 micrometers and separations larger than 5 micrometers were fabricated using standard photolithography and KOH anisotropic etching on a (100) Si wafer. Because the KOH attacks the (100) facet at a much higher rate than the (111) facet, inverted pyramids were etched with a 70.54° at the tip. When a nominally 30 nm Ag film was evaporated, the silver layer was continuous

on the (100) facet, but discontinuous and rough on the high angle (111) facet (see Figure 5.4). We drop-cast microliter droplets of dilute (less than 0.1 optical density in dispersion at the band-edge absorption) core nanocrystals, and obtained a concentration gradient within the array of pyramidal trench pits (Figure 5.3). When deposited into silicon inverted pyramids with native oxide, the quantum dots showed only band-edge emission. On top of rough silver in the inverted Si pyramids, the deep-trap emission was significant. The resulting concentration gradient leads to different colors of emission in the pyramid array (Figure 5.3).

When we evaporated an additional 200 nm of silver into the pyramids after drop-casting the quantum dots, we formed a three layer *rough silver-quantum dot-thick silver* sandwich. After template-stripping this structure from the silicon template, we observed strongly enhanced deep trap emission from even the red quantum dots.[48] In some cases, the deep trap emission intensity was more than twice that of the band-edge intensity.

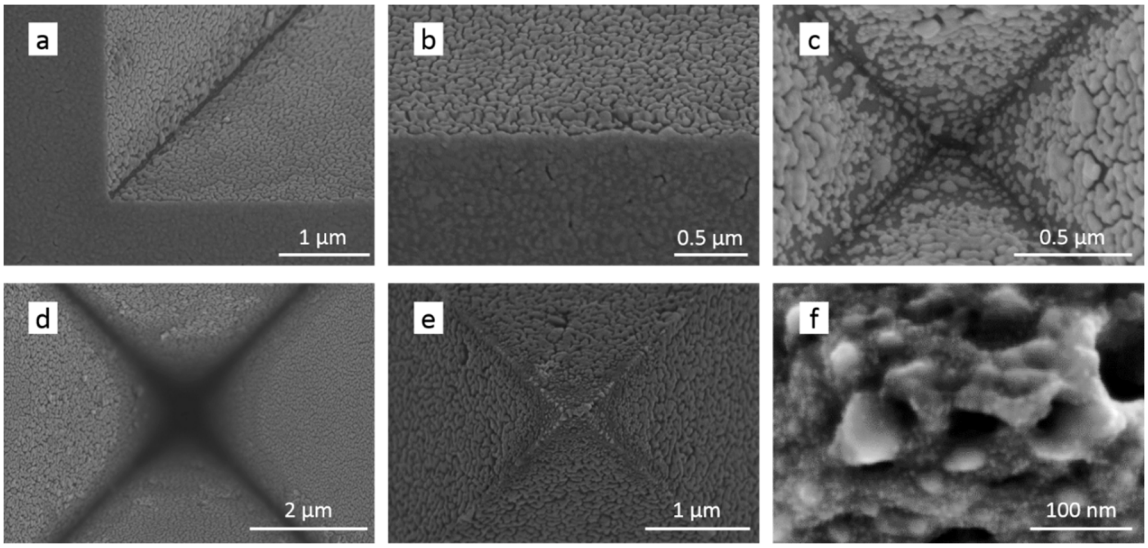

Figure 5.4 Scanning electron micrographs of quantum dots at rough silver pyramid tips. (a) The corner of a 15 micrometer Si pyramid trench with 30 nm of silver. As evident in (a) and (b), the silver is flat and continuous outside the pyramid and rough and discontinuous inside due to the high angle of deposition on the (111) plane. (c) SEM image shows the silver is not continuous at the bottom of the pyramid. (d) SEM image showing quantum dots drop-cast into the pyramid. An optically thick layer of 200 nm Ag was evaporated and then the sample was template stripped. (e) SEM shows the pyramid tip. (f) Zoomed SEM of (e), showing clearly resolved quantum dots at the tip.

Even though the effect of the silver on the quantum-dot emission is obvious, we haven't yet ruled out silver/silver oxide fluorescence, or doping or chemical modification on the quantum dot surface as the cause. It has previously been reported that silver nanoclusters can fluoresce.[49-54] In the sub-nanometer regime, metal/metal oxide nanoclusters can behave like a semiconductor. We can eliminate this possibility here because we did not detect any emission from the rough silver films without quantum dots. Furthermore, our emission spectra show strong spectral dependence on the size of the quantum dot.

We also believe that doping (for example, with Ag) or another chemical modification of the nanocrystals is not the reason for deep-trap-like emission. As we will show below, in many cases, we saw deep-trap emission even when a thin spacer layer, typically 5 – 10 nm of alumina deposited by atomic layer deposition, was coated on the silver before spin-coating the quantum dots.

While we are able to obtain strong deep-trap emission, it is unclear if we can tune the emission spectrum of the quantum dots. Due to photobleaching in air, the emission from the band edge and the deep trap is time-dependent. To be able to tune the emission color, we first need to address the issue of photostability of the quantum dots. Then, we can tailor plasmonic structures to exhibit resonances at the desired wavelengths to control the spectrum.

The photostability of the quantum dots is a strong function of their environment.[5, 55-57] It has previously been shown that they are more photostable in an inert atmostphere. Furthermore, photobrightening and photodarkening have been linked to the presence of oxygen and water. By sealing our samples in a dry nitrogen atmosphere inside a glovebox using a two-part chemical epoxy and microscope cover slide with thickness number 1.5, we observed that the trap emission from the nanocrystals was more stable, and the quantum dots did not photodarken even after three hours of constant illumination at intensities of 0.6 W/cm^2 from the 436 nm line of a Hg arc lamp (Figure 5.5). The effect of nitrogen was strongest in the smallest dots, which have the highest surface to volume ratio. Furthermore, the deep-trap emission was also enhanced in nitrogen, consistent with the claims that deep-trap emission result from surface states and that oxygen and water passivate surface sites.

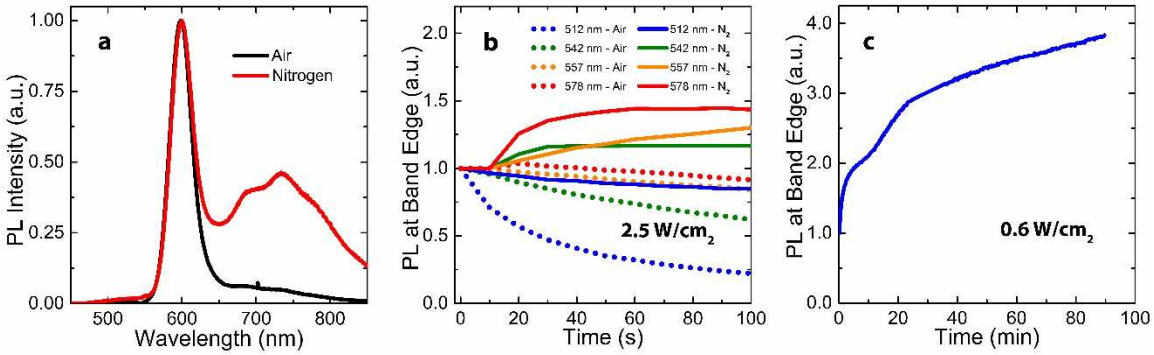

Figure 5.5. Enhanced deep-trap emission and photostability in nitrogen. (a) Emission spectra of CdSe nanocrystals on 10 nm rough silver sealed in air and in nitrogen. Both the samples were prepared under identical conditions. The deep-trap emission is enhanced relative to the band edge when the sample is sealed in nitrogen. (b) Time trace of the band-edge intensity at a constant illumination intensity of 2.5 W/cm^2 for four different CdSe nanocrystals on 10-nm-thick rough silver films in air and in nitrogen. All the nanocrystals photodarken over time in air. In nitrogen, the three largest nanocrystals photobrighten, and while the smallest nanocrystal bleaches a little, it is significantly more stable than in air. (c) Photobrightening of the 512 nm band-edge nanocrystals on the 10 nm rough silver film in nitrogen at a lower intensity of 0.6 W/cm^2. Even after an hour and half, the nanocrystals do not photodarken.

To tune the emission from these nanocrystals, we deposited them on silver nanohole arrays and silver bull's eyes with the desired periodicities. We first grew 200 nm thick films of silver epitaxially on top of mica to obtain ultra-flat single-crystalline silver.[58] Typical roughness on these films was lower than 0.5 nm over a 2.5 µm x 2.5 µm area (see Materials and Methods). Subsequently, we used focused ion beam at an acceleration voltage of 30 kV and an ion beam current of 40 pA to mill hole arrays. The hole diameter for all hole arrays was half the periodicity. By changing the periodicity of the hole array, we can tune the surface plasmon resonance.[16] In 1998, plasmonic structures were first shown to exhibit extraordinary optical transmission through sub-diffraction structures due to surface-plasmon resonances. More light is transmitted at the surface-plasmon resonance because surface plasmons funnel the electromagnetic energy from one side of the metal to the other through sub-diffraction volumes. This is evident in the transmission spectra of our silver nanohole arrays (Figure 5.6).

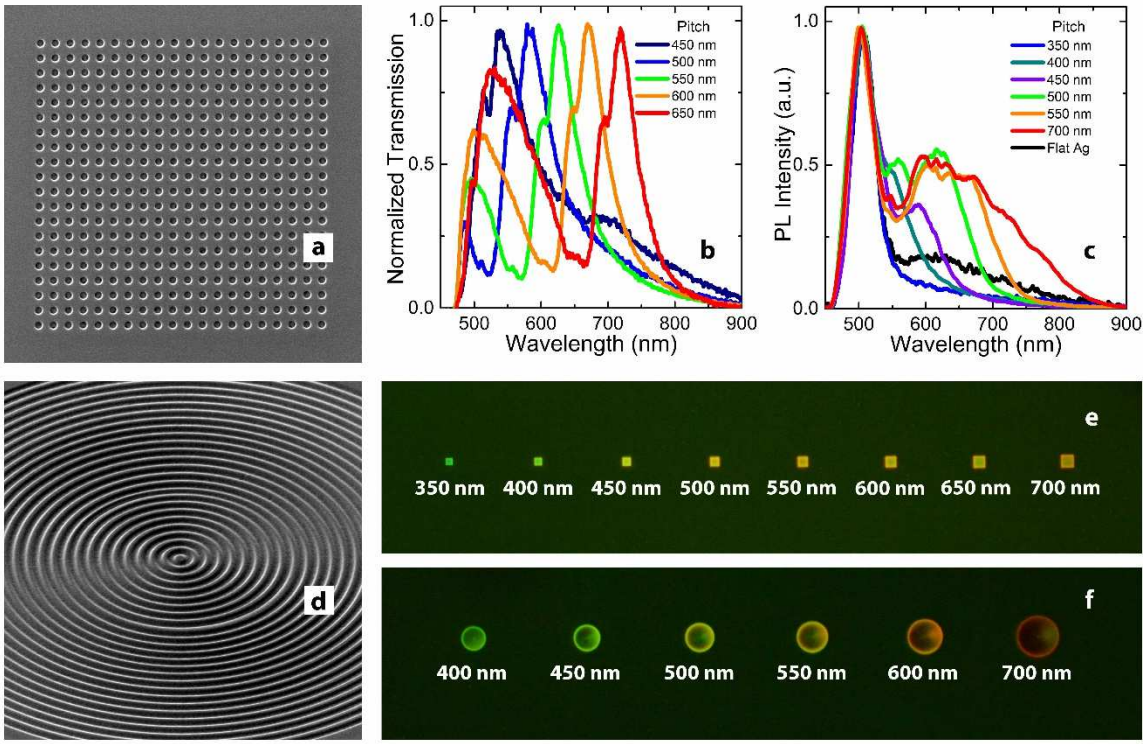

Figure 5.6 Color-tunable emission from CdSe nanocrystals on tailored plasmonic structures. (a) Hole arrays of different pitches are milled into an ultra-smooth single-crystalline silver film using focused ion beam. The hole array in the scanning electron micrograph has a pitch of 600 nm. The hole diameter is set to one-half of the pitch. (b) Transmission spectra of hole arrays of different pitches collected using a tungsten-halogen lamp. Different pitches of hole arrays support different surface plasmon polariton wavelength; these manifest as maxima in the transmission. (c) After depositing 10 nm of alumina by atomic layer deposition and spin-coating 2 nm CdSe nanocrystals at an optical density of 2 at the band-edge absorption, the photoluminescence of the nanocrystals at different periodicities were collected. A continuous change in deep-trap emission relative to the band-edge emission is observed with changing pitch, and is consistent with the transmission spectra in (b). (d) A scanning electron micrograph of 400 nm pitch bull's eye structure on silver milled using a focused ion beam. Due to the rotational symmetry, the surface-plasmon-polariton resonances are stronger and narrower in linewidth. (e) Fluorescence images recorded from the 2 nm nanocrystals in the hole arrays, confirming the changing color with the changing periodicity. The green on the flat areas is indicative of fluorescence on unstructured silver. The pitch is indicated above each structure. (f) Fluorescence image of the nanocrystals in the bull's eye structure, showing a purer emission color. Note the color of the same nanocrystals can be changed continuously from green to red at the spatial position of choice.

At the surface-plasmon resonances, the local density of states is enhanced. So quantum dots near these hole arrays should exhibit large spectrally dependent Purcell factors. The surface-plasmon-polariton field is strongest inside the hole and not near the edges. Therefore, self-assembled monolayers of core quantum dots exhibited noticeable

but little deep-trap enhancement. Instead, we chose to spin-coat our quantum dots dispersed in octane at optical densities of 2 at the band edge. On the flat areas, this results in a sub-monolayer. In the hole arrays, the quantum dots partially fill up the hole arrays. As a result, the quantum dots are located at the optimal position for the strongest exciton-surface plasmon interactions.

Additionally, we found that the enhancement is strongest when we have a small spacer layer to separate the quantum dots from the silver hole arrays. Therefore, we deposited 10 nm alumina using atomic layer deposition at 100°C. This allowed us to rule out any chemical modifications or silver doping of the CdSe nanocrystals for the enhanced deep-trap emission. Figure 5.6 shows that the emission from the 2.5 nm nanocrystals can be tuned continuously throughout the visible. The deep-trap contribution increases with increasing periodicity. In fact, for the smallest hole array, the deep trap is suppressed relative to the band edge, resulting in emission with narrower linewidth. This implies that plasmonic structures can be designed to control emission from ultrasmall nanocrystals for generating nearly monochromatic blue light. Presently, when ultrasmall blue nanocrystals are synthesized, there is significant unwanted contribution from the deep trap.[9, 11, 15]

The color-tuning in Figure 5.6 is not a mere suppression of the band-edge. Note that the spectrum is continuously changing with the hole array periodicity. If the band edge was suppressed, the deep-trap part of the spectrum would not change in shape. It is very difficult to estimate the absolute Purcell enhancements. However, to qualitatively show the effect of hole arrays, we divide the emission from the hole arrays by the emission outside the hole arrays and normalize to their respective areas (Figure 5.7). This is strictly valid only if there is only one layer of quantum dots in hole arrays, but nonetheless gives the wavelength dependence and trends in Purcell enhancement. As expected, the estimated Purcell enhancement red-shifts with increasing periodicity, and is in agreement with the statement that this is not merely a suppression of the band-edge emission.

Note that while plasmonic hole arrays are a well-studied system and are relatively easy to understand, they can support surface plasmon resonances at multiple different wavelengths. To obtain a single desired resonance, we moved to bull's eye structures made of 25 concentric rings separated by a defined periodicity. Because of the rotational

symmetry in this structure, the SPP resonance is sharper and stronger.[59] When we deposit our nanocrystals on these bull's eyes, the color indeed appears purer (Figure 5.6f). However, the spin-coating of the nanocrystals onto the bull's eyes was non-uniform, as shown in Figure 5.8, resulting in one side looking more colored in each of the bull's eyes in Figure 5.6f.

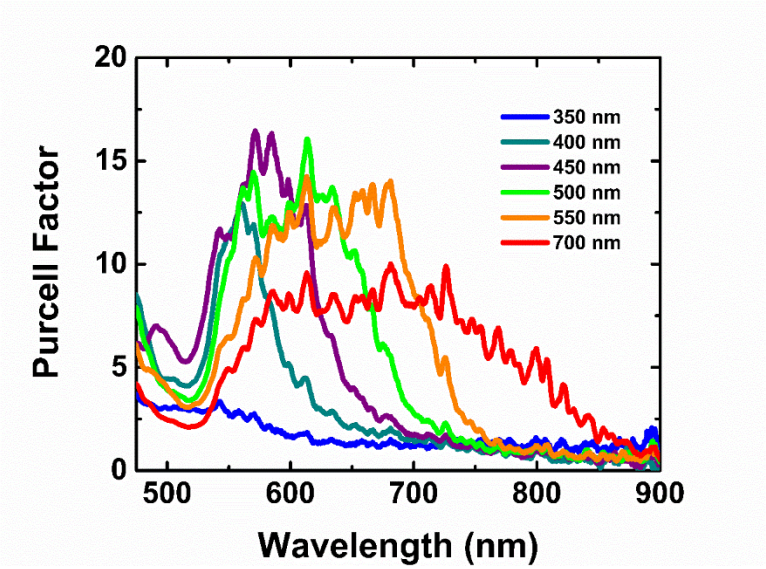

Figure 5.7 The Purcell factor calculated by normalizing the emission in the hole array to the emission on a flat unstructured silver of the same area. However, the enhancement is qualitative at best because quantum dots are not deposited as a monolayer, but are spin-coated, which results in multilayer filling in the holes. The actual Purcell factors are smaller, but the shape of the above plot is correct.

Both of the above proof-of-concept results also have implications for a new semiconductor-metal hybrid system in which the metal underneath the semiconductor can be structured to obtain the desired color of choice at the spatial position of choice. This is complimentary to the expensive and precise positioning techniques for quantum dots. Furthermore, because all the colors are coming from the same quantum dots and there are no absorption features exist between the band edge and the deep trap, no reabsorption losses occur in this system as in the multilayered multi-quantum-dot systems.[60-63]

Presently, the deep-trap emission is understood to arise from the presence of optically active hole-trapping states in the quantum dots, presumably unpassivated surface Se sites. To further understand the role of surface states, we used a gel-electrolyte to gate

the quantum dots on the plasmonic structures and observe if the deep-trap emission could be modulated. We start by assuming the energy schematic shown in Figure 5.9. Specifically, we assume that the Fermi level lies above some surface state in the quantum dot and that a state other than the band edge is feeding the deep-trap state.

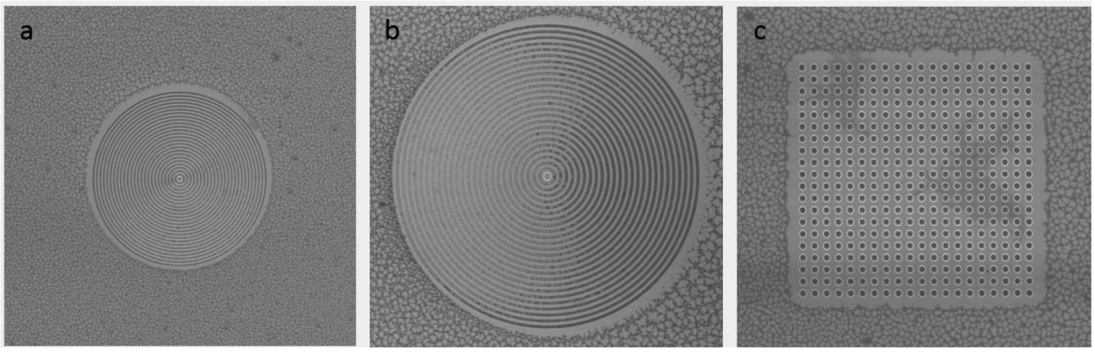

Figure 5.8 Scanning electron micrographs of quantum dots on plasmonic structures. (a) Quantum dots spin-coated into 400 nm bull's eye show a nearly uniform distribution. (b) In the 700 nm bull's eye, the deposition is more concentrated on one side, resulting in the non-uniform fluorescence seen in Figure 5.6. (c) The quantum dots in the vicinity of the 700 nm hole array are funneled into the holes. In the fluorescence images in Figure 5.6, more emission is seen at the end of the bull's eyes. In the SEM images here, particularly in (b), there is no accumulation of quantum dots at the last ring. This is in line with the idea that the quantum dots first excite surface plasmons in the bull's eye patterns, which then scatter strongly at the last ring (where the periodicity, and therefore, the Bloch condition is broken).

A schematic of our electrochemistry set up is shown in Figure 5.9a. CdSe nanocrystals are deposited by using a self-assembled monolayer technique on silver. A thin Pt wire was used as a reference electrode. Because a majority of the nanocrystals are not inside the hole, the deep-trap emission is not as strong as when they were spin-coated. Regardless, we had sufficient trap-state emission to observe noticeable changes under an applied potential.

When a positive potential is applied, the Fermi level is lowered and the deep trap emission decreases (Figures 5.9d and 5.9e). The band-edge emission either remains constant or increases a little. This is the first direct observation that the deep-trap emission results from hole-trap states within the band-gap of the nanocrystals. At even larger potentials, the deep-trap emission decreases further. It is difficult to determine if this is consistent with the recent prediction that the surface-state emission is coming from a single

state.[30] At different oxidizing potentials, the deep-trap emission decreases as a whole, but the deep-trap emission at different wavelengths changes by a different relative amount.

Meanwhile, a negative potential increases the Fermi level, and the deep trap remains constant while the band edge decreases. At large enough negative potentials, an electron is injected into the conduction band of the nanocrystal, and the band-edge emission decreases. The band-edge emission decreases presumably because Auger recombination is dominant once a quantum dot is charged. Counter to expectation, the deep-trap emission does not decrease until large negative potentials. If the deep hole trap was recombining with an electron in the conduction band edge of the excited quantum dot, at negative potentials, the deep-trap emission would decrease in a fashion similar to the band-edge emission. Initially, this might seem puzzling. To clarify this, we put the quantum dots in a poly-lauryl methacrylate matrix, and conducted photoluminescence excitation (PLE) measurement at 10K. PLE curves tell us what energy levels are contributing to the emission at the monitored wavelength.[64] From the PLE data, it appears that the band-edge state is not feeding the deep trap state, consistent with the electrochemistry result. It seems another electronic state is responsible for deep-trap emission, as illustrated in Figure 5.9b.

The fact that different electronic states are responsible for the band-edge emission and the deep-trap emission is an important result for color modulation from the quantum dots. The two emissions can be independently modulated to give an additional level of control over the color of the quantum dot similar to the recent dot-in-bulk work.[47] While this set up is not as robust and photostable as the dot-in-bulk structure, two key advantages in our system are that the ratio of the band-edge and deep-trap emissions is not power dependent (Figure 5.3f), and both the emissions can be tuned spatially and electrochemically.

Conclusion

In this work, we have shown that deep-trap emission from CdSe nanocrystals of all sizes can be enhanced and tuned by designing plasmonic structures with the appropriate photonic density of states. The electrochemistry result shows that the deep-trap emission likely arises from deep hole-trap states, and that the emission from the band-edge and the

deep trap can be tuned independently. This control allows us to generate the color of choice at the position of choice from the same nanocrystals by patterning the metal underneath and to further electrochemically modulate this color in real time. Finally, both the plasmonic structure and electrochemistry can be used to generate narrow linewidth colors from nanocrystals with significant deep-trap contribution.

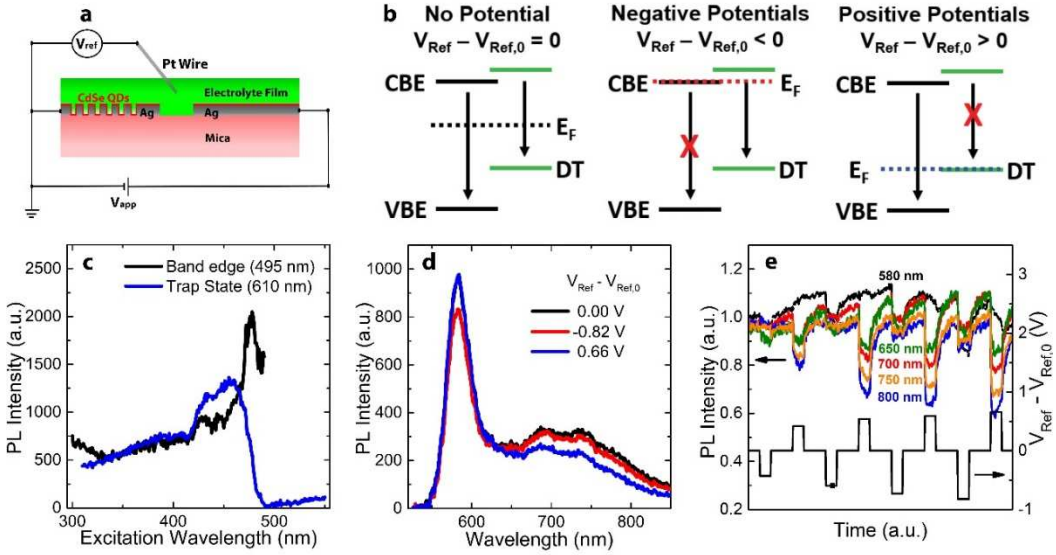

Figure 5.9 Electrochemical control of emission in CdSe nanocrystals. (a) Schematic of the electrochemical cell. The silver working electrode is patterned with hole arrays. A self-assembled monolayer of CdSe nanocrystals is formed on the silver using 1,10-decanedithiol. The overall area of the Ag counter-electrode is twice as large as that of the working electrode. A Pt wire is used as a reference, and a polyelectrolyte film was used as the capacitor. At 0V applied potential, the reference voltage was -0.33V, denoted as $V_{Ref,0}$. (b) A potential energy-level diagram consistent with the electrochemical measurements and photoluminescence excitation measurements is shown. Briefly, an electronic state other than the conduction band-edge (CBE) is responsible for recombination with the deep hole trap (DT). Without any applied potential, both the band-edge recombination and the deep trap are emissive. When a large enough negative potential is applied, electrons are injected into the CBE and only deep-trap emission is observed. At positive potentials, holes are injected into the DT state, and only the band-edge emission is observed. (c) To confirm this, photoluminescence excitation (PLE) studies were conducted on 2.5 nm CdSe cast in a poly-lauryl methacrylate matrix at 10K. Clearly, the 480 nm state feeds the band-edge emission at 495 nm, but not the deep-trap emission at 610 nm. (d) In the electrochemical experiments, a positive potential leads to a reduced deep-trap emission while the band-edge emission remains constant. A negative potential, when large enough, lowers the band-edge emission but not the deep trap emission, except at extremely negative values. (e) Time traces are provided for the nanocrystals emission at 580 nm (black), 650 nm (green), 700 nm (red), 750 nm (yellow-orange), and 800 nm (blue) along with the potential (black). The nanocrystals are stable and the band-edge and deep-trap emissions return to the original intensity (within error) when the potential is set to 0V. The results are consistent with the deep trap emission resulting from hole traps.

5.3 Materials and Methods

CdSe Nanocrystal Synthesis

Chemicals

Cadmium oxide (CdO, 99.999%, 48-0800) was purchased from Strem Chemicals. n-dodecylphosphonic acid (DDPA, 98%, 08118) was purchased from Epsilon Chimie. 1-butanol (ACS Grade, 101990) was purchased from Merck KGaA. Acetontrile (99.5%, 360457), cadmium acetate dihydrate [$Cd(OAc)_2 \cdot 2H_2O$] (98%, 289159)], chloroform (99.8%, 132950), ethanol (96%, 02850), hexadecylamine (HDA, 90%, H7408), hexane (95%, 208752), 1-hexanethiol (95%, 234192), methanol (99.9%, 34860), octylamine (99%, O5802), selenium shot (99.999%, 204307), trioctylphosphine (TOP, 90%, 117854), trioctylphosphine oxide (TOPO, 90%, 346187), and anhydrous toluene (99.8%, 244511) were purchased from Sigma and used as received.

Blue Quantum Dots

Blue emitting CdSe QDs were synthesized following Dolai *et. al.*[65] Briefly, 1.0 g of $Cd(OAc)_2 \cdot 2H_2O$ and 25 mL of octylamine were combined in a 250 mL 4-neck round-bottom flask. The mixture was stirred at 1000 rpm under positive nitrogen pressure with a needle outlet valve for thirty minutes. After thirty minutes, the needle outlet valve was removed. The mixture was then diluted with 30 mL of anhydrous toluene.

In air, 0.3 g of selenium powder was freshly made by grinding selenium pellets with a mortar and pestle. In a 20 mL glass vial, selenium powder was combined with 1.075 mL of 1-hexanethiol and 4.0 mL of octylamine. The vial was capped with a septum, the mixture was stirred at 600 rpm and nitrogen was bubbled for ten minutes with a metal cannula and outlet needle. After degassing, the mixture was taken up in a syringe and rapidly injected into the 250 mL flask with cadmium precursor.

The reaction mixture was stirred at 1000 rpm for 4 hours after selenium precursor addition. The absorption peak was monitored throughout the reaction. After 4 hours, 20 mL of chloroform was added, followed by dropwise addition of a 1:1 acetonitrile:methanol mixture until turbidity to crash out the nanocrystals. The mixture was divided evenly into three 50-mL centrifuge tubes and centrifuged at 7000 rpm for 5 minutes. The supernatant

was discarded. The bright precipitate was redispersed in a total of 25 mL of chloroform, precipitated with 1:1 acetonitrile:methanol mixture until turbidity, and centrifuged at 7000 rpm for 5 minutes to crash out the nanocrystals once more. The supernatant was discarded. The bright precipitate was redispersed in a total of 20 mL of chloroform and centrifuged at 7000 rpm for 5 minutes to crash out unreacted material. The supernatant was saved and stored in chloroform in the dark until needed. The absorption spectrum of the nanocrystals is sharp and well-defined, exhibiting the lowest exciton energy at 419 nm right after synthesis. Over the course of a month, the absorption spectrum redshifts and broadens, indicating presumably slow growth. Despite the evolving spectra, the dispersion remains a bright, fluorescent blue.

Other Quantum Dots

CdSe QDs were synthesized *via* a modified version of the procedure by Reiss *et al.*[66] Briefly, 822 mg of CdO, 16.2 g TOPO, 37 g of HAD, and 3.125 g of DDPA were combined in a 250 mL 4-neck round-bottom flask and heated to 90°C under nitrogen. At 90°C, the mixture was degassed three times to below 0.1 Torr while stirred at 1000 RPM. The flask was returned to nitrogen and heated to 320°C. The reaction mixture was held at 320°C for fifteen minutes after the solution turned clear and colorless. The temperature was then reduced to 280°C, the stir rate reduced to 300 rpm, and 40 mL of 0.2 M Se in TOP was rapidly injected. The stir rate was increased back to 1000 rpm and the temperature was maintained at 270°C. The size was monitored with a UV-vis absorbance spectrum. Once the desired size was reached, the growth was quenched by removing the heating mantle, immersing the reaction flask in a water bath at 200°C, and injecting 40 mL of 1-butanol at 130°C to prevent solidification.

To purify the quantum dots, the reaction mixture was then split into six 50 mL falcon tubes. Methanol was added to each tube to reach a total volume of 50 mL and centrifuged at 4000 rpm for ten minutes. The supernatant was discarded. In each centrifuge tube, the QDs were redispersed in 20 mL of hexane (120 mL total), and left undisturbed overnight in the dark to precipitate unreacted material. The tubes were centrifuged at 4000 rpm for 20 minutes. The precipitate was discarded. The supernatant was transferred to six, clean 50 mL centrifuge tubes and precipitated with ethanol until the

dispersion turned turbid. The tubes were centrifuged at 4000 rpm for 10 minutes. The supernatant was discarded. In each centrifuge tube, the QDs were redispersed in 4 mL of hexane (24 mL total), precipitated with ethanol until turbid, and centrifuged at 4000 rpm for 10 minutes. The supernatant was discarded. The QDs were redispersed in a concentrated hexane solution (typically 20 mL) and stored in the dark until needed.

Low Temperature Photoluminescence Excitation Measurements

CdSe nanocrystals were dispersed in a polylaurylmethacrylate polymer by following a previously reported protocol.[67] Briefly, 5 mg of azobisisobutyronitrile initiator was added to 100 microliters of ethyleneglycol dimethacrylate cross-linker and 400 microliters of laurylmethacrylate monomer in a nitrogen glovebox. This mixture was used to disperse a small amount of quantum dots. 20 microliters from this solution was drop cast onto a 1 cm sapphire disc and cured for 2 hours at 75˚C. The sample was loaded into a Janis ST-300 cryostat and cooled to 10K.

Photoluminescence measurements were performed by first measuring the photoluminescence curve at 350 nm excitation. Subsequently, photoluminescence excitation data were collected with the emission at the band-edge peak of 495 nm and scanning the excitation wavelength from 300 nm to the band-edge peak. For the deep trap, the emission wavelength was fixed at 610 nm and the excitation source was scanned from 300 nm to 550 nm.

Fabrication of Silicon Pyramids

Chemicals

Potassium hydroxide solution (KOH, 30%) was purchased from Technic France. Hyrdrofluoric acid (HF, 49%) was purchased from Fluka. All chemicals were used as received without further purification, unless noted below.

Substrates

Four-inch, single-side-polished, single-crystalline Si(100) wafers with <0.4 nm root-mean-square (RMS) roughness were purchased from Silicon Valley Microelectronics, Inc.

Fabrication of pyramid templates

Si wafers were patterned prior to metal deposition; these would act as templates for the plasmonic structures. Polished Si (100) wafers were first covered with 100 nm of SiN_x via plasma-enhanced chemical vapor deposition (Oxford Instruments PECVD 80+). Subsequently, a soft mask was formed by spin-coating AZ1505 photo resist at 4000 rpm, and then exposed to 12 mW/cm^2 of a 405 nm source for 4 seconds using a mask aligner (MA6, Karl Suess) and developed for 1 minute using the AZ726 MiF developer. Arrays of circles were first patterned into the photoresist during the photolithography step and then transferred into the SiN_x mask using reactive ion etching (Oxford Plasma, Plasmalab RIE80). Before etching the Si wafer, the photoresist was removed via sonication in acetone. Anisotropic etching in a 60°C KOH bath (341 g KOH, 159 g DI) for 60 minutes under vigorous stirring produced pyramidal-trench pits defined by the (111) planes of the Si wafer. After a 10 minute rinse in DI water, the SiN_x mask was removed by soaking in 1:10 HF(49%):H_2O for 1 minute, resulting in the final Si templates.

Thermal Evaporation of Silver Films

Flat (100) Si wafers were cleaned by sonication in acetone, isopropanol, methanol, and water for 10 minutes. Structured Si wafers were cleaned in a 3:1 H_2O:H_2NO_3, thoroughly rinsed in deionized water, then submerged in a 1:1 H_2SO_4:H_2O_2, and rinsed again in deionized water. Silver films were evaporated using 99.99% Ag pellets (Kurt J. Lesker) at room temperature and a chamber pressure below 4 x 10^{-6} Torr in a Kurt J. Lesker Nano 36 thermal evaporator. The resulting films for various deposition thicknesses are shown in Figure 5.2.

Spectrally Dependent Lifetime Measurements

Lifetime measurements were collected using a picosecond pulsed laser (LDH-D-C 405, Picoquant) as the excitation source and a Micro Photon Devices single-photon avalanche photodiode detector connected to a Picoharp timing module (both purchased from Picoquant). Lifetimes, shown in Figure 5.10 were measured for CdSe nanocrystals with a 578 nm band-edge absorption on a rough silver film. A 600 nm +/- 20 nm bandpass filter was used for the band edge, and a 665 nm longpass filter was used for the deep trap.

As expected from the literature, the lifetime at the deep trap is much longer than the band edge because the oscillator strength of the deep trap recombination is weaker than the band edge.

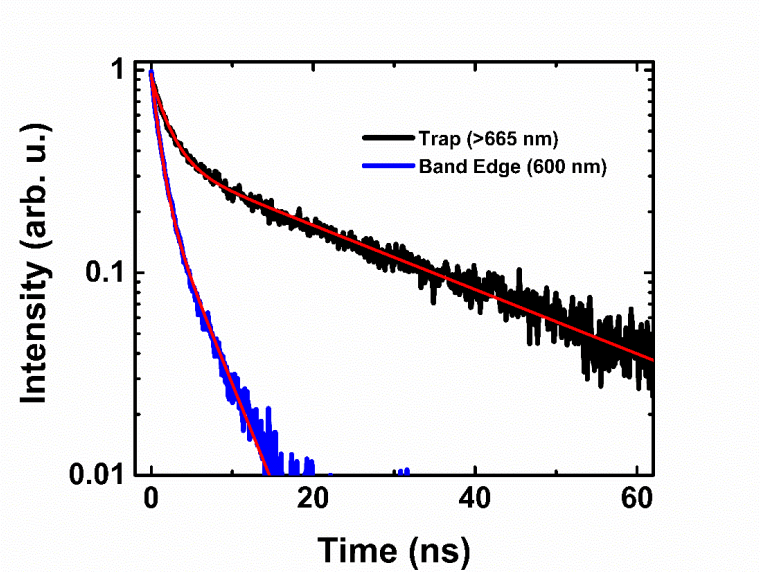

Figure 5.10 Lifetimes of CdSe nanocrystals with absorption maximum at 578 nm spin coated onto a nominally 10 nm thick rough silver film without an alumina layer. The red lines are biexponential fits to the data.

Preparation and Characterization of Single Crystalline Silver Films

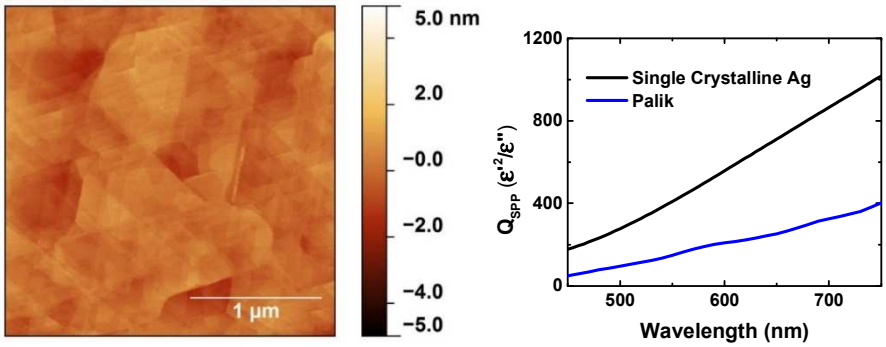

Figure 5.11 Characterization of single-crystalline silver films. (a) Atomic force microscope scan of a single-crystalline silver film measured with a ScanAsyst tip on a Bruker FastScan. The film had a roughness of 0.46 nm over a 2.5 x 2.5 µm^2 area after removing a third degree background in Gwyddion. (b) The quality factor of the surface plasmon polariton comparing our silver film to Palik's data. Dielectric constant data for our film was obtained using a Woollam Vase variable angle ellipsometer and fitted to a 2 layer air-metal model. The quality factor is obtained by dividing the square of the real part of the dielectric constant by the imaginary part.

Single-crystalline silver films, shown in Figure 5.11 were prepared following a previous recipe.[58] Freshly cleaved mica from Ted Pella was loaded into a Kurt J. Lesker PVD 75 sputterer. Once the pressure decreased below 2 x 10^{-6} Torr, temperature was ramped up at a rate of 3°C/min to 360°C. After pre-annealing for 1 hour, silver was sputtered at 110 nm/min at a target-substrate distance of 17 cm under an argon pressure of 6 mTorr. After a 30 minute post-anneal, the sample was allowed to cool to room temperature.

Fabrication of Hole Arrays and Bull's Eye Structures

Hole arrays and bull's-eye structures on single-crystalline silver films were milled using a FEI Helios dual beam focused ion beam at an acceleration voltage of 30 kV and an ion-beam current of 40 pA. A 20 by 20 array of holes with the diameter of each hole set to one-half of the periodicity of the array. For bull's-eye structures, the number of rings was set to 25, and the groove depth was about 80 nm.

After focused-ion-beam etching of the structures on silver film, the sample was loaded into a Picosun atomic layer deposition at 100°C. 10 nm of alumina was deposited at 100°C with alternating cycles of trimethylaluminum and water.

Nitrogen Sealing of Samples in Glovebox

After preparation, samples were sealed inside a nitrogen glovebox by attaching a cover slip on top using a 2-part chemical epoxy (Araldite).

Quantum-Dot Deposition in Plasmonic Structures and Qualitative Purcell Factors

While the color of the emission is tunable both in the hole arrays and bull's-eye patterns, the emission in the bull's-eye patterns is not rotationally symmetric. We confirmed that this is not an imaging artifact; instead, this is a result of the spin-coating of the dots. Figure 5.8 shows SEM images of quantum dots in hole arrays and bull's eye from the same structure imaged in Figure 5.6. The deposition patterns match the emission pattern.

The emission spectra were from the nanocrystals in each of the hole arrays and a corresponding spectrum on the unstructured area with the same pixel area as the hole array were recorded using a Triax 320 imaging spectrometer coupled to a Nikon TE200 inverted microscope. The spectrum from each of the hole arrays was normalized by the corresponding spectrum outside the hole array to obtain the estimated Purcell factors. As explained previously, the spin-coating of the CdSe nanocrystals in the hole arrays resulted in different morphologies inside and outside the nanoholes. Therefore, these Purcell factors are qualitative at best (see Figure 5.7).

Quantum Dots at Silver Pyramid Tips

Using conventional deposition techniques such as spin-coating or dip coating, it is very difficult to precisely position the nanocrystals. To get around this, a nominally 30 nm thick silver film was thermally evaporated onto Si wafer with pyramids. While the silver on the flat was continuous and smooth, the silver in the pyramids was rough and discontinuous due to the angled deposition. A microliter droplet of CdSe nanocrystals from a dilute dispersion was then drop-cast. Finally, a 200 nm thick layer of silver was deposited to form a metal-insulator-metal structure. This was finally template stripped, leaving a few nanocrystals at the tip (Figure 5.4).

Electrochemical Control of Deep Trap Emission

Silver samples were patterned with hole arrays and bull's-eye structures as described previously. No alumina was deposited. A self-assembled monolayer on the silver was formed by soaking the sample in 2 mM ethanolic solution of 1,10-Decanedithiol for 16 hours.[68] Subsequently, the silver film was rinsed thoroughly with absolute ethanol, and soaked in a CdSe dispersion in hexane. The concentration of the CdSe nanocrystals was kept above an optical density of 30 at the absorption band-edge. The sample was finally thoroughly rinsed with hexane and then dried under a nitrogen flow. As evident in the SEM images, a sub-monolayer resulted (Figure 5.12).

A gel-electrolyte film was placed on top on the silver structure, the silver counter electrode, and a Pt quasi-reference electrode. The area of the counter-electrode was kept to at least twice that of the working electrode. A Keithley Model 2400 SourceMeter was used

to apply a potential between the working and the counter electrodes. A separate Keithley Model 2400 SourceMeter was used to measure the potential between the counter electrode and the platinum reference. A calibration chart for the applied and measured potentials is shown in Figure 5.13.

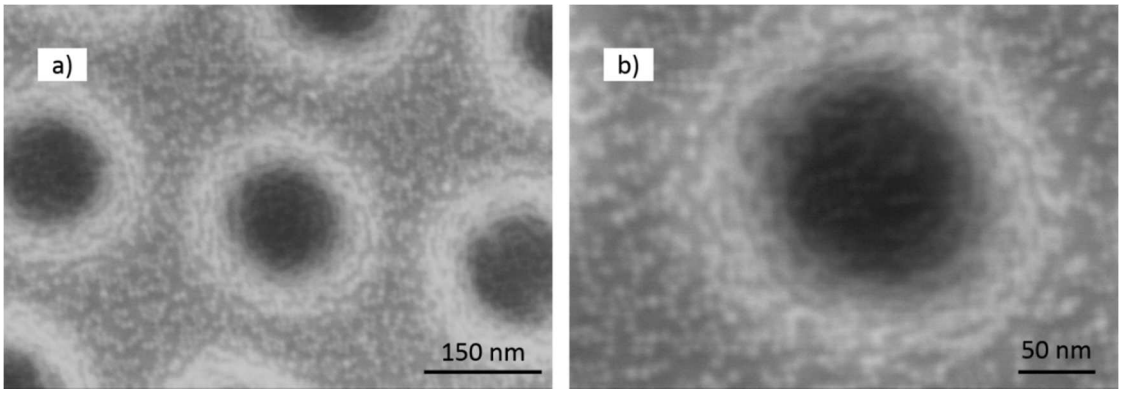

Figure 5.12 Scanning electron microscope image of CdSe self-assembled monolayer on a silver hole array. The silver sample was soaked in a 3 mM ethoanolic solution of 1,10-decanedithiol for >16 hours. Subsequently, the silver sample was rinsed in ethanol and then soaked in a quantum dot dispersion of optical density greater than 30 at the band-edge absorption peak. A sub-monolayer is evident at the bottom of the hole as well as on the flat area outside the hole.

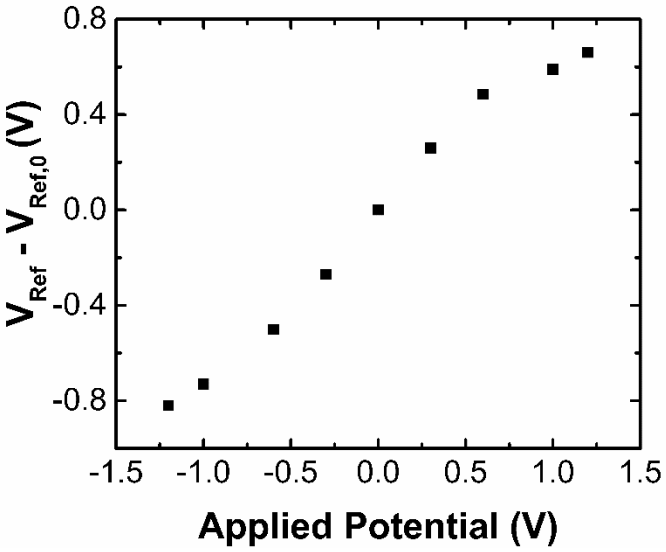

Figure 5.13: Calibration data for the measured potential as a function of the applied potential between the working and counter electrodes. The change in potential measured by the reference is recorded on the y-axis, where $V_{Ref,0}$ is the potential measured at 0V of applied potential and is equal to -0.33V.

Optical Measurements and Analysis

All photoluminescence and electrochemistry measurements were conducted on a Nikon TE 200 inverted microscope equipped with a Nikon high pressure mercury arc lamp mounted at the epi-illumination port. The 436 nm line of the Hg lamp was used to excite the quantum dots and the emission was collected using either a 100x/0.9NA or 10x/0.4NA objective and sent to the 100 micrometer entrance slit of Jobin Yvon Triax 320 imaging spectrometer. A 150 lines/mm grating blazed at 500 nm was used to disperse the light onto a Princeton Instruments Spec-10 liquid-nitrogen-cooled CCD camera mounted onto the spectrometer. The required number of spectra were recorded using a WinSpec 32 software with the appropriate exposure time and interval time between frames.

For the electrochemistry experiments, a typical exposure time of 2 or 3s was used and spectra were recorded in 5s intervals.

5.4 References

[1] S. Coe, W.-K. Woo, M. Bawendi, V. Bulović, "Electroluminescence from single monolayers of nanocrystals in molecular organic devices." *Nature* **420**, 800-803 (2002).

[2] I. Gur, N. A. Fromer, M. L. Geier, A. P. Alivisatos, "Air-stable all-inorganic nanocrystal solar cells processed from solution." *Science* **310**, 462-465 (2005).

[3] V. Klimov, A. Mikhailovsky, S. Xu, A. Malko, J. Hollingsworth, C. Leatherdale, H.-J. Eisler, M. Bawendi, "Optical gain and stimulated emission in nanocrystal quantum dots." *Science* **290**, 314-317 (2000).

[4] G. Kalyuzhny, R. W. Murray, "Ligand effects on optical properties of CdSe nanocrystals." *The Journal of Physical Chemistry B* **109**, 7012-7021 (2005).

[5] J. Jasieniak, P. Mulvaney, "From Cd-rich to Se-rich-the manipulation of CdSe nanocrystal surface stoichiometry." *Journal of the American Chemical Society* **129**, 2841-2848 (2007).

[6] A. Puzder, A. Williamson, F. Gygi, G. Galli, "Self-healing of CdSe nanocrystals: First-principles calculations." *Physical Review Letters* **92**, (2004).

[7] D. R. Baker, P. V. Kamat, "Tuning the emission of CdSe quantum dots by controlled trap enhancement." *Langmuir* **26**, 11272-11276 (2010).

[8] A. D. Dukes, 3rd, P. C. Samson, J. D. Keene, L. M. Davis, J. P. Wikswo, S. J. Rosenthal, "Single-nanocrystal spectroscopy of white-light-emitting CdSe nanocrystals." *Journal of Physical Chemistry A* **115**, 4076-4081 (2011).

[9] M. A. Schreuder, J. R. McBride, A. D. Dukes III, J. A. Sammons, S. J. Rosenthal, "Control of surface state emission via phosphonic acid modulation in ultrasmall CdSe nanocrystals: The role of ligand electronegativity." *The Journal of Physical Chemistry C* **113**, 8169-8176 (2009).

[10] C. Murray, D. J. Norris, M. G. Bawendi, "Synthesis and characterization of nearly monodisperse CdE (E= sulfur, selenium, tellurium) semiconductor nanocrystallites." *Journal of the American Chemical Society* **115**, 8706-8715 (1993).

[11] T. E. Rosson, S. M. Claiborne, J. R. McBride, B. S. Stratton, S. J. Rosenthal, "Bright white light emission from ultrasmall cadmium selenide nanocrystals." *Journal of the American Chemical Society* **134**, 8006-8009 (2012).

[12] S. Sapra, S. Mayilo, T. A. Klar, A. L. Rogach, J. Feldmann, "Bright white-light emission from semiconductor nanocrystals: By chance and by design." *Advanced Materials* **19**, 569-572 (2007).

[13] M. A. Schreuder, K. Xiao, I. N. Ivanov, S. M. Weiss, S. J. Rosenthal, "White light-emitting diodes based on ultrasmall CdSe nanocrystal electroluminescence." *Nano Letters* **10**, 573-576 (2010).

[14] M. J. Bowers Ii, J. R. McBride, M. D. Garrett, J. A. Sammons, A. D. Dukes Iii, M. A. Schreuder, T. L. Watt, A. R. Lupini, S. J. Pennycook, S. J. Rosenthal, "Structure and ultrafast dynamics of white-light-emitting CdSe nanocrystals." *Journal of the American Chemical Society* **131**, 5730-5731 (2009).

[15] M. J. Bowers, J. R. McBride, S. J. Rosenthal, "White-light emission from magic-sized cadmium selenide nanocrystals." *Journal of the American Chemical Society* **127**, 15378-15379 (2005).

[16] T. W. Ebbesen, H. Lezec, H. Ghaemi, T. Thio, P. Wolff, "Extraordinary optical transmission through sub-wavelength hole arrays." *Nature* **391**, 667-669 (1998).

[17] K. Shimizu, W. Woo, B. Fisher, H. Eisler, M. Bawendi, "Surface-enhanced emission from single semiconductor nanocrystals." *Physical Review Letters* **89**, (2002).

[18] J.-H. Song, T. Atay, S. Shi, H. Urabe, A. V. Nurmikko, "Large enhancement of fluorescence efficiency from CdSe/ZnS quantum dots induced by resonant coupling to spatially controlled surface plasmons." *Nano Letters* **5**, 1557-1561 (2005).

[19] W. Barnes, "Fluorescence near interfaces: The role of photonic mode density." *journal of Modern Optics* **45**, 661-699 (1998).

[20] R. Chance, A. Prock, R. Silbey, "Molecular fluorescence and energy transfer near interfaces." *Advanced Chemical Physics* **37**, 65 (1978).

[21] E.-S. Kwak, J. Henzie, S.-H. Chang, S. K. Gray, G. C. Schatz, T. W. Odom, "Surface plasmon standing waves in large-area subwavelength hole arrays." *Nano Letters* **5**, 1963-1967 (2005).

[22] K. A. Willets, R. P. Van Duyne, "Localized surface plasmon resonance spectroscopy and sensing." *Annual Review of Physical Chemistry* **58**, 267-297 (2007).

[23] Y. C. Jun, K. C. Huang, M. L. Brongersma, "Plasmonic beaming and active control over fluorescent emission." *Nature Communications* **2**, 283 (2011).

[24] T. W. Ebbesen, C. Genet, S. I. Bozhevolnyi, "Surface-plasmon circuitry." *Physics Today* **61**, 44 (2008).

[25] A. Akimov, A. Mukherjee, C. Yu, D. Chang, A. Zibrov, P. Hemmer, H. Park, M. Lukin, "Generation of single optical plasmons in metallic nanowires coupled to quantum dots." *Nature* **450**, 402-406 (2007).

[26] W. Qin, P. Guyot-Sionnest, "Evidence for the role of holes in blinking: Negative and oxidized CdSe/CdS dots." *ACS Nano* **6**, 9125-9132 (2012).

[27] S. K. Sharma, K. Sudarshan, P. Maheshwari, D. Dutta, P. K. Pujari, C. P. Shah, M. Kumar, P. Bajaj, "Direct evidence of Cd vacancies in CdSe nanoparticles: Positron annihilation studies." *The European Physical Journal B* **82**, 335-340 (2011).

[28] S. W. Eijt, A. T. van Veen, H. Schut, P. E. Mijnarends, A. B. Denison, B. Barbiellini, A. Bansil, "Study of colloidal quantum-dot surfaces using an innovative thin-film positron 2D-ACAR method." *Nature Materials* **5**, 23-26 (2006).

[29] S. Fengler, E. Zillner, T. Dittrich, "Density of surface states at CdSe quantum dots by fitting of temperature-dependent surface photovoltage transients with random walk simulations." *The Journal of Physical Chemistry C* **117**, 6462-6468 (2013).

[30] J. Mooney, M. Krause, J. Saari, P. Kambhampati, "Challenge to the deep-trap model of the surface in semiconductor nanocrystals." *Physical Review B* **87**, (2013).

[31] M. M. Krause, J. Mooney, P. Kambhampati, "Chemical and thermodynamic control of the surface of semiconductor nanocrystals for designer white light emitters." *ACS Nano* **7**, 5922-5929 (2013).

[32] G. A. Beane, A. J. Morfa, A. M. Funston, P. Mulvaney, "Defect-mediated energy transfer between ZnO nanocrystals and a conjugated dye." *The Journal of Physical Chemistry C* **116**, 3305-3310 (2012).

[33] C. Galland, Y. Ghosh, A. Steinbruck, M. Sykora, J. A. Hollingsworth, V. I. Klimov, H. Htoon, "Two types of luminescence blinking revealed by spectroelectrochemistry of single quantum dots." *Nature* **479**, 203-207 (2011).

[34] P. Guyot-Sionnest, "Charging colloidal quantum dots by electrochemistry." *Microchimica Acta* **160**, 309-314 (2008).

[35] P. Guyot-Sionnest, E. Lhuillier, H. Liu, "A mirage study of CdSe colloidal quantum dot films, urbach tail, and surface states." *Journal of Chemical Physics* **137**, 154704 (2012).

[36] P. Guyot-Sionnest, B. Wehrenberg, D. Yu, "Intraband relaxation in CdSe nanocrystals and the strong influence of the surface ligands." *Journal of Chemical Physics* **123**, 074709 (2005).

[37] C. Wang, M. Shim, P. Guyot-Sionnest, "Electrochromic nanocrystal quantum dots." *Science* **291**, 2390-2392 (2001).

[38] C. Wang, M. Shim, P. Guyot-Sionnest, "Electrochromic semiconductor nanocrystal films." *Applied Physics Letters* **80**, 4 (2002).

[39] S. Brovelli, C. Galland, R. Viswanatha, V. I. Klimov, "Tuning radiative recombination in Cu-doped nanocrystals via electrochemical control of surface trapping." *Nano Letters* **12**, 4372-4379 (2012).

[40] P. Guyot-Sionnest, M. Shim, C. Matranga, M. Hines, "Intraband relaxation in CdSe quantum dots." *Physical Review B* **60**, R2181 (1999).

[41] P. P. Jha, P. Guyot-Sionnest, "Electrochemical switching of the photoluminescence of single quantum dots." *The Journal of Physical Chemistry C* **114**, 21138-21141 (2010).

[42] H. Liu, A. Pourret, P. Guyot-Sionnest, "Mott and Efros-Shklovskii variable range hopping in CdSe quantum dots films." *ACS Nano* **4**, 5211-5216 (2010).

[43] W. Qin, R. A. Shah, P. Guyot-Sionnest, "CdseS/ZnS alloyed nanocrystal lifetime and blinking studies under electrochemical control." *ACS Nano* **6**, 912-918 (2011).

[44] W. Qin, H. Liu, P. Guyot-Sionnest, "Small bright charged colloidal quantum dots." *ACS Nano* **8**, 283-291 (2013).

[45] A. K. Gooding, D. E. Gómez, P. Mulvaney, "The effects of electron and hole injection on the photoluminescence of CdSe/CdS/ZnS nanocrystal monolayers." *ACS Nano* **2**, 669-676 (2008).

[46] P. Guyot-Sionnest, C. Wang, "Fast voltammetric and electrochromic response of semiconductor nanocrystal thin films." *The Journal of Physical Chemistry B* **107**, 7355-7359 (2003).

[47] S. Brovelli, W. K. Bae, C. Galland, U. Giovanella, F. Meinardi, V. I. Klimov, "Dual-color electroluminescence from dot-in-bulk nanocrystals." *Nano Letters* **14**, 486-494 (2014).

[48] P. Nagpal, N. C. Lindquist, S.-H. Oh, D. J. Norris, "Ultrasmooth patterned metals for plasmonics and metamaterials." *Science* **325**, 594-597 (2009).

[49] C.-M. Chuang, M.-C. Wu, W.-F. Su, K.-C. Cheng, Y.-F. Chen, "High intensity fluorescence of photoactivated silver oxide from composite thin film with periodic array structure." *Applied Physics Letters* **89**, 061912 (2006).

[50] I. Diez, R. H. Ras, "Fluorescent silver nanoclusters." *Nanoscale* **3**, 1963-1970 (2011).

[51] C. Mihalcea, D. Büchel, N. Atoda, J. Tominaga, "Intrinsic fluorescence and quenching effects in photoactivated reactively sputtered silver oxide layers." *Journal of the American Chemical Society* **123**, 7172-7173 (2001).

[52] L. A. Peyser, T.-H. Lee, R. M. Dickson, "Mechanism of Ag n nanocluster photoproduction from silver oxide films." *The Journal of Physical Chemistry B* **106**, 7725-7728 (2002).

[53] J. Zheng, P. R. Nicovich, R. M. Dickson, "Highly fluorescent noble-metal quantum dots." *Annual Review of Physical Chemistry* **58**, 409-431 (2007).

[54] L. A. Peyser, A. E. Vinson, A. P. Bartko, R. M. Dickson, "Photoactivated fluorescence from individual silver nanoclusters." *Science* **291**, 103-106 (2001).

[55] H. Asami, Y. Abe, T. Ohtsu, I. Kamiya, M. Hara, "Surface state analysis of photobrightening in CdSe nanocrystal thin films." *The Journal of Physical Chemistry B* **107**, 12566-12568 (2003).

[56] S. F. Lee, M. A. Osborne, "Brightening, blinking, bluing and bleaching in the life of a quantum dot: Friend or foe?" *Chemphyschem* **10**, 2174-2191 (2009).

[57] M. Oda, A. Hasegawa, N. Iwami, K. Nishiura, N. Ando, A. Nishiyama, H. Horiuchi, T. Tani, "Reversible photobluing of CdSe/ZnS/TOPO nanocrystals." *Colloids and Surfaces B Biointerfaces* **56**, 241-245 (2007).

[58] J. H. Park, P. Ambwani, M. Manno, N. C. Lindquist, P. Nagpal, S. H. Oh, C. Leighton, D. J. Norris, "Single-crystalline silver films for plasmonics." *Advanced Materials* **24**, 3988-3992 (2012).

[59] S. Han, "Theory of thermal emission from periodic structures." *Physical Review B* **80**, (2009).

[60] M. Gao, B. Richter, S. Kirstein, "White-light electroluminescence from self-assembled q-CdSe/PPV multilayer structures." *Advanced Materials* **9**, 802-805 (1997).

[61] E. Jang, S. Jun, H. Jang, J. Lim, B. Kim, Y. Kim, "White-light-emitting diodes with quantum dot color converters for display backlights." *Advanced Materials* **22**, 3076-3080 (2010).

[62] A. H. Mueller, M. A. Petruska, M. Achermann, D. J. Werder, E. A. Akhadov, D. D. Koleske, M. A. Hoffbauer, V. I. Klimov, "Multicolor light-emitting diodes based on semiconductor nanocrystals encapsulated in GaN charge injection layers." *Nano Letters* **5**, 1039-1044 (2005).

[63] S. K. Panda, S. G. Hickey, H. V. Demir, A. Eychmuller, "Bright white-light emitting manganese and copper Co-doped ZnSe quantum dots." *Angewandte Chemie International Edition in English* **50**, 4432-4436 (2011).

[64] D. Norris, A. L. Efros, M. Rosen, M. Bawendi, "Size dependence of exciton fine structure in CdSe quantum dots." *Physical Review B* **53**, 16347 (1996).

[65] S. Dolai, P. R. Nimmala, M. Mandal, B. B. Muhoberac, K. Dria, A. Dass, R. Sardar, "Isolation of bright blue light-emitting CdSe nanocrystals with 6.5 kda core in gram scale: High photoluminescence efficiency controlled by surface ligand chemistry." *Chemistry of Materials* **26**, 1278-1285 (2014).

[66] P. Reiss, J. Bleuse, A. Pron, "Highly luminescent CdSe/ZnSe core/shell nanocrystals of low size dispersion." *Nano Letters* **2**, 781-784 (2002).

[67] J. Lee, V. C. Sundar, J. R. Heine, M. G. Bawendi, K. F. Jensen, "Full color emission from ii–vi semiconductor quantum dot–polymer composites." *Advanced Materials* **12**, 1102-1105 (2000).

[68] T. Nakanishi, B. Ohtani, K. Uosaki, "Fabrication and characterization of CdS-nanoparticle mono-and multilayers on a self-assembled monolayer of alkanedithiols on gold." *The Journal of Physical Chemistry B* **102**, 1571-1577 (1998).

Chapter 6.

Polariton Emission from Strongly Coupled Quantum Dots on Plasmonic Films[4]

In the strong-coupling regime, light and matter states hybridize to form "dressed" states, which are different in energy from the original light and matter states. Strong coupling of light and matter can lead to important technological advances in quantum information processing and thresholdless lasers. The high field-confinement of surface plasmons in plasmonic structures and the unique optical properties of semiconductor quantum dots should enable studies in the strong-coupling regime. Despite their promise, very few works have reported strong coupling between the quantum dots and surface plasmons. Here, we demonstrate strong coupling, manifesting as an avoided crossing in the surface-plasmon-dispersion plot, between high-quality plasmonic structures and CdSe/CdS/ZnS core/shell/shell nanocrystals. Furthermore, we observe polariton emission from these states at room temperature, and obtain a Rabi splitting of 80 meV. We further analyze the dynamics of polariton emission through spectrally resolved lifetimes and pump-intensity dependence of emission spectra.

[4] This chapter is under preparation for submission as Sriharsha V. Jayanti*, Kevin M. McPeak*, David K. Kim*, Paul Erickson, Jian Cui, Ferry Prins, Stephan J. P. Kress, Aurelio Rossinelli, Krishtopher McNeill, & David J. Norris, "Polariton emission from strongly coupled quantum dots on plasmonic films".

** authors contributed equally*

6.1 Introduction

The strength of light-matter interactions qualitatively falls into two categories: weak coupling and strong coupling regimes. In the weak coupling regime, an emitter and an optical cavity interact and exchange energy without modifying the dispersion. In this regime, the emission rates and directionality can be modified, but not the energy levels.[1, 2] In the strong coupling regime, the energy levels of the cavity and the emitter hybridize to form the so-called "dressed states."[3-5] When strongly coupled, the emitter and the cavity exchange energy, called Rabi oscillations, at a faster rate than any decoherence or loss mechanisms. The resultant hybrid states are split in energy by the Rabi splitting. Strong coupling is directly linked to coherence[6, 7]; therefore, it could open up novel applications for quantum-information processing,[8, 9] coherent perfect absorbers[10], and thresholdless lasers[4, 6, 11-14].

When the emitter and cavity are in resonance, the Rabi splitting is given by $\hbar\Omega_R = \sqrt{4\Delta^2 - (\Gamma_c - \Gamma_e)^2}$, where Δ is the strength of the interaction, Γ_c is the linewidth of the cavity mode, and Γ_e is the linewidth of the emitter.[15, 16] The splitting can be increased by increasing the Δ or by decreasing the difference between the cavity and emitter linewidths.

One way to increase the strength of interaction is to choose an emitter with a large transition dipole. While J-aggregates, dye, and quantum dots all have large dipoles, quantum dots are an ideal choice of emitter because they are color-tunable, have high fluorescence quantum yields, and are highly photostable.[17-22] Previously, strong coupling has been observed in single quantum dots grown via molecular beam epitaxy (MBE).[8, 23-25] In one of the first demonstrations, a temperature-dependent avoided-crossing in the two photoluminescence peaks at low temperature.[25] The Rabi splitting was about 170 μeV.

The strength of the cavity-emitter interaction can be enhanced in regions of high field densities. Compared to photonic cavities, plasmonic cavities support sub-diffraction resonances and can offer much smaller mode volumes. Therefore, moving to plasmonic structures could lead to enhanced interactions and even allow room-temperature observation of strong coupling. However, plasmonic structures also exhibit large Ohmic losses, leading to broader cavity linewidths. Larger linewidths make it more difficult to

distinguish the Rabi splitting in the experimental spectra[4, 26]. While plasmonic structures hold promise, very few reports have observed strong coupling with quantum dots.

Rather, strong coupling on plasmonic materials has been demonstrated using various emitters, such as J-aggregates and dyes.[27-32] Recently, photochromic molecules were used to demonstrate Rabi splittings as large as 700 meV,[33] three orders of magnitude larger than that observed for a single MBE-grown quantum dot in a photonic cavity. The primary reason for this is that the Rabi splitting scales with the square root of number density of emitters.

Strong coupling using colloidal quantum dots on plasmonic substrates was recently reported.[34, 35] Using a thick film of CdSe nanocrystals, an anticrossing was observed in the SPP dispersion by measuring the reflectivity in a Kretchmann configuration.[34] Note that the Rabi splitting was only observed by probing the absorption of light in these sample. While useful for some applications, emission from strongly coupled states is a prerequisite for gain or lasing. No Rabi splittings in the photoluminescence have been reported in colloidal quantum dot-plasmonic systems.

In this work, we demonstrate emission from strongly coupled states, also known as polariton states, between colloidal quantum dots and plasmonic hole arrays. We first design high-quality metal structures with low plasmonic losses. We also synthesize highly photostable and > 80% quantum yield CdSe/CdS/ZnS core/shell/shell quantum dots. With the aid of simulations, we optimize the design of our plasmonic structure, and place a packed film of quantum dots in the field maxima to obtain the strongest interaction. We see Rabi splittings in transmission measurements of quantum dots in micrometer-scale silver (Ag) hole arrays, and in photoluminescence measurements on centimeter-scale Ag hole array samples. In some of our samples, we see very little background emission from uncoupled quantum dots. Therefore, our geometry is a great platform to study the polariton dynamics. Finally, we study spectrally dependent lifetimes and the power dependence of the polariton emission.

6.2 Results and Discussion

To observe Rabi splittings in the optical regime, a key requirement is that the rate of Rabi oscillations is larger than the mean of the surface-plasmon decay rate and the exciton decay rate. The exciton decay rate in our quantum dots (~0.1 GHz) is orders of magnitude lower than the surface-plasmon decay rate (~10 THz). Because damping of the surface plasmons plays a vital role in observation of strong coupling, the quality of the metal is paramount. We made low-loss single-crystalline Ag films by sputtering (PVD 75, Kurt J. Lesker) onto mica at 360°C.[36] Typical surface plasmon damping rates on these films are of the order of 100 fs at 620 nm.

High-quality CdSe/CdS/ZnS core/shell/shell quantum dots with fluorescence quantum yields over 80% were synthesized.[20] The photostability and amplified spontaneous emission form these nanocrystals is shown in Figure 6.1. We note that when the quantum dot layer was thicker than 200 nm, we see amplified spontaneous emission from the two different energy levels at 635 nm and 590 nm (Figure 6.1). This leads us to believe that the transition dipoles at both energy levels are large enough that both states could partake in strong coupling, unlike previous quantum-dot-plasmonic reports.

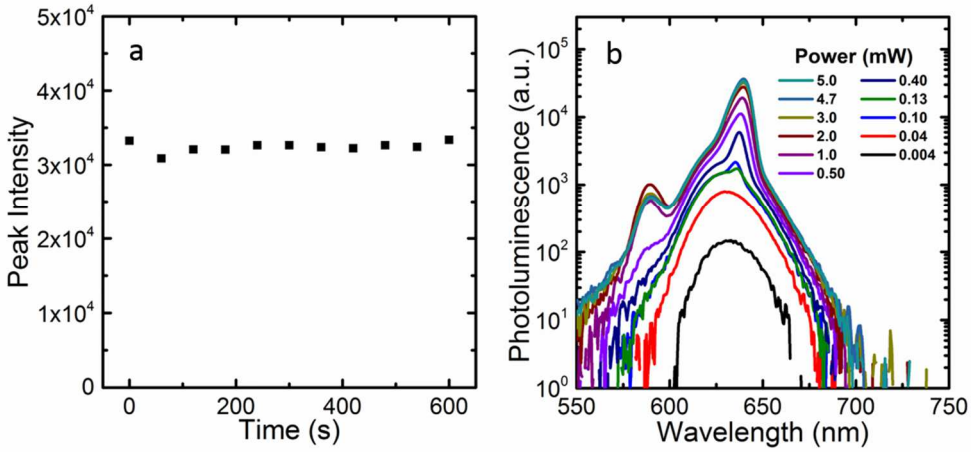

Figure 6.1 Photostability of 320 nm thick film of CdSe/CdS/ZnS core/shell/shell nanocrystals on glass pumped with a 400 nm laser of 80 fs pulse width and fluence of 785 μJ/cm^2. Over the course of 10 minutes, little or no change is observed in the maximum intensity. b) Spectra from the film at various powers. An amplified spontaneous emission peak develops at 635 nm with a threshold near 0.10 mW power, and a second one near 585 nm develops at powers of 1 mW. The linewidth of both the ASE peaks is about 10 – 12 nm.

Figure 6.2 shows the strong coupling between the quantum dots and hole arrays on a single-crystalline silver film. Figure 6.2a shows the absorption and photoluminescence of the quantum dots used for the study. They have a band-edge absorption feature at 612 nm and another at 585 nm, consistent with the amplified spontaneous emission peaks in Figure 6.1. Photoluminescence from a thin layer of quantum dots deposited on Ag with a 10 nm spacer and excited at low pump fluence is shown in the same plot.

Hole arrays on a 300 nm thick Ag film were etched using a FEI Helios dual-beam focused ion beam at an acceleration voltage of 30 kV and 40 pA. The periodicity was varied from 400 to 700 nm in intervals of 5 nm, and the hole diameter was kept to a third of the periodicity. The transmission through the hole arrays was measured on a Nikon TE200 inverted microscope using a tungsten halogen lamp as the white light source. The spectra were obtained using a Spex Triax 320 imaging spectrometer equipped with a Princeton Instruments Spec-10 liquid-nitrogen-cooled CCD camera.

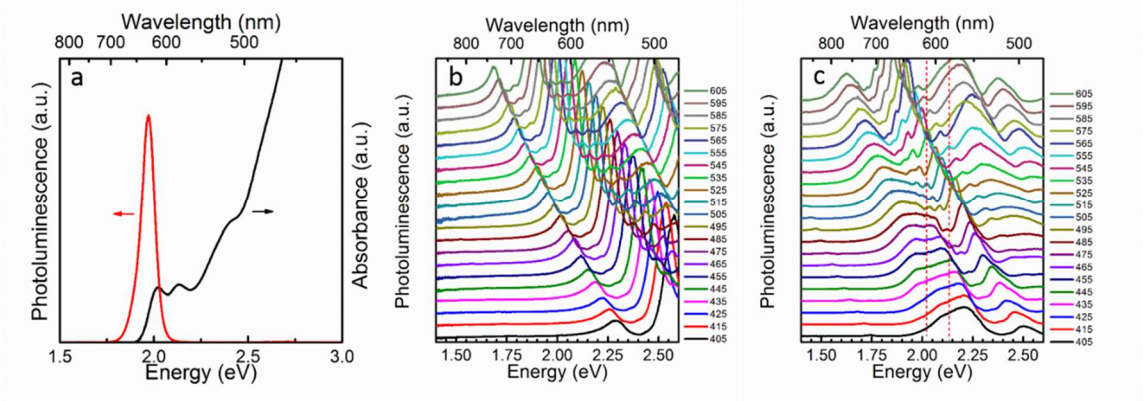

Figure 6.2 Strong coupling in transmission measurements. (a) Absorption spectrum of CdSe/CdS/ZnS core/shell/shell quantum dots in a hexane dispersion, and the photoluminescence of the quantum dots on flat Ag with 10 nm of alumina. The full-width-at-half-maximum is 27 nm in the photoluminescence. (b) Transmission spectra on bare silver hole arrays etched into a single-crystalline Ag film grown on mica. The peak energy changes with changing periodicity, labeled to the right. Note that the lowest energy resonance, corresponding to the Ag-mica resonance, changes continuously as a single peak. (c) Once the quantum dots are spin-coated into the hole arrays, the lowest-energy resonance shows a second feature when the quantum-dot and the surface-plasmon energies overlap. An avoided crossing occurs at an energy of 2.02 eV, corresponding to the band-edge energy of the quantum dots. A second avoided crossing is at an energy of 2.12 eV, corresponding to the second energy level of the quantum dots. This is clarified in Figure 6.3.

Since the surface-plasmon resonance is dependent on the periodicity of the hole array, the overlap between the surface-plasmon resonance and the quantum-dot emission can be tuned. At resonance, strong coupling should appear as a splitting in the surface-plasmon peak in the transmission spectra. The transmission spectra from the bare hole arrays are plotted in Figure 6.2b. Note that no splitting or anti-crossing exists in the mica-Ag surface-plasmon resonances (lowest energy peaks in Figure 6.2b). Quantum dots were then spin-coated onto the hole arrays from a dispersion in octane at optical density of 3 at the lowest absorption feature. The resulting transmission spectra are shown in Figure 6.2c. Note that the field is maximum at the center of the holes. Because the quantum dots are at the bottom of the holes, and rest on top of the mica, the anti-crossing should appear in the Ag-mica dispersion. The higher refractive index of mica compared to air red-shifts the Ag-mica resonance relative to the Ag-air interface. Two anti-crossings appear in the (1,0) surface-plasmon resonance at the Ag-mica interface (see also Figure 6.3a). The first anti-crossing occurs at the lowest absorption energy of the quantum dots at 2.02 eV. The Rabi splitting here is about 65 meV. A second anticrossing is also apparent at 2.12 eV, with a Rabi splitting of about 57 meV. These values are lower than the Rabi splitting previously reported for CdSe nanocrystals on Ag films.[34] However, previously only a single anti-crossing was observed at the lowest absorption feature.

Surface-plasmon-mediated strong coupling of two different sizes of quantum dots on plasmonic structures was recently reported.[37] Two avoided crossings were observed, as we see in transmission here in Figure 6.2c. The important difference is that we see two avoided crossings due to different energy levels of the same quantum dots. A similar observation was reported using Rhodamine 6G as the emitter.[32]

The photoluminescence spectra from the same sample measured by exciting with a low-power picosecond 405 nm laser (Picoquant, LDH-D-C 405) are shown in Figure 6.3b. Any strong coupling is not directly obvious since only one peak is present. Clearly the peak energy is shifting with the wavevector, and in a manner consistent the transmission spectra. For example, in both the transmission and the photoluminescence dispersion curves, at 0.13 nm^{-1}, an anti-crossing seems to appear. However, it is difficult to distinguish between any weak coupling from polariton emission. Lifetime measurements obtained in each of the

hole arrays are plotted in Figure 6.3c. The lifetimes decrease with increasing (decreasing) wavevector (hole array periodicity). This most likely arises from the increased confinement of fields. The lifetimes exhibit a discrete fall at the wavevector corresponding to the avoided crossing.

We therefore shifted to a different sample geometry. We decided to use a large-scale hexagonal hole array fabricated by colloidal lithography (see Materials and Methods). Compared to the square lattice that was milled into the single crystalline Ag film, the strength of quantum-dot-surface-plasmon interaction at the (1,0) resonance on a hexagonal lattice should be stronger due to the increased number of nearest neighbors. Specifically, it should be stronger by a factor of $\sqrt{6/4}$ due to the $\sqrt{N}$ dependence of the Rabi splitting. Note the 6 and 4 correspond to the nearest neighbors in the hexagonal and square lattice.

To optimize the interaction between the quantum dots and hole arrays, we modeled the system using finite-element simulations (JCMwave). Figure 6.4 shows the model and the field maps at the surface-plasmon resonances. Initially, we fixed the hole array periodicity at 522 nm (since this is readily available for colloidal nanolithography) and the hole diameter at 261 nm. A far-field plane-wave excitation source was used to obtain the extinction spectra as a function of the thickness of the Ag layer. As the Ag-layer thickness increases, the ratio of the intensities of the peaks at 575 nm and 690 nm increases. These resonances correspond to the surface plasmons at the Ag-air and the Ag-SiO_2 interfaces, respectively. More importantly, note that the field maps in Figure 6.4c indicate that the field is maximum inside the hole and in the plane of the Ag-dielectric interface. In other words, to optimize the interaction between the quantum dots and the surface plasmons, the quantum dots need to be in the center and at the top of the hole. To do so, we first deposited our quantum dots onto an ultra-flat borosilicate glass and placed this on top of the hole array.

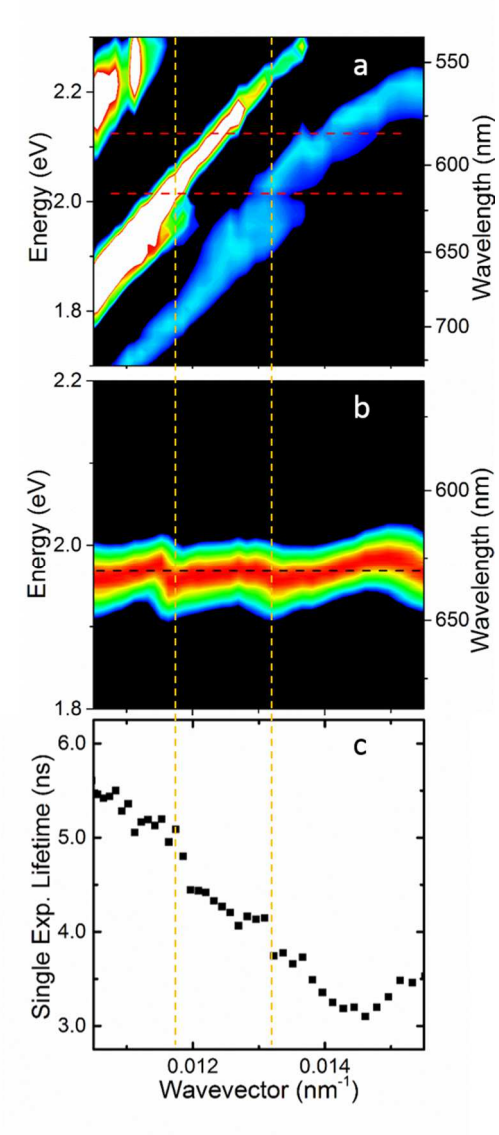

Figure 6.3 Transmission and photoluminescence dispersion curves and lifetimes. (a) The dispersion curve was obtained by stitching the transmission spectra from the data shown in Figure 6.1c. Note that the two avoided crossings are more clearly observed here, as indicated by the horizontal dashed lines at 2.02 eV and 2.12 eV. (b) The photoluminescence from quantum dots in hole arrays of different periodicities was measured and stitched to obtain the dispersion curve shown. Note that there appear to be avoided crossings at the wavevectors indicated by the vertical dashed lines. In particular, the higher-wavevector avoided crossing is consistent with the transmission measurements. The splitting at the smaller wavevector is consistent with the avoided crossing in transmission at the (1,0) Ag-air interface. (c) The lifetimes of the quantum dots in the hole arrays decrease with increasing wavevector; this is expected since the field is more confined in the hole arrays with smaller (larger) periodicity (wavevector). The lifetimes also show a sudden dip at the wavevectors where strong coupling is observed in the transmission and photoluminescence.

Simulations were also conducted to improve the quality factor, or Q-factor (related to the spectral linewidth) of the plasmonic resonances, and obtain them in a more realistic geometry. Figure 6.5 shows that as the hole diameter decreases, the Q-factor increases. However, note that arbitrarily decreasing the hole diameter will reduce the field intensities below an optimal value. In our experiments, the hole diameter was kept between 100 and 300 nm. Polariton emission was observed on hole arrays with hole diameters of approximately 120-130 nm. Figure 6.5c includes a layer for the quantum dots and the glass above it, as in the experiments. Note that the resonances occur at around 600 or 610 nm, close to the band-edge absorption of the quantum dots at 612 nm.

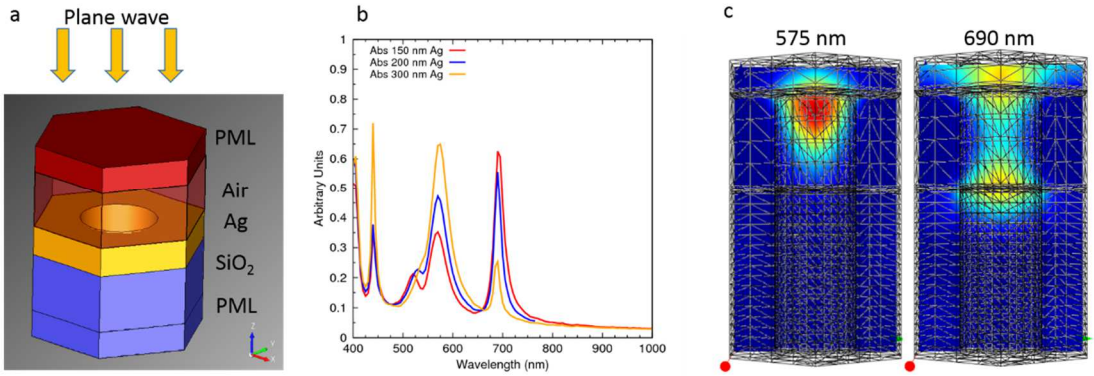

Figure 6.4 Modeling of surface-plasmon resonances in hole arrays. (a) Set up of the model used for hole-array simulations. A hexagonal lattice is generated in a 4-layer geometry consisting of air, Ag, and Si or SiO_2. Here, a perfectly matched layer (PML) is assumed for the boundary conditions at the top and bottom, and a periodic boundary condition is set at the sides. We assume a plane-wave excitation incident at an angle of incidence of 0°. Extinction spectra were calculated for a 522 nm pitch hole array and 260 nm hole diameter for various thickness of the Ag layer. (c) Field maps were generated for the two lowest-energy peaks. The Ag-air surface-plasmon resonance has a field maximum at the top in the center of the hole, while that of the Ag-SiO_2 is in the center of the hole but at the top and bottom. Note that the quantum dots should be placed in regions of high field to attain strong coupling.

Hexagonal hole arrays of 522 nm periodicity were fabricated using a silicon hole array template (see section 6.3). A thin layer of Ge was deposited before evaporating 300 nm of silver to improve wetting and flatness.[38] Subsequently, the film was heated to 350˚C in a nitrogen glovebox to improve the roughness and reduce grain boundaries (Figure 6.7a). A 5 to 10 nm layer of alumina was deposited on top using atomic layer deposition as a spacer before quantum dot deposition. To place the quantum dots in the hole or at the top of the hole, we first drop-cast them onto a flat alumino-borosilicate slide, and just as the

edges began to dry, we placed the hole-array sample on the drying quantum dots. After heating for 30 minutes at 70°C, we held the sample together in place by using binder clips. Therefore, a glass-QD-hole array sandwich was formed.

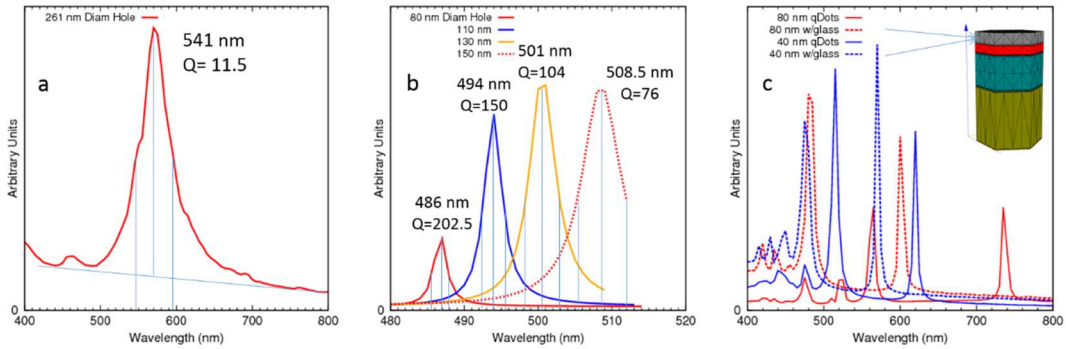

Figure 6.5 Quality factors in hole arrays obtained using JCMWave simulations. (a) The quality factor of a 522 nm hole array with 261 nm hole diameter is only 11.5. (b) At the same periodicity, decreasing the hole diameter leads to significant improvements in the quality factor. When the hole diameter is 80 nm, the Q factor jumps to 202.5. Note also the strength of the resonance decreases if the hole size is too small. This is largely because the radiative damping decreases with decreasing hole size. In our experiments, the hole sizes were in the 100 to 130 nm range when strong coupling was observed. (c) Simulations were performed for a more realistic experimental scenario by adding a quantum dot layer (red) and glass layer (grey). The thickness of the quantum-dot layer is about 80 nm, as in the experiments. Note that the resonances occur at approximately 600 or 610 nm, very close the quantum-dot band-edge absorption of 612 nm.

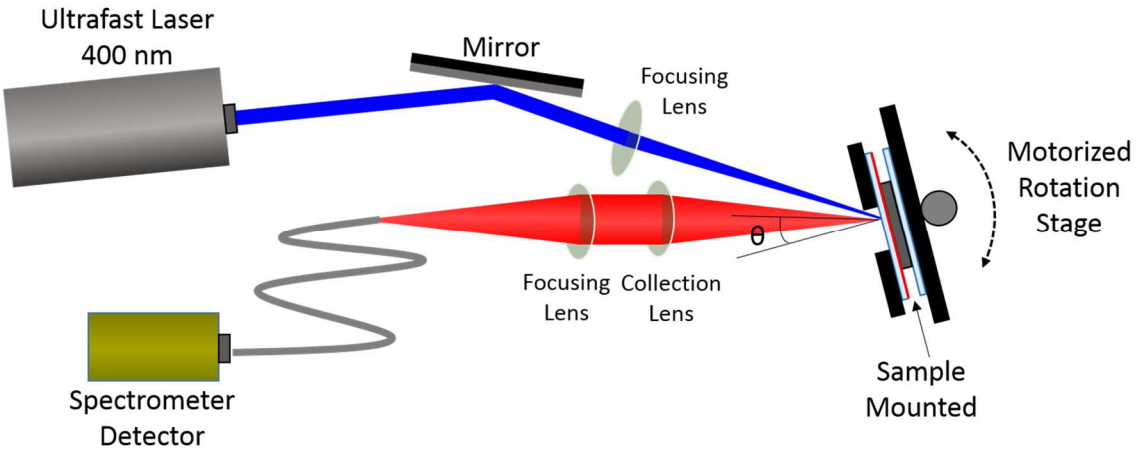

Figure 6.6 Experimental set up for polariton emission nmeasurements. The sample is mounted onto a motorized rotation stage. A laser pulse of 80 fs pulse width and 400 nm in wavelength is focused to a 0.9 mm spot on the sample. The emission from the sample is collected and focused into a fiber-based spectrophotometer. By rotation of the stage, the emission angle can be adjusted. Note that the incidence angle also changes as a result; however, various measurements were conducted to rule out emission changes due to incidence angle.

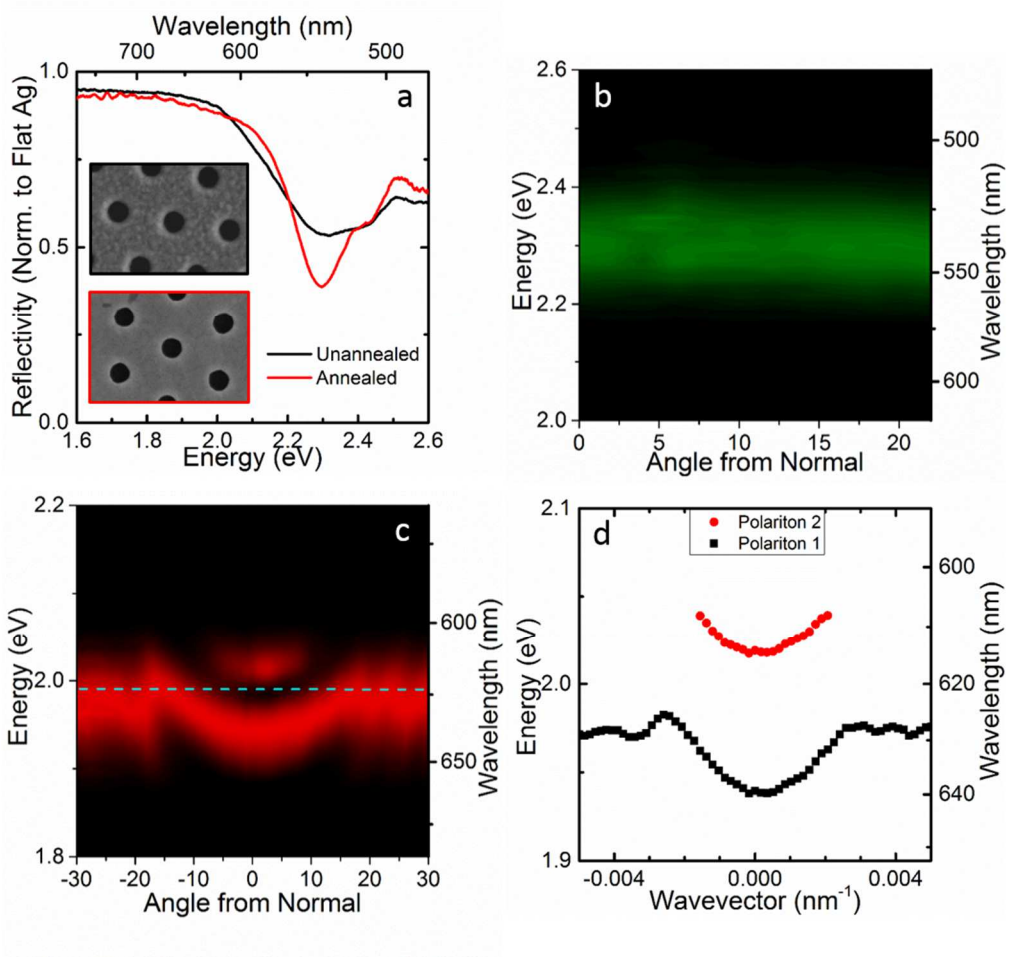

Figure 6.7 Polariton emission from strongly coupled quantum dots on hexagonal hole arrays. (a) While the fabrication is described later, the film quality improved noticeably when annealed in nitrogen at 350°C for 3 minutes. The reflectivity measurements were obtained from hole arrays of 522 nm periodicity and hole diameter close to 200 nm. This is different from the samples on which the strong coupling was observed. Those have the same periodicity, but a hole diameter close to 120 nm. In the hole arrays with 120 nm hole diameter, the peaks in the reflectivity measurements were difficult to resolve. This is because the radiative losses/coupling is severely reduced in hole arrays with smaller diameters. (b) Photoluminescence from green-emitting quantum dots on 522 nm hole array (surface plasmon resonance near 610 nm) at different angles. In this control sample, the quantum dots are not strongly coupled to the hole arrays. (c) Red-emitting quantum dots are strongly coupled to the hole array and show an angle dependent dispersion. Two polariton peaks are clearly resolved, and very little uncoupled emission is observed between the two polariton peaks. (d) The peaks in part (c) were fit with two Gaussians, and the data resulting data is plotted on a energy-wavevector plot to accurately determine the Rabi splitting. Here, it is 80 meV.

The sample was mounted onto a motorized rotation stage and excited with 400 nm laser pulses of 80 fs focused to a 0.9 mm diameter spot (Figure 6.6). The emission from the sample was collected using a 0.1 numerical aperture, 25 mm diameter collection lens

and focused onto a fiber-based spectrophotometer from Ocean Optics. Because both the detector and the excitation source were fixed, the angle of excitation and the angle of emission detection were always changed together. We assume that the emission and any strong coupling behavior are independent of the angle of excitation. Based on control experiments, this is a valid assumption.

Figure 6.7c shows the emission as a function of the angle of detection (from the normal). At normal angle (0˚), we see a clear splitting of the energy levels. In fact, very little emission is detected at the emission wavelength of uncoupled QDs. As we scan through the angles, the spectra change as expected from a strongly coupled system. The lower polariton asymptotically reaches the energy of the uncoupled QDs of 1.98 eV (627 nm).

The nature of the higher energy polariton is unclear at this point. While it follows the behavior expected of an upper polariton, transmission measurements indicate that more than one quantum dot state could be participating in strong coupling. Therefore, the higher energy polariton could be the middle polariton, with the highest energy polariton or the real upper polariton not emissive enough to be detected here. Alternatively, only one quantum dot level could be strongly coupled, in which case we see both the upper and lower polaritons. The corresponding Rabi splitting is 80 meV, in perfect agreement with the expected increase from a square lattice.

To test our results, we performed several control experiments. First, the same quantum dots on another hole array of the same periodicity, but larger hole size of 200 nm did not show much splitting. In the best case, the sample showed some shoulder but not a clear avoided crossing. Second, we replaced the red-emitting QDs with green-emitting QDs on an identical hole array. The photoluminescence of this sample at various angles is shown in Figure 6.7b. Clearly no splitting or even photoluminescence modification is observed since the QD energy of 2.3 eV is far from the surface plasmon resonance. All of these data eliminate interference effects in our samples as a possible explanation.

To further understand the polariton emission in our samples, we measured spectrally resolved lifetimes on a similar sample. The spectrum at high pump powers is shown in Figure 6.8a. Note that in addition to the two polariton peaks, another peak near

2.12 eV appears that wasn't obvious in Figure 6.7. This could be either the upper polariton (resulting from a strongly coupled state) or a multi-exciton feature from uncoupled quantum dots (see Figure 6.1b). The lifetime curves are shown in Figure 6.7b. The lifetimes are similar at all wavelengths along the spectrum, and increase at the reddest wavelength of 648 nm. As expected from previous reports on surface-plasmon-based strong coupling, the lifetime of the lower polariton is similar to the lifetime of the uncoupled QDs (about 10-15 ns).[31, 39, 40] Surprisingly, the lifetimes at the higher energy polariton are also similar. Based on previous reports, thermalization from the upper polariton to the lower polariton should result in a much shorter lifetime for the higher energy polariton.[31, 41, 42] Note, however, that this explanation is valid in the non-Markovian regime, where the Rabi splitting is much larger than the thermal energy, kT. In our case, the energy difference (80 meV) between the lower polariton and the higher energy peak is about 3kT (77 meV at 298K), so enough thermal energy is available for polaritons to access the upper polariton from the lower polariton state.[43]

As discussed previously, the higher energy polariton may not be the true upper polariton due to multiple avoided crossings, making this a more difficult system that needs further attention. To complicate matters more, it may not be a valid assumption to model the quantum dots as two-level systems, due to the many energy states near the band-edge; two examples are the dark exciton and the biexciton.

Finally, we note the peculiar power dependence of the polariton emission as shown in Figure 6.8c. When pumped at 400 nm with 80 fs pulses at low fluences, the emission is dominated by the lower polariton. As the fluence increases, the contribution from the higher energy peak increases and eventually equals or overtakes the lower polariton. Based on this, we hypothesize that occupancy of the lower polariton and the upper polariton is defined by the Boltzmann factor. As the pump intensity increases, the local temperature increases, and the contribution of the upper polariton increases. A similar explanation was previously given for emission tuning of QDs at high pump intensities.[44] This is further supported by the fact that both the upper and lower polaritons red-shift with increasing fluence by up to 20 meV each.

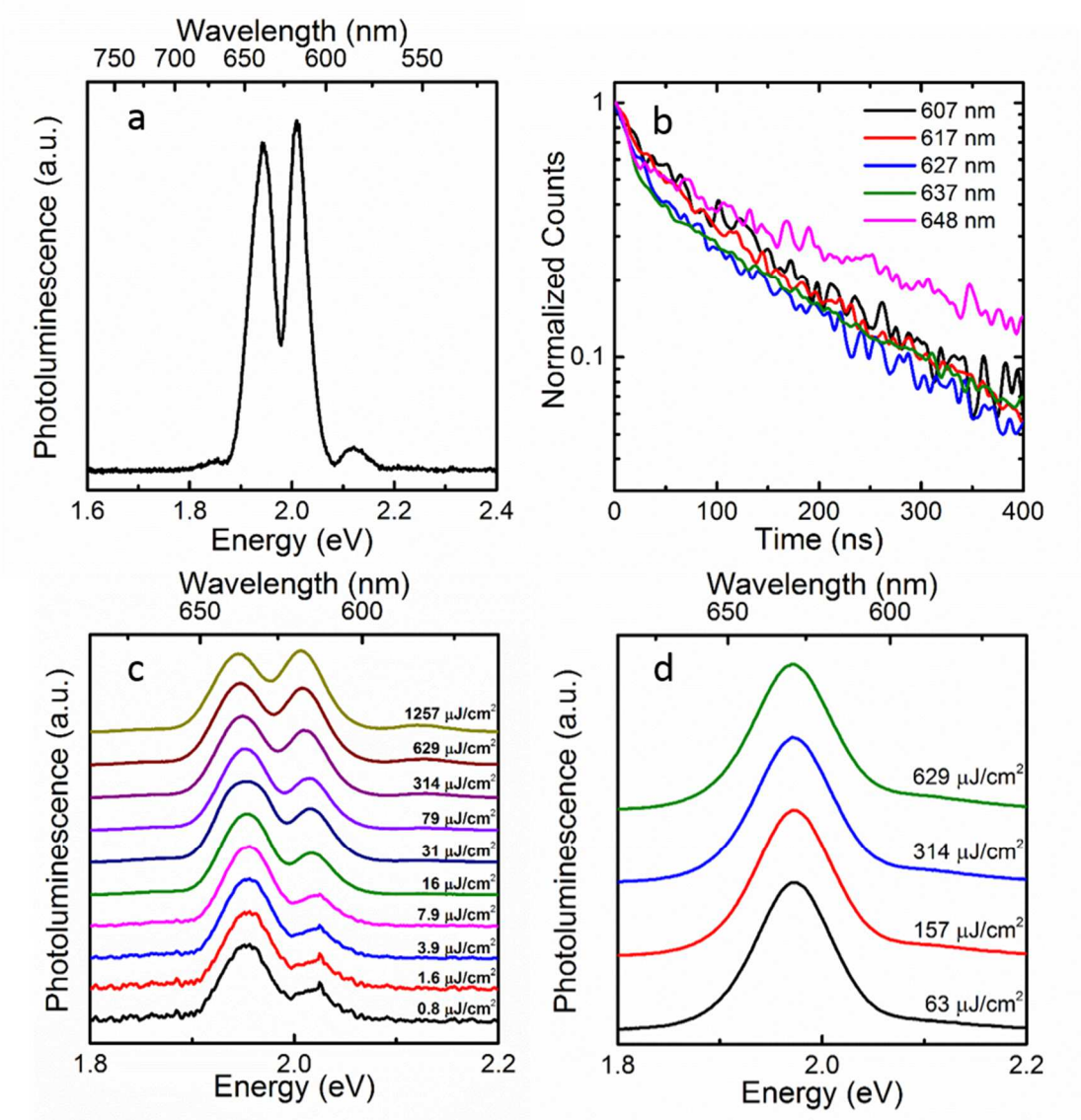

Figure 6.8 Polariton emission dynamics. (a) Polariton emission obtained at a pump fluence of 1257 μJ/cm^2 on a new (but identical to that in Figure 6.4c) sample. (b) Lifetimes obtained at different spectral positions. All lifetimes look similar, with that at 648 nm slightly higher. (c) Power dependence of the polariton emission spectra. The higher polariton increases more quickly with pump power relative to the lower energy polariton. (d) In a control sample, a quantum-dot film of similar thickness was deposited on flat Ag film with 10 nm of alumina. Note no additional feature appears at high pump fluences. Although not obvious, multi-exciton emission increases at the highest pump fluences tested.

The fact that the Rabi splitting is observed at the lowest pump fluence, and that it only depends weakly on the pump fluence indicates that this is vacuum Rabi splitting. It

only depends on the density of the dots and not on the number of photons or surface plasmons in the cavity.

Because the idea of strong coupling is linked to coherence over large distances[7, 45], it has important implications for quantum information processing and thresholdless lasers. Conventional lasers require stimulated emission based amplification of photons or surface plasmons, which in turn requires population inversion.[6, 12] In a strongly coupled state, the polariton emission is coherent by nature and does not require stimulated emission.

In conclusion, we have shown strong coupling in transmission and in photoluminescence between quantum dots and surface plasmons. The Rabi splittings range from 50 meV to 80 meV. Designing plasmonic resonators with higher surface plasmon confinement would lead to larger splittings. We demonstrate the room temperature polariton emission from QD-plasmonic structures. At this moment, it is difficult to conclude whether we saw emission from the upper polariton or a middle polariton. To further clarify this, the decay dynamics in transmission and photoluminescence need to be studied in detail.

6.3 Materials and Methods

Quantum Dot Synthesis

Materials

Cadmium oxide (CdO, 99.999%, 48-0800) was purchased from Strem Chemicals. n-dodecylphosphonic acid (DDPA, 98%, 08118) was purchased from Epsilon Chimie. Diphenylphosphine (DPP, 98%, 252964), hexadecylamine (HDA, 90%, H7408), selenium shot (99.999%, 204307), trioctylphosphine (TOP, 97%, 718165), trioctylphosphine oxide (TOPO, 90%, 346187), 1-octadecene (ODE, 90%, O806), 1-octanethiol (98.5%, 471836), oleylamine (OAm, 70%, O7805), oleic acid (OLA, 90%, 364525), and zinc acetate [$Zn(ac)_2$, 99.99%, 383317] were purchased from Sigma. Anhydrous butanol (99.8%, 281549), hexane (95%, 296090), and methanol (99.8%, 322415) were purchased from Sigma. Anhydrous ethanol (99.5%, MFCD00003568) was purchased from Acros.

Synthesis of Core CdSe Nanocrystals

CdSe cores with a diameter of 4.2 nm with a lowest energy exciton of 592 nm (determined by Yu *et. al.*)[46] were synthesized following a modified recipe by Reiss *et al*.[47] Briefly, 822 mg of CdO, 16.2 g of TOPO, 37.0 g of HDA, and 3.215 g of DDPA were loaded into a four-neck 250 mL round-bottom flask and heated to 90ºC under nitrogen while stirring at 1000 rpm. At 90ºC, the mixture was degassed three times to below 0.1 torr. The flask was returned to nitrogen and then heated to 320ºC until the solution became clear and colorless. The temperature was maintained at 320ºC for an additional fifteen minutes. The temperature was reduced to 260 ºC, the stir rate reduced to 300 rpm and then 8 mL of 1M TOP:Se with 85 µL of DPP was swiftly injected. The stir rate was increased back to 1000 rpm after injection and the temperature maintained at 260ºC. Small aliquots were taken to monitor the spectral position of the lowest energy exciton with a UV-visible spectrometer (Varian Cary 300, UV-vis). To quench the reaction, the heating mantle was removed and cooled with a compressed air-gun to 200ºC. At 200ºC, the flask was submerged in a water bath and at 130ºC 40 mL of anhydrous butanol to prevent solidification of the reaction mixture.

The reaction mixture was then transferred into a nitrogen glovebox, and the mixture was evenly split between six 50 mL centrifuge tubes. Anhydrous methanol was added to each tube to yield a total volume of 50 mL, and centrifuged at 4000 rpm for ten minutes. The clear supernatant was discarded. The precipitate in each tube was redispersed in 20 mL of anhydrous hexane (120 mL total) and left undisturbed overnight. The following day, the tubes were centrifuged at 4000 rpm for 20 minutes to precipitate unreacted material. The supernatant was transferred to six fresh centrifuge tubes. Anhydrous ethanol was added to each tube until the mixture turned turbid, and was centrifuged at 4000 rpm for ten minutes. The supernatant was discarded. The precipitate in each tube was redispersed in 4 mL of anhydrous hexane (24 mL total) and precipitated with ethanol once more until the mixture turned turbid, then centrifuged at 4000 rpm for ten minutes. The supernatant was discarded. The precipitate was redispersed in a total of 20 mL of anhydrous hexane and stored as a concentrated stock solution of cores in an amber vial in the dark until further use.

Cadmium Oleate Stock for CdS Shelling

Cadmium oleate stock was prepared by combining 0.256 g of CdO, 2.6 mL of OLA, and 20 mL ODE in a three-neck 100 mL round-bottom flask and degassed three times at room temperature to below 0.1 torr. The mixture was returned to nitrogen and raised to 270°C until a clear, colorless solution was formed, and then maintained for thirty minutes. The temperature was reduced to 150°C and 1.3 mL of degassed OAm was added to prevent solidification at room temperature. The temperature was then reduced to 100°C, degassed for thirty minutes and then transferred into a nitrogen glovebox for future use.

Zinc Oleate Stock for ZnS Shelling

Zinc oleate stock was prepared by combining 1.1 g of $Zn(ac)_2$, 3.4 mL of OLA, and 21 mL ODE in a three-neck 100 mL round-bottom flask and degassed three times at room temperature to below 0.1 torr while stirring at 800 rpm. The mixture was returned to nitrogen and raised to 200°C until a clear, colorless solution was formed and then maintained for thirty minutes. The temperature was reduced to 150°C and 3.2 mL of degassed OAm was added to prevent solidification at room temperature. The temperature was then reduced to 100°C, degassed for thirty minutes, and then transferred into a nitrogen glovebox for future use.

Growth of CdS/ZnS Shell/Shell on CdSe Nanocrystals

The CdS/ZnS shell/shell was grown on CdSe NCs following Boldt *et al.*[20] Briefly, 100 nmol of CdSe nanocrystals in hexane, 3 mL of ODE, and 3 mL of OAm were combined in a three-neck 100 mL round-bottom flask. The mixture was degassed at room temperature for an hour, then raised to 120°C for twenty minutes while stirring at 800 rpm. The mixture was switched to nitrogen and heated to 305°C at a rate of 16°C/min. At 210°C, two separate syringes of cadmium oleate (0.23 mmol) and octanethiol (a 1.2-fold excess) precursors were each diluted in ODE to give a total volume of 3 mL and injected with a syringe pump at a rate of 1.5 mL/hour for two hours. After precursor injection, the temperature was lowered to 200°C, 1 mL of degassed OLA was added dropwise, and the mixture annealed for an hour at 200°C.

After annealing, the temperature was lowered to 120°C and the reaction mixture was degassed for thirty minutes under vacuum to remove volatiles created or added during

CdS shell growth. After degassing, the flask was switched to nitrogen and the temperature was raised to 280ºC at a rate of 16ºC/min. At 210ºC, two separate syringes of zinc oleate (0.245 mmol) and octanethiol (a 2-fold excess) precursors were each diluted in ODE to give a total volume of 3 mL and injected with a syringe pump at a rate of 2.5 mL/hour for 72 minutes. After precursor injection, the temperature was reduced to 100°C, degassed for ten minutes under vacuum to remove volatiles created or added during ZnS growth, and then transferred into a nitrogen glovebox.

To precipitate and clean the nanocrystals, an equivalent amount of anhydrous ethanol to reaction mixture was added and centrifuged at 4000 rpm for ten minutes. The clear supernatant was discarded. The bright precipitate was redispersed in 4 mL of anhydrous hexane, precipitated with 10 mL of anhydrous ethanol, and centrifuged at 4000 rpm for ten minutes. The clear supernatant was discarded. The precipitate was redispersed in 2 mL of anhydrous hexane, precipitated with 5 mL of anhydrous ethanol, and centrifuged at 4000 rpm for 10 minutes. The clear supernatant was discarded. The nanocrystals were dispersed in 4 mL of anhydrous hexane and stored in the dark until future use. The recipe resulted in core/shell/shell nanocrystals with a first excitonic absorption at 614 nm and emission at 624 nm.

Single-Crystalline Silver Film Deposition and Hole-Array Fabrication

Single-crystalline silver films were prepared following a previously reported recipe.[36] Briefly, the sputterer was initially baked out by running a trial deposition before loading the mica samples. 15 mm squares of highest grade mica (Ted Pella) were cleaved and loaded into a Kurt J. Lesker PVD 75 sputterer. The substrate-source distance was set to 17 cm. Once the chamber was pumped to a pressure of 2×10^{-6} Torr, the temperature was ramped to 360°C at a rate of 3°C/min. After pre-annealing of 1 hour, Ag was sputtered at a rate of 110 nm/min under a 6 mTorr Ar pressure. The sample was allowed to post-anneal for 30 minutes before it was cooled to room temperature. The final thickness of the Ag film was 300 nm and typical AFM scans showed root-mean-squared roughness of 0.5 nm or less.

The sample was carried to the cleanroom in a nitrogen purged bag, and loaded into a dual-beam FEI Helios focused ion beam. 20 x 20 patterns of hole arrays were milled

using a 30 kV acceleration voltage and 40 pA ion-beam current. The periodicity was varied from 400 to 700 nm in steps of 5 nm and the hole diameter was a third of the periodicity.

Transmission and Photoluminescence Measurements

The sample was loaded into a Nikon TE200 inverted microscope, and a tungsten-halogen lamp driven by a Nikon power supply at 150W was used as the white light source. The light transmitted through the sample was collected by a 10x/0.4 NA objective and sent to a Horiba Jobin Yvon Spex Triax 320 imaging spectrometer. A Spec-10 Princeton Instrument charge-coupled device (CCD) was used to record the spectra and images.

Lifetime in Single-Crystalline Ag Hole Arrays

A 405 nm picosecond pulsed laser (LDH-D-C 405, Picoquant) was used to illuminate the sample through the epi-illumination port on the Nikon TE200 inverted microscope. The emission was directed to a single-photon-counting avalanche diode (MPD-SPAD, Picoquant) and measurements were taken with 4 ps binning intervals using the Picoharp module (Picoquant).

Photoluminescence and Lifetime Measurements with Ultrafast Ti:Sapphire Laser

A Spectra-Physics Mai Tai ultrafast oscillator doubled to 400 nm was used to excite the quantum dots on the hole arrays at a repetition rate of 1 kHz. The pulse width was about 80-100 fs, similar to the SPP decay rate, but orders of magnitude faster than QD lifetimes.

Large-Scale Hexagonal Hole Array Fabrication

A monolayer of 522 nm diameter polystyrene beads was spin-coated into a Si wafer with native oxide. The beads were shrunk with UV ozone to a diameter of 260 nm or 160 nm (this would define the hole diameter). A 10 nm Cr layer was evaporated, and subsequently, the beads were removed by sonicating in toluene. Micrometer-deep hole were etched through the silicon using deep reactive ion etching. Finally, a 5 nm Ge layer and 300 nm of Ag were evaporated; the final hole diameter shrunk to about 120 nm (200 nm) for 160 nm (260 nm) beads.

6.4 References

[1] M. G. Harats, N. Livneh, G. Zaiats, S. Yochelis, Y. Paltiel, E. Lifshitz, R. Rapaport, "Full spectral and angular characterization of highly directional emission from nanocrystal quantum dots positioned on circular plasmonic lenses." *Nano Letters* **14**, 5766-5771 (2014).

[2] Y. C. Jun, K. C. Huang, M. L. Brongersma, "Plasmonic beaming and active control over fluorescent emission." *Nature Communications* **2**, 283 (2011).

[3] F. Bernardot, P. Nussenzveig, M. Brune, J. Raimond, S. Haroche, "Vacuum Rabi splitting observed on a microscopic atomic sample in a microwave cavity." *Europhysics Letters* **17**, 33 (1992).

[4] P. Törmä, W. Barnes, "Strong coupling between surface plasmon polaritons and emitters." *Reports on Progress in Physics* **78**, 013901 (2015).

[5] R. Thompson, G. Rempe, H. Kimble, "Observation of normal-mode splitting for an atom in an optical cavity." *Physical Review Letters* **68**, 1132-1135 (1992).

[6] H. Deng, H. Haug, Y. Yamamoto, "Exciton-polariton Bose-Einstein condensation." *Reviews of Modern Physics* **82**, 1489-1537 (2010).

[7] L. Shi, T. K. Hakala, H. T. Rekola, J. P. Martikainen, R. J. Moerland, P. Törmä, "Spatial coherence properties of organic molecules coupled to plasmonic surface lattice resonances in the weak and strong coupling regimes." *Physical Review Letters* **112**, (2014).

[8] K. Hennessy, A. Badolato, M. Winger, D. Gerace, M. Atature, S. Gulde, S. Falt, E. L. Hu, A. Imamoglu, "Quantum nature of a strongly coupled single quantum dot-cavity system." *Nature* **445**, 896-899 (2007).

[9] A. Imamog, D. D. Awschalom, G. Burkard, D. P. DiVincenzo, D. Loss, M. Sherwin, A. Small, "Quantum information processing using quantum dot spins and cavity QED." *Physical Review Letters* **83**, 4204 (1999).

[10] C. Ciuti, "Polaritons: Hungry cavities." *Nature Physics* **10**, 796-797 (2014).

[11] A. Das, J. Heo, M. Jankowski, W. Guo, L. Zhang, H. Deng, P. Bhattacharya, "Room temperature ultralow threshold GaN nanowire polariton laser." *Physical Review Letters* **107**, (2011).

[12] H. Deng, G. Weihs, D. Snoke, J. Bloch, Y. Yamamoto, "Polariton lasing vs. photon lasing in a semiconductor microcavity." *Proceedings of the National Academy of Sciences of the United States of America* **100**, 15318-15323 (2003).

[13] J. Kasprzak, M. Richard, S. Kundermann, A. Baas, P. Jeambrun, J. M. Keeling, F. M. Marchetti, M. H. Szymanska, R. Andre, J. L. Staehli, V. Savona, P. B. Littlewood, B. Deveaud, S. Dang le, "Bose-Einstein condensation of exciton polaritons." *Nature* **443**, 409-414 (2006).

[14] D. Snoke, P. Littlewood, "Polariton condensates." *Physics Today* **63**, 42-47 (2010).

[15] R. Houdré, "Early stages of continuous wave experiments on cavity-polaritons." P*hysica Status Solidi (b)* **242**, 2167-2196 (2005).

[16] V. Savona, L. Andreani, P. Schwendimann, A. Quattropani, "Quantum well excitons in semiconductor microcavities: Unified treatment of weak and strong coupling regimes." *Solid State Communications* **93**, 733-739 (1995).

[17] C. Murray, D. J. Norris, M. G. Bawendi, "Synthesis and characterization of nearly monodisperse CdE (E= sulfur, selenium, tellurium) semiconductor nanocrystallites." *Journal of the American Chemical Society* **115**, 8706-8715 (1993).

[18] O. Chen, J. Zhao, V. P. Chauhan, J. Cui, C. Wong, D. K. Harris, H. Wei, H.-S. Han, D. Fukumura, R. K. Jain, "Compact high-quality CdSe–CdS core–shell nanocrystals with narrow emission linewidths and suppressed blinking." *Nature Materials* **12**, 445-451 (2013).

[19] B. Mahler, P. Spinicelli, S. Buil, X. Quelin, J.-P. Hermier, B. Dubertret, "Towards non-blinking colloidal quantum dots." *Nature Materials* **7**, 659-664 (2008).

[20] K. Boldt, N. Kirkwood, G. A. Beane, P. Mulvaney, "Synthesis of highly luminescent and photo-stable, graded shell CdSe/$Cd_xZn_{1-x}S$ nanoparticles by in situ alloying." *Chemistry of Materials* **25**, 4731-4738 (2013).

[21] S. Brovelli, R. Schaller, S. Crooker, F. García-Santamaría, Y. Chen, R. Viswanatha, J. Hollingsworth, H. Htoon, V. Klimov, "Nano-engineered electron–hole exchange

interaction controls exciton dynamics in core–shell semiconductor nanocrystals." *Nature Communications* **2**, 280 (2011).

[22] Y. Chen, J. Vela, H. Htoon, J. L. Casson, D. J. Werder, D. A. Bussian, V. I. Klimov, J. A. Hollingsworth, ""Giant" multishell cdse nanocrystal quantum dots with suppressed blinking." *Journal of the American Chemical Society* **130**, 5026-5027 (2008).

[23] D. Englund, A. Faraon, I. Fushman, N. Stoltz, P. Petroff, J. Vuckovic, "Controlling cavity reflectivity with a single quantum dot." *Nature* **450**, 857-861 (2007).

[24] D. Englund, A. Majumdar, M. Bajcsy, A. Faraon, P. Petroff, J. Vučković, "Ultrafast photon-photon interaction in a strongly coupled quantum dot-cavity system." *Physical Review Letters* **108**, (2012).

[25] T. Yoshie, A. Scherer, J. Hendrickson, G. Khitrova, H. Gibbs, G. Rupper, C. Ell, O. Shchekin, D. Deppe, "Vacuum Rabi splitting with a single quantum dot in a photonic crystal nanocavity." *Nature* **432**, 200-203 (2004).

[26] J. A. Faucheaux, J. Fu, P. K. Jain, "Unified theoretical framework for realizing diverse regimes of strong coupling between plasmons and electronic transitions." *The Journal of Physical Chemistry C* **118**, 2710-2717 (2014).

[27] J. Bellessa, C. Bonnand, J. Plenet, J. Mugnier, "Strong coupling between surface plasmons and excitons in an organic semiconductor." *Physical Review Letters* **93**, (2004).

[28] J. Dintinger, S. Klein, F. Bustos, W. Barnes, T. Ebbesen, "Strong coupling between surface plasmon-polaritons and organic molecules in subwavelength hole arrays." *Physical Review B* **71**, (2005).

[29] A. Salomon, R. J. Gordon, Y. Prior, T. Seideman, M. Sukharev, "Strong coupling between molecular excited states and surface plasmon modes of a slit array in a thin metal film." *Physical Review Letters* **109**, (2012).

[30] A. Salomon, S. Wang, J. A. Hutchison, C. Genet, T. W. Ebbesen, "Strong light-molecule coupling on plasmonic arrays of different symmetry." *Chemphyschem* **14**, 1882-1886 (2013).

[31] S. Wang, T. Chervy, J. George, J. A. Hutchison, C. Genet, T. W. Ebbesen, "Quantum yield of polariton emission from hybrid light-matter states." *The Journal of Physical Chemistry Letters* **5**, 1433-1439 (2014).

[32] T. Hakala, J. Toppari, A. Kuzyk, M. Pettersson, H. Tikkanen, H. Kunttu, P. Törmä, "Vacuum Rabi splitting and strong-coupling dynamics for surface-plasmon polaritons and Rhodamine 6G molecules." *Physical Review Letters* **103**, 053602 (2009).

[33] T. Schwartz, J. A. Hutchison, C. Genet, T. W. Ebbesen, "Reversible switching of ultrastrong light-molecule coupling." *Physical Review Letters* **106**, (2011).

[34] D. Gomez, K. Vernon, P. Mulvaney, T. Davis, "Surface plasmon mediated strong exciton–photon coupling in semiconductor nanocrystals." *Nano Letters* **10**, 274-278 (2009).

[35] D. E. Gomez, S. S. Lo, T. J. Davis, G. V. Hartland, "Picosecond kinetics of strongly coupled excitons and surface plasmon polaritons." *Journal of Physical Chemistry B* **117**, 4340-4346 (2013).

[36] J. H. Park, P. Ambwani, M. Manno, N. C. Lindquist, P. Nagpal, S. H. Oh, C. Leighton, D. J. Norris, "Single-crystalline silver films for plasmonics." *Advanced Materials* **24**, 3988-3992 (2012).

[37] D. Gomez, K. Vernon, P. Mulvaney, T. Davis, "Coherent superposition of exciton states in quantum dots induced by surface plasmons." *Applied Physics Letters* **96**, 073108 (2010).

[38] W. Chen, K. Chen, M. D. Thoreson, A. Kildishev, V. M. Shalaev, "Ultrathin, ultrasmooth, and low-loss silver films via wetting and annealing." *Applied Physics Letters* **97**, 211107 (2010).

[39] K. H. Madsen, P. Lodahl, "Quantitative analysis of quantum dot dynamics and emission spectra in cavity quantum electrodynamics." *New Journal of Physics* **15**, 025013 (2013).

[40] T. Schwartz, J. A. Hutchison, J. Leonard, C. Genet, S. Haacke, T. W. Ebbesen, "Polariton dynamics under strong light-molecule coupling." *Chemphyschem* **14**, 125-131 (2013).

[41] A. Canaguier-Durand, C. Genet, A. Lambrecht, T. W. Ebbesen, S. Reynaud, "Non-markovian polariton dynamics in organic strong coupling." *arXiv preprint arXiv:1307.8378*, (2013).

[42] C. Genet, A. Lambrecht, T. W. Ebbesen, S. Reynaud, "Non-markovian polariton dynamics in organic strong coupling." *arXiv preprint arXiv:1307.8378*, (2013).

[43] C. Weisbuch, H. Benisty, R. Houdré, "Overview of fundamentals and applications of electrons, excitons and photons in confined structures." *Journal of Luminescence* **85**, 271-293 (2000).

[44] R. Moerland, H. Rekola, G. Sharma, A.-P. Eskelinen, A. Väkeväinen, P. Törmä, "Surface plasmon polariton-controlled tunable quantum-dot emission." *Applied Physics Letters* **100**, 221111 (2012).

[45] S. A. Guebrou, C. Symonds, E. Homeyer, J. Plenet, Y. N. Gartstein, V. M. Agranovich, J. Bellessa, "Coherent emission from a disordered organic semiconductor induced by strong coupling with surface plasmons." *Physical Review Letters* **108**, 066401 (2012).

[46] W. W. Yu, L. Qu, W. Guo, X. Peng, "Experimental determination of the extinction coefficient of CdTe, CdSe, and CdS nanocrystals." *Chemistry of Materials* **15**, 2854-2860 (2003).

[47] P. Reiss, J. Bleuse, A. Pron, "Highly luminescent CdSe/ZnSe core/shell nanocrystals of low size dispersion." *Nano Letters* **2**, 781-784 (2002).

Chapter 7.

Exciton Decay in Ag Doped CdSe Nanocrystals[5]

Electronic impurity doping of semiconductor nanocrystals can enhance their conductivity and optical properties. Recently, light doping of CdSe semiconductor nanocrystals with silver (Ag) atoms was shown to enhance the photoluminescence by a factor of as much as 1000%. We investigate the exciton decay dynamics in doped nanocrystals using photoluminescence excitation, fluorescence line narrowing, and lifetime measurements. When the nanocrystals are doped with a single or a few Ag atoms, the photoluminescence and the lifetime increase, revealing a decrease in both the radiative and the non-radiative rates. At low temperature, the lifetime of lightly doped nanocrystals decrease below that of the undoped nanocrystals. Furthermore, fluorescence line narrowing and photoluminescence excitation measurements at 10K reveal an increased longitudinal optical phonon coupling strength. In heavily doped nanocrystals, decreased photoluminescence and lifetimes suggest increased non-radiative pathways. In the low-doping regime, our measurements indicate that one or both of the electron and hole in the excited nanocrystal are stabilized within the core of the nanocrystal, leading to reduced overlap with the surface. These results are consistent with suggestions of a Ag cation in the nanocrystal at low doping concentrations, and a Ag_2Se phase forming at high concentrations.

[5] This chapter is under preparation for submission as Vincent C. Holmberg*, Sriharsha V. Jayanti*, Lisa Poulikakos, Marianne Aellen, Ayaskanta Sahu, & David J. Norris, "Exciton decay in Ag doped CdSe nanocrystals".

** authors contributed equally*

7.1 Introduction

Quantum-confined semiconductor nanocrystals are color-tunable emitters[1] with high quantum yields[2, 3] and photostabilities.[4, 5] They are important technological materials due to their applications in solid-state lighting[6] and solar cells.[7] For these applications, it is important to increase the traditionally limited conductivity in these materials. One option is to add electronic impurities that provide an electron (n-type doping) or hole (p-type doping) and enhance the conduction. However, introducing a few impurities in a controlled way into nanoscale particles is synthetically challenging.[8] Most of the doping studies have either introduced isovalent atoms[9] or incorporated a large number of impurity atoms.[10, 11] Isovalent impurities do not provide an extra carrier (electron or hole) and therefore, do not improve conductivity. In reports that attempted to add heterovalent impurities such as Cd, Cu, Ag, and Au into InAs nanocrystals (NCs), hundreds of atoms were added to each nanocrystals, likely coating the NC surface.[10, 11]

Recently, introducing a few Ag impurities into CdSe NCs was shown to significantly increase the photoluminescence and electron mobilities.[12] The photoluminescence at a doping concentration of a few Ag atoms per NC increased by up to 1000%, although in most cases the enhancements were about 100%. Beyond an optimal number of dopants, the photoluminescence quantum yield and the electron mobilities decreased monotonically.

However, the effect of Ag impurities on the exciton dynamics and the fine structure is not well understood. Various mechanisms were proposed[12] to explain the large photoluminescence enhancement when a single or few Ag atoms are introduced into each nanocrystal (Figure 7.1). First, the Ag atom could provide an extra carrier into the nanocrystal. Electrochemical doping experiments have previously shown increased radiative rates from trions (negative charged excitons).[13, 14] This is unlikely because Auger recombination is dominant in the presence of charged excitons and leads to quenching of the NCs. Second, the Ag atoms could passivate the trap states in one of two ways: binding to the surface site or by incorporating into the NC as a substitutional impurity and donating a carrier.[15] If Ag^{+} substitutes for Cd^{2+}, this introduces a hole into the system (p-type

doping). Third, the silver atom donates an electron and incorporates into the NC as an interstitial cation (n-type doping). The electron can passivate surface sites. Meanwhile, the ionized silver atom introduces a charge into the core, leading to increased brightness.

More recently, the observed trends in quantum yields with doping were explained using density functional theory and kinetic Monte-Carlo simulations.[15] In the low doping regime, the Ag atoms are interstitial cations that diffuse throughout the nanocrystal. As the concentration increases, repulsive forces push them towards the surface, where they are attracted by a substitutional Ag at the surface previously formed by a kick out reaction of a Cd atom. This leads to the formation of Ag_2Se phase at the surface.

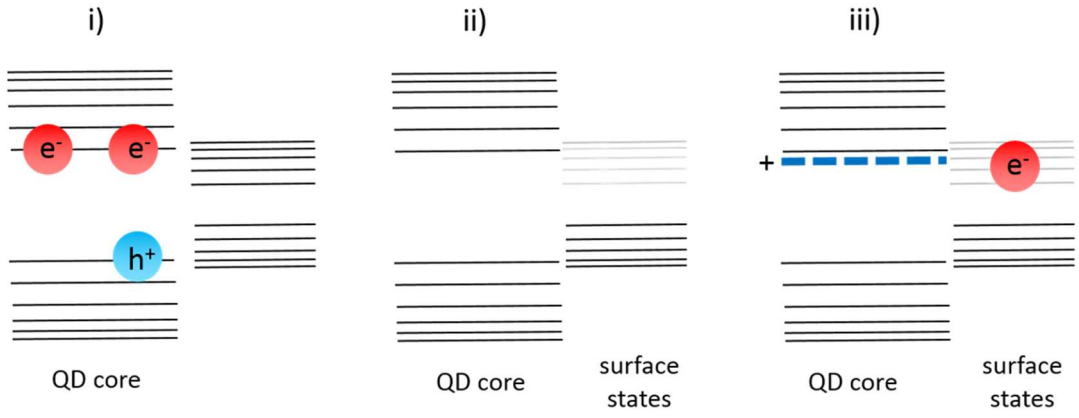

Figure 7.1 Possible mechanisms for fluorescence enhancement in lightly doped CdSe nanocrystals. i) The Ag could introduce a carrier into the nanocrystal, which forms a trion in the excited state, leading to enhanced radiative rates and photoluminescence. ii) The Ag atom could bind to the surface of the nanocrystal, or donate a carrier and incorporate into the nanocrystal. Either way, it could passivate a surface state, which acts as a non-radiative recombination center. These mid-band gap states are indicated by the grayed out energy levels. iii) A Ag atom could donate a carrier, presumably an electron, that passivates surface sites and the Ag cation can incorporate into the nanocrystal as an interstitial dopant. The presence of the cation in the core is the expected reason for 10-fold PL enhancement previously observed.

Based on this, the third mechanism above seems the likely explanation. When the doping concentration is low, Ag atoms could donate electrons that passivate surface sites, and form interstitial cations diffusing within the nanocrystal. The presence of this positive charge in the core could lead to observed fluorescence enhancement. When the doping concentration is high, an Ag_2Se phase could begin to form on the surface, with few or no

interstitial Ag cations. This could increase the non-radiative recombination in the nanocrystals, leading to low PL efficiency.

We conducted temperature dependent photoluminescence, photoluminescence excitation (PLE), fluorescence line narrowing (FLN), and lifetime measurements to understand the mechanism of exciton decay. Photoluminescence excitation and fluorescence line narrowing experiments probe a very small subset of the NC population and as a result, give important information about the electronic structure.[16, 17] Room temperature photoluminescence and lifetime measurements indicate that the increased brightness in lightly doped dots comes from a mix of decreased non-radiative rate and decreased radiative rate of the exciton. PLE and FLN experiments at 10K suggest an increased phonon coupling strength at light doping concentration and decreased coupling strength in heavily doped nanocrystals. All of our results are consistent with, but don't directly confirm, the presence of an interstitial Ag cation in lightly doped NCs.

7.2 Results and Discussion

CdSe NCs of various sizes were synthesized, and doped following a previously established protocol (see section 7.3). The doping concentration was calibrated using inductively coupled plasma-atomic emission spectra (ICP-AES). Figure 7.2 shows the photoluminescence (PL) spectra for NCs with different doping concentrations. Note that the samples were prepared by fixing the absorbance at the band-edge peak to a constant value. As a result, the integrated PL gives the relative quantum yield. When the NCs were doped with a single or few Ag atoms, increased quantum yields were observed. Further increases in the Ag doping concentration decreased the quantum yield. While NCs of all sizes showed the same trend, the typical PL increases were about 30%. We observed a maximum increase of 90%, much lower than some of the results that were reported previously.[12]

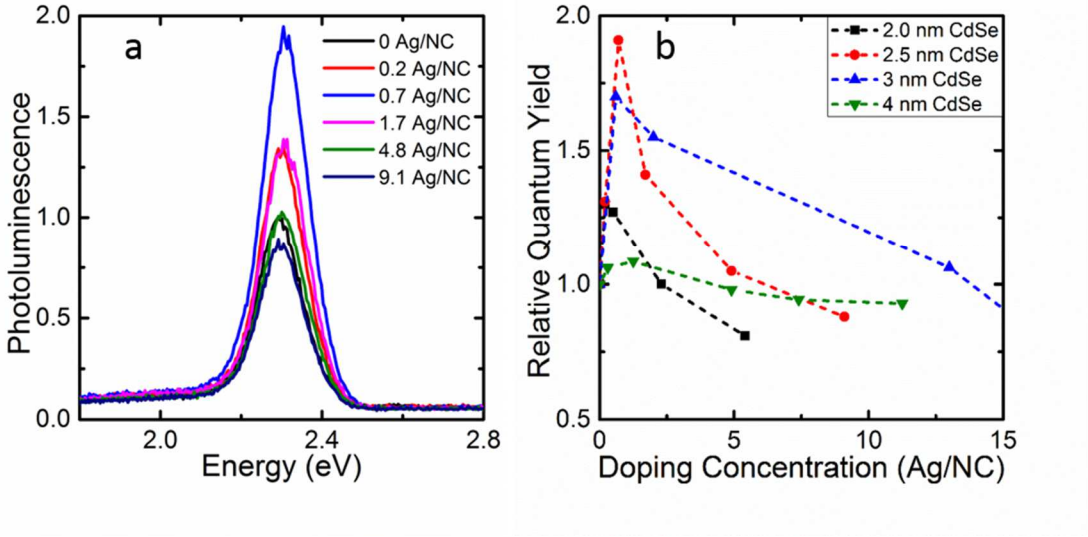

Figure 7.2 Photoluminescence spectra and relative quantum yields of NCs for various sizes and doping concentrations. a) PL spectra of 2.5 nm NCs as a function of average doping concentration. The doping concentration was determined using ICP-AES prior to PL measurements. b) Relative quantum yields as a function of doping. In all sizes of NCs, the quantum yield peaks in the presence of a few dopants per NC, and decreases at high doping levels. The quantum yield increases by a maximum of about 90%, with typical increases close to 30%.

While there are many explanations for this, we consider two possibilities. First, the observed PL enhancement could be strongly dependent on the initial quantum yield of the undoped NCs. The effect of the dopant could be stronger in nanocrystals with lower quantum yields. Once the nanocrystals reach a quantum yield close to 30-40%, the dopants only minimally affect the quantum yield. To rule this out, we measured the quantum yield of NCs as a function of the number of washes of the nanocrystals. Each wash consisted of one cycle of precipitation with ethanol and then redispersion in toluene. With each round, the surface passivation of the NCs should decrease and lead to lower quantum yield. Figure 7.3 shows that the effect of doping is more or less constant and independent of the initial quantum yield. In all cases, the PL increases by a factor 30-70% at low doping concentrations and then decreases.

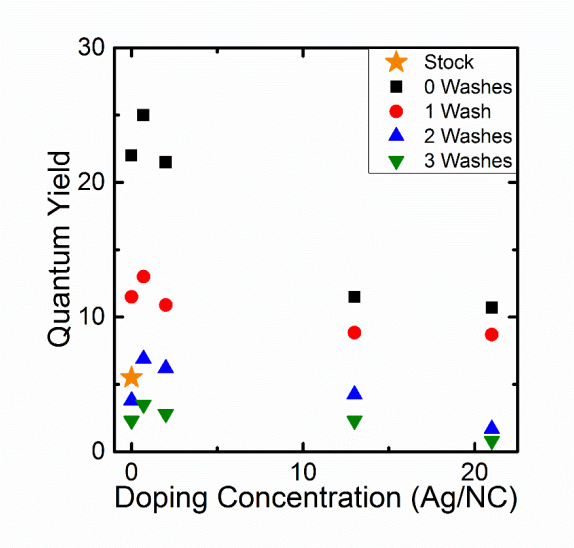

Figure 7.3 Quantum yield for doped 3 nm CdSe NCs after different washes. Each wash involves precipitation with ethanol and redispersion in toluene. Each wash decreases the ligand passivation on the surface, and the quantum yield. The enhancement with doping is nearly constant and irrespective of the washing. The stock undoped quantum dots, denoted by the gold star, are the as-synthesized nanocrystals before making a control to account for the doping procedure.

Another potential reason for lower enhancements in our experiments is the surface stoichiometry. Surface stoichiometry can strongly affect the optical properties in quantum confined NCs.[18] Because of the large surface-to-volume ratio, between 30% and 60% of the atoms are on the surface in our NCs. The PL is known to be quenched in a Se-rich surface, and enhanced in a Cd-rich surface. The PL can also be enhanced by adding tri-octyl phosphine (TOP), which binds to the surface Se atoms. In the case of doped NCs, the surface stoichiometry could determine how the Ag is incorporated. If the Se atoms dominate the surface, the Ag could bind to the Se, and passivate the surface site, instead of incorporating into the NC as an interstitial cation [mechanism (ii) in Figure 7.1]. When Cd atoms are dominant, an Ag atom is more likely to donate a carrier to reduce surface traps and incorporate into the nanocrystal as a cation (mechanism iii). In our case, if we have a Se-dominated surface, the observed changes in PL would result from surface passivation of traps. Meanwhile, researchers in Ref. 12 could have had a Cd-rich surface, leading to large enhancements in PL.

To understand the mechanism further, the PL and lifetime of 2 nm NCs in toluene were measured at room temperature. Lifetimes were measured by exciting the NCs using a picosecond pulsed laser (LDH-D-C 405, Picoquant) at 405 nm and collecting the emission using a single-photon-counting avalanche photodiode (MPD-SPAD, Picoquant) connected to a Picoharp module. The excitation intensity was kept very low to excite the NCs in the single-exciton regime. Figure 7.4 shows the absorption spectra, emission spectra, and the lifetimes as a function of doping. The absorption spectra at all doping levels look identical. The combination of relative quantum yields and lifetime allows a deeper understanding of the exciton decay. The lifetime and quantum yield can be written as

$$\tau = \frac{1}{k_r + k_{nr}} \quad (1)$$

$$QY = \frac{k_r}{k_r + k_{nr}} \quad (2)$$

where k_r is the radiative rate and k_{nr} is the non-radiative rate. The lifetime of the exciton is the inverse of the total rate, and the quantum yield is the percentage of radiative decay. Note that by knowing both of the lifetime and quantum yield, we can calculate both the radiative and the non-radiative rate. If only the surface traps were passivated as in mechanism (ii), the non-radiative rates would decrease, but the radiative rate would not be strongly affected. If a Ag cation stabilizes the electron and keeps it in the core, this would reduce the radiative rate and the non-radiative rate [mechanism (iii)]. The non-radiative rate would decrease due to lowered electron overlap with the surface. Note that both the scenarios would lead to an increased lifetime; to be more specific, we need to look at the relative values. The k_r and k_{nr} can be written as

$$k_r = \frac{QY}{\tau} \quad (3)$$

$$k_{nr} = \frac{1 - QY}{\tau} \quad (4)$$

Assuming a typical quantum yield of 10% for the undoped NCs, we obtained the radiative and the non-radiative rates in Figure 7.5. Both the rates decrease with increasing doping, suggesting that the mechanism (iii) is more likely than mechanism (ii). However, this does not rule out mechanism (ii).

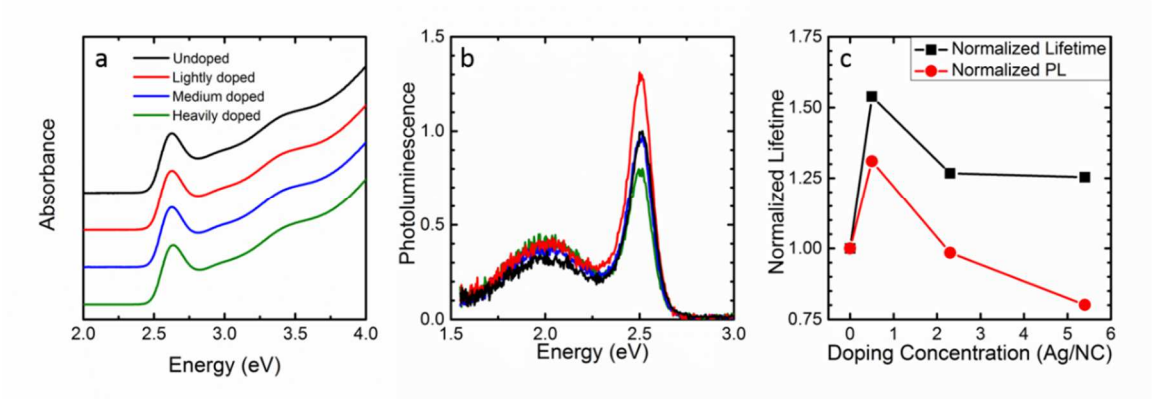

Figure 7.4 Characterization of Ag doped 2 nm nanocrystals in a toluene dispersion. a) The absorption spectra look identical for all doping concentrations. The undoped, lightly doped, medium doped, and heavy doping concentrations are 0 Ag/NC, 0.5 Ag/NC, 2.3 Ag/NC, and 5.4 Ag/NC. b) PL spectra for the different doping concentraitons. The lightly doped and the medium doped correspond to 0.5 and 2.3 Ag/NC. c) Lifetime and PL normalized to undoped NCs. Lifetime of the undoped NCs is 27.25 ns. Note that the increase in the lifetime and PL rule out mechanism i) in Figure 7.1, and in general, any mechanism which involves increased rates.

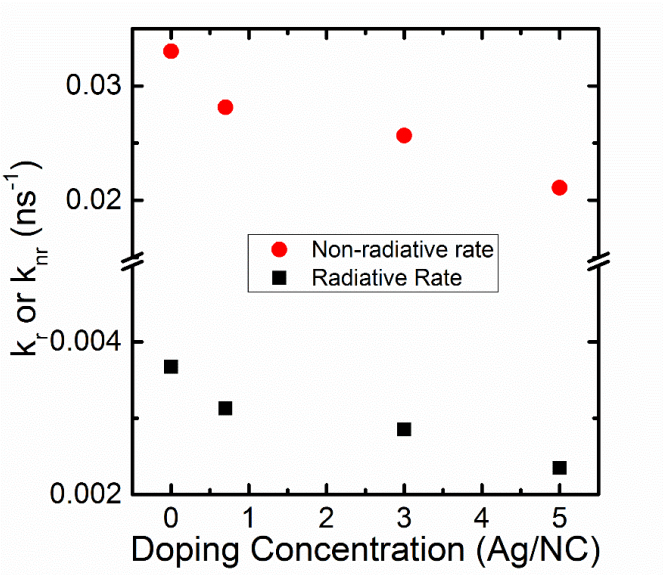

Figure 7.5 The radiative and the non-radiative rates of 2 nm NCs in toluene at room temperature as a function of doping assuming a 10% quantum yield.

Temperature-dependent photoluminescence measurements in 3 nm NCs are shown in Figure 7.6. Measurements were conducted on both freshly prepared doped NCs and another batch washed twice more (from Figure 7.3). The NCs were dispersed in a poly-lauryl methacrylate (PLMA) matrix, which was previously shown to preserve the NC quantum yield.[19] The samples were loaded into a Janis ST-300 cryostat equipped with an

optical window in both right angle and transmission configurations. Figures 7.6a and 7.6b show the photoluminescence spectra of the NCs at various temperatures for the NCs washed 0 and 2 times, respectively. The deep-trap emission is very weak in the unwashed spectra, as expected in well-passivated high-quantum-yield NCs. However, surprisingly, the deep trap emission is weak even at low temperatures. This could result from the use of PLMA matrix. Most of the previous studies were conducted in other matrices or neat films, in which the QDs may not have dispersed very well or were interacting with each other. The NCs that were washed twice had a lower room temperature QY and show a pronounced deep-trap emission peak.

The integrated band-edge intensities at different doping concentrations are shown in Figures 7.6c and 7.6d. Because the intensities at room temperature were fixed to the quantum yields measured in Figure 7.3, these represent qualitative quantum yields as a function of temperature. Note this is not exact since the quantum yield in toluene would be different than in PLMA; however, because PLMA preserves quantum yield, this is reasonable. The undoped and lightly doped NCs both increase in a similar fashion. The PL in heavily doped NCs increases at a dramatically slower rate. At 10K, the emission from the heavily doped NCs appears to be a quarter of that from the undoped NCs. A closer look at the trap emission is useful. The trap emission from the doped NCs includes both the deep-trap emission and a defect-state emission that overlaps with the deep trap. The trap-to-band edge ratio increases much more than that of the undoped dots. Therefore, it appears that the band-edge emission in the heavily doped NCs decreases at the cost of the defect emission.

Meanwhile, the trap emission to band-edge ratio in the lightly doped NCs decreases compared to that in undoped NCs. This is additional support to the idea of decreasing trap recombination in lightly doped NCs.

Figure 7.7 shows the band-edge lifetimes of the differently doped NCs as a function of temperature for various sizes of dots. Consistent with the measurements in dispersion, the lifetimes of lightly doped NCs are always larger than those of undoped at room temperature. Interestingly, at low temperatures, the lifetimes in lightly doped NCs are lower, indicating an increase in the radiative rates in lightly doped NCs at lower

temperature (by looking at the integrated PL in Figure 7.6d divided by lifetime). In the case of heavily doped NCs, the integrated PL decreased more than the lifetimes, indicating slower radiative rates at low temperatures.

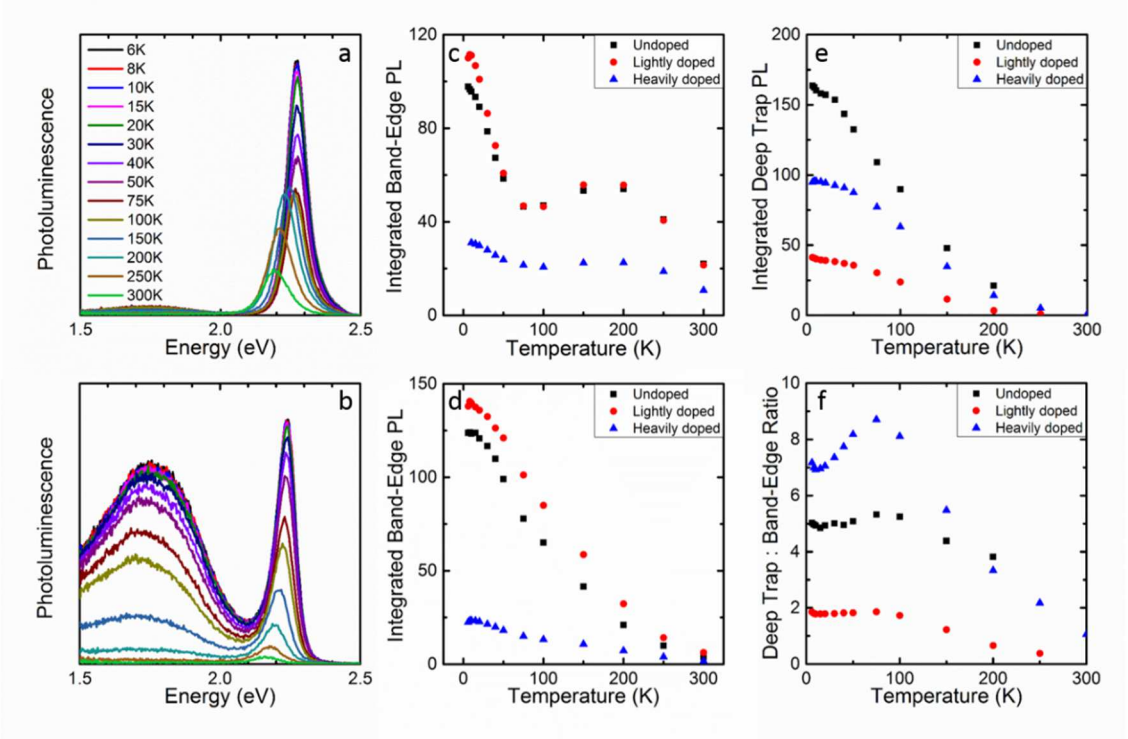

Figure 7.6 Temperature-dependent PL measurements in poly-lauryl methacrylate matrix. a) PL spectra of undoped 3 nm CdSe NCs after 0 washes, as in Figure 7.3, at various temperatures. Very little deep trap emission at lower energy is observed, even at low temperatures. b) PL spectra of the nanocrystals after 2 washes. Because of the lower initial quantum yields, more trap-state emission is evident. c) The band-edge PL of the NCs in a) as a function of temperature. The values were obtained fitting the spectra with 2 Gaussians, and calculating the area in the band-edge Gaussian. d) The band-edge PL of the NCs in b) as a function of temperature. Because the quantum yield of the NCs in b) is lower at room temperature compared to those in a), the band-edge PL increases by a larger factor at lower temperature. In both c) and d), the band-edge PL was normalized to its quantum yield at RT. This is not completely accurate since the PL quantum yield in the PLMA matrix would be different from that in toluene. However, it is not unreasonable because PLMA has been shown to preserve quantum yields. This approach gives a qualitative value for the quantum yield as a function of temperature. Note that while the lightly doped and the undoped are within error, the heavily doped NCs show quantum yields lower than 40% even at low temperatures. This could be a result of silver selenide phase appearing at the NC surface, significantly lowering the band-edge recombination at the expense of defect recombination. To clarify this, e) and f) plot the trap-state emission and the ratio of the trap to the band-edge emission in NCs with 2 washes, respectively. Note that e) shows that the trap emission is lowered in lightly doped NCs. From f), it is clear the trap emission dominates in heavily doped NCs. This trap emission includes the deep trap emission as well the defect emission, a result previously observed in highly doped systems.

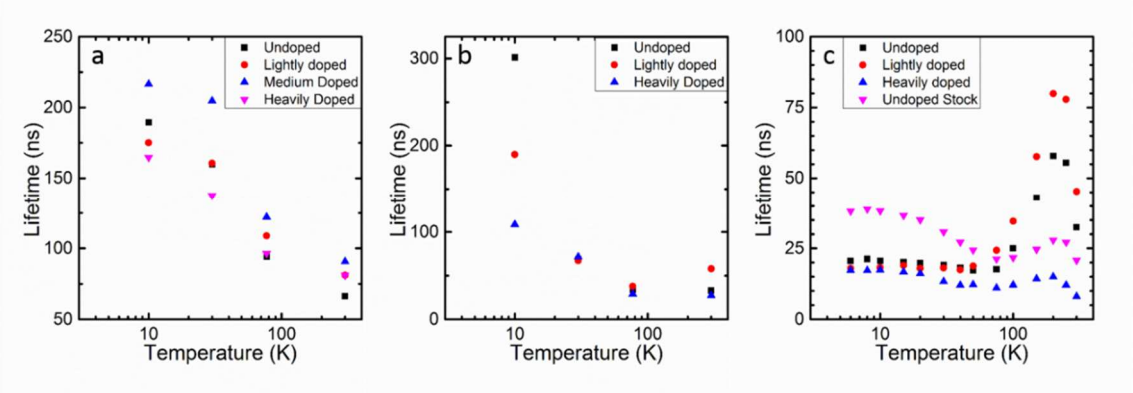

Figure 7.7 Lifetimes as a function of temperature for various doping concentrations in a) 2 nm NCs, b) 2.5 nm NCs, and c) 3 nm NCs. Comparing just the undoped and the lightly doped cases, the lifetime of the lightly doped NCs is always longer at room temperature, and lower at 10K. The heavily doped nanocrystals have the shortest lifetimes at low temperatures. In c), the lifetimes were measured for the NCs with 2 washes. A control was done to measure the lifetimes in the stock undoped NCs. The unexpected decrease in the lifetimes in c) below 200K is due to the surface passivation (or lack of), and not a result of doping.

These results are well supported and further clarified by the fluorescence line narrowing and photoluminescence excitation measurements. In fluorescence line narrowing measurements, a small population of NCs is excited by choosing a wavelength near the red edge of the band-edge absorption line.[16] As a result, a single NC-like spectrum is obtained such that phonon progressions appear in the emission spectra (Figure 7.8b). These phonon replica are periodic with an energy spacing of 25 meV and are termed the zero-phonon line (closest to the excitation energy), one-phonon line, and so on. The sharp peak at 2.27 eV is reflection from the excitation source and is included as a guide. The zero-phonon line is Stokes-shifted from the excitation line by about 11 meV, consistent with previous observations.[20] In photoluminescence excitation, the emission is monitored at a fixed wavelength and the excitation wavelength is scanned. Again, phonon progression are evident in the PLE spectra. The ratio of integrated area under the one-phonon line to the zero-phonon line indicates the strength of the LO-phonon and exciton coupling.[17] In Figure 7.8b, all the FLN and PLE are normalized to the zero phonon line. Note that the lightly doped NCs show an enhanced one-phonon line compared to that of the undoped NCs and the heavily doped NCs show a weaker one-phonon line.

To analyze this quantitatively, we must recognize that each FLN and PLE spectrum is a convolution of the single NC absorption spectrum, single NC emission spectrum, and

the inhomogeneous broadening. We evaluated the convolution integral following the previously established method.[17]

$$I(\nu) = \int A(\nu_{exc}, \nu')\, F(\nu, \nu') e^{-\frac{(\nu'-\nu_0)^2}{2\gamma_{inh}^2}}\, d\nu' \quad (5)$$

Here A is the single NC absorption spectrum evaluated at fixed excitation energy ν_{exc}, and F is the single particle emission spectrum. The exponential term account for the inhomogeneous broadening of the NC ensemble, where ν_0 is the peak energy of ensemble emission and γ_{inh} is the inhomogeneous linewidth. The single NC spectra are given by

$$A(\nu_{exc}, \nu') = \sum_{k=0}^{2} \frac{a_a^k}{k!} exp\left\{-\frac{\left(\nu_{exc}-(\nu'+k\omega_{LO})\right)^2}{2\gamma_{a,k}^2}\right\} \quad (6)$$

$$F(\nu, \nu') = \sum_{b=0}^{2} \frac{a_f^b}{b!} exp\left\{-\frac{\left(\nu-(\nu'-b\omega_{LO}-\Delta)\right)^2}{2\gamma_{f,b}^2}\right\} \quad (7)$$

Note that both the absorption and fluorescence account for two additional phonon replicas (phonon assisted emission or aborption). The longitudinal optical phonon energy is given by ω_{LO}, and the constants a_a and a_f indicate the coupling strength of the phonons (also known as the Huang-Rhys parameter). Δ is the shift between the excitation line and the zero-phonon line.

Our fits are shown in Figure 7.8d. The Huang-Rhys parameter was found to be 0.55, 0.65, and 0.45 for the undoped, lightly doped and heavily doped NCs. The lifetime, the FLN, and PLE measurements indicate that the coupling strength of the LO phonon to the exciton is increased in lightly doped nanocrystals.

We now aim to unify all of our observations. Before doing so, we briefly describe only the relevant fine structure in CdSe NCs. The NCs are have a bright and a dark exciton state.[21, 22] The bright exciton is responsible for the room-temperature emission that we observe. Emission from the dark exciton is forbidden in the dipole approximation, such that little or no emission is observed. The dark exciton state is approximately 10 meV lower than the bright exciton state in NCs of 3 nm diameter.[16] At room temperature, enough thermal energy is available promote the electron from the dark to the bright state. However at temperature of 10K or lower, an electron in the dark state cannot be promoted to the

bright state very easily. Therefore, the lifetimes are much longer, and phonon assisted emission can be observed from the dark state.

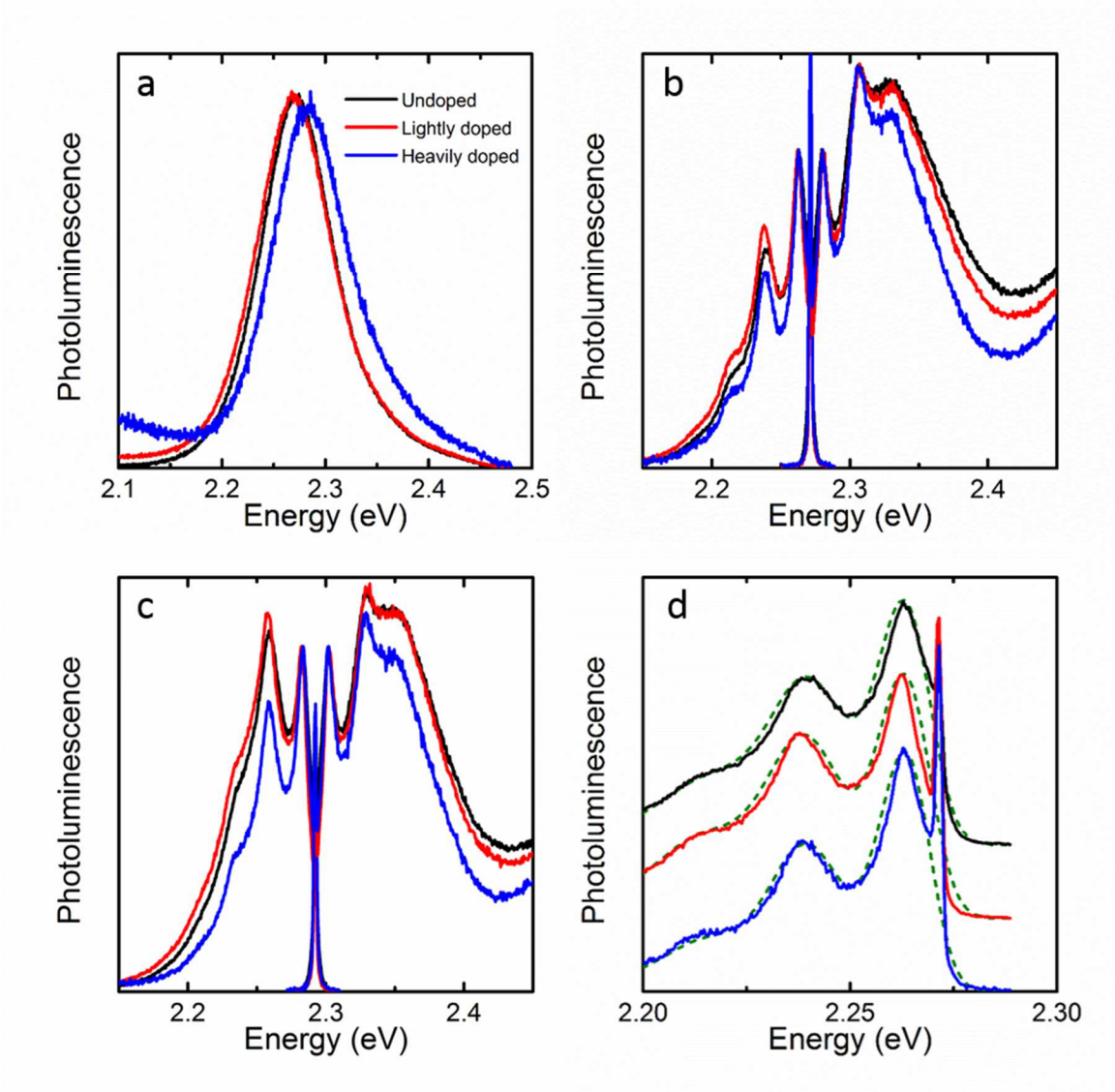

Figure 7.8 Fine structure in doped NCs. a) PL spectra at 10K of 3 nm CdSe NCs with different doping levels. b) Fluorescence-line-narrowing (photoluminescence excitation) spectra obtained by fixing the excitation (emission) at 545 nm. A clear phonon progression is observed. Note the enhanced 1-phonon line compared to the 0-phonon line in the FLN spectra. c) The same trend is observed in FLN (PLE) spectra obtained when excitation (emission) is fixed at 540 nm. d) Best fits (dashed green lines) to the FLN spectra in b) obtained by iteratively reconvoluting the single dot absorption, single dot emission and inhomogeneous broadening spectra. The Huang-Rhys parameter, which indicates the strength of the LO-phonon and exciton coupling, is 0.55, 0.65, and 0.45 for the undoped, lightly doped, and heavily doped NCs.

In the lightly doped case, the Ag atom most likely donates an electron that passivates some of the traps and incorporates into the NC core as an interstitial cation. Calculations suggest that when there is a single Ag dopant, it spends most time in the center of the NC. In our case, this explains the observed lifetime and temperature dependent measurements. The effect of the Ag cation is two-fold: it stabilizes the electron and it draws the electron towards the center of the core. The first decreases the radiative rate at room temperature. The second reduces the overlap with the surface, decreasing the non-radiative rate and the trap state emission in the lightly doped nanocrystals (Figure 7.6). At room temperature, the surface-based effect appears to be the stronger of the two and the lifetime increases. At low temperatures, the Ag^+ cation increases the phonon coupling strength of the exciton and increases the rate.

This raises the question why the increased phonon coupling strength does not significantly enhance the radiative rate at room temperature. At room temperature, the effect of the increased phonon coupling is not as important since abundant thermal energy is available.

In the heavily doped NCs, the Ag atoms incorporate at the surface forming a Ag_2Se phase. While this could reduce some of the surface trap sites, it also adds non-radiative recombination pathways. This explains the reduced emission from these NCs. At low temperatures, the phonon coupling strength is lowered compared to undoped NCs, and the NCs remain dim. As a result, lifetimes are also shorter.

In summary, our experiments characterize the emission dynamics in heterovalently doped CdSe NCs. Room temperature measurement indicate that in the light doping regime, the lifetime increases and the radiative and the non-radiative rates decrease. At low temperature, the increased phonon coupling strength enhances the emission rate. In the heavy doping regime, the PL and the lifetimes decreased and additional trap pathways increase. At low temperature, the phonon coupling strength is reduced. However, the surface of the NCs needs more attention, since its stoichiometry could have a profound effect on the incorporation of Ag dopants.

7.3 Materials and Methods

CdSe Nanocrystal Synthesis

A modified version of a previously established procedure[23] was used to synthesize the CdSe nanocrystals. Briefly, 820 mg (6.4 mmol) CdO, 3.22 g (12.8 mmol) n-dodecylphosphonic acid, 16.2 g (41.9 mmol) trioctylphosphine oxide, and 37.0 g (153 mmol) hexadecylamine were degassed at 90°C in a 250 mL 4-neck flask. The reaction mixture was heated to 320°C under nitrogen and held there until the solution turned clear.

To synthesize 2.0 nm nanocrystals, the heating mantle was removed, and once the temperature reached 300°C, 40 mL of 0.2 M trioctylphosphine selenide (TOP:Se) in trioctylphosphine were rapidly injected while stirring at 300 rpm. The reaction mixture was immediately quenched by cooling the flask with compressed air to 200°C, and then plunging it into an ice bath. As the temperature dropped to 130˚C, 40 mL of 1-butanol were injected.

To obtain 2.5 nm nanocrystals, the temperature was lowered to 290°C and 40 mL of 0.2 M trioctylphosphine selenide (TOP:Se) in trioctylphosphine were rapidly injected. The growth of the nanocrystals at ~280°C was monitored using UV-vis absorbance spectroscopy. Once the nanocrystals reached the desired size, the heating mantle was removed. A water bath was added when the reaction mixture had cooled to 200°C, and 40 mL of 1-butanol were injected at 130°C.

For 3.0 nm nanocrystals, an injection temperature of 285°C was used along with a growth temperature of ~275°C.

For 4.0 nm nanocrystals, an injection temperature of 280°C and a growth temperature of ~270°C were used.

The nanocrystals were washed by precipitating with the addition of 1:1 methanol and centrifuging at 4000 rpm. After re-dispersing in n-hexanes, the nanocrystals were allowed to sit overnight and centrifuged again to precipitate additional unreacted organic material. The supernatant containing the nanocrystals was then washed twice by precipitation with ethanol, followed by centrifugation and re-dispersion in n-hexanes. After

the final wash, the nanocrystals were re-dispersed in toluene at 50 mM CdSe concentration (atomic basis).

Doping Procedure

5 mL of the nanocrystal stock dispersion (250 mmol CdSe atomic units) in toluene and a stir bar were added to a 20 mL scintillation vial. The vial was heated to 60˚C in an oil bath and stirred for 5 minutes at 1200 rpm. Subsequently, 1.25 mL of trioctylphospine were injected. 30 seconds later, a predetermined amount of 0.1 M silver nitrate in ethanol was injected (e.g. for a 1:1 Cd:Ag ratio in the vial, 2.5 mL of $AgNO_3$ would be injected into 5 mL of CdSe nanocrystals in toluene). After 1 minute, a fixed volume of ethanol was injected to quench the reaction (resulting in an identical tolune:ethanol ratio for each sample). The nanocrystals were precipitated by centrifugation for 10 minutes at 4000 rpm (centrifugation was started precisely 5 minutes after the initial trioctylphosphine injection). After washing the nanocrystals with identical quantities of ethanol, the nanocrystals were re-suspended in a concentrated toluene dispersion, and stored in amber vials.

Nanocrystal Packaging in Polylaurylmethacrylate Matrix

CdSe nanocrystals were packaged in polylaurylmethacrylate polymer by a previously established protocol.[19] In a nitrogen glovebox, 5 mg of azobisisobutyronitrile initiator, 100 microliter ethyleneglycol dimethacrylate cross-linker, and 400 microliters of laurylmethacrylate monomer were mixed. A small amount of this mixture was added to dried nanocrystals in a vial. 20 microliters of this dispersion was drop cast onto a 1 cm sapphire disc. The polymer was cured on a hot plate for 2 hours at 75˚C.

Lifetime Measurements

Nanocrystal samples were loaded into a Janis ST-300 compact cryostat with optical windows on three sides. The samples were excited with a 405 nm picosecond pulsed laser (LDH-D-C 405, Picoquant) at a repetition rate of 1 MHz or lower. The emission was sent through a 1/8 m monochromator (Cornerstone 230), and a narrow spectral range was

selected. The emission was sent to a single-photon-counting avalanche photodiode (MPD SPAD, Picoquant) and the data was collected using the Picoharp module (Picoquant).

7.4 References

[1] C. Murray, D. J. Norris, M. G. Bawendi, "Synthesis and characterization of nearly monodisperse CdE (E= sulfur, selenium, tellurium) semiconductor nanocrystallites." *Journal of the American Chemical Society* **115**, 8706-8715 (1993).

[2] B. Dabbousi, J. Rodriguez-Viejo, F. V. Mikulec, J. Heine, H. Mattoussi, R. Ober, K. Jensen, M. Bawendi, "(CdSe) ZnS core-shell quantum dots: Synthesis and characterization of a size series of highly luminescent nanocrystallites." *The Journal of Physical Chemistry B* **101**, 9463-9475 (1997).

[3] O. Chen, J. Zhao, V. P. Chauhan, J. Cui, C. Wong, D. K. Harris, H. Wei, H.-S. Han, D. Fukumura, R. K. Jain, "Compact high-quality CdSe–CdS core–shell nanocrystals with narrow emission linewidths and suppressed blinking." *Nature Materials* **12**, 445-451 (2013).

[4] Y. Chen, J. Vela, H. Htoon, J. L. Casson, D. J. Werder, D. A. Bussian, V. I. Klimov, J. A. Hollingsworth, "“Giant” multishell CdSe nanocrystal quantum dots with suppressed blinking." *Journal of the American Chemical Society* **130**, 5026-5027 (2008).

[5] X. Wang, X. Ren, K. Kahen, M. A. Hahn, M. Rajeswaran, S. Maccagnano-Zacher, J. Silcox, G. E. Cragg, A. L. Efros, T. D. Krauss, "Non-blinking semiconductor nanocrystals." *Nature* **459**, 686-689 (2009).

[6] S. Coe, W.-K. Woo, M. Bawendi, V. Bulović, "Electroluminescence from single monolayers of nanocrystals in molecular organic devices." *Nature* **420**, 800-803 (2002).

[7] I. Gur, N. A. Fromer, M. L. Geier, A. P. Alivisatos, "Air-stable all-inorganic nanocrystal solar cells processed from solution." *Science* **310**, 462-465 (2005).

[8] D. J. Norris, A. L. Efros, S. C. Erwin, "Doped nanocrystals." *Science* **319**, 1776-1779 (2008).

[9] R. Bhargava, D. Gallagher, X. Hong, A. Nurmikko, "Optical properties of manganese-doped nanocrystals of ZnS." *Physical Review Letters* **72**, 416 (1994).

[10] S. M. Geyer, P. M. Allen, L.-Y. Chang, C. R. Wong, T. P. Osedach, N. Zhao, V. Bulovic, M. G. Bawendi, "Control of the carrier type in inas nanocrystal films by predeposition incorporation of Cd." *ACS Nano* **4**, 7373-7378 (2010).

[11] D. Mocatta, G. Cohen, J. Schattner, O. Millo, E. Rabani, U. Banin, "Heavily doped semiconductor nanocrystal quantum dots." *Science* **332**, 77-81 (2011).

[12] A. Sahu, M. S. Kang, A. Kompch, C. Notthoff, A. W. Wills, D. Deng, M. Winterer, C. D. Frisbie, D. J. Norris, "Electronic impurity doping in CdSe nanocrystals." *Nano Letters* **12**, 2587-2594 (2012).

[13] C. Wang, M. Shim, P. Guyot-Sionnest, "Electrochromic nanocrystal quantum dots." *Science* **291**, 2390-2392 (2001).

[14] Y.-S. Park, A. V. Malko, J. Vela, Y. Chen, Y. Ghosh, F. Garcia-Santamaria, J. A. Hollingsworth, V. I. Klimov, H. Htoon, "Near-unity quantum yields of biexciton emission from CdSe/CdS nanocrystals measured using single-particle spectroscopy." *Physical Review Letters* **106**, 187401 (2011).

[15] F. D. Ott, L. L. Spiegel, D. J. Norris, S. C. Erwin, "Microscopic theory of cation exchange in CdSe nanocrystals." *Physical Review Letters* **113**, 156803 (2014).

[16] D. Norris, A. L. Efros, M. Rosen, M. Bawendi, "Size dependence of exciton fine structure in CdSe quantum dots." *Physical Review B* **53**, 16347 (1996).

[17] M. Nirmal, C. Murray, M. Bawendi, "Fluorescence-line narrowing in CdSe quantum dots: Surface localization of the photogenerated exciton." *Physical Review B* **50**, 2293 (1994).

[18] J. Jasieniak, P. Mulvaney, "From Cd-rich to Se-rich-the manipulation of CdSe nanocrystal surface stoichiometry." *Journal of the American Chemical Society* **129**, 2841-2848 (2007).

[19] J. Lee, V. C. Sundar, J. R. Heine, M. G. Bawendi, K. F. Jensen, "Full color emission from ii–vi semiconductor quantum dot–polymer composites." *Advanced Materials* **12**, 1102-1105 (2000).

[20] M. Nirmal, D. Norris, M. Kuno, M. Bawendi, A. L. Efros, M. Rosen, "Observation of the" dark exciton" in CdSe quantum dots." *Physical Review Letters* **75**, 3728 (1995).

[21] A. L. Efros, M. Rosen, M. Kuno, M. Nirmal, D. Norris, M. Bawendi, "Band-edge exciton in quantum dots of semiconductors with a degenerate valence band: Dark and bright exciton states." *Physical Review B* **54**, 4843 (1996).

[22] D. Norris, M. Bawendi, "Measurement and assignment of the size-dependent optical spectrum in CdSe quantum dots." *Physical Review B* **53**, 16338 (1996).

[23] P. Reiss, J. Bleuse, A. Pron, "Highly luminescent CdSe/ZnSe core/shell nanocrystals of low size dispersion." *Nano Letters* **2**, 781-784 (2002).

Bibliography

Chapter 1

[1] A. Boltasseva, H. A. Atwater, "Low-loss plasmonic metamaterials." *Science* **331**, 290-291 (2011).

[2] D. James, *Custom Integrated Circuits Conference*. (IEEE, 2012).

[3] T. W. Ebbesen, H. Lezec, H. Ghaemi, T. Thio, P. Wolff, "Extraordinary optical transmission through sub-wavelength hole arrays." *Nature* **391**, 667-669 (1998).

[4] W. L. Barnes, A. Dereux, T. W. Ebbesen, "Surface plasmon subwavelength optics." *Nature* **424**, 824-830 (2003).

[5] M. Steel, "Quantum plasmonics: Two-plasmon interference." *Nature Photonics* **8**, 273-275 (2014).

[6] P. Berini, I. De Leon, "Surface plasmon-polariton amplifiers and lasers." *Nature Photonics* **6**, 16-24 (2012).

[7] M. Nezhad, K. Tetz, Y. Fainman, "Gain assisted propagation of surface plasmon polaritons on planar metallic waveguides." *Optics Express* **12**, 4072-4079 (2004).

[8] D. K. Gramotnev, S. I. Bozhevolnyi, "Plasmonics beyond the diffraction limit." *Nature Photonics* **4**, 83-91 (2010).

[9] M. I. Stockman, "Spaser action, loss compensation, and stability in plasmonic systems with gain." *Physical Review Letters* **106**, 156802 (2011).

[10] P. Bolger, W. Dickson, A. Krasavin, L. Liebscher, S. Hickey, D. Skryabin, A. Zayats, "Amplified spontaneous emission of surface plasmon polaritons and limitations on the increase of their propagation length." *Optics Letters* **35**, 1197-1199 (2010).

[11] I. De Leon, P. Berini, "Amplification of long-range surface plasmons by a dipolar gain medium." *Nature Photonics* **4**, 382-387 (2010).

[12] S. M. García-Blanco, M. Pollnau, S. I. Bozhevolnyi, "Loss compensation in long-range dielectric-loaded surface plasmon-polariton waveguides." *Optics Express* **19**, 25298-25311 (2011).

[13] S. p. Kéna-Cohen, P. N. Stavrinou, D. D. Bradley, S. A. Maier, "Confined surface plasmon–polariton amplifiers." *Nano Letters* **13**, 1323-1329 (2013).

[14] M. Noginov, V. A. Podolskiy, G. Zhu, M. Mayy, M. Bahoura, J. Adegoke, B. Ritzo, K. Reynolds, "Compensation of loss in propagating surface plasmon polariton by gain in adjacent dielectric medium." *Optics Express* **16**, 1385-1392 (2008).

[15] D. J. Bergman, M. I. Stockman, "Surface plasmon amplification by stimulated emission of radiation: Quantum generation of coherent surface plasmons in nanosystems." *Physical Review Letters* **90**, 027402 (2003).

[16] M. I. Stockman, "The spaser as a nanoscale quantum generator and ultrafast amplifier." *Journal of Optics* **12**, 024004 (2010).

[17] R. Flynn, C. Kim, I. Vurgaftman, M. Kim, J. Meyer, A. Mäkinen, K. Bussmann, L. Cheng, F.-S. Choa, J. Long, "A room-temperature semiconductor spaser operating near 1.5 μm." *Optics Express* **19**, 8954-8961 (2011).

[18] M. Noginov, G. Zhu, A. Belgrave, R. Bakker, V. Shalaev, E. Narimanov, S. Stout, E. Herz, T. Suteewong, U. Wiesner, "Demonstration of a spaser-based nanolaser." *Nature* **460**, 1110-1112 (2009).

[19] N. I. Zheludev, S. Prosvirnin, N. Papasimakis, V. Fedotov, "Lasing spaser." *Nature Photonics* **2**, 351-354 (2008).

[20] K. Shimizu, W. Woo, B. Fisher, H. Eisler, M. Bawendi, "Surface-enhanced emission from single semiconductor nanocrystals." *Physical Review Letters* **89**, 117401 (2002).

[21] Y. C. Jun, K. C. Huang, M. L. Brongersma, "Plasmonic beaming and active control over fluorescent emission." *Nature Communications* **2**, 283 (2011).

[22] P. Andrew, W. Barnes, "Energy transfer across a metal film mediated by surface plasmon polaritons." *Science* **306**, 1002-1005 (2004).

[23] S. Coe, W.-K. Woo, M. Bawendi, V. Bulović, "Electroluminescence from single monolayers of nanocrystals in molecular organic devices." *Nature* **420**, 800-803 (2002).

[24] I. Gur, N. A. Fromer, M. L. Geier, A. P. Alivisatos, "Air-stable all-inorganic nanocrystal solar cells processed from solution." *Science* **310**, 462-465 (2005).

[25] P. V. Kamat, "Quantum dot solar cells. Semiconductor nanocrystals as light harvesters†." *The Journal of Physical Chemistry C* **112**, 18737-18753 (2008).

[26] X. Michalet, F. F. Pinaud, L. A. Bentolila, J. M. Tsay, S. Doose, J. J. Li, G. Sundaresan, A. M. Wu, S. S. Gambhir, S. Weiss, "Quantum dots for live cells, in vivo imaging, and diagnostics." *Science* **307**, 538-544 (2005).

[27] V. Klimov, A. Mikhailovsky, S. Xu, A. Malko, J. Hollingsworth, C. Leatherdale, H.-J. Eisler, M. Bawendi, "Optical gain and stimulated emission in nanocrystal quantum dots." *Science* **290**, 314-317 (2000).

[28] C. Murray, D. J. Norris, M. G. Bawendi, "Synthesis and characterization of nearly monodisperse cde (e= sulfur, selenium, tellurium) semiconductor nanocrystallites." *Journal of the American Chemical Society* **115**, 8706-8715 (1993).

[29] O. Chen, J. Zhao, V. P. Chauhan, J. Cui, C. Wong, D. K. Harris, H. Wei, H.-S. Han, D. Fukumura, R. K. Jain, "Compact high-quality cdse–cds core–shell nanocrystals with narrow emission linewidths and suppressed blinking." *Nature Materials* **12**, 445-451 (2013).

[30] Y. Chen, J. Vela, H. Htoon, J. L. Casson, D. J. Werder, D. A. Bussian, V. I. Klimov, J. A. Hollingsworth, ""Giant" multishell CdSe nanocrystal quantum dots with suppressed blinking." *Journal of the American Chemical Society* **130**, 5026-5027 (2008).

[31] W. Barnes, "Fluorescence near interfaces: The role of photonic mode density." *journal of Modern Optics* **45**, 661-699 (1998).

[32] J. Jasieniak, P. Mulvaney, "From Cd-rich to Se-rich-the manipulation of CdSe nanocrystal surface stoichiometry." *Journal of the American Chemical Society* **129**, 2841-2848 (2007).

[33] P. Nagpal, N. C. Lindquist, S.-H. Oh, D. J. Norris, "Ultrasmooth patterned metals for plasmonics and metamaterials." *Science* **325**, 594-597 (2009).

[34] J.-S. G. Bouillard, W. Dickson, D. P. O'Connor, G. A. Wurtz, A. V. Zayats, "Low-temperature plasmonics of metallic nanostructures." *Nano Letters* **12**, 1561-1565 (2012).

[35] M. Liu, M. Pelton, P. Guyot-Sionnest, "Reduced damping of surface plasmons at low temperatures." *Physical Review B* **79**, 035418 (2009).

[36] M. Mayy, G. Zhu, E. Mayy, A. Webb, M. Noginov, "Low temperature studies of surface plasmon polaritons in silver films." *Journal of Applied Physics* **111**, 094103 (2012).

[37] D. R. Baker, P. V. Kamat, "Tuning the emission of CdSe quantum dots by controlled trap enhancement." *Langmuir* **26**, 11272-11276 (2010).

[38] M. J. Bowers, J. R. McBride, S. J. Rosenthal, "White-light emission from magic-sized cadmium selenide nanocrystals." *Journal of the American Chemical Society* **127**, 15378-15379 (2005).

[39] M. A. Schreuder, K. Xiao, I. N. Ivanov, S. M. Weiss, S. J. Rosenthal, "White light-emitting diodes based on ultrasmall CdSe nanocrystal electroluminescence." *Nano Letters* **10**, 573-576 (2010).

[40] P. Törmä, W. Barnes, "Strong coupling between surface plasmon polaritons and emitters." *Reports on Progress in Physics* **78**, 013901 (2015).

[41] S. A. Guebrou, C. Symonds, E. Homeyer, J. Plenet, Y. N. Gartstein, V. M. Agranovich, J. Bellessa, "Coherent emission from a disordered organic semiconductor induced by strong coupling with surface plasmons." *Physical Review Letters* **108**, 066401 (2012).

[42] L. Shi, T. Hakala, H. Rekola, J.-P. Martikainen, R. Moerland, P. Törmä, "Spatial coherence properties of organic molecules coupled to plasmonic surface lattice resonances in the weak and strong coupling regimes." *Physical Review Letters* **112**, 153002 (2014).

[43] A. Sahu, M. S. Kang, A. Kompch, C. Notthoff, A. W. Wills, D. Deng, M. Winterer, C. D. Frisbie, D. J. Norris, "Electronic impurity doping in CdSe nanocrystals." *Nano Letters* **12**, 2587-2594 (2012).

[44] H. Raether, *Surface Plasmons on Smooth Surfaces*. (Springer, 1988).

[45] S. A. Maier, *Plasmonics: Fundamentals and Applications*. (Springer Science & Business Media, 2007).

[46] M. Moskovits, "Surface-enhanced spectroscopy." *Reviews of Modern Physics* **57**, 783 (1985).

[47] V. I. Klimov, *Semiconductor and metal nanocrystals: Synthesis and electronic and optical properties*. (CRC Press, 2003).

[48] R. Chance, A. Prock, R. Silbey, "Molecular fluorescence and energy transfer near interfaces." *Advances in Chemical Physics* **37**, 65 (1978).

[49] C. B. Murray, C. Kagan, M. Bawendi, "Synthesis and characterization of monodisperse nanocrystals and close-packed nanocrystal assemblies." *Annual Review of Materials Science* **30**, 545-610 (2000).

[50] X. Huang, E. Lindgren, J. R. Chelikowsky, "Surface passivation method for semiconductor nanostructures." *Physical Review B* **71**, 165328 (2005).

[51] W. Li, S. Xie, L. Qian, B. Chang, B. Zou, W. Zhou, R. Zhao, G. Wang, "Large-scale synthesis of aligned carbon nanotubes." *Science* **274**, 1701-1703 (1996).

[52] S. Kim, B. Fisher, H.-J. Eisler, M. Bawendi, "Type-ii quantum dots: CdTe/CdSe (core/shell) and CdSe/ZnTe (core/shell) heterostructures." *Journal of the American Chemical Society* **125**, 11466-11467 (2003).

[53] P. Reiss, J. Bleuse, A. Pron, "Highly luminescent CdSe/ZnSe core/shell nanocrystals of low size dispersion." *Nano Letters* **2**, 781-784 (2002).

Chapter 2

[1] B. A. Movchan, A. V. Demchishin, "Investigation of the structure and properties of thick vacuum-deposited films of nickel, titanium, tungsten, alumina and zirconium dioxide." *Fizika Metallov i Metallovedenie* **28**, 653-660 (1969).

[2] C. R. M. Grovenor, H. T. G. Hentzell, D. A. Smith, "The development of grain structure during growth of metallic films." *Acta Metallurgica* **32**, 773-781 (1984).

[3] J. A. Thornton, "The microstructure of sputter-deposited coatings." *Journal of Vacuum Science & Technology A* **4**, 3059-3065 (1986).

[4] I. Petrov, P. B. Barna, L. Hultman, J. E. Greene, "Microstructural evolution during film growth." *Journal of Vacuum Science & Technology A* **21**, S117-S128 (2003).

[5] C. Delacour, S. Blaize, P. Grosse, J. M. Fedeli, A. l. Bruyant, R. Salas-Montiel, G. Lerondel, A. Chelnokov, "Efficient directional coupling between silicon and copper plasmonic nanoslot waveguides: Toward metal−oxide−silicon nanophotonics." *Nano Letters* **10**, 2922-2926 (2010).

[6] S. Yokogawa, S. P. Burgos, H. A. Atwater, "Plasmonic color filters for CMOS image sensor applications." *Nano Letters* **12**, 4349-4354 (2012).

[7] M. W. Knight, N. S. King, L. F. Liu, H. O. Everitt, P. Nordlander, N. J. Halas, "Aluminum for plasmonics." *ACS Nano* **8**, 834-840 (2014).

[8] Y. Ekinci, H. H. Solak, J. F. Loffler, "Plasmon resonances of aluminum nanoparticles and nanorods." *Journal of Applied Physics* **104**, 083107 (2008).

[9] P. B. Barna, M. Adamik, "Fundamental structure forming phenomena of polycrystalline films and the structure zone models." *Thin Solid Films* **317**, 27-33 (1998).

[10] R. C. O'Handley, D. K. Burge, S. N. Jasperson, E. J. Ashley, "Residual gas and the optical properties of silver films." *Surface Science* **50**, 407-433 (1975).

[11] D. Flötotto, Z. M. Wang, L. P. H. Jeurgens, E. Bischoff, E. J. Mittemeijer, "Effect of adatom surface diffusivity on microstructure and intrinsic stress evolutions during Ag film growth." *Journal of Applied Physics* **112**, 043503 (2012).

[12] C. V. Thompson, "Solid-state dewetting of thin films." *Annual Review of Materials Research* **42**, 399-434 (2012).

[13] R. A. Outlaw, in *Handbook of Vacuum Science and Technology,* D. M. Hoffman, B. Singh, J. H. Thomas, Eds. (Academic Press, San Diego, 1998), 335-375.

[14] J. W. Geus, in *Chemisorption and Reactions on Metallic Films,* J. R. Anderson, Ed. (Academic Press, 1971), Volume 1, 129-224.

[15] K. Yoshihara, K. Nii, "The effect of oxygen potential on the surface self-diffusion coefficient of silver." *Transactions of the Japanese Institute of Metals* **20**, 533-542 (1979).

[16] G. Hass, "Filmed surfaces for reflecting optics." *Journal of the Optical Society of America* **45**, 945-952 (1955).

[17] M. G. Blaber, M. D. Arnold, M. J. Ford, "A review of the optical properties of alloys and intermetallics for plasmonics." *Journal of Physics-Condensed Matter* **22**, 143201 (2010).

[18] H. Savaloni, M. A. Player, "Influence of deposition conditions and of substrate on the structure of UHV deposited erbium films." *Vacuum* **46**, 167-179 (1995).

[19] P. R. Gadkari, A. P. Warren, R. M. Todi, R. V. Petrova, K. R. Coffey, "Comparison of the agglomeration behavior of thin metallic films on sio_2." *Journal of Vacuum Science & Technology A* **23**, 1152-1161 (2005).

[20] H. C. Kim, T. L. Alford, D. R. Allee, "Thickness dependence on the thermal stability of silver thin films." *Applied Physics Letters* **81**, 4287-4289 (2002).

[21] A. N. Pargellis, "Evaporating and sputtering: Substrate heating dependence on deposition rate." *Journal of Vacuum Science & Technology A* **7**, 27-30 (1989).

[22] M. Hegner, P. Wagner, G. Semenza, "Ultralarge atomically flat template-stripped Au surfaces for scanning probe microscopy." *Surface Science* **291**, 39-46 (1993).

[23] P. Nagpal, N. C. Lindquist, S.-H. Oh, D. J. Norris, "Ultrasmooth patterned metals for plasmonics and metamaterials." *Science* **325**, 594-597 (2009).

[24] E. D. Palik, *Handbook of optical constants of solids*. E. D. Palik, Ed., (Academic Press, Burlington, 1997).

[25] A. D. Rakić, "Algorithm for the determination of intrinsic optical constants of metal films: Application to aluminum." *Applied Optics* **34**, 4755-4767 (1995).

[26] P. B. Johnson, R. W. Christy, "Optical constants of the noble metals." *Physical Review B* **6**, 4370-4379 (1972).

[27] K. S. Gadre, T. L. Alford, "Contact angle measurements for adhesion energy evaluation of silver and copper films on parylene-n and SiO_2 substrates." *Journal of Applied Physics* **93**, 919-923 (2003).

[28] K. K. Kakati, H. Wilman, "The development of oriented crystal growth during condensation of gold, silver and copper films in vacuum, and its systematic dependence on the residual gas pressure and adsorption, and the film thickness, atomic mobility and chemical reactivity." *Journal of Physics D: Applied Physics* **6**, 1307-1317 (1973).

[29] M. E. Stewart, C. R. Anderton, L. B. Thompson, J. Maria, S. K. Gray, J. A. Rogers, R. G. Nuzzo, "Nanostructured plasmonic sensors." *Chemical Reviews* **108**, 494-521 (2008).

[30] P. K. Jain, X. H. Huang, I. H. El-Sayed, M. A. El-Sayed, "Noble metals on the nanoscale: Optical and photothermal properties and some applications in imaging, sensing, biology, and medicine." *Accounts of Chemica Research* **41**, 1578-1586 (2008).

[31] M. Hu, J. Y. Chen, Z. Y. Li, L. Au, G. V. Hartland, X. D. Li, M. Marquez, Y. N. Xia, "Gold nanostructures: Engineering their plasmonic properties for biomedical applications." *Chemical Society Reviews* **35**, 1084-1094 (2006).

[32] K. Ray, M. H. Chowdhury, J. R. Lakowicz, "Aluminum nanostructured films as substrates for enhanced fluorescence in the ultraviolet-blue spectral region." *Analytical Chemistry* **79**, 6480-6487 (2007).

[33] S. K. Jha, Z. Ahmed, M. Agio, Y. Ekinci, J. F. Loffler, "Deep-UV surface-enhanced resonance raman scattering of adenine on aluminum nanoparticle arrays." *Journal of the American Chemical Society* **134**, 1966-1969 (2012).

[34] T. Dorfer, M. Schmitt, J. Popp, "Deep-UV surface-enhanced raman scattering." *Journal of Raman Spectroscopy* **38**, 1379-1382 (2007).

[35] M. Castro-Lopez, D. Brinks, R. Sapienza, N. F. van Hulst, "Aluminum for nonlinear plasmonics: Resonance-driven polarized luminescence of Al, Ag, and Au nanoantennas." *Nano Letters* **11**, 4674-4678 (2011).

[36] F. Bisio, R. Proietti Zaccaria, R. Moroni, G. Maidecchi, A. Alabastri, G. Gonella, A. Giglia, L. Andolfi, S. Nannarone, L. Mattera, M. Canepa, "Pushing the high-energy limit of plasmonics." *ACS Nano* **8**, 9239-9247 (2014).

[37] M. Kuttge, E. J. R. Vesseur, J. Verhoeven, H. J. Lezec, H. A. Atwater, A. Polman, "Loss mechanisms of surface plasmon polaritons on gold probed by cathodoluminescence imaging spectroscopy." *Applied Physics Letters* **93**, 113110 (2008).

[38] B. J. Wiley, D. J. Lipomi, J. Bao, F. Capasso, G. M. Whitesides, "Fabrication of surface plasmon resonators by nanoskiving single-crystalline gold microplates." *Nano Letters* **8**, 3023-3028 (2008).

[39] J. S. Huang, V. Callegari, P. Geisler, C. Bruning, J. Kern, J. C. Prangsma, X. F. Wu, T. Feichtner, J. Ziegler, P. Weinmann, M. Kamp, A. Forchel, P. Biagioni, U. Sennhauser, B. Hecht, "Atomically flat single-crystalline gold nanostructures for plasmonic nanocircuitry." *Nature Communications* **1**, 150 (2010).

[40] J. H. Park, P. Ambwani, M. Manno, N. C. Lindquist, P. Nagpal, S. H. Oh, C. Leighton, D. J. Norris, "Single-crystalline silver films for plasmonics." *Advanced Materials* **24**, 3988-3992 (2012).

[41] Y. J. Lu, J. Kim, H. Y. Chen, C. H. Wu, N. Dabidian, C. E. Sanders, C. Y. Wang, M. Y. Lu, B. H. Li, X. G. Qiu, W. H. Chang, L. J. Chen, G. Shvets, C. K. Shih, S. Gwo, "Plasmonic nanolaser using epitaxially grown silver film." *Science* **337**, 450-453 (2012).

[42] Y. W. Wu, C. D. Zhang, N. M. Estakhri, Y. Zhao, J. Kim, M. Zhang, X. X. Liu, G. K. Pribil, A. Alu, C. K. Shih, X. Q. Li, "Intrinsic optical properties and enhanced plasmonic response of epitaxial silver." *Advanced Materials* **26**, 6106-6110 (2014).

Chapter 3

[1] H. Raether, *Surface plasmons on smooth surfaces*. (Springer, 1988).

[2] S. A. Maier, *Plasmonics: Fundamentals and applications*. (Springer, New York, 2007).

[3] W. L. Barnes, A. Dereux, T. W. Ebbesen, "Surface plasmon subwavelength optics." *Nature* **424**, 824-830 (2003).

[4] R. Gordon, D. Sinton, K. L. Kavanagh, A. G. Brolo, "A new generation of sensors based on extraordinary optical transmission." *Acc. Chem. Res.* **41**, 1049-1057 (2008).

[5] J. Homola, "Surface plasmon resonance sensors for detection of chemical and biological species." *Chemical Reviews* **108**, 462-493 (2008).

[6] M. Moskovits, "Surface-enhanced raman spectroscopy: A brief retrospective." *Journal of Raman Spectroscopy* **36**, 485-496 (2005).

[7] T. W. Ebbesen, C. Genet, S. I. Bozhevolnyi, "Surface-plasmon circuitry." *Physics Today* **61**, 44-50 (2008).

[8] P. Bai, H. Son Chu, M. Gu, O. Kurniawan, E. Li, "Integration of plasmonics into nanoelectronic circuits." *Physica B: Condensed Matter* **405**, 2978-2981 (2010).

[9] A. Boltasseva, H. A. Atwater, "Low-loss plasmonic metamaterials." *Science* **331**, 290-291 (2011).

[10] J.-S. G. Bouillard, W. Dickson, D. P. O'Connor, G. A. Wurtz, A. V. Zayats, "Low-temperature plasmonics of metallic nanostructures." *Nano Letters* **12**, 1561-1565 (2012).

[11] P. B. Johnson, R. W. Christy, "Optical constants of the noble metals." *Physical Review B* **6**, 4370-4379 (1972).

[12] T. Holstein, "Optical and infrared volume absorptivity of metals." *Physical Review* **96**, 535 (1954).

[13] R. Gurzhi, "On the theory of the infrared absorptivity of metals." *Soviet Journal of Experimental and Theoretical Physics* **6**, 506 (1958).

[14] R. Gurzhi, "Mutual electron correlations in metal optics." *Soviet Journal of Experimental and Theoretical Physics* **8**, 673-675 (1959).

[15] H. Ehrenreich, H. R. Philipp, "Optical properties of Ag and Cu." *Physical Review* **128**, 1622-1629 (1962).

[16] T. Holstein, "Theory of transport phenomena in an electron-phonon gas." *Annals of Physics* **29**, 410-535 (1964).

[17] W. E. Lawrence, J. W. Wilkins, "Umklapp electron-phonon scattering in the low-temperature resistivity of polyvalent metals." *Physical Review B* **6**, 4466-4482 (1972).

[18] W. E. Lawrence, J. W. Wilkins, "Electron-electron scattering in the transport coefficients of simple metals." *Physical Review B* **7**, 2317-2332 (1973).

[19] W. E. Lawrence, "Electron-electron scattering in the low-temperature resistivity of the noble metals." *Physical Review B* **13**, 5316-5319 (1976).

[20] J. A. McKay, J. A. Rayne, "Temperature dependence of the infrared absorptivity of the noble metals." *Physical Review B* **13**, 673-685 (1976).

[21] R. T. Beach, R. W. Christy, "Electron-electron scattering in the intraband optical conductivity of Cu, Ag, and Au." *Physical Review B* **16**, 5277-5284 (1977).

[22] G. R. Parkins, W. E. Lawrence, R. W. Christy, "Intraband optical conductivity σ(ω,t) of cu, ag, and au: Contribution from electron-electron scattering." *Physical Review B* **23**, 6408-6416 (1981).

[23] E. J. R. Vesseur, R. de Waele, H. J. Lezec, H. A. Atwater, F. J. G. de Abajo, A. Polman, "Surface plasmon polariton modes in a single-crystal au nanoresonator fabricated using focused-ion-beam milling." *Applied Physics Letters* **92**, 083110 (2008).

[24] P. Nagpal, N. C. Lindquist, S. H. Oh, D. J. Norris, "Ultrasmooth patterned metals for plasmonics and metamaterials." *Science* **325**, 594-597 (2009).

[25] N. C. Lindquist, T. W. Johnson, D. J. Norris, S.-H. Oh, "Monolithic integration of continuously tunable plasmonic nanostructures." *Nano Letters* **11**, 3526-3530 (2011).

[26] J. Hyuk Park, P. Nagpal, S.-H. Oh, D. J. Norris, "Improved dielectric functions in metallic films obtained via template stripping." *Applied Physics Letters* **100**, 081105 (2012).

[27] Y. J. Lu, J. Kim, H. Y. Chen, C. H. Wu, N. Dabidian, C. E. Sanders, C. Y. Wang, M. Y. Lu, B. H. Li, X. G. Qiu, W. H. Chang, L. J. Chen, G. Shvets, C. K. Shih, S. Gwo, "Plasmonic nanolaser using epitaxially grown silver film." *Science* **337**, 450-453 (2012).

[28] J. H. Park, P. Ambwani, M. Manno, N. C. Lindquist, P. Nagpal, S.-H. Oh, C. Leighton, D. J. Norris, "Single-crystalline silver films for plasmonics." *Advanced Materials* **24**, 3988-3992 (2012).

[29] Y. Wu, C. Zhang, N. M. Estakhri, Y. Zhao, J. Kim, M. Zhang, X.-X. Liu, G. K. Pribil, A. Alù, C.-K. Shih, X. Li, "Intrinsic optical properties and enhanced plasmonic response of epitaxial silver." *Advanced Materials* **26**, 6106-6110 (2014).

[30] M. Liu, M. Pelton, P. Guyot-Sionnest, "Reduced damping of surface plasmons at low temperatures." *Physical Review B* **79**, (2009).

[31] M. Mayy, G. Zhu, E. Mayy, A. Webb, M. A. Noginov, "Low temperature studies of surface plasmon polaritons in silver films." *Journal of Applied Physics* **111**, 094103 (2012).

[32] M. Hegner, P. Wagner, G. Semenza, "Ultralarge atomically flat template-stripped Au surfaces for scanning probe microscopy." *Surface Science* **291**, 39-46 (1993).

[33] K. M. McPeak, S. V. Jayanti, S. J. P. Kress, S. Meyer, S. Iotti, A. Rossinelli, D. J. Norris, "Plasmonic films can easily be better: Rules and recipes." *ACS Photonics* **2**, 326-333 (2015).

[34] F. C. Nix, D. MacNair, "The thermal expansion of pure metals. Ii: molybdenum, palladium, silver, tantalum, tungsten, platinum, and lead." *Physical Review* **61**, 74-78 (1942).

Chapter 4

[1] W. L. Barnes, A. Dereux, T. W. Ebbesen, "Surface plasmon subwavelength optics." *Nature* **424**, 824-830 (2003).

[2] T. W. Ebbesen, C. Genet, S. I. Bozhevolnyi, "Surface-plasmon circuitry." *Physics Today* **61**, 44 (2008).

[3] T. W. Johnson, Z. J. Lapin, R. Beams, N. C. Lindquist, S. G. Rodrigo, L. Novotny, S.-H. Oh, "Highly reproducible near-field optical imaging with sub-20-nm resolution based on template-stripped gold pyramids." *ACS Nano* **6**, 9168-9174 (2012).

[4] S. Kawata, Y. Inouye, P. Verma, "Plasmonics for near-field nano-imaging and superlensing." *Nature Photonics* **3**, 388-394 (2009).

[5] E. J. Sánchez, L. Novotny, X. S. Xie, "Near-field fluorescence microscopy based on two-photon excitation with metal tips." *Physical Review Letters* **82**, 4014 (1999).

[6] A. V. Zayats, I. I. Smolyaninov, A. A. Maradudin, "Nano-optics of surface plasmon polaritons." *Physics Reports* **408**, 131-314 (2005).

[7] K. Catchpole, A. Polman, "Plasmonic solar cells." *Optics Express* **16**, 21793-21800 (2008).

[8] V. E. Ferry, M. A. Verschuuren, H. B. Li, E. Verhagen, R. J. Walters, R. E. Schropp, H. A. Atwater, A. Polman, "Light trapping in ultrathin plasmonic solar cells." *Optics Express* **18**, A237-A245 (2010).

[9] M. A. Green, S. Pillai, "Harnessing plasmonics for solar cells." *Nature Photonics* **6**, 130-132 (2012).

[10] X. Li, W. C. Choy, L. Huo, F. Xie, W. E. Sha, B. Ding, X. Guo, Y. Li, J. Hou, J. You, "Dual plasmonic nanostructures for high performance inverted organic solar cells." *Advanced Materials* **24**, 3046-3052 (2012).

[11] S. Pillai, K. Catchpole, T. Trupke, M. Green, "Surface plasmon enhanced silicon solar cells." *Journal of Applied Physics* **101**, 093105 (2007).

[12] P. Berini, I. De Leon, "Surface plasmon-polariton amplifiers and lasers." *Nature Photonics* **6**, 16-24 (2012).

[13] D. J. Bergman, M. I. Stockman, "Surface plasmon amplification by stimulated emission of radiation: Quantum generation of coherent surface plasmons in nanosystems." *Physical Review Letters* **90**, 027402 (2003).

[14] M. Noginov, G. Zhu, A. Belgrave, R. Bakker, V. Shalaev, E. Narimanov, S. Stout, E. Herz, T. Suteewong, U. Wiesner, "Demonstration of a spaser-based nanolaser." *Nature* **460**, 1110-1112 (2009).

[15] M. I. Stockman, "Spaser action, loss compensation, and stability in plasmonic systems with gain." *Physical Review Letters* **106**, 156802 (2011).

[16] N. I. Zheludev, S. Prosvirnin, N. Papasimakis, V. Fedotov, "Lasing spaser." *Nature Photonics* **2**, 351-354 (2008).

[17] T. Liebermann, W. Knoll, "Surface-plasmon field-enhanced fluorescence spectroscopy." *Colloids and Surfaces A: Physicochemical and Engineering Aspects* **171**, 115-130 (2000).

[18] P. Pompa, L. Martiradonna, A. Della Torre, F. Della Sala, L. Manna, M. De Vittorio, F. Calabi, R. Cingolani, R. Rinaldi, "Metal-enhanced fluorescence of colloidal nanocrystals with nanoscale control." *Nature Nanotechnology* **1**, 126-130 (2006).

[19] K. Shimizu, W. Woo, B. Fisher, H. Eisler, M. Bawendi, "Surface-enhanced emission from single semiconductor nanocrystals." *Physical Review Letters* **89**, 117401 (2002).

[20] E. Ozbay, "Plasmonics: Merging photonics and electronics at nanoscale dimensions." S*cience* **311**, 189-193 (2006).

[21] F. López-Tejeira, S. G. Rodrigo, L. Martín-Moreno, F. J. García-Vidal, E. Devaux, T. W. Ebbesen, J. R. Krenn, I. Radko, S. I. Bozhevolnyi, M. U. González, "Efficient unidirectional nanoslit couplers for surface plasmons." *Nature Physics* **3**, 324-328 (2007).

[22] H. Ditlbacher, A. Hohenau, D. Wagner, U. Kreibig, M. Rogers, F. Hofer, F. R. Aussenegg, J. R. Krenn, "Silver nanowires as surface plasmon resonators." *Physical Review Letters* **95**, 257403 (2005).

[23] A. Hohenau, J. R. Krenn, A. L. Stepanov, A. Drezet, H. Ditlbacher, B. Steinberger, A. Leitner, F. R. Aussenegg, "Dielectric optical elements for surface plasmons." *Optics Letters* **30**, 893-895 (2005).

[24] P. Törmä, W. Barnes, "Strong coupling between surface plasmon polaritons and emitters." *Reports on Progress in Physics* **78**, 013901 (2015).

[25] A. Boltasseva, H. A. Atwater, "Low-loss plasmonic metamaterials." *Science* **331**, 290-291 (2011).

[26] J.-S. G. Bouillard, W. Dickson, D. P. O'Connor, G. A. Wurtz, A. V. Zayats, "Low-temperature plasmonics of metallic nanostructures." *Nano Letters* **12**, 1561-1565 (2012).

[27] T. Holstein, "Theory of transport phenomena in an electron-phonon gas." *Annals of Physics* **29**, 410-535 (1964).

[28] W. Lawrence, "Electron-electron scattering in the low-temperature resistivity of the noble metals." *Physical Review B* **13**, 5316 (1976).

[29] W. Lawrence, J. Wilkins, "Umklapp electron-phonon scattering in the low-temperature resistivity of polyvalent metals." *Physical Review B* **6**, 4466 (1972).

[30] W. E. Lawrence, J. W. Wilkins, "Electron-electron scattering in the transport coefficients of simple metals." *Physical Review B* **7**, 2317-2332 (1973).

[31] H. Ehrenreich, H. Philipp, "Optical properties of Ag and Cu." *Physical Review* **128**, 1622 (1962).

[32] P. B. Johnson, R.-W. Christy, "Optical constants of the noble metals." *Physical Review B* **6**, 4370 (1972).

[33] R. Beach, R. Christy, "Electron-electron scattering in the intraband optical conductivity of Cu, Ag, and Au." *Physical Review B* **16**, 5277 (1977).

[34] V. Logeeswaran, N. P. Kobayashi, M. S. Islam, W. Wu, P. Chaturvedi, N. X. Fang, S. Y. Wang, R. S. Williams, "Ultrasmooth silver thin films deposited with a germanium nucleation layer." *Nano Letters* **9**, 178-182 (2008).

[35] K. M. McPeak, S. V. Jayanti, S. J. Kress, S. Meyer, S. Iotti, A. Rossinelli, D. J. Norris, "Plasmonic films can easily be better: Rules and recipes." *ACS Photonics*, (2015).

[36] P. Nagpal, N. C. Lindquist, S.-H. Oh, D. J. Norris, "Ultrasmooth patterned metals for plasmonics and metamaterials." *Science* **325**, 594-597 (2009).

[37] S. V. Jayanti, J.-H. Park, A. Dejneka, D. Chvostova, K. M. McPeak, X. Chen, S.-H. Oh, D. J. Norris, "Low-temperature enhancement of plasmonic performance in silver films." *Optical Materials Express* **5**, 5 (2015).

[38] I. De Leon, P. Berini, "Modeling surface plasmon-polariton gain in planar metallic structures." *Optics Express* **17**, 20191-20202 (2009).

[39] M. C. Gather, K. Meerholz, N. Danz, K. Leosson, "Net optical gain in a plasmonic waveguide embedded in a fluorescent polymer." *Nature Photonics* **4**, 457-461 (2010).

[40] D. Y. Fedyanin, A. V. Krasavin, A. V. Arsenin, A. V. Zayats, "Surface plasmon polariton amplification upon electrical injection in highly integrated plasmonic circuits." *Nano Letters* **12**, 2459-2463 (2012).

[41] J. Grandidier, G. C. Des Francs, S. Massenot, A. Bouhelier, L. Markey, J.-C. Weeber, C. Finot, A. Dereux, "Gain-assisted propagation in a plasmonic waveguide at telecom wavelength." *Nano Letters* **9**, 2935-2939 (2009).

[42] M. Nezhad, K. Tetz, Y. Fainman, "Gain assisted propagation of surface plasmon polaritons on planar metallic waveguides." *Optics Express* **12**, 4072-4079 (2004).

[43] S. p. Kéna-Cohen, P. N. Stavrinou, D. D. Bradley, S. A. Maier, "Confined surface plasmon–polariton amplifiers." *Nano Letters* **13**, 1323-1329 (2013).

[44] I. De Leon, P. Berini, "Amplification of long-range surface plasmons by a dipolar gain medium." *Nature Photonics* **4**, 382-387 (2010).

[45] C. Murray, D. J. Norris, M. G. Bawendi, "Synthesis and characterization of nearly monodisperse CdE (E= sulfur, selenium, tellurium) semiconductor nanocrystallites." *Journal of the American Chemical Society* **115**, 8706-8715 (1993).

[46] C. Leatherdale, W.-K. Woo, F. Mikulec, M. Bawendi, "On the absorption cross section of CdSe nanocrystal quantum dots." *The Journal of Physical Chemistry B* **106**, 7619-7622 (2002).

[47] W. W. Yu, L. Qu, W. Guo, X. Peng, "Experimental determination of the extinction coefficient of CdTe, CdSe, and CdS nanocrystals." *Chemistry of Materials* **15**, 2854-2860 (2003).

[48] B. Dabbousi, J. Rodriguez-Viejo, F. V. Mikulec, J. Heine, H. Mattoussi, R. Ober, K. Jensen, M. Bawendi, "(CdSe) ZnS core-shell quantum dots: Synthesis and characterization of a size series of highly luminescent nanocrystallites." *The Journal of Physical Chemistry B* **101**, 9463-9475 (1997).

[49] O. Chen, J. Zhao, V. P. Chauhan, J. Cui, C. Wong, D. K. Harris, H. Wei, H.-S. Han, D. Fukumura, R. K. Jain, "Compact high-quality CdSe–CdS core–shell nanocrystals with narrow emission linewidths and suppressed blinking." *Nature Materials* **12**, 445-451 (2013).

[50] X. Wang, X. Ren, K. Kahen, M. A. Hahn, M. Rajeswaran, S. Maccagnano-Zacher, J. Silcox, G. E. Cragg, A. L. Efros, T. D. Krauss, "Non-blinking semiconductor nanocrystals." *Nature* **459**, 686-689 (2009).

[51] Y. Chen, J. Vela, H. Htoon, J. L. Casson, D. J. Werder, D. A. Bussian, V. I. Klimov, J. A. Hollingsworth, "“Giant” multishell CdSe nanocrystal quantum dots with suppressed blinking." *Journal of the American Chemical Society* **130**, 5026-5027 (2008).

[52] O. Labeau, P. Tamarat, B. Lounis, "Temperature dependence of the luminescence lifetime of single CdSe/ZnS quantum dots." *Physical Review Letters* **90**, 257404 (2003).

[53] C. de Mello Donegá, M. Bode, A. Meijerink, "Size-and temperature-dependence of exciton lifetimes in CdSe quantum dots." *Physical Review B* **74**, 085320 (2006).

[54] S. Crooker, T. Barrick, J. Hollingsworth, V. Klimov, "Multiple temperature regimes of radiative decay in cdse nanocrystal quantum dots: Intrinsic limits to the dark-exciton lifetime." *Applied Physics Letters* **82**, 2793-2795 (2003).

[55] S. Brovelli, R. Schaller, S. Crooker, F. García-Santamaría, Y. Chen, R. Viswanatha, J. Hollingsworth, H. Htoon, V. Klimov, "Nano-engineered electron–hole exchange interaction controls exciton dynamics in core–shell semiconductor nanocrystals." *Nature Communications* **2**, 280 (2011).

[56] A. Nozik, "Quantum dot solar cells." *Physica E: Low-dimensional Systems and Nanostructures* **14**, 115-120 (2002).

[57] I. L. Medintz, H. T. Uyeda, E. R. Goldman, H. Mattoussi, "Quantum dot bioconjugates for imaging, labelling and sensing." *Nature Materials* **4**, 435-446 (2005).

[58] J. Caruge, J. Halpert, V. Wood, V. Bulović, M. Bawendi, "Colloidal quantum-dot light-emitting diodes with metal-oxide charge transport layers." *Nature Photonics* **2**, 247-250 (2008).

[59] Q. Sun, Y. A. Wang, L. S. Li, D. Wang, T. Zhu, J. Xu, C. Yang, Y. Li, "Bright, multicoloured light-emitting diodes based on quantum dots." *Nature Photonics* **1**, 717-722 (2007).

[60] V. Klimov, A. Mikhailovsky, S. Xu, A. Malko, J. Hollingsworth, C. Leatherdale, H.-J. Eisler, M. Bawendi, "Optical gain and stimulated emission in nanocrystal quantum dots." *Science* **290**, 314-317 (2000).

[61] E. Rafailov, M. Cataluna, W. Sibbett, "Mode-locked quantum-dot lasers." *Nature Photonics* **1**, 395-401 (2007).

[62] S. A. Maier, *Plasmonics: Fundamentals and applications*. (Springer Science & Business Media, 2007).

[63] E. Rabani, B. Hetenyi, B. J. Berne, L. E. Brus, "Electronic properties of CdSe nanocrystals in the absence and presence of a dielectric medium." *The Journal of Chemical Physics* **110**, 5355-5369 (1999).

[64] J. Reynolds, J. Hough, "Formulae for dielectric constant of mixtures." *Proceedings of the Physical Society. Section B* **70**, 769 (1957).

[65] B. Jensen, A. Torabi, "Refractive index of hexagonal ii–vi compounds CdSe, CdS, and $CdSe_xS_{1-x}$." *Journal of the Optical Society of America B* **3**, 857-863 (1986).

[66] L. Nair, "Dye lasers." *Progress in Quantum Electronics* **7**, 153-268 (1982).

[67] R. Chance, A. Prock, R. Silbey, "Lifetime of an emitting molecule near a partially reflecting surface." *The Journal of Chemical Physics* **60**, 2744-2748 (1974).

[68] R. Chance, A. Prock, R. Silbey, "Molecular fluorescence and energy transfer near interfaces." *Advanced Chemical Physics* **37**, 65 (1978).

[69] E. H. Hellen, D. Axelrod, "Fluorescence emission at dielectric and metal-film interfaces." *Journal of the Optical Society of America B* **4**, 337-350 (1987).

[70] W. Barnes, "Fluorescence near interfaces: The role of photonic mode density." *Journal of Modern Optics* **45**, 661-699 (1998).

[71] E. Fort, S. Grésillon, "Surface enhanced fluorescence." *Journal of Physics D: Applied Physics* **41**, 013001 (2008).

[72] G. W. Ford, W. H. Weber, "Electromagnetic interactions of molecules with metal surfaces." *Physics Reports* **113**, 195-287 (1984).

[73] S. F. Lee, M. A. Osborne, "Brightening, blinking, bluing and bleaching in the life of a quantum dot: Friend or foe?" *ChemPhysChem* **10**, 2174-2191 (2009).

[74] M. Oda, A. Hasegawa, N. Iwami, K. Nishiura, N. Ando, A. Nishiyama, H. Horiuchi, T. Tani, "Reversible photobluing of CdSe/ZnS/TOPO nanocrystals." *Colloids and Surfaces B: Biointerfaces* **56**, 241-245 (2007).

[75] H. Asami, Y. Abe, T. Ohtsu, I. Kamiya, M. Hara, "Surface state analysis of photobrightening in CdSe nanocrystal thin films." *The Journal of Physical Chemistry B* **107**, 12566-12568 (2003).

[76] H. Asami, I. Kamiya, M. Hara, "Photobrightening and photodarkening in CdSe nanocrystal/polymer thin films." *International Journal of Nanoscience* **1**, 641-644 (2002).

[77] J. Jasieniak, P. Mulvaney, "From Cd-rich to Se-rich-the manipulation of CdSe nanocrystal surface stoichiometry." *Journal of the American Chemical Society* **129**, 2841-2848 (2007).

[78] J. H. Park, P. Ambwani, M. Manno, N. C. Lindquist, P. Nagpal, S. H. Oh, C. Leighton, D. J. Norris, "Single-crystalline silver films for plasmonics." *Advanced Materials* **24**, 3988-3992 (2012).

[79] P. Reiss, J. Bleuse, A. Pron, "Highly luminescent CdSe/ZnSe core/shell nanocrystals of low size dispersion." *Nano Letters* **2**, 781-784 (2002).

Chapter 5

[1] S. Coe, W.-K. Woo, M. Bawendi, V. Bulović, "Electroluminescence from single monolayers of nanocrystals in molecular organic devices." *Nature* **420**, 800-803 (2002).

[2] I. Gur, N. A. Fromer, M. L. Geier, A. P. Alivisatos, "Air-stable all-inorganic nanocrystal solar cells processed from solution." *Science* **310**, 462-465 (2005).

[3] V. Klimov, A. Mikhailovsky, S. Xu, A. Malko, J. Hollingsworth, C. Leatherdale, H.-J. Eisler, M. Bawendi, "Optical gain and stimulated emission in nanocrystal quantum dots." *Science* **290**, 314-317 (2000).

[4] G. Kalyuzhny, R. W. Murray, "Ligand effects on optical properties of CdSe nanocrystals." *The Journal of Physical Chemistry B* **109**, 7012-7021 (2005).

[5] J. Jasieniak, P. Mulvaney, "From Cd-rich to Se-rich-the manipulation of CdSe nanocrystal surface stoichiometry." *Journal of the American Chemical Society* **129**, 2841-2848 (2007).

[6] A. Puzder, A. Williamson, F. Gygi, G. Galli, "Self-healing of CdSe nanocrystals: First-principles calculations." *Physical Review Letters* **92**, (2004).

[7] D. R. Baker, P. V. Kamat, "Tuning the emission of CdSe quantum dots by controlled trap enhancement." *Langmuir* **26**, 11272-11276 (2010).

[8] A. D. Dukes, 3rd, P. C. Samson, J. D. Keene, L. M. Davis, J. P. Wikswo, S. J. Rosenthal, "Single-nanocrystal spectroscopy of white-light-emitting CdSe nanocrystals." *Journal of Physical Chemistry A* **115**, 4076-4081 (2011).

[9] M. A. Schreuder, J. R. McBride, A. D. Dukes III, J. A. Sammons, S. J. Rosenthal, "Control of surface state emission via phosphonic acid modulation in ultrasmall CdSe nanocrystals: The role of ligand electronegativity." *The Journal of Physical Chemistry C* **113**, 8169-8176 (2009).

[10] C. Murray, D. J. Norris, M. G. Bawendi, "Synthesis and characterization of nearly monodisperse CdE (E= sulfur, selenium, tellurium) semiconductor nanocrystallites." *Journal of the American Chemical Society* **115**, 8706-8715 (1993).

[11] T. E. Rosson, S. M. Claiborne, J. R. McBride, B. S. Stratton, S. J. Rosenthal, "Bright white light emission from ultrasmall cadmium selenide nanocrystals." *Journal of the American Chemical Society* **134**, 8006-8009 (2012).

[12] S. Sapra, S. Mayilo, T. A. Klar, A. L. Rogach, J. Feldmann, "Bright white-light emission from semiconductor nanocrystals: By chance and by design." *Advanced Materials* **19**, 569-572 (2007).

[13] M. A. Schreuder, K. Xiao, I. N. Ivanov, S. M. Weiss, S. J. Rosenthal, "White light-emitting diodes based on ultrasmall CdSe nanocrystal electroluminescence." *Nano Letters* **10**, 573-576 (2010).

[14] M. J. Bowers Ii, J. R. McBride, M. D. Garrett, J. A. Sammons, A. D. Dukes Iii, M. A. Schreuder, T. L. Watt, A. R. Lupini, S. J. Pennycook, S. J. Rosenthal, "Structure and ultrafast dynamics of white-light-emitting CdSe nanocrystals." *Journal of the American Chemical Society* **131**, 5730-5731 (2009).

[15] M. J. Bowers, J. R. McBride, S. J. Rosenthal, "White-light emission from magic-sized cadmium selenide nanocrystals." *Journal of the American Chemical Society* **127**, 15378-15379 (2005).

[16] T. W. Ebbesen, H. Lezec, H. Ghaemi, T. Thio, P. Wolff, "Extraordinary optical transmission through sub-wavelength hole arrays." *Nature* **391**, 667-669 (1998).

[17] K. Shimizu, W. Woo, B. Fisher, H. Eisler, M. Bawendi, "Surface-enhanced emission from single semiconductor nanocrystals." *Physical Review Letters* **89**, (2002).

[18] J.-H. Song, T. Atay, S. Shi, H. Urabe, A. V. Nurmikko, "Large enhancement of fluorescence efficiency from CdSe/ZnS quantum dots induced by resonant coupling to spatially controlled surface plasmons." *Nano Letters* **5**, 1557-1561 (2005).

[19] W. Barnes, "Fluorescence near interfaces: The role of photonic mode density." *journal of Modern Optics* **45**, 661-699 (1998).

[20] R. Chance, A. Prock, R. Silbey, "Molecular fluorescence and energy transfer near interfaces." *Advanced Chemical Physics* **37**, 65 (1978).

[21] E.-S. Kwak, J. Henzie, S.-H. Chang, S. K. Gray, G. C. Schatz, T. W. Odom, "Surface plasmon standing waves in large-area subwavelength hole arrays." *Nano Letters* **5**, 1963-1967 (2005).

[22] K. A. Willets, R. P. Van Duyne, "Localized surface plasmon resonance spectroscopy and sensing." *Annual Review of Physical Chemistry* **58**, 267-297 (2007).

[23] Y. C. Jun, K. C. Huang, M. L. Brongersma, "Plasmonic beaming and active control over fluorescent emission." *Nature Communications* **2**, 283 (2011).

[24] T. W. Ebbesen, C. Genet, S. I. Bozhevolnyi, "Surface-plasmon circuitry." *Physics Today* **61**, 44 (2008).

[25] A. Akimov, A. Mukherjee, C. Yu, D. Chang, A. Zibrov, P. Hemmer, H. Park, M. Lukin, "Generation of single optical plasmons in metallic nanowires coupled to quantum dots." *Nature* **450**, 402-406 (2007).

[26] W. Qin, P. Guyot-Sionnest, "Evidence for the role of holes in blinking: Negative and oxidized CdSe/CdS dots." *ACS Nano* **6**, 9125-9132 (2012).

[27] S. K. Sharma, K. Sudarshan, P. Maheshwari, D. Dutta, P. K. Pujari, C. P. Shah, M. Kumar, P. Bajaj, "Direct evidence of Cd vacancies in CdSe nanoparticles: Positron annihilation studies." *The European Physical Journal B* **82**, 335-340 (2011).

[28] S. W. Eijt, A. T. van Veen, H. Schut, P. E. Mijnarends, A. B. Denison, B. Barbiellini, A. Bansil, "Study of colloidal quantum-dot surfaces using an innovative thin-film positron 2D-ACAR method." *Nature Materials* **5**, 23-26 (2006).

[29] S. Fengler, E. Zillner, T. Dittrich, "Density of surface states at CdSe quantum dots by fitting of temperature-dependent surface photovoltage transients with random walk simulations." *The Journal of Physical Chemistry C* **117**, 6462-6468 (2013).

[30] J. Mooney, M. Krause, J. Saari, P. Kambhampati, "Challenge to the deep-trap model of the surface in semiconductor nanocrystals." *Physical Review B* **87**, (2013).

[31] M. M. Krause, J. Mooney, P. Kambhampati, "Chemical and thermodynamic control of the surface of semiconductor nanocrystals for designer white light emitters." *ACS Nano* **7**, 5922-5929 (2013).

[32] G. A. Beane, A. J. Morfa, A. M. Funston, P. Mulvaney, "Defect-mediated energy transfer between ZnO nanocrystals and a conjugated dye." *The Journal of Physical Chemistry C* **116**, 3305-3310 (2012).

[33] C. Galland, Y. Ghosh, A. Steinbruck, M. Sykora, J. A. Hollingsworth, V. I. Klimov, H. Htoon, "Two types of luminescence blinking revealed by spectroelectrochemistry of single quantum dots." *Nature* **479**, 203-207 (2011).

[34] P. Guyot-Sionnest, "Charging colloidal quantum dots by electrochemistry." *Microchimica Acta* **160**, 309-314 (2008).

[35] P. Guyot-Sionnest, E. Lhuillier, H. Liu, "A mirage study of CdSe colloidal quantum dot films, urbach tail, and surface states." *Journal of Chemical Physics* **137**, 154704 (2012).

[36] P. Guyot-Sionnest, B. Wehrenberg, D. Yu, "Intraband relaxation in CdSe nanocrystals and the strong influence of the surface ligands." *Journal of Chemical Physics* **123**, 074709 (2005).

[37] C. Wang, M. Shim, P. Guyot-Sionnest, "Electrochromic nanocrystal quantum dots." *Science* **291**, 2390-2392 (2001).

[38] C. Wang, M. Shim, P. Guyot-Sionnest, "Electrochromic semiconductor nanocrystal films." *Applied Physics Letters* **80**, 4 (2002).

[39] S. Brovelli, C. Galland, R. Viswanatha, V. I. Klimov, "Tuning radiative recombination in Cu-doped nanocrystals via electrochemical control of surface trapping." *Nano Letters* **12**, 4372-4379 (2012).

[40] P. Guyot-Sionnest, M. Shim, C. Matranga, M. Hines, "Intraband relaxation in CdSe quantum dots." *Physical Review B* **60**, R2181 (1999).

[41] P. P. Jha, P. Guyot-Sionnest, "Electrochemical switching of the photoluminescence of single quantum dots." *The Journal of Physical Chemistry C* **114**, 21138-21141 (2010).

[42] H. Liu, A. Pourret, P. Guyot-Sionnest, "Mott and Efros-Shklovskii variable range hopping in CdSe quantum dots films." *ACS Nano* **4**, 5211-5216 (2010).

[43] W. Qin, R. A. Shah, P. Guyot-Sionnest, "CdseS/ZnS alloyed nanocrystal lifetime and blinking studies under electrochemical control." *ACS Nano* **6**, 912-918 (2011).

[44] W. Qin, H. Liu, P. Guyot-Sionnest, "Small bright charged colloidal quantum dots." *ACS Nano* **8**, 283-291 (2013).

[45] A. K. Gooding, D. E. Gómez, P. Mulvaney, "The effects of electron and hole injection on the photoluminescence of CdSe/CdS/ZnS nanocrystal monolayers." *ACS Nano* **2**, 669-676 (2008).

[46] P. Guyot-Sionnest, C. Wang, "Fast voltammetric and electrochromic response of semiconductor nanocrystal thin films." *The Journal of Physical Chemistry B* **107**, 7355-7359 (2003).

[47] S. Brovelli, W. K. Bae, C. Galland, U. Giovanella, F. Meinardi, V. I. Klimov, "Dual-color electroluminescence from dot-in-bulk nanocrystals." *Nano Letters* **14**, 486-494 (2014).

[48] P. Nagpal, N. C. Lindquist, S.-H. Oh, D. J. Norris, "Ultrasmooth patterned metals for plasmonics and metamaterials." *Science* **325**, 594-597 (2009).

[49] C.-M. Chuang, M.-C. Wu, W.-F. Su, K.-C. Cheng, Y.-F. Chen, "High intensity fluorescence of photoactivated silver oxide from composite thin film with periodic array structure." *Applied Physics Letters* **89**, 061912 (2006).

[50] I. Diez, R. H. Ras, "Fluorescent silver nanoclusters." *Nanoscale* **3**, 1963-1970 (2011).

[51] C. Mihalcea, D. Büchel, N. Atoda, J. Tominaga, "Intrinsic fluorescence and quenching effects in photoactivated reactively sputtered silver oxide layers." *Journal of the American Chemical Society* **123**, 7172-7173 (2001).

[52] L. A. Peyser, T.-H. Lee, R. M. Dickson, "Mechanism of Ag n nanocluster photoproduction from silver oxide films." *The Journal of Physical Chemistry B* **106**, 7725-7728 (2002).

[53] J. Zheng, P. R. Nicovich, R. M. Dickson, "Highly fluorescent noble-metal quantum dots." *Annual Review of Physical Chemistry* **58**, 409-431 (2007).

[54] L. A. Peyser, A. E. Vinson, A. P. Bartko, R. M. Dickson, "Photoactivated fluorescence from individual silver nanoclusters." *Science* **291**, 103-106 (2001).

[55] H. Asami, Y. Abe, T. Ohtsu, I. Kamiya, M. Hara, "Surface state analysis of photobrightening in CdSe nanocrystal thin films." *The Journal of Physical Chemistry B* **107**, 12566-12568 (2003).

[56] S. F. Lee, M. A. Osborne, "Brightening, blinking, bluing and bleaching in the life of a quantum dot: Friend or foe?" *Chemphyschem* **10**, 2174-2191 (2009).

[57] M. Oda, A. Hasegawa, N. Iwami, K. Nishiura, N. Ando, A. Nishiyama, H. Horiuchi, T. Tani, "Reversible photobluing of CdSe/ZnS/TOPO nanocrystals." *Colloids and Surfaces B Biointerfaces* **56**, 241-245 (2007).

[58] J. H. Park, P. Ambwani, M. Manno, N. C. Lindquist, P. Nagpal, S. H. Oh, C. Leighton, D. J. Norris, "Single-crystalline silver films for plasmonics." *Advanced Materials* **24**, 3988-3992 (2012).

[59] S. Han, "Theory of thermal emission from periodic structures." *Physical Review B* **80**, (2009).

[60] M. Gao, B. Richter, S. Kirstein, "White-light electroluminescence from self-assembled q-CdSe/PPV multilayer structures." *Advanced Materials* **9**, 802-805 (1997).

[61] E. Jang, S. Jun, H. Jang, J. Lim, B. Kim, Y. Kim, "White-light-emitting diodes with quantum dot color converters for display backlights." *Advanced Materials* **22**, 3076-3080 (2010).

[62] A. H. Mueller, M. A. Petruska, M. Achermann, D. J. Werder, E. A. Akhadov, D. D. Koleske, M. A. Hoffbauer, V. I. Klimov, "Multicolor light-emitting diodes based on semiconductor nanocrystals encapsulated in GaN charge injection layers." *Nano Letters* **5**, 1039-1044 (2005).

[63] S. K. Panda, S. G. Hickey, H. V. Demir, A. Eychmuller, "Bright white-light emitting manganese and copper Co-doped ZnSe quantum dots." *Angewandte Chemie International Edition in English* **50**, 4432-4436 (2011).

[64] D. Norris, A. L. Efros, M. Rosen, M. Bawendi, "Size dependence of exciton fine structure in CdSe quantum dots." *Physical Review B* **53**, 16347 (1996).

[65] S. Dolai, P. R. Nimmala, M. Mandal, B. B. Muhoberac, K. Dria, A. Dass, R. Sardar, "Isolation of bright blue light-emitting CdSe nanocrystals with 6.5 kda core in gram scale: High photoluminescence efficiency controlled by surface ligand chemistry." *Chemistry of Materials* **26**, 1278-1285 (2014).

[66] P. Reiss, J. Bleuse, A. Pron, "Highly luminescent CdSe/ZnSe core/shell nanocrystals of low size dispersion." *Nano Letters* **2**, 781-784 (2002).

[67] J. Lee, V. C. Sundar, J. R. Heine, M. G. Bawendi, K. F. Jensen, "Full color emission from ii–vi semiconductor quantum dot–polymer composites." *Advanced Materials* **12**, 1102-1105 (2000).

[68] T. Nakanishi, B. Ohtani, K. Uosaki, "Fabrication and characterization of CdS-nanoparticle mono-and multilayers on a self-assembled monolayer of alkanedithiols on gold." *The Journal of Physical Chemistry B* **102**, 1571-1577 (1998).

Chapter 6

[1] M. G. Harats, N. Livneh, G. Zaiats, S. Yochelis, Y. Paltiel, E. Lifshitz, R. Rapaport, "Full spectral and angular characterization of highly directional emission from nanocrystal quantum dots positioned on circular plasmonic lenses." *Nano Letters* **14**, 5766-5771 (2014).

[2] Y. C. Jun, K. C. Huang, M. L. Brongersma, "Plasmonic beaming and active control over fluorescent emission." *Nature Communications* **2**, 283 (2011).

[3] F. Bernardot, P. Nussenzveig, M. Brune, J. Raimond, S. Haroche, "Vacuum Rabi splitting observed on a microscopic atomic sample in a microwave cavity." *Europhysics Letters* **17**, 33 (1992).

[4] P. Törmä, W. Barnes, "Strong coupling between surface plasmon polaritons and emitters." *Reports on Progress in Physics* **78**, 013901 (2015).

[5] R. Thompson, G. Rempe, H. Kimble, "Observation of normal-mode splitting for an atom in an optical cavity." *Physical Review Letters* **68**, 1132-1135 (1992).

[6] H. Deng, H. Haug, Y. Yamamoto, "Exciton-polariton Bose-Einstein condensation." *Reviews of Modern Physics* **82**, 1489-1537 (2010).

[7] L. Shi, T. K. Hakala, H. T. Rekola, J. P. Martikainen, R. J. Moerland, P. Törmä, "Spatial coherence properties of organic molecules coupled to plasmonic surface lattice resonances in the weak and strong coupling regimes." *Physical Review Letters* **112**, (2014).

[8] K. Hennessy, A. Badolato, M. Winger, D. Gerace, M. Atature, S. Gulde, S. Falt, E. L. Hu, A. Imamoglu, "Quantum nature of a strongly coupled single quantum dot-cavity system." *Nature* **445**, 896-899 (2007).

[9] A. Imamog, D. D. Awschalom, G. Burkard, D. P. DiVincenzo, D. Loss, M. Sherwin, A. Small, "Quantum information processing using quantum dot spins and cavity QED." *Physical Review Letters* **83**, 4204 (1999).

[10] C. Ciuti, "Polaritons: Hungry cavities." *Nature Physics* **10**, 796-797 (2014).

[11] A. Das, J. Heo, M. Jankowski, W. Guo, L. Zhang, H. Deng, P. Bhattacharya, "Room temperature ultralow threshold GaN nanowire polariton laser." *Physical Review Letters* **107**, (2011).

[12] H. Deng, G. Weihs, D. Snoke, J. Bloch, Y. Yamamoto, "Polariton lasing vs. photon lasing in a semiconductor microcavity." *Proceedings of the National Academy of Sciences of the United States of America* **100**, 15318-15323 (2003).

[13] J. Kasprzak, M. Richard, S. Kundermann, A. Baas, P. Jeambrun, J. M. Keeling, F. M. Marchetti, M. H. Szymanska, R. Andre, J. L. Staehli, V. Savona, P. B. Littlewood, B. Deveaud, S. Dang le, "Bose-Einstein condensation of exciton polaritons." *Nature* **443**, 409-414 (2006).

[14] D. Snoke, P. Littlewood, "Polariton condensates." *Physics Today* **63**, 42-47 (2010).

[15] R. Houdré, "Early stages of continuous wave experiments on cavity-polaritons." P*hysica Status Solidi (b)* **242**, 2167-2196 (2005).

[16] V. Savona, L. Andreani, P. Schwendimann, A. Quattropani, "Quantum well excitons in semiconductor microcavities: Unified treatment of weak and strong coupling regimes." *Solid State Communications* **93**, 733-739 (1995).

[17] C. Murray, D. J. Norris, M. G. Bawendi, "Synthesis and characterization of nearly monodisperse CdE (E= sulfur, selenium, tellurium) semiconductor nanocrystallites." *Journal of the American Chemical Society* **115**, 8706-8715 (1993).

[18] O. Chen, J. Zhao, V. P. Chauhan, J. Cui, C. Wong, D. K. Harris, H. Wei, H.-S. Han, D. Fukumura, R. K. Jain, "Compact high-quality CdSe–CdS core–shell nanocrystals with narrow emission linewidths and suppressed blinking." *Nature Materials* **12**, 445-451 (2013).

[19] B. Mahler, P. Spinicelli, S. Buil, X. Quelin, J.-P. Hermier, B. Dubertret, "Towards non-blinking colloidal quantum dots." *Nature Materials* **7**, 659-664 (2008).

[20] K. Boldt, N. Kirkwood, G. A. Beane, P. Mulvaney, "Synthesis of highly luminescent and photo-stable, graded shell CdSe/$Cd_xZn_{1-x}S$ nanoparticles by in situ alloying." *Chemistry of Materials* **25**, 4731-4738 (2013).

[21] S. Brovelli, R. Schaller, S. Crooker, F. García-Santamaría, Y. Chen, R. Viswanatha, J. Hollingsworth, H. Htoon, V. Klimov, "Nano-engineered electron–hole exchange interaction controls exciton dynamics in core–shell semiconductor nanocrystals." *Nature Communications* **2**, 280 (2011).

[22] Y. Chen, J. Vela, H. Htoon, J. L. Casson, D. J. Werder, D. A. Bussian, V. I. Klimov, J. A. Hollingsworth, ""“Giant” multishell cdse nanocrystal quantum dots with suppressed blinking." *Journal of the American Chemical Society* **130**, 5026-5027 (2008).

[23] D. Englund, A. Faraon, I. Fushman, N. Stoltz, P. Petroff, J. Vuckovic, "Controlling cavity reflectivity with a single quantum dot." *Nature* **450**, 857-861 (2007).

[24] D. Englund, A. Majumdar, M. Bajcsy, A. Faraon, P. Petroff, J. Vučković, "Ultrafast photon-photon interaction in a strongly coupled quantum dot-cavity system." *Physical Review Letters* **108**, (2012).

[25] T. Yoshie, A. Scherer, J. Hendrickson, G. Khitrova, H. Gibbs, G. Rupper, C. Ell, O. Shchekin, D. Deppe, "Vacuum Rabi splitting with a single quantum dot in a photonic crystal nanocavity." *Nature* **432**, 200-203 (2004).

[26] J. A. Faucheaux, J. Fu, P. K. Jain, "Unified theoretical framework for realizing diverse regimes of strong coupling between plasmons and electronic transitions." *The Journal of Physical Chemistry C* **118**, 2710-2717 (2014).

[27] J. Bellessa, C. Bonnand, J. Plenet, J. Mugnier, "Strong coupling between surface plasmons and excitons in an organic semiconductor." *Physical Review Letters* **93**, (2004).

[28] J. Dintinger, S. Klein, F. Bustos, W. Barnes, T. Ebbesen, "Strong coupling between surface plasmon-polaritons and organic molecules in subwavelength hole arrays." *Physical Review B* **71**, (2005).

[29] A. Salomon, R. J. Gordon, Y. Prior, T. Seideman, M. Sukharev, "Strong coupling between molecular excited states and surface plasmon modes of a slit array in a thin metal film." *Physical Review Letters* **109**, (2012).

[30] A. Salomon, S. Wang, J. A. Hutchison, C. Genet, T. W. Ebbesen, "Strong light-molecule coupling on plasmonic arrays of different symmetry." *Chemphyschem* **14**, 1882-1886 (2013).

[31] S. Wang, T. Chervy, J. George, J. A. Hutchison, C. Genet, T. W. Ebbesen, "Quantum yield of polariton emission from hybrid light-matter states." *The Journal of Physical Chemistry Letters* **5**, 1433-1439 (2014).

[32] T. Hakala, J. Toppari, A. Kuzyk, M. Pettersson, H. Tikkanen, H. Kunttu, P. Törmä, "Vacuum Rabi splitting and strong-coupling dynamics for surface-plasmon polaritons and Rhodamine 6G molecules." *Physical Review Letters* **103**, 053602 (2009).

[33] T. Schwartz, J. A. Hutchison, C. Genet, T. W. Ebbesen, "Reversible switching of ultrastrong light-molecule coupling." *Physical Review Letters* **106**, (2011).

[34] D. Gomez, K. Vernon, P. Mulvaney, T. Davis, "Surface plasmon mediated strong exciton–photon coupling in semiconductor nanocrystals." *Nano Letters* **10**, 274-278 (2009).

[35] D. E. Gomez, S. S. Lo, T. J. Davis, G. V. Hartland, "Picosecond kinetics of strongly coupled excitons and surface plasmon polaritons." *Journal of Physical Chemistry B* **117**, 4340-4346 (2013).

[36] J. H. Park, P. Ambwani, M. Manno, N. C. Lindquist, P. Nagpal, S. H. Oh, C. Leighton, D. J. Norris, "Single-crystalline silver films for plasmonics." *Advanced Materials* **24**, 3988-3992 (2012).

[37] D. Gomez, K. Vernon, P. Mulvaney, T. Davis, "Coherent superposition of exciton states in quantum dots induced by surface plasmons." *Applied Physics Letters* **96**, 073108 (2010).

[38] W. Chen, K. Chen, M. D. Thoreson, A. Kildishev, V. M. Shalaev, "Ultrathin, ultrasmooth, and low-loss silver films via wetting and annealing." *Applied Physics Letters* **97**, 211107 (2010).

[39] K. H. Madsen, P. Lodahl, "Quantitative analysis of quantum dot dynamics and emission spectra in cavity quantum electrodynamics." *New Journal of Physics* **15**, 025013 (2013).

[40] T. Schwartz, J. A. Hutchison, J. Leonard, C. Genet, S. Haacke, T. W. Ebbesen, "Polariton dynamics under strong light-molecule coupling." *Chemphyschem* **14**, 125-131 (2013).

[41] A. Canaguier-Durand, C. Genet, A. Lambrecht, T. W. Ebbesen, S. Reynaud, "Non-markovian polariton dynamics in organic strong coupling." *arXiv preprint arXiv:1307.8378*, (2013).

[42] C. Genet, A. Lambrecht, T. W. Ebbesen, S. Reynaud, "Non-markovian polariton dynamics in organic strong coupling." *arXiv preprint arXiv:1307.8378*, (2013).

[43] C. Weisbuch, H. Benisty, R. Houdré, "Overview of fundamentals and applications of electrons, excitons and photons in confined structures." *Journal of Luminescence* **85**, 271-293 (2000).

[44] R. Moerland, H. Rekola, G. Sharma, A.-P. Eskelinen, A. Väkeväinen, P. Törmä, "Surface plasmon polariton-controlled tunable quantum-dot emission." *Applied Physics Letters* **100**, 221111 (2012).

[45] S. A. Guebrou, C. Symonds, E. Homeyer, J. Plenet, Y. N. Gartstein, V. M. Agranovich, J. Bellessa, "Coherent emission from a disordered organic semiconductor induced by strong coupling with surface plasmons." *Physical Review Letters* **108**, 066401 (2012).

[46] W. W. Yu, L. Qu, W. Guo, X. Peng, "Experimental determination of the extinction coefficient of CdTe, CdSe, and CdS nanocrystals." *Chemistry of Materials* **15**, 2854-2860 (2003).

[47] P. Reiss, J. Bleuse, A. Pron, "Highly luminescent CdSe/ZnSe core/shell nanocrystals of low size dispersion." *Nano Letters* **2**, 781-784 (2002).

Chapter 7

[1] C. Murray, D. J. Norris, M. G. Bawendi, "Synthesis and characterization of nearly monodisperse CdE (E= sulfur, selenium, tellurium) semiconductor nanocrystallites." *Journal of the American Chemical Society* **115**, 8706-8715 (1993).

[2] B. Dabbousi, J. Rodriguez-Viejo, F. V. Mikulec, J. Heine, H. Mattoussi, R. Ober, K. Jensen, M. Bawendi, "(CdSe) ZnS core-shell quantum dots: Synthesis and characterization of a size series of highly luminescent nanocrystallites." *The Journal of Physical Chemistry B* **101**, 9463-9475 (1997).

[3] O. Chen, J. Zhao, V. P. Chauhan, J. Cui, C. Wong, D. K. Harris, H. Wei, H.-S. Han, D. Fukumura, R. K. Jain, "Compact high-quality CdSe–CdS core–shell nanocrystals with narrow emission linewidths and suppressed blinking." *Nature Materials* **12**, 445-451 (2013).

[4] Y. Chen, J. Vela, H. Htoon, J. L. Casson, D. J. Werder, D. A. Bussian, V. I. Klimov, J. A. Hollingsworth, "“Giant” multishell CdSe nanocrystal quantum dots with suppressed blinking." *Journal of the American Chemical Society* **130**, 5026-5027 (2008).

[5] X. Wang, X. Ren, K. Kahen, M. A. Hahn, M. Rajeswaran, S. Maccagnano-Zacher, J. Silcox, G. E. Cragg, A. L. Efros, T. D. Krauss, "Non-blinking semiconductor nanocrystals." *Nature* **459**, 686-689 (2009).

[6] S. Coe, W.-K. Woo, M. Bawendi, V. Bulović, "Electroluminescence from single monolayers of nanocrystals in molecular organic devices." *Nature* **420**, 800-803 (2002).

[7] I. Gur, N. A. Fromer, M. L. Geier, A. P. Alivisatos, "Air-stable all-inorganic nanocrystal solar cells processed from solution." *Science* **310**, 462-465 (2005).

[8] D. J. Norris, A. L. Efros, S. C. Erwin, "Doped nanocrystals." *Science* **319**, 1776-1779 (2008).

[9] R. Bhargava, D. Gallagher, X. Hong, A. Nurmikko, "Optical properties of manganese-doped nanocrystals of ZnS." *Physical Review Letters* **72**, 416 (1994).

[10] S. M. Geyer, P. M. Allen, L.-Y. Chang, C. R. Wong, T. P. Osedach, N. Zhao, V. Bulovic, M. G. Bawendi, "Control of the carrier type in inas nanocrystal films by predeposition incorporation of Cd." *ACS Nano* **4**, 7373-7378 (2010).

[11] D. Mocatta, G. Cohen, J. Schattner, O. Millo, E. Rabani, U. Banin, "Heavily doped semiconductor nanocrystal quantum dots." *Science* **332**, 77-81 (2011).

[12] A. Sahu, M. S. Kang, A. Kompch, C. Notthoff, A. W. Wills, D. Deng, M. Winterer, C. D. Frisbie, D. J. Norris, "Electronic impurity doping in CdSe nanocrystals." *Nano Letters* **12**, 2587-2594 (2012).

[13] C. Wang, M. Shim, P. Guyot-Sionnest, "Electrochromic nanocrystal quantum dots." *Science* **291**, 2390-2392 (2001).

[14] Y.-S. Park, A. V. Malko, J. Vela, Y. Chen, Y. Ghosh, F. Garcia-Santamaria, J. A. Hollingsworth, V. I. Klimov, H. Htoon, "Near-unity quantum yields of biexciton emission from CdSe/CdS nanocrystals measured using single-particle spectroscopy." *Physical Review Letters* **106**, 187401 (2011).

[15] F. D. Ott, L. L. Spiegel, D. J. Norris, S. C. Erwin, "Microscopic theory of cation exchange in CdSe nanocrystals." *Physical Review Letters* **113**, 156803 (2014).

[16] D. Norris, A. L. Efros, M. Rosen, M. Bawendi, "Size dependence of exciton fine structure in CdSe quantum dots." *Physical Review B* **53**, 16347 (1996).

[17] M. Nirmal, C. Murray, M. Bawendi, "Fluorescence-line narrowing in CdSe quantum dots: Surface localization of the photogenerated exciton." *Physical Review B* **50**, 2293 (1994).

[18] J. Jasieniak, P. Mulvaney, "From Cd-rich to Se-rich-the manipulation of CdSe nanocrystal surface stoichiometry." *Journal of the American Chemical Society* **129**, 2841-2848 (2007).

[19] J. Lee, V. C. Sundar, J. R. Heine, M. G. Bawendi, K. F. Jensen, "Full color emission from ii–vi semiconductor quantum dot–polymer composites." *Advanced Materials* **12**, 1102-1105 (2000).

[20] M. Nirmal, D. Norris, M. Kuno, M. Bawendi, A. L. Efros, M. Rosen, "Observation of the" dark exciton" in CdSe quantum dots." *Physical Review Letters* **75**, 3728 (1995).

[21] A. L. Efros, M. Rosen, M. Kuno, M. Nirmal, D. Norris, M. Bawendi, "Band-edge exciton in quantum dots of semiconductors with a degenerate valence band: Dark and bright exciton states." *Physical Review B* **54**, 4843 (1996).

[22] D. Norris, M. Bawendi, "Measurement and assignment of the size-dependent optical spectrum in CdSe quantum dots." *Physical Review B* **53**, 16338 (1996).

[23] P. Reiss, J. Bleuse, A. Pron, "Highly luminescent CdSe/ZnSe core/shell nanocrystals of low size dispersion." *Nano Letters* **2**, 781-784 (2002).